DEVELOPMENT AND DEMONSTRATION OF NEW FOCAL PLANE WAVEFRONT SENSING TECHNIQUES FOR HIGH-CONTRAST DIRECT IMAGING OF EXOPLANETS

by

Kelsey L. Miller

A Dissertation Submitted to the Faculty of the

COLLEGE OF OPTICAL SCIENCES

In Partial Fulfillment of the Requirements
For the Degree of

DOCTOR OF PHILOSOPHY

In the Graduate College

THE UNIVERSITY OF ARIZONA

2018

THE UNIVERSITY OF ARIZONA
GRADUATE COLLEGE

As members of the Dissertation Committee, we certify that we have read the dissertation prepared by ***Kelsey Miller***, titled ***Development and Demonstration of Linear Dark Field Control for High-Contrast Imaging of Exoplanets*** and recommend that it be accepted as fulfilling the dissertation requirement for the Degree of Doctor of Philosophy.

Olivier Guyon Date: 11/16/18

Jared Males Date: 11/16/18

Michael Hart Date: 11/16/18

Final approval and acceptance of this dissertation is contingent upon the candidate's submission of the final copies of the dissertation to the Graduate College.

We hereby certify that we have read this dissertation prepared under our direction and recommend that it be accepted as fulfilling the dissertation requirement.

Olivier Guyon Date: 11/16/18
Associate Professor/Associate Astronomer
Optical Sciences/Steward Observatory

Jared Males Date: 11/16/18
Assistant Astronomer
Steward Observatory

ACKNOWLEDGEMENTS

To my fellow lab mates, Justin Knight, Jhen Lumbres, Alex Rodack, Kyle Van Gorkom, Joseph Long, Alex Hedglen, Chris Bohlman, Maggie Kautz, Lauren Schatz, Madison Jean and my office mate Eckhart Spalding - thank you for the camaraderie, support, and friendship, and for making the long hours and the rough days bearable. To Mary Liang, my first lab mate and Purveyor of Alignment Wisdom - thank you for being my friend and mentor, especially in the early days when I knew nothing about optics. To my committee: Drs. Olivier Guyon, Jared Males, and Michael Hart - thank you for being constant sources of encouragement and wisdom. A special thanks in particular to adviser # 2, Dr. Jared Males - thank you for bringing me onboard the MagAO-X project and for being a source of help and advice long before becoming my official adviser. To Dr. Katie Morzinski - thank you for being a boundless fount of knowledge regarding the mysterious workings of MEMs deformable mirrors. I'd like to also acknowledge Dr. Sandrine Thomas for her expertise and advice in implementing electric field conjugation in simulation and helping me create my first dark hole. A special thanks also to Kim Chapman and Matt Thrasher for all the comforting afternoon chats when I was avoiding work, the long hours of endless paperwork, and for keeping the lights on in CAAO.

To my family, Dennis, Kerry, and Delaney Miller - thank you for being The Original Support Team and for taking all the late-night panicked phone calls. To Dr. Silvana Ayala, my dissertation writing buddy - this dissertation wouldn't exist without you. To all of the friends I have made in the last six years who have become my Tucson family - there aren't words. You kept me sane and you made this whole journey a wonderful and worthwhile experience.

DEDICATION

This dissertation is dedicated to all of the wonderful friends and family without whom I would never have made it through this degree. As the saying goes: it takes a village. I am so thankful for the constant love and support you all have shown me. All of you mean the world to me, and I am genuinely, deeply grateful. Thank you.

TABLE OF CONTENTS

TABLE OF CONTENTS – *Continued*

TABLE OF CONTENTS – *Continued*

LIST OF FIGURES

LIST OF FIGURES – *Continued*

LIST OF FIGURES – *Continued*

LIST OF FIGURES – *Continued*

LIST OF TABLES

ABSTRACT

With extremely large telescopes coming online over the next few decades, the ability to directly image and characterize Earth-like exoplanets is finally within reach. With state-of-the-art technology, coronagraphs and phase conjugation techniques are now capable of creating regions of high contrast, known as dark holes, within which light from an exoplanet can be made visible above the stellar signal at small separations from the star. This will allow for direct imaging of an exoplanet in reflected light. Maintaining the high-contrast within the dark hole to keep the exoplanet visible over long observation runs, however, has proven to be a challenge.

In this dissertation, I demonstrate new methods of maintaining high-contrast to allow for continuous direct imaging of an exoplanet within the dark hole both in simulation and in laboratory experiments. These techniques, known as modal wavefront sensing (MWFS) and linear dark field control (LDFC), use the science image detector as the wavefront sensor and allow for precision monitoring of aberrations in the image that destroy the high-contrast within the dark hole and overwhelm the light from the exoplanet. With these algorithms, the dark hole contrast is stabilized, and the exoplanet remains visible for direct imaging over long observation periods. The substantial increase in uninterrupted observation time that MWFS and LDFC provide over current stabilization methods will result in an overall increase in the number of exoplanets detected and analyzed over the lifetime of an instrument, thereby bringing the current state of technology one step closer to finding and characterizing another Earth-like planet.

CHAPTER 1

High-Contrast Direct Exoplanet Imaging

In less than three decades, the existence of 3,826 exoplanets has been confirmed.[1] In the upcoming era of 30 meter class ground-based telescopes and new space-based observatories, there is the promise of discovery, even characterization, of many more exoplanets; this includes potentially Earth-like worlds. With such powerful instruments on the horizon, it has become imperative to push the boundaries of astronomical instrumentation and develop new technologies that will provide these observatories with the ability to detect the faint signal emanating from an exoplanet.

Such technology includes instruments and algorithms that can (1) deliver high-precision imaging, and (2) suppress the light from the star that dominates the faint exoplanetary signal. The field of astronomical instrumentation is growing quickly, and the hardware and algorithms for achieving these goals are continually being developed and improved upon. This chapter will provide an overview of the fundamentals of direct exoplanet imaging. Section 1.1 will review the basic principles of light propagation through an optical imaging system. Section 1.2 describes the challenges faced by direct imaging systems. Section 1.3 reviews current direct imaging methods and their operating principles. Finally, Section 1.4 introduces the need for new techniques that will allow for continuous direct imaging capabilities and an introduction to the following chapters of this paper.

1.1 Light propagation and image formation

To understand direct imaging techniques and the associated challenges to overcome, it must first be understood how light propagates through space, through the Earth's atmosphere to the telescope, and through the subsequent imaging system to the detector.

[1] http://exoplanetarchive.ipac.caltech.edu/cgi-bin/TblView/nph-tblView?app=ExoTbls&config=planets

1.1.1 Fourier optics

1.1.1.1 Diffraction-limited imaging

Light is electromagnetic radiation that travels through any media as a transverse wave which can be described in terms of its electric field component. After propagating from an astronomical source, the light, also simply referred to as the "field", incident on a telescope aperture is represented by a complex amplitude function $\psi(\xi, \eta)$ which describes the finite aperture of the telescope pupil itself and the effect of the media through which the light has propagated. The spatial coordinates within the telescope pupil plane are denoted by ξ and η. The complex amplitude is comprised of the real-valued binary telescope pupil amplitude $P(\xi, \eta)$ and the phase ϕ which encodes the field fluctuations across the pupil.

$$\psi(\xi, \eta) = P(\xi, \eta)e^{i\phi} \tag{1.1}$$

As an example, for a binary telescope pupil defined simply as a circular aperture such that $q = \sqrt{\xi^2 + \eta^2}$, the pupil function is defined as

$$P(\xi, \eta) = P(q) = \begin{cases} 1 & if\ q\ \leq\ \frac{D}{2} \\ 0 & otherwise \end{cases} \tag{1.2}$$

where D is the diameter of the telescope aperture. The surface over which ϕ is constant is referred to as a wavefront. This quantity ϕ is wavelength dependent and is a function of the variations in the refractive index of the media the light encounters as it propagates, known as the optical path difference (OPD), such that

$$\phi = \frac{2\pi}{\lambda} OPD. \tag{1.3}$$

For a perfect system, there are no deviations in the light path caused by aberrations, thereby making OPD $= 0$. The quantity ϕ is then also equal to 0, and the complex amplitude $\psi(\xi, \eta)$ becomes $P(\xi, \eta)e^{i0}$ or simply $P(\xi, \eta)$; otherwise, in the presence of an atmosphere, ϕ will be non-zero.

To first understand the basics, we assume the perfect system in which $\phi = 0$ and $\psi(\xi, \eta) = P(\xi, \eta)$. Furthermore, when the propagation distance between the light source and the observer is large in comparison to the observational area, the wavefront can be approximated as a plane wave. This is an effect of Fraunhofer diffraction and is known commonly as the far-field approximation (Tyson, 2015). Mathematically, it is defined as the case in which the square of the collecting aperture diameter (D) is much smaller than the product of the observation wavelength λ and the propagation distance z from the source to the aperture

$$D^2 \ll \lambda z. \tag{1.4}$$

This is the case for light from astronomical point sources captured by a telescope. In the far-field approximation, the propagation of the wavefront from the telescope pupil to the image plane is represented by a Fourier transform of the complex wavefront $\psi(\xi, \eta)$. In the case of an error-free system, this is simply the diffraction pattern for a binary pupil

$$\Psi(x, y) = \frac{e^{i\kappa z} e^{i\frac{\kappa}{2z}(x^2+y^2)}}{i\lambda z} \iint_{-\infty}^{\infty} P(\xi, \eta) e^{i\frac{2\pi}{\lambda z}(x\xi + y\eta)} d\xi d\eta \tag{1.5}$$

evaluated at spatial frequencies $k_X = \frac{x}{\lambda z}$ and $k_Y = \frac{y}{\lambda z}$ in the Fourier domain and where the quantity κ is defined as $\frac{2\pi}{\lambda}$ (Goodman, 1996). Returning again to the generalized case of a circular telescope aperture, this integral simplifies even futher by assuming circular symmetry such that the radial coordinate in the telescope aperture plane is again $q = \sqrt{\xi^2 + \eta^2}$ and $\rho = \sqrt{(k_X)^2 + (k_Y)^2}$ in the image plane. This simplification leads to a straightforward modified Bessel solution for the field in the image plane

$$\Psi(r) = \frac{e^{i\kappa z} e^{i\frac{\kappa}{2z} r^2}}{i\lambda z} \frac{A}{i\lambda z} \left[\frac{2J_1(\kappa D r / 2z)}{\kappa D r / 2z} \right] \tag{1.6}$$

where r is the radius coordinate in the image plane such that $\rho = \frac{r}{\lambda z}$ (Goodman, 1996). The telescope aperture area here is given as $A = \frac{\pi D^2}{4}$, and J_1 is a Bessel function of the first kind of order one. The image that is formed on the detector in intensity is the system point spread function (PSF) given by the modulus squared of the field

$$PSF_{circle} = I(r) = \mid \Psi(r) \mid^2 = \frac{A^2}{(\lambda z)^2} \left[\frac{2J_1(\kappa D r / 2z)}{\kappa D r / 2z} \right]^2. \tag{1.7}$$

When assuming Fraunhofer diffraction, the mathematical expression for the PSF for any complex amplitude is commonly shortened to simply

$$PSF = |\mathcal{F}(\psi(\xi, \eta))|^2 = |\Psi(x, y)|^2 \tag{1.8}$$

where $\mathcal{F}$ is shorthand notation for the Fourier transform. The particular solution for a circular aperture in eq 1.7 is known as an Airy pattern (fig. 1.1) (Goodman, 1996). Here it is easy to visualize the relationship between the telescope pupil and its Fourier transform, the PSF. The PSF "core" is defined by the light within the first dark ring. The angular size of the core is defined by the position of the first zero of the J_1 Bessel function at $\pm 1.22\ \lambda/D$, thereby making the full extent of the core $2.44\ \lambda/D$. The unit λ/D is used throughout this work as a unit of angular measurement in the image plane; the reasons for this will be explained shortly.

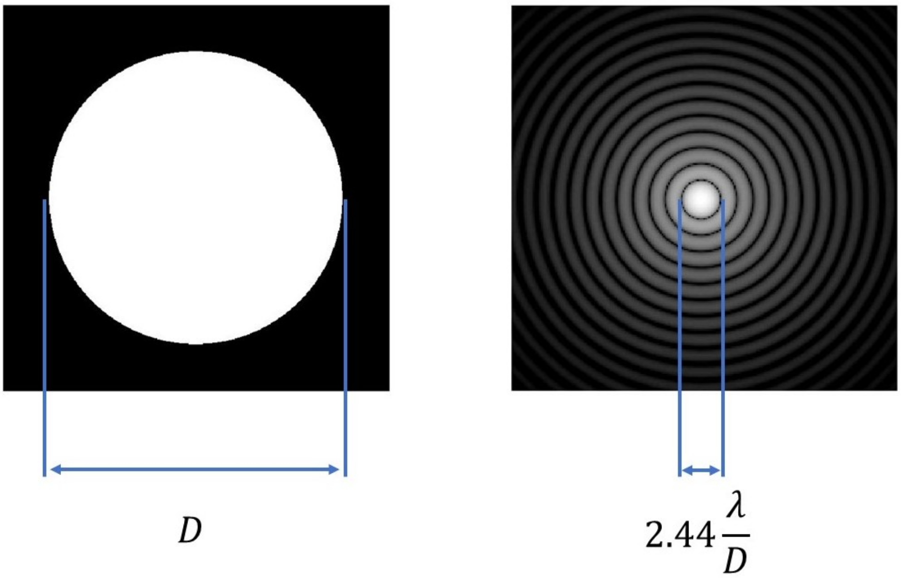

Figure 1.1: The Airy pattern PSF in the image plane, shown in $\log_{10}$ scale, resulting from the Fourier transform of a circular binary aperture with a diameter D and phase $\phi = 0$

While circular in shape, standard telescope pupils are annular due to the shadow of the secondary mirror over the primary mirror (also referred to as the central obscuration), and the pupil is not always circularly symmetric due to the support struts (known as "spiders") that suspend the secondary mirror above the primary. These features modify the solution in eqs 1.6 and 1.7 via Babinet's principle (Traub and Oppenheimer, 2010) by

$$PSF_{annulus} = \frac{1}{(\lambda z)^2}\left[\frac{2J_1(kDr/2z)}{kDr/2z}A_D - \frac{2J_1(kdr/2z)}{kdr/2z}A_d\right]^2 \tag{1.9}$$

where A_D is the area of the telescope and A_d is the area of the central obscuration. The far-field approximation still holds, resulting in an image that is simply the Fourier transform of the complex amplitude function $\psi(\xi, \eta)$ (fig 1.2).

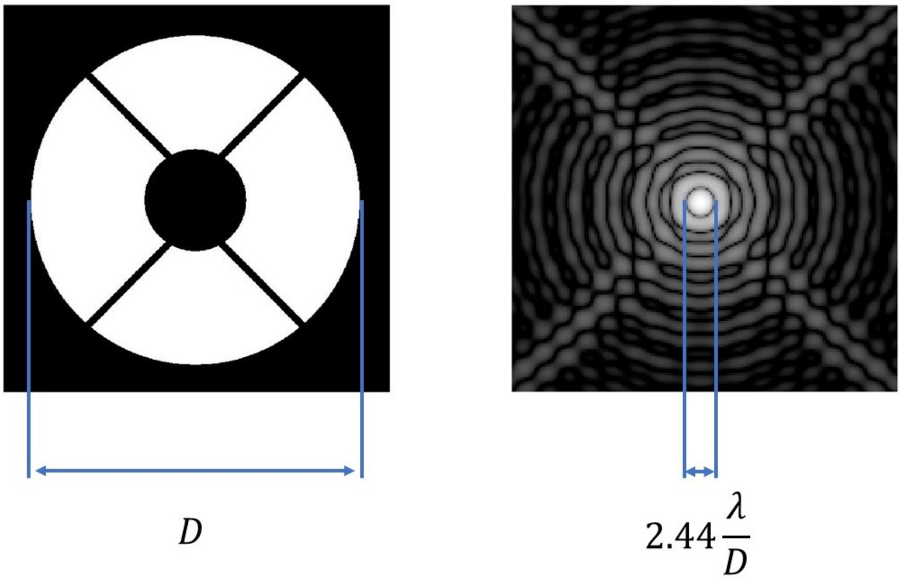

Figure 1.2: The image plane PSF resulting from the Fourier transform of a telescope aperture with a diameter D and a secondary obscuration and spider features

The examples shown above have explored simple modifications to the binary pupil ($\psi(\xi, \eta) = P(\xi, \eta)$) which lead to error-free PSFs in the image plane. These resulting PSFs in each case are therefore "diffraction-limited" - meaning that the diffraction pattern is affected only by the clean binary pupil and not by any aberration across the pupil. However when ϕ is non-zero, it represents a departure from the diffraction-limited case, degrading the quality of the PSF. This is the case for all ground-based telescopes imaging through an atmosphere.

1.1.1.2 Imaging through turbulence

For ground-based telescopes, imaging through the atmosphere is an unavoidable problem. Small temperature fluctuations in the atmosphere cause random changes in wind velocities which we see as turbulent motion. These temperature changes lead to shifts in atmospheric density, and the result is a change in the local index of refraction n - an optical quantity which describes the speed with which light will travel through a particular medium. These variations in the index of refraction throughout the atmosphere accumulate, and in effect, act as tiny lenses in the atmosphere through which the light from an astronomical source must propagate to reach the telescope (Tyson, 2015).

Observing at visible wavelengths, the incident wavefront is usually distorted by aberrations as small as 0.4 cm and as large as 20 meters (Traub and Oppenheimer, 2010). Respectively, these two quantities are known as the inner scale, l_0 and the outer scale L_0. A mathematically important definition for quantifying the wavefront aberration is the diameter of the region over which the aberrated wavefront has a root mean square (rms) variation of approximately 1 rad (the aberration amplitude scaled by the observation wavelength); this diameter, r_0 is referred to as the Fried parameter (Fried, 1966). In the visible spectrum, r_0 is roughly 10 cm. This means that if the telescope diameter D is also 10 cm, the PSF seen at the image plane will be diffraction-limited. When the diameter of the telescope is larger than r_0, the aberration ϕ_a dominates the imaging performance of the instrument, and the image is no longer diffraction-limited, but is instead referred to as "seeing-limited".

It is now important to define atmospheric turbulence in greater detail. The movement of these regions with varying refractive indices can be described statistically in terms of their spatial frequency k content. The Kolmogorov spectrum is the power spectral density (PSD) that is often used to define atmospheric turbulence. It defines l_0 as 0 and L_0 as ∞. The resulting spectrum is given as (Tyson, 2015)

$$\Phi_n(k) = 0.033\ C_n^2\ |k|^{-\frac{11}{3}} \tag{1.10}$$

where C_n is a measure of the turbulence strength, referred to as the refractive index structure constant. For the scope of this paper, all injected aberrations are approximately Kolmogorov turbulence.

Returning to Fourier optics, in the presence of an aberration, the complex amplitude across the pupil becomes $\psi_a(\xi, \eta) = P(\xi, \eta)e^{i\phi_a}$ which includes the phase aberration ϕ_a (where ϕ_a is described by Kolmogorov turbulence) as seen in fig 1.3a.

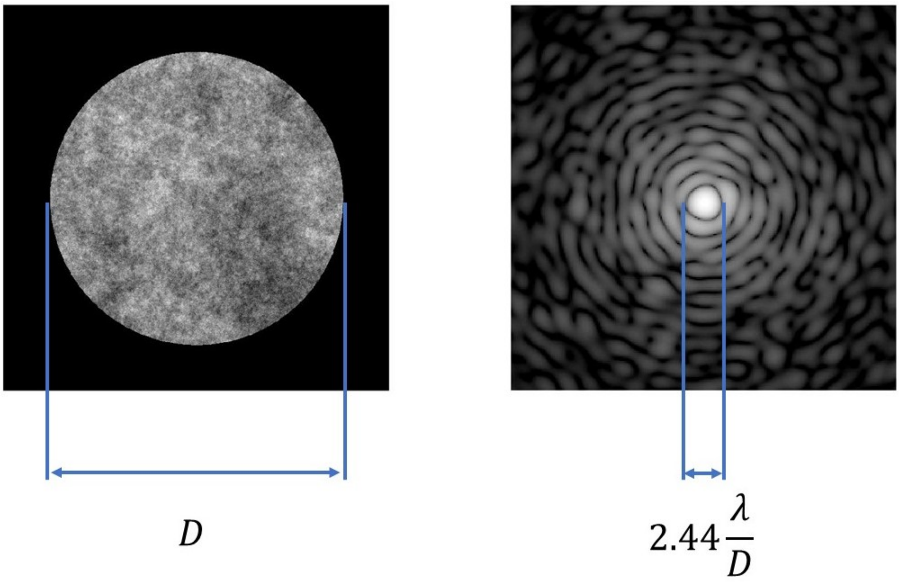

Figure 1.3: An example of a Kolmogorov phase aberration ϕ_a with approximately ± 2 nm amplitude fluctuations in the pupil and the resulting aberrated PSF shown in $\log_{10}$ scale.

The resulting Fourier transform of this aberrated complex amplitude is given as

$$\Psi_a(x,y) = \frac{e^{i\kappa z} e^{i\frac{\kappa}{2z}(x^2+y^2)}}{i\lambda z} \iint_{-\infty}^{\infty} P(\xi,\eta) e^{i\phi_a} e^{i\frac{2\pi}{\lambda z}(x\xi+y\eta)} d\xi d\eta \tag{1.11}$$

The aberrations introduced in eq 1.11 modify the diffraction limited image PSF_0, resulting in the aberrated image PSF_a

$$PSF_a = |\mathcal{F}(\psi_a(\xi,\eta))|^2 = |\Psi_a(x,y)|^2, \tag{1.12}$$

an example of which is shown in fig 1.3b alongside the phase aberration that induced it. The aberrated image is modified from the diffraction-limited case in a number of ways. Firstly, the core of the PSF is less well-defined. The intensity throughout the first ring around the PSF core is misshapen and not evenly illuminated. This effect is due to aberrations with low spatial frequencies, or low-order modes. These low-order aberrations can be thought of as the rough overall shape, or distortion, of the incoming wavefront and manifest themselves as aberrations in the low λ/D regime in the image plane as seen in fig 1.4. Low-order aberrations can also be induced by aberrations in the optical system due to beam tip and tilt or misalignment. Such aberrations are commonly optically described by the Zernike polynomial set (see Chapter 3).

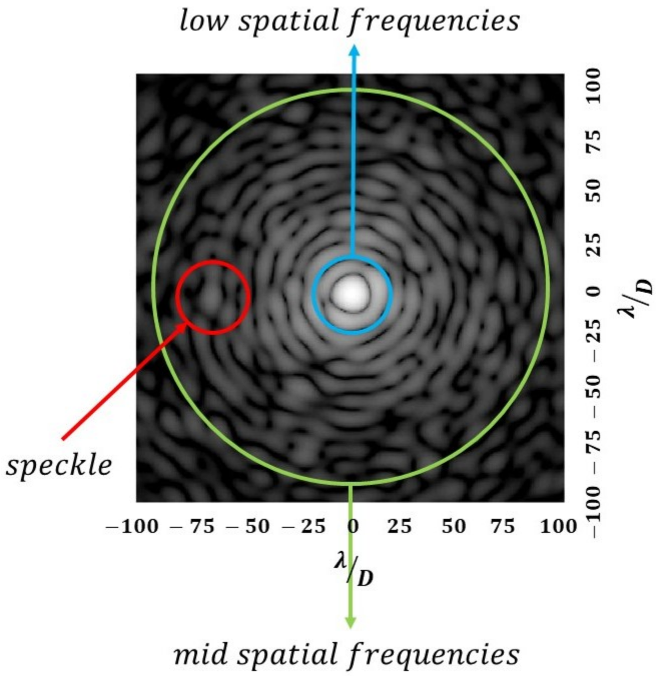

Figure 1.4: Aberrated PSF showing speckles and the approximate ranges of low and mid spatial frequencies in the Fourier plane

A second effect which can be seen throughout the image is what is referred to as speckle. Speckles are the halo of small fluctuations seen everywhere across the PSF in fig 1.4 that cause the PSF to deviate from its diffraction-limited case. They occur due to wavefront aberrations and manifest as tiny copies of the PSF throughout the image. For example, the Fourier transform of a sine wave with frequency $\frac{1}{D}$ in the pupil produces two speckles, one at $+\frac{\lambda}{D}$ and one at $-\frac{\lambda}{D}$ in the image. When the amplitude of the aberration inducing the speckles is large, the speckles will dominate the image, and the stellar PSF becomes lost in the image as just another speckle (Traub and Oppenheimer, 2010). In the case of high-contrast imaging, the presence of speckles in the image dominates the very faint planetary PSF. Suppressing speckle formation is therefore imperative for enabling direct high-contrast imaging.

Having characterized atmospheric turbulence and its impact on diffraction-limited imaging, we explore strategies to compensate for the effects imposed by imaging through Earth's atmosphere.

1.1.2 Adaptive optics

The purpose of adaptive optics (AO) is to correct the aberrated image to a diffraction-limited state. To achieve this, an AO system must consist of at least two main components: a wavefront sensor (WFS) and wavefront corrector. The former determines the shape of the aberrated wavefront, and the latter applies the correct shape to cancel that aberration. This is referred to as phase conjugation (Tyson, 2015) - the method of adding an additional correcting phase term ϕ_c to the pupil aberration ϕ_a such that

$$\phi_a + \phi_c = 0. \tag{1.13}$$

This means that $\phi_c = -\phi_a$, or in other words, the phase correction is the conjugate of the phase aberration. Recalling the equation for the propagation of an aberrated wavefront given in eq 1.11, the new corrected wavefront $\Psi_c(x, y)$ becomes

$$\Psi_c(x, y) = \frac{e^{i\kappa z} e^{i\frac{\kappa}{2z}(x^2+y^2)}}{i\lambda z} \iint P(\xi, \eta) e^{i(\phi_a+\phi_c)} e^{i\frac{2\pi}{\lambda z}(x\xi+y\eta)} d\xi d\eta \tag{1.14}$$

The wavefront is only corrected over the area of the correcting element, and the resolution of the correction is limited by the resolution of the correcting element. In most AO systems, the correcting element is a deformable mirror (DM) which is placed in a pupil plane that is conjugate to the entrance pupil (see Chapter 2 for greater detail). There are many categories of DMs, but for the scope of this work, we will focus on one type: continuous surface, micro-electro-mechanical (MEMS) devices with actuators attached to the back side of the surface which deform the DM to create the appropriate shape ϕ_c (a more in-depth discussion of the DM used in the following work can be found in Chapter 2).

In general summary, an AO system works as follows: (1) an aberrated wavefront ϕ_a is sensed by the wavefront sensor, (2) the appropriate correction to cancel this aberration ϕ_c is calculated, (3) the correction is applied by moving the actuators on the back of the DM so that the surface takes the shape ϕ_c, (4) the phase of the aberrated wavefront after reflecting off the DM should then be $\phi_a + \phi_c = \phi_\Delta$. In an ideal system, ϕ_Δ would be equal to zero, but the correction is limited by the perfomance of the WFS and the DM's ability to match the aberration shape.

1.1.2.1 Wavefront sensing

As previously mentioned, the first step in an AO system is to sense the aberration that is degrading the optical quality of the PSF. There are many flavors of WFS, but two dominant categories: those that sample the pupil plane, and those that sample at the focal plane (Guyon, 2005). WFSs that sample the pupil like the Shack-Hartmann (Roddier, 1999) and Pyramid WFS (Ragazzoni, 1996) are very common in astronomical instrumentation, but they will not be discussed here. The work presented in this document focuses on focal plane wavefront sensing (FPWFS). Rather than sampling the pupil, where the aberration occurs, FPWFS monitors changes in the focal plane and relates those changes back to aberrations in the pupil plane. There are different categories of FPWFS: those that probe the field in the detector and return an estimate of the phase in the image plane, and those that monitor changes in intensity in the image. A discussion of phase estimation methods follows in Section 1.3.2, but to understand the basic principles of WFS, we will first examine the latter technique: monitoring variations in intensity.

One widely-used WFS technique that monitors intensity changes is the low-order wavefront sensor (LOWFS) (Singh et al., 2015; Guyon et al., 2009; Huby et al., 2017; SHI, 2016; Vogt et al., 2011). The signal used by LOWFS is commonly an image formed after a reflection off of an occulting mask (coronagraph) somewhere in the post-telescope optical system (see Section 1.3.1 and fig 1.10 for more details on this type of system), but the image on the main science detector can also be used. The following is a general sequence for techniques like low-order wavefront sensing that monitor changes in intensity: (Guyon et al., 2009)
(1) Acquire an image
(2) Compute the difference between this image and the reference image obtained (or computed) with no aberrations
(3) Decompose this difference into a linear sum of the WFS response to a series of known shapes referred to as "modes"
(4) Use the derived coefficients for each of these modes to drive the DM actuators to remove the measured aberrations

Once an image of the aberrated PSF has been taken and reference subtracted, the image is then fit to a "dictionary" of WFS images, each encoded with the WFS response to a known aberration. These known aberrations are referred to as modes, and the resulting WFS image dictionary is known as the response matrix (RM).

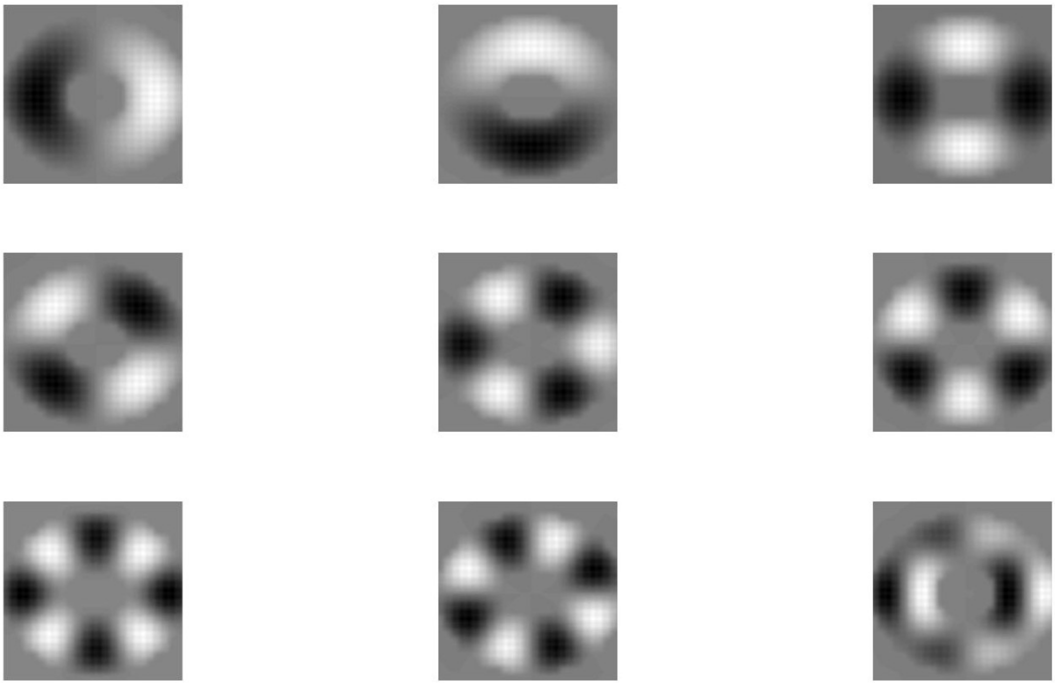

Figure 1.5: Low-order modes used to build the response matrix

The RM is built by applying the modes on the DM (as seen in fig 1.6) one at a time and recording the WFS response. For FPWFS, this WFS response is simply the difference between the focal plane image with the mode applied with a positive amplitude I_{m+} and the image with the mode applied with a negative amplitude I_{m-}, such that

$$\Delta I_m = I_{m+} - I_{m-} \tag{1.15}$$

where each image has been reordered to be a single vector of pixels. The RM is then defined as

$$RM = \begin{bmatrix} \Delta I_1 & \dots & \Delta I_M \end{bmatrix} \tag{1.16}$$

where M is the number of modes used in the RM. Each column in the RM is a single WFS image corresponding to a single mode that records how the image has changed with the application of each mode. Examples of the images recorded in the RM are shown in fig 1.6 where each image is the PSF response to each mode applied on the DM shown in fig 1.5.

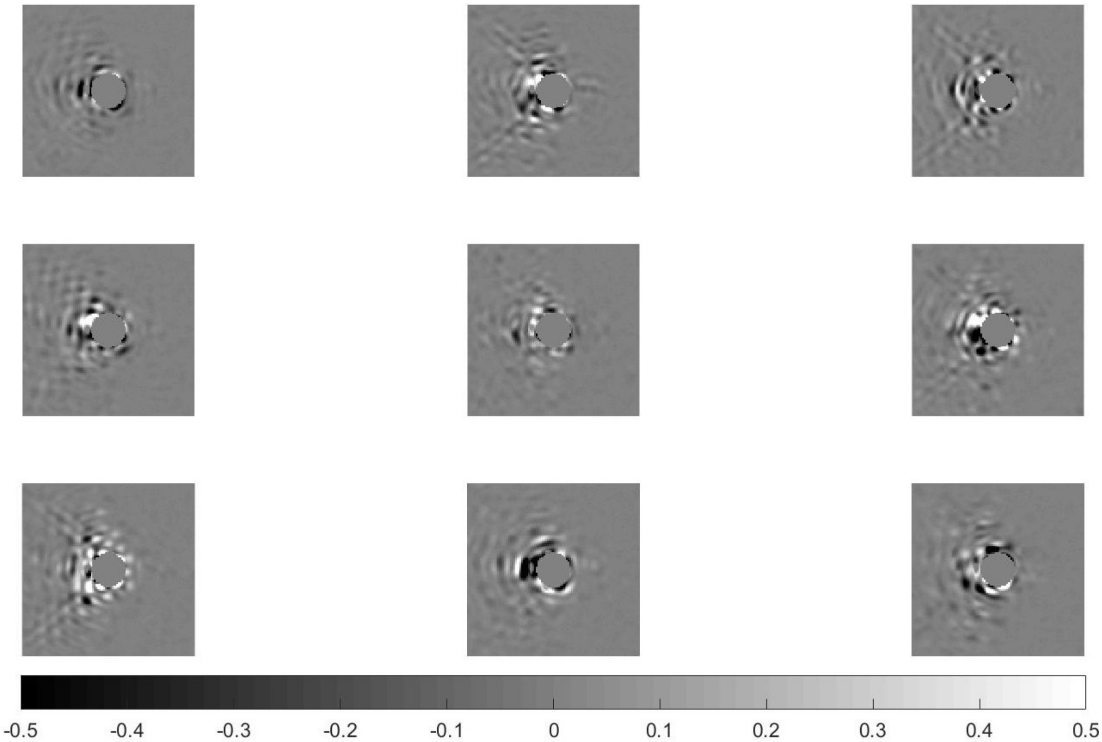

Figure 1.6: Focal plane WFS image response to 9 low-order modes with the reference image subtracted and the oversaturated core masked. These 9 images comprise the first 9 columns of the response matrix

Now with the RM built, the aberrated image I_a (created by an input pupil aberration ϕ_a) can be decomposed into a linear sum of the RM modes by a least-squares fit to the inverted response matrix. With more pixels (N_{pixels}) in each WFS image than modes (M_{modes}) in the response matix, the RM of size [N_{pixels} x M_{modes}] is overdetermined, and therfore the pseudo-inverse must be used. The aberrated wavefront is therefore decomposed into a linear sum of modes by

$$\bar{u} = (RM^T RM)^{-1} RM^T \ I_a \ , \tag{1.17}$$

where the term $(RM^T RM)^{-1} RM^T$ is the pseudo-inverse of the response matrix, often referred to as the control matrix, and $\bar{u}$ is a vector containing the amplitude for each mode in the RM. The control matrix is an [M_{modes} x N_{pixels}] matrix, and the aberrated image I_a is a single column vector of size [N_{pixels} x 1]. When I_a is fit to the control matrix, the result is the single column [M_{modes} x 1] vector $\bar{u}$. Each element in this resulting vector is an amplitude value for each mode in the response matrix; these amplitudes define the numerical contribution of each mode in the aberrated image. Multiplying $\bar{u}$ by the RM then reconstructs the pupil aberration responsible for the aberrated image I_a by multiplying each mode by its calculated amplitude in $\bar{u}$ and then linearly summing these weighted modes together. The DM corrective shape ϕ_c to cancel this aberration is then simply the negative of the reconstructed aberration and is computed by

$$\phi_c = -RM\ \bar{u} \tag{1.18}$$

where the negative sign creates a shape on the DM of equal amplitude to the aberration ϕ_a sensed in the entrance pupil but of opposite sign so that the two cancel as shown previously in 1.13.

This process of sensing an aberration, decomposing it into a linear sum of modes, and computing and applying the correct shape on the DM is repeated in "closed-loop" - meaning that there is continuous feedback from the WFS to update the shape of the DM with the appropriate correction until the aberration is nulled. Due to noise in a real system either from photons from the star or read noise at the sensor, a multiplicative gain $g < 1$ is applied to eq 1.18 so that errors in the correction are minimized, and the DM shape is changed slowly over multiple iterations to converge to the correct shape.

1.1.2.2 Wavefront control

The WFS performance is also driven by the DM's ability to match the aberration shape; this ability is limited by the number of actuators on the DM. The frequency content of the shapes that can be fit by the DM is determined by the number of actuators within the illuminated region. In the image plane, this means that the DM can control aberrations only over a finite area known as the control region. The maximum spatial frequency extent of this region is known as the control radius. The shape of the control region is determined by the actuator grid pattern and the modal basis set used in the control matrix. For a mirror with a square grid actuator layout, taking advantage of all available degrees of freedom by using a basis set like Fourier modes creates a square control region of size $N\frac{\lambda}{D}$ x $N\frac{\lambda}{D}$ where N is the number of actuators across the diameter of the beam footprint on the DM. Using modes that truncate the spatial frequency content to a circular region, like

Zernike modes (and the modes used in the control matrix throughout the following work), creates a circular control region defined by $\frac{N}{2}\frac{\lambda}{D}$. The DM therefore acts as a high-pass filter: it can correct spatial frequencies up to the control radius.

So, assuming a perfect WFS and a circular control region defined by the modal basis set, $\phi_a + \phi_c = 0$ for spatial frequencies up to $\frac{N}{2}\frac{\lambda}{D}$. An example of this ideal case is shown in figs 1.7 and 1.8. In the lefthand image, a Kolmogorov phase aberration in a circular pupil is injected into a simulated telescope-AO system. The aberrations contains low-order frequency content (seen as the large, overall deformation) as well as mid and high spatial frequency content (the smaller, grainy features). The spatial frequency content of the aberration that the DM can fit is seen in the center image. To correct this aberration, the DM would apply the negative of this shape, and the result is seen in the righthand image. Again assuming a perfect WFS, after correction by the DM, the residual wavefront is composed only of errors with spatial frequency content beyond the control radius of the DM. In the image plane (fig 1.8), this corresponds to a PSF that is corrected (returned to its diffraction-limited state) out to $\frac{N}{2}\frac{\lambda}{D}$.

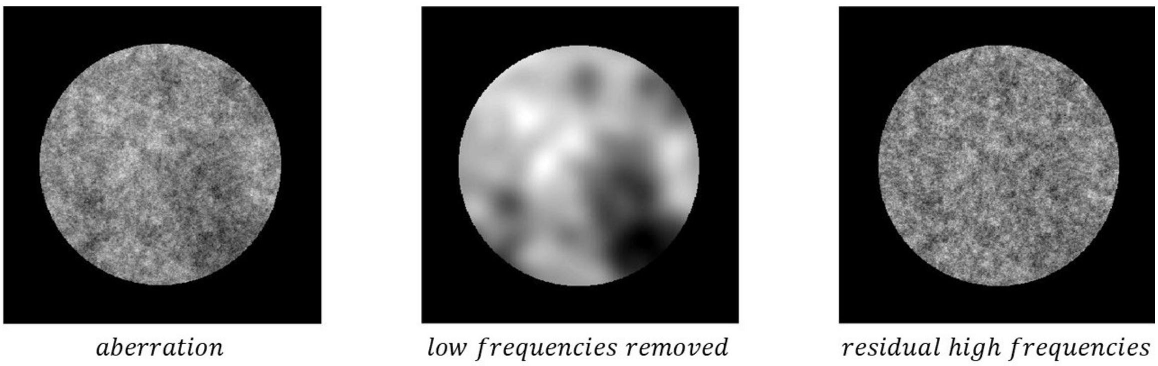

Figure 1.7: An example of the high-pass filter effect of wavefront control. Left to right: (a) An input aberration ϕ_a containing low, mid, and high spatial frequencies. (b) The low-order modes the DM can remove based on the number of actuators across the illuminated region (the negative of this image is therfore ϕ_c). (c) The residual mid and high spatial frequencies that remain uncorrected by the DM.

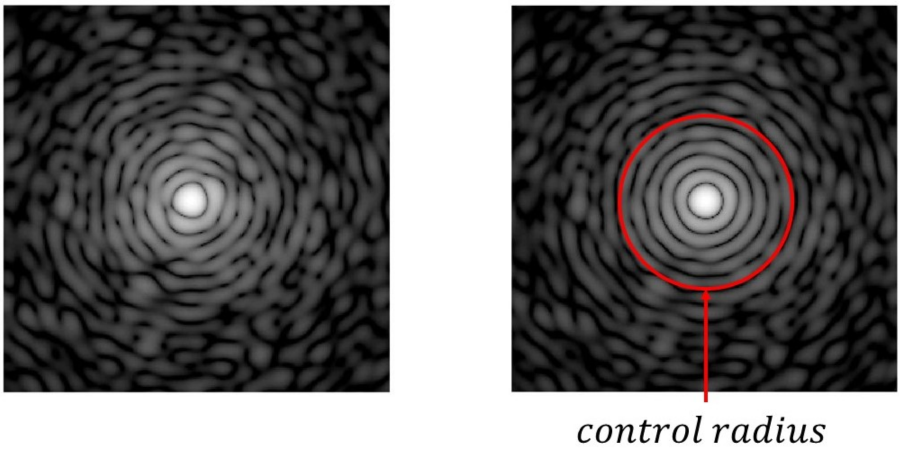

Figure 1.8: (a) A PSF aberrated by ϕ_a and (b) the PSF after correction by the DM. Diffraction-limited quality is restored out to the control radius (shown in red) of the DM. Beyond the control radius, the PSF remains aberrated by the residual mid and high spatial frequencies that are unreachable by the DM.

With an AO system integrated into the optical system, the image delivered by the telescope is once again diffraction-limited (out to the control radius of the DM). We can now turn to the challenges presented when trying to sense light not from the star, but from an orbiting exoplanet companion.

1.2 Direct imaging challenges

In the case of a star-exoplanet system, light from both the star and exoplanet light arrive at the telescope as separate plane waves that are incoherent with one another. Since the plane waves from both the star and the exoplanet are incident on the same telescope aperture, both sources produce PSFs in the image plane that are identical in shape but vary in magnitude (this is assuming both the star and planet remain unresolved by the telescope, which is the case for all exoplanetary systems and single ground-based telescopes). Since the light from the star and exoplanet are incoherent with one another, a property of Fourier transforms dictates that the fields from the star and exoplanet do not interact in phase, but instead, the PSFs from the two sources add in intensity in the image plane; an example of this interaction is seen in fig 1.9.

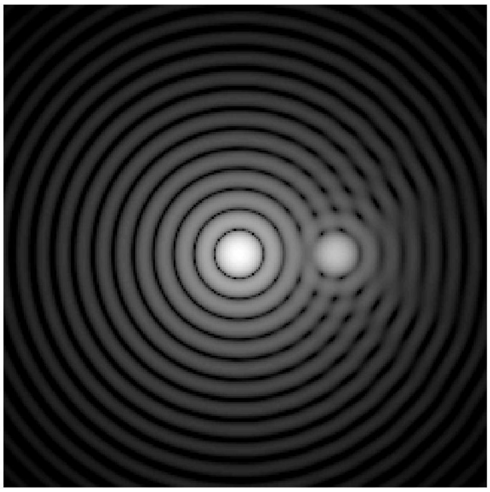

Figure 1.9: Example of the addition of two incoherent point source PSFs in the image plane

To directly image the light from an exoplanet, there are two key factors that must be addressed: close proximity of the planet to its parent star and high star-planet contrast.

1.2.1 Close star-planet proximity

The problem with star-planet proximity is a geometry problem. As the distance from the telescope increases, the on-sky angle subtended by the star-planet pair decreases for any given planetary system. This angle, in astronomy, is often given in units of arcseconds on-sky; however, for the purposes of this paper, this angle will always be addressed in units of $\frac{\lambda}{D}$ at the detector. This relates the angle back to the optical system parameters: the central observation wavelength λ and the telescope diameter D.

This is easiest to understand when related to an actual telescope and planetary system. Take for example the newly discovered planet Proxima Centauri b orbiting within the habitable zone of the red dwarf star Proxima Centauri (Snellen, 2017). At only 4.24 light years (ly) away, this is the closest planetary system to our own and is a very promising target for characterization with future, even some current, large telescopes. The maximum separation this planet achieves from its star in its elliptical orbit is approximately 0.0485 astronomical units (AU) which, at 4.2 ly away gives an angular subtense between star and planet of 37 millarcseconds (mas). Whether or not a telescope could image this planet as a separate object from the star is dependent on the size of the telescope (D) and the wavelength (λ) at which the system is being observed. The ability of a telescope instrument to image two sources as spatially separate entities is referred to as the system resolution. In many optical applications, two objects are considered to be spatially resolved when they are separated by at least 1.22 λ/D (Hecht, 2002). For the Magellan Telescope in the Atacama Desert, with a 6.5 m diameter primary mirror observing in the visible band at 656 nm, the quantity 1 $\frac{\lambda}{D}$ corresponds to 21 mas. Therefore, at its greatest distance from the star of 37 mas, the Magellan Telescope would be able to resolve visible light from Proxima b as an individual source separated from its host star by 1.8 $\frac{\lambda}{D}$ in the image plane.

At such small angular separations near the diffraction limit of the telescope ($\sim 1\lambda/D$), the light from the planet is buried beneath the stellar PSF very near the stellar core where most of the stellar light is focused, creating a significant challenge for light suppression techniques. Light leakage near the stellar PSF core due to aberrations limit the inner working angle (IWA) and often mimic the signal of potential planetary companions (Mawet et al., 2012). The dominant source of error at small separations is low-order aberrations which include but are not limited to: accurate pointing of the telescope, jitter/drift, and defocus. To allow for direct imaging of a planet in this region requires exquisite control of these errors which can push both an AO system's hardware and software limits (Mawet et al., 2014).

1.2.2 High star-planet contrast

Spatially resolving the planet PSF as a separate source from the star PSF is only half the battle. Even with light from the planet spatially separated from light from the star at the detector, the light coming from the planet is still many magnitudes dimmer than the light from the star. The ratio here between stellar and planetary light is referred to as the contrast. Throughout this paper, contrast C for a star-planet system will be defined as the planetary irradiance across the planetary PSF core I_{planet} normalized by the stellar irradiance across the stellar PSF core I_{star} in the image plane.

$$C = \frac{I_{planet}}{I_{star}} \tag{1.19}$$

In previous work (Traub and Oppenheimer, 2010), contrast has been defined as the ratio of the stellar and planetary fluxes across a specific wavelength band such that $C = \frac{F_\lambda(planet)}{F_\lambda(star)}$ where flux is measured in photons/sec. This flux-based definition of contrast is directly proportional to the definition given in eq 1.19. Upon reaching the detector, the flux F is measured in counts and is defined as the irradiance integrated over a given number of pixels on the detector, denoted by area A such that

$$F = \int_A I \, dA. \tag{1.20}$$

Therefore, integration over the same area A, or same number of pixels, for both the stellar PSF and the planetary PSF yields a direct relationship between source flux and detector irradiance such that

$$C = \frac{F_{planet}}{F_{star}} = \frac{\int_A I_{planet} \, dA}{\int_A I_{star} \, dA}. \tag{1.21}$$

For this work, The star-planet contrast ratio is defined as the ratio of the peak planetary flux per pixel to the peak stellar flux per pixel, thereby defining A as the single pixel at the peak of the stellar PSF and the single pixel at the peak of the planetary PSF. This then becomes a ratio of the peak planetary irradiance and peak stellar irradiance

$$C = \frac{I_{planet}}{I_{star}}. \tag{1.22}$$

It should also be noted that this definition of contrast is assuming no interference by a mask at the focal plane that will affect the flux relationship between star and planet. For the work done in this dissertation, no such filtering occurs in the focal plane.

Given this definition of contrast, the relationship between stellar and planetary flux and irradiance can be now be understood. As an example, for an Earth-Sun system being observed in the visible spectrum, the flux received at the detector from the planet is about 10 billion times lower than the flux received from the star leading to a contrast of 10^{-10} (Traub and Oppenheimer, 2010). This drastic difference in flux between the star and the planet presents a second major challenge facing direct imaging known as high contrast. At the detector, this high contrast means that the planetary PSF that is so easily seen in fig 1.9 next to the on-axis stellar PSF is actually buried beneath the noise from the stellar signal.

1.3 Generating high contrast

To directly detect any light from the exoplanet, stellar flux within the region around the planet at the detector must be suppressed to a level at which light from the planet can be detected above the stellar signal. The region over which this suppression is achieved is called the dark hole (DH). The average contrast within the DH must be below the planet-star contrast in order for the planet to be detected. The DH average irradiance is defined as the sum of the flux within the dark hole divided by the total number of dark hole pixels, N, such that

$$I_{DH} = \frac{\sum_N F_{DH}}{N}. \tag{1.23}$$

The DH contrast is this irradiance normalized by the maximum stellar flux per pixel found at the peak of the stellar PSF, I_{star},

$$C = \frac{I_{DH}}{I_{star}}. \tag{1.24}$$

Eq 1.24 serves as the primary performance metric for the wavefront sensing and control algorithms presented in Chapters 5 and 4 that control stellar suppression.

There are multiple methods by which this DH can be created, but they all function on one of two basic principles: (1) block starlight with a series of masks and (2) force starlight to interfere with itself destructively over a selected region of interest in the image plane to create an area that is largely devoid of starlight. Two techniques will be explored here: coronagraphy and electric field conjugation. For dark hole generation, coronagraphy and field conjugation are not mutually exclusive techniques, as one can be used in place of the other. They can also be combined to augment a system's stellar suppression capabilities. With the advent of extreme adaptive optics systems with high actuator count deformable mirrors and low readnoise cameras, wavefront sensing and control with a DM can be harnessed to create deep-contrast, dark regions largely devoid of stellar light in the science image, thereby taking the place of traditional mask coronagraphs. Both methods of creating a DH are detailed in the following section.

1.3.1 Coronagraphy

Historically, a coronagraph consisted of a series of masks placed throughout the optical system to block on-axis star light and allow off-axis planet light to pass through to the detector. The most famous example of this type of coronagraph is the Lyot coronagraph shown in fig 1.10. The main function of a Lyot coronagaph was to act as a high-pass filter; a small circular mask placed on-axis in an intermediate focal plane blocks the stellar PSF core while allowing off-axis planet light to pass. While successfully blocking a significant fraction of starlight on-axis, this small mask also diffracts that star light out to the edges of the pupil in the following pupil plane. To deal with this light, a second mask, called a Lyot stop, is then placed in the following pupil plane. This mask's features are oversized and the outer diameter undersized in order to block the starlight at the pupil edges and keep it from propagating to the final image plane.

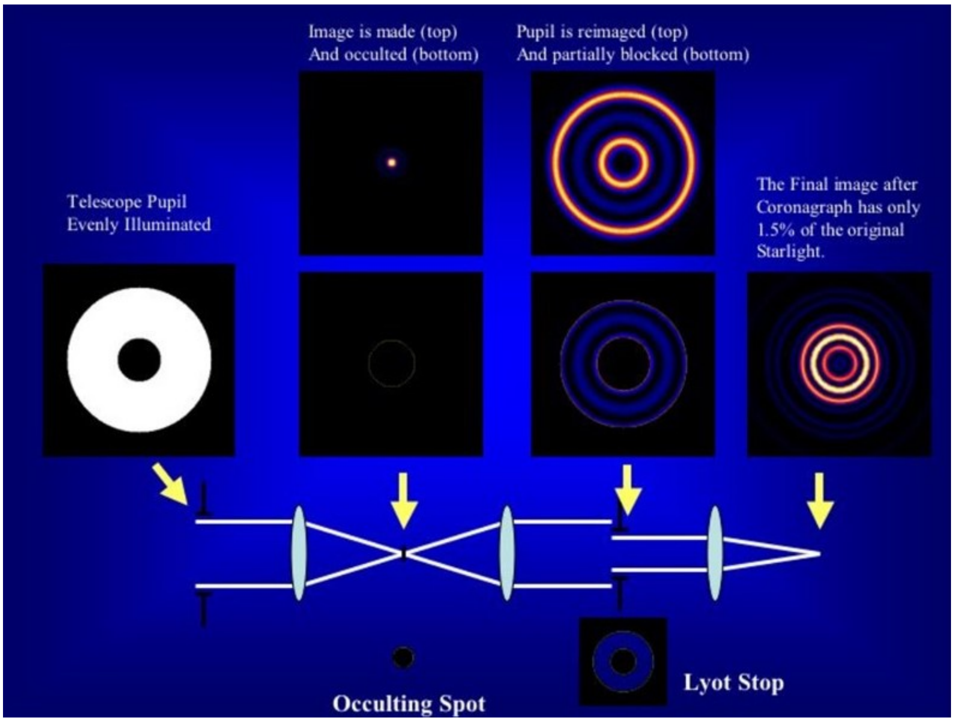

Figure 1.10: Demonstration of Lyot coronagraph operation (adapted from Sivaramakrishnan et al. 2001)

There are many variations of the Lyot coronagraph as well as many other types of coronagraph architectures; some combine focal plane and pupil plane masks like the Lyot coronagraph, as well as beam-reshaping optics and phase masks like phase-induce amplitude apodization (PIAA) and its extension with complex masks (PIAACMC) (Guyon et al., 2006, May 2014). Other architectures only utilize pupil plane phase masks, like the vector apodizing phase plate (vAPP) coronagraph which will be discussed in further detail in Chapters 2 and 3. Due to their differences in design, the performace metrics used in the optimization process vary for each coronagraph type, but a key design feature in each design is the inner working angle (IWA). The IWA of a coronagraph is defined as the point at which the source throughput is 50% of the max throughput (Mawet et al., 2012). It is the inner-most edge of the DH nearest the PSF core (see fig 1.11). Physically, when trying to image an exoplanet orbiting a star, the IWA determines how close to the star the coronagaph is able to suppress starlight to allow for the exoplanet to be seen. Referring back to the example of Proxima b, the IWA of a coronagraph on the Magellan Telescope would have to be $< 1.8\ \lambda/D$ to directly image Proxima b in the visible spectrum.

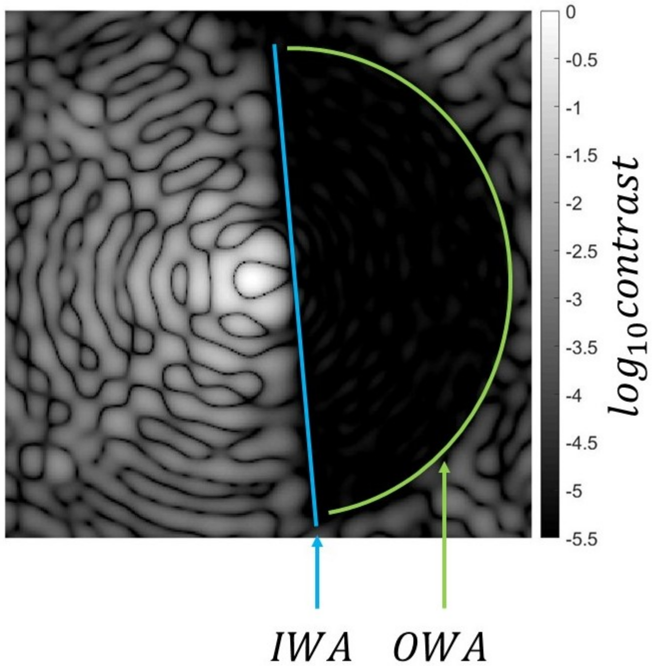

Figure 1.11: Log_{10} scaled image of a high-contrast dark hole generated by a coronagraph. The IWA and OWA defining the full extent of the coronagraph's region of stellar suppression are denoted in blue and green respectively.

For some coronagraphs, like the one seen in fig 1.11, there is also an outer-working angle (OWA) which defines the outermost point in the image plane at which the throughput is equal to 50% of the max throughput; this defines the outermost extent of the DH. In a full AO system, the OWA can also be defined by the control-radius of the DM. This is the case when the DH is not created by a coronagraph, but is instead generated using FPWFS and a DM.

1.3.2 Electric field conjugation

Another method for generating a DH involves FPWFS. Like the techniques discussed in Section 1.1.2.1, this form of FPWFS also relies on variations in intensity in the science image. However, rather than using these intensity fluctuations to determine the presence of specific aberrations, these methods use the measured intensity variations to directly calculate the full phase, or electric field E, in the image plane. By measuring the phase directly, the conjugate of the phase can be applied to cancel the phase over a specified region in the image, thereby creating a DH.

There are variations on this technique, (Bottom et al., 2016; Give'on et al., 2007) but one of the most common is known as electric field conjugation (EFC) (Groff et al., 2015). EFC uses the DM to probe a specific region in the image plane in order to estimate the electric field $\hat{E}$, and then uses the same DM to apply the conjugate field to suppress the starlight in that region. Since the measurements being made with EFC are not in intensity, but rather in complex phase, the RM cannot simply contain intensity images. Instead, the RM must also be complex. This information cannot be acquired with hardware alone in an optical setup; it also requires a model of the optical system. Using this model, a complex response matrix G can be built. This is done by actuating or "poking" each individual n^{th} actuator on the model DM and propagating the resulting field through to the image plane where the final complex field is $h_{n(poked)}$. The reference field at the detector h_0, acquired with no actuators is then subtracted, resulting in the change in field h_n resulting from the poke

$$h_n = h_{n(poked)} - h_0. \tag{1.25}$$

The complex response matrix G is then built just as it was in Section 1.1.2.1 where each column is now the change in the complex field at the detector in response to the single acutator poke such that

$$G = \begin{bmatrix} \Re(G) \\ \Im(G) \end{bmatrix} = \begin{bmatrix} \Re(h_1) & \dots & \Re(h_n) \\ \Im(h_1) & \dots & \Im(h_n)) \end{bmatrix}. \tag{1.26}$$

Following the generation of G, all of the next steps in this section describe the EFC process for a single iteration. The number of iterations required depends on the desired dark hole contrast; the following sequence of equations is repeated until the desired contrast is reached.

After the complex response matrix G has been built, the first step is to estimate the electric field complex phase at the detector. To do so, the field must first be probed. By applying a shape on the DM, a light probe is created in the image plane which is then shifted across the region of interest to probe the field. The ideal probe shape is created by a applying a sinc function on the DM, resulting Fourier transform in the image plane is a pair of rectangular probes with a flat intensity profile denoted by φ and described mathematically as

$$\varphi_{\pm} = \pm c\ sinc(w_x X)\ sinc(w_y Y)\ cos(aX)\ cos(bY). \tag{1.27}$$

where w_x and w_y scale the respective widths of the rectangular probes p in X and Y in the image plane, and a and b are the spatial frequencies that shift the probes in the image plane by the characteristic frequencies of the cosine, $\pm\frac{a}{2\pi}$ in X and $\pm\frac{b}{2\pi}$ in Y (Groff et al., 2015). An example of the sinc probe applied on the DM can be seen in the upper left of fig 1.12.

To probe the field over a selected region of interest, j probes are applied across the field. The complex field due to these probes must also be determined, and to do so, the probes are propagated through the simulated complex response matrix G

$$p_{j\pm} = \pm G u_{j\pm}. \tag{1.28}$$

The complex field of these probes generated with the simulated complex response matrix are shown in the lower left of fig 1.12 along with their intensity counterparts when applied in the physical system, shown in the upper right of fig 1.12.

From these probe fields, the observation matrix H is built which contains the real and imaginary parts of the simulated probe fields at the detector

$$H = \begin{bmatrix} \Re(p_1) & \Im(p_1) \\ \vdots & \vdots \\ \Re(p_j) & \Im(p_j) \end{bmatrix}. \tag{1.29}$$

These probes are also applied in the real optical system, using the real DM, and the intensity images at the detector are recorded for each probe pair. These images are reshaped into column vectors and transposed to form row vectors. The result is the matrix z in which each row is a single probe image such that

$$z = \begin{bmatrix} \Delta I_1^T \\ \vdots \\ \Delta I_j^T \end{bmatrix}. \tag{1.30}$$

Using these intensity images taken from the real system in conjunction with the complex fields associated with the same probes determined with the model, an estimate of the electric field $\hat{E}$ over the region of interest can be derived
$\hat{E}$ = the electric field estimate derived using the observation matrix H and the intensity image matrix z

$$\hat{E} = \frac{1}{4}(H^T H)^{-1} H^T \; z. \tag{1.31}$$

$$\begin{bmatrix} \Re(\hat{E}) \\ \Im(\hat{E}) \end{bmatrix} = \frac{1}{4} \begin{bmatrix} \Re(p_1) & \dots & \Re(p_{np}) \\ \Im(p_1) & \dots & \Im(p_{np})) \end{bmatrix} \begin{bmatrix} \Delta I_1 \\ \vdots \\ \Delta I_{np} \end{bmatrix} \tag{1.32}$$

A simulated example of the real and imaginary parts of $\hat{E}$ can be seen in the upper left fig 1.13 alongside the actual real and imaginary field components applied in simulation.

Now that we have a field estimate, the goal is to determine the correct shape to place on the DM that will cancel that field over the region of interest. The complex response matrix G relates the field at the detector back to each individual actuator on the DM. To cancel the field, a specific shape must be applied to the DM. This shape is defined by the vector $\bar{u}$ which is a vector containing an amplitude value for each actuator. So for a given field estimate $\hat{E}$, there is a shape $\bar{u}$ that can be placed on the DM such that, when propagated to the detector by G, the resulting field will cancel $\hat{E}$

$$G\bar{u} + \hat{E} = 0. \tag{1.33}$$

To determine $\bar{u}$ from eq 1.33, the command matrix M is first derived by taking the pseudo-inverse of the complex response matrix G

$$M = (G^T G)^{-1} G^T \;\; = \begin{bmatrix} \Re(G) \\ \Im(G) \end{bmatrix}^{+}. \tag{1.34}$$

The vector of actuator amplitude $\bar{u}$ is then determined by

$$\bar{u} = -M \; \hat{E}. \tag{1.35}$$

Or written out in full, the DM shape is determined by

$$\bar{u} = \begin{bmatrix} \Re(G) \\ \Im(G) \end{bmatrix}^{+} \begin{bmatrix} \Re(\hat{E}) \\ \Im(\hat{E}) \end{bmatrix}. \tag{1.36}$$

An example of the DM shape derived by EFC to cancel the estimated field is shown in the bottom left of fig 1.13. The EFC algorithm, as it is implemented in simulation, is summed up in the flow chart in fig 1.14, and the full Matlab code can be found in the Code Appendix.

As previously mentioned, it takes multiple iterations of these steps to finally converge to the desired dark hole contrast. The right side of fig 1.13 shows an example of an aberrated dark hole being driven back to its initial contrast in 15 iterations of EFC. Both the aberrated and EFC-corrected dark holes are shown as is the contrast convergence per iteration.

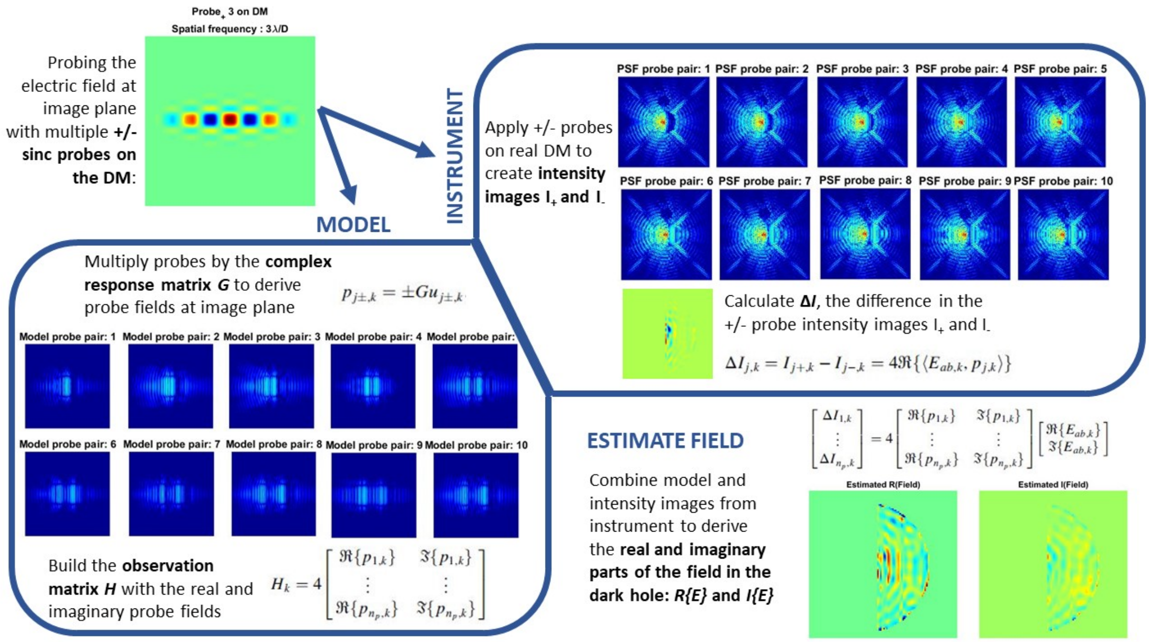

Figure 1.12: Demonstrating pair-wise probing with a vAPP coronagraph in simulation to derive an estimage of the electric field within the aberrated dark hole created by the vAPP. (Equations from (Groff et al., 2015))

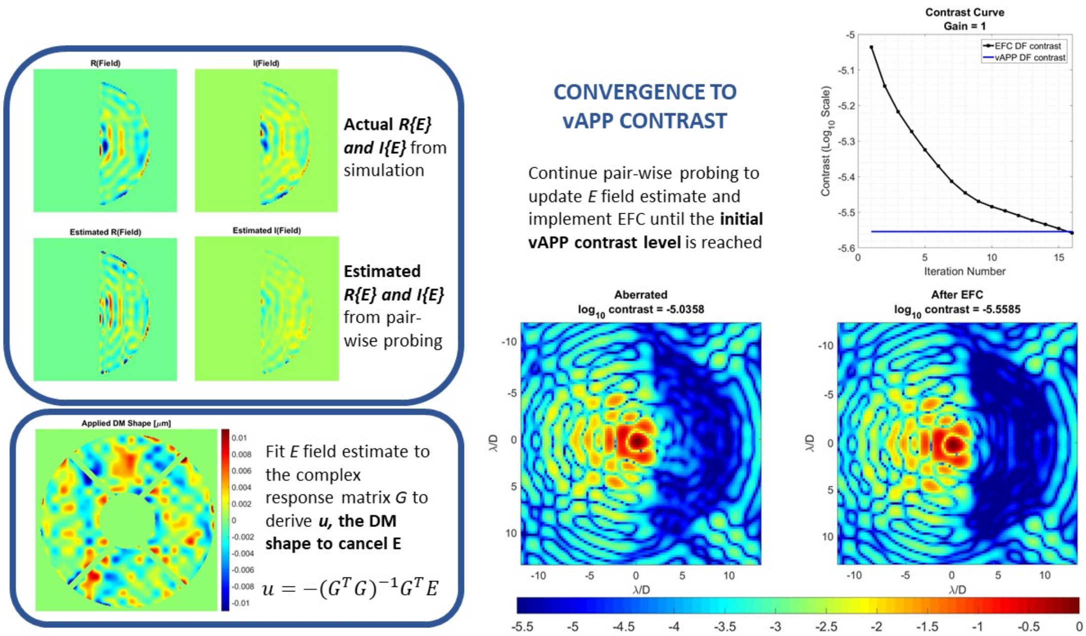

Figure 1.13: Comparison of the actual field, both the real and imaginary components, and of the estimate derived by pair-wise probing. The aberrated dark hole seen at the bottom right was driven back to its initial ideal contrast by estimating the field in the dark hole using pair-wise probing and then forcing the appropriate shape on the deformable mirror to apply the estimated field's complex conjugate to cancel the aberrations in the region of interest. (Equations from (Groff et al., 2015))

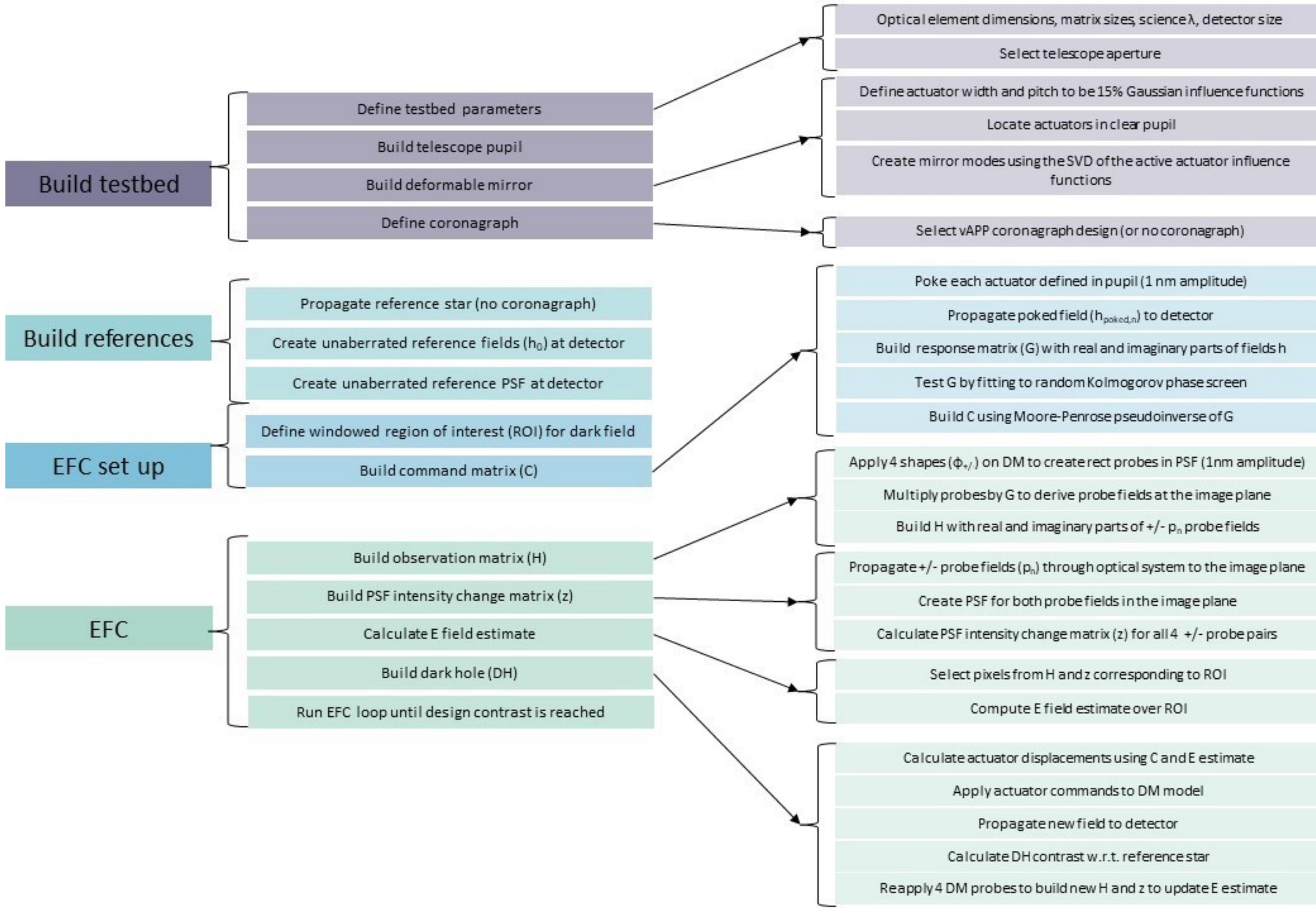

Figure 1.14: Electric field conjugation simulation code flow chart

1.4 High contrast stabilization

Whether generated by a coronagraph or by EFC, depending on the depth of contrast, a DH allows for light from an exoplanet to be seen above the otherwise much brighter stellar signal. However, the DH is very susceptible to small dynamic aberrations in the beam path, and over time, these aberrations will create speckles in the image that once again dominate the planetary signal. Such aberrations produce post-coronagraph stellar light leakage and result in a quasi-static speckle field in the image plane that limits the DH contrast (Traub and Oppenheimer, 2010). One of the main sources of these aberrations is non-common path (NCP) errors.

Any wavefront sensor that contains optics not seen by the science camera or is blind to optics seen by the science camera is NCP with the science camera. This category includes most current wavefront sensor systems including the pyramid wavefront sensor used on Subaru Telescope's SCExAO (Jovanovic et al., 2015), the Large Binocular Telescope Adaptive Optics system (LBTAO), and the Magellan Adaptive Optics instrument (MagAO). While state-of-the-art, these wavefront sensors still suffer from being blind to portions of the optical system prior to the science camera. This becomes an issue in a high-precision imaging instrument where minute aberrations left unsensed by the NCP wavefront sensor go uncorrected, and the resulting quasi-static aberrations can eventually become larger than the residual dynamic wavefront errors after correction by the WFS control loop. This allows stellar speckles to form and dominate the faint planetary signal in the region of interest. For high contrast imaging, the WFS should ideally be common path with all of the optics seen by the science instrument to allow access to all aberrations created in the science beam; it is therefore beneficial to use the science image itself as the wavefront sensor.

For this reason, when aberrations begin to dominate the contrast in the DH, FPWFS is used to return the DH to its initial contrast. This can be done using EFC to rebuild the DH. However, EFC requires field information from the DH. Therefore, as the DH contrast gets deeper, there is less light from which a field estimate can be built, so exposure times must be increased. The result is a process that can take hours to return to the initial DH contrast. It would be much more time-efficient if, instead of measuring and correcting the field within the DH after it has been degraded by aberrations, the DH could be stabilized by making fast measurements of changes that have occurred in the science image.

In the following chapters, we will present the theory, development, and demonstration of new FPWFS technologies that will allow for continuous direct observations of faint exoplanetary companions. The development and design of the lab in which these demonstrations were carried out is addressed in Chapter 2. In Chapter 3, a new method for sensing low-order aberrations in the science image using a "modal wavefront sensor" is presented. The theory and development of a new method for stabilizing the dark hole contrast using only light outside of the dark hole is the focus of Chapter 4, and its development in both simulation and in the lab is presented in Chapter 5. All of the work presented here has been specifically tailored to inform the design and performance of FPWFS techniques that will be deployed on the Magellan Extreme Adaptive Optics Instrument (MagAO-X) in 2019. For this reason, Chapter 6 consists of the work done for the MagAO-X preliminary design review. Finally, Chapter 7 concludes this paper with an overview of the future of this work on MagAO-X and next steps to take in the development of this technology. A section containing the code used throughout this work in both simulation and the lab has also been appended.

CHAPTER 2

University of Arizona Extreme Wavefront Control Laboratory

The University of Arizona's Extreme Wavefront Control Laboratory consists of two separate optical tables; the first of which is the actual instrument bench for MagAO-X. This bench is housed in a cleanroom environment while the instrument is being assembled and serviced in the lab. The MagAO-X instrument has been designed so that the entire bench (sans table legs) will be transported back and forth between the lab in Tucson and the Magellan Clay Telescope at the Las Campanas Observatory (LCO) in Chile.

(a) Full view of both optical benches in the lab

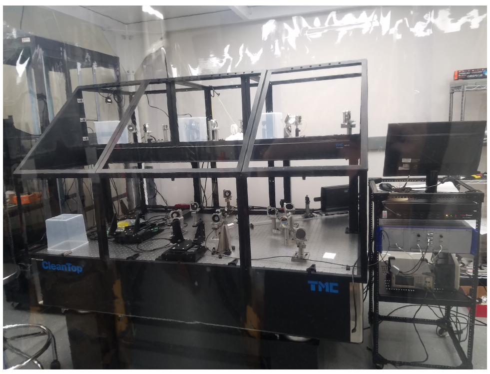

(b) The MagAO-X instrument bench in the cleanroom environment

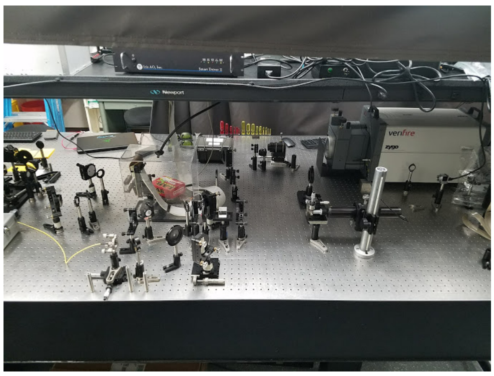

(c) The lab bench hosting the Zygo interferometer and high contrast imaging setup

Figure 2.1: The two optical tables in the University of Arizona Extreme Wavefront Control Lab

The second optical table is the main workhorse of the lab on which all experiments are conducted. This bench currently houses the Zygo interferometer which is used to analyze the surface quality of all of MagAO-X's optical elements and to flatten and calibrate the deformable mirrors (DMs) used on both the lab bench and on MagAO-X. This bench is also the future home of the laser guide star project (LGS) and a pyramid wavefront sensor (PyWFS) testbed. Currently, this optical table is hosting a high-contrast imaging testbed designed to allow for rapid prototyping and testing of multiple coronagraph architectures, wavefront sensors, and control algorithms. The design allows for access to mulitple focal and pupil planes at which several different coronagraphic masks could be placed. The system also contains a DM with which wavefront sensing and control algorithms can be implemented. Throughout the rest of this document, when the UA Extreme Wavefront Control Laboratory testbed is mentioned, it is referring to this testbed. A discussion on the design, deveolpment, and alignment of this testbed follows in 2.1 and an overview of the MagAO-X instrument is given in section 2.2.

2.1 The Extreme Wavefront Control Testbed

2.1.1 Optical design

The front end of the University of Arizona's Extreme Wavefront Control Laboratory testbed consists of a telescope simulator mimicking the Magellan Clay Telescope at LCO in Chile. The illuminating source approximating a broadband stellar point source is a Fianium WhiteLase Micro Supercontinuum laser which diverges from the fiber optic source onto the bench. The laser source bandwidth is 400 nm to 2000 nm; this wavelength range is limited by an NIR filter which passes only light up to 800 nm, thereby only allowing visible spectrum light onto the testbed. To allow for nearly monochromatic testing, a filter wheel follows the NIR filter and contains 3 bandpass filters, two of which are centered at 600 nm with bandwidths of 10 nm and 40 nm. The third bandpass filter is centered at 660 nm with a bandwidth of 10 nm. For all testing done on the bench in the following document with the vector apodizing phase plate (vAPP) coronagraph, the third filter was used because its central wavelength is only 4 nm off of 656 nm, the central design wavelength for the MagAO-X coronagraph being tested in the lab. As shown in figs 2.2 and 2.3, the remaining diverging light within this limited bandwidth is then collimated by the first off-axis parabolic (OAP) mirror and sent to the pupil mask which defines the system entrance pupil (PP1); this pupil mask is a reflective aluminum mask designed to simulate the Magellan Clay Telescope. This pupil is relayed by off-axis parabolic (OAP) mirrors to a conjugate pupil plane (PP2) where a 32 x 32 actuator Boston Micromachines deformable mirror is placed; the DM is used both to inject aberrations into the system and to apply corrections sensed by the wavefront sensor. Another OAP and an achromatic doublet then relay the pupil-DM conjugate plane to the vAPP coronagraph mask (PP3). This final pupil plane is then brought to focus at the science detector by a single lens. The designs of the Magellan pupil mask and vAPP coronagraph are described in greater detail throughout this chapter in sections 2.1.1.1 and 2.1.1.3 as is the calibration of the DM in section 2.1.1.2 (all three of these pupil plane optics are shown in fig 2.4). The alignment of the testbed is discussed in section 2.1.2.

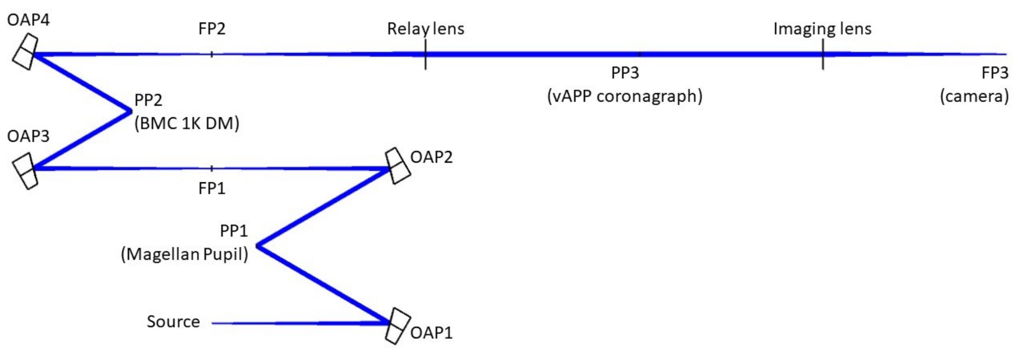

Figure 2.2: Zemax model of the testbed (courtesy of J. Lumbres)

Throughout the telescope simulator and DM up to the coronagraph arm, each conjugate pupil plane is brought to focus and recollimated by off-axis parabolic mirrors (OAPs) with a 272.24 mm effective focal length (f) and an angle of 30°. This 30° angle is maintained throughtout the system such that the beam footprint at each pupil plane is defined by a cross-sectional area with a $\frac{1}{cos(30°)}$ elongation along the x-axis. The reflective Magellan mask was designed to compensate for this elongation, and the modal basis set built for the wavefront control algorithms on the bench was defined by this ellipitical beam footprint on the DM (see Chapter 5). The DM is conjugate to the pupil mask in the second system pupil plane. In the third and final pupil plane, the vAPP testplate with 7 masks is mounted on a translation stage to allow for easy mask selection.

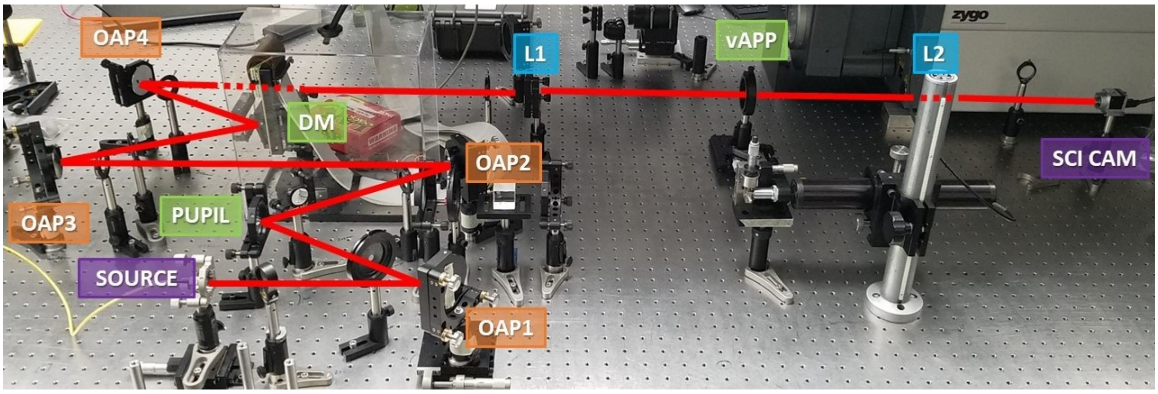

Figure 2.3: The Extreme Wavefront Control Laboratory testbed

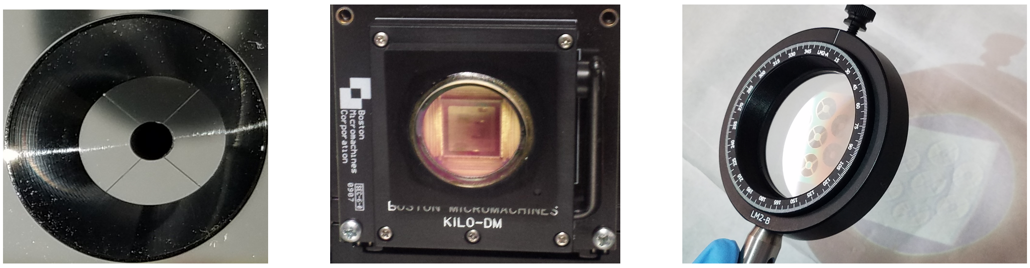

(a) Reflective Magellan pupil mask

(b) BMC 1K DM

(c) Mounted transmissive vAPP testplate with 7 masks

Figure 2.4: The testbed's three conjugate pupil plane optics

2.1.1.1 Reflective Magellan pupil mask

The testbed pupil mask was designed to simulate the circular Magellan pupil in reflection (fig 2.5a). Due to the beam's 30^o angle of incidence with respect to the mask, the beam cross-section seen by the mask is a cross-section with a $\frac{1}{cos(30°)}$ elongation along the x-axis (fig 2.5b). To match this elongated beam footprint, the mask was designed with the same ellipticity (fig 2.5c).

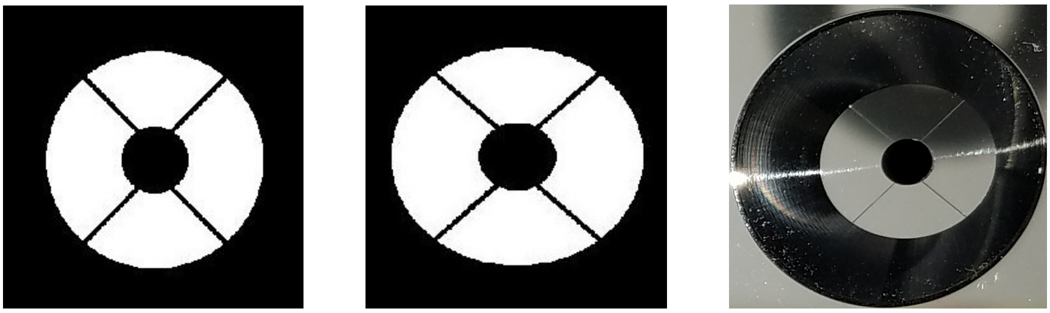

(a) Magellan pupil (b) Stretched by cos(30^o) (c) Pupil mask in the lab

Figure 2.5: The reflective Magellan pupil and its elliptical shape elongated in X to match the beam footprint at a 30^o angled cross section. Shown in simulation (left and center) and in the lab (right).

The diameter of the reflective Magellan mask was chosen to be 6.7 mm in the Y direction so that it could be easily reimaged to an 8.6 mm pupil in the third and final conjugate pupil plane in the system using the OAPs already in place on the testbed and an off-the-shelf 350 mm focal length lens. The pupil was designed to be 8.6 mm in diameter at the third pupil plane to match the vAPP coronagraph masks placed in that plane. The vAPP coronagraph on the MagAO-X instrument was designed to be 8.6 mm in diameter, and one of the main goals for this testbed was to test multiple vAPP masks before finalizing the design for the coronagraph on MagAO-X. The pupil mask was also designed with very thin spiders (the support structures on the telescope suspending the secondary mirror over the primary seen as the 'x' shape across the pupil) and a slightly undersized central obscuration (the shadow of the secondary mirror over the primary mirror) and slightly oversized outer diameter so that, when relayed to the third pupil plane with the vAPP coronagraph mask, it would overfill the vAPP, thereby making the vAPP the system stop. By matching the shape of the vAPP mask, but undersizing the mask features and making the vAPP the system stop, it was ensured that the vAPP's performance would not be limited by underfilling the full vAPP aperture.

The pupil mask (shown in fig 2.6) was tooled from a circular 2 inch diameter aluminum plate by Dr. Ron Liang's group at UA's College of Optical Sciences using a CNC machine. The surface mimicking the reflective telescope pupil was diamond turned, resulting in a residual RMS surface error of less than 12.5 nm. To define the edge and features of the pupil with high precision, anodization of the aluminum outside the polished pupil was considered. Given the source bandwidth across the visible and near-IR spectrum made available by the supercontinuum laser, one goal of the mask design was to not limit the bandwidth of the system by choosing an anodization with high performance (less than 4% reflection) only across a finite bandwidth in either the visibile or near-IR. No anodization technique was capable of delivering this performance across the full 400 - 2000 nm bandwidth of the supercontinuum laser. This forced the design to evolve from an anodized outer edge to an angled cut. The pupil was designed to have a 45° angled cut sloping down and away from the pupil so that light outside the pupil edge was reflected out of the sytem. The central obscuration was made by cutting through the aluminum disk also with a 45° angled cut so that light passing through the central obscuration would exit through the back of the mask and not reflect off an inner edge back out into the beam path. The spiders were inscribed with an angled cutting tool to a depth of 10 μm, deep enough that light did not reflect back out into the pupil.

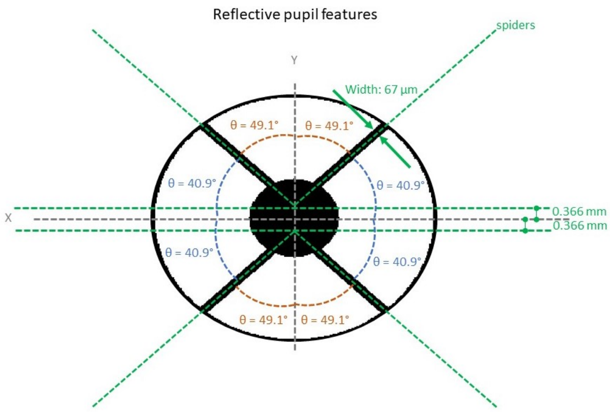

(a) Reflective pupil features

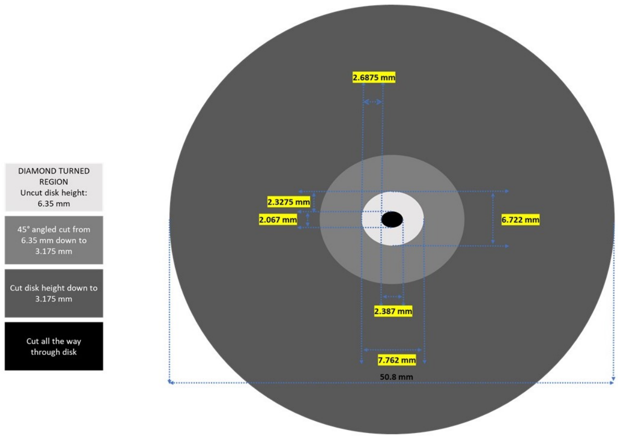

(b) Full Magellan mask design

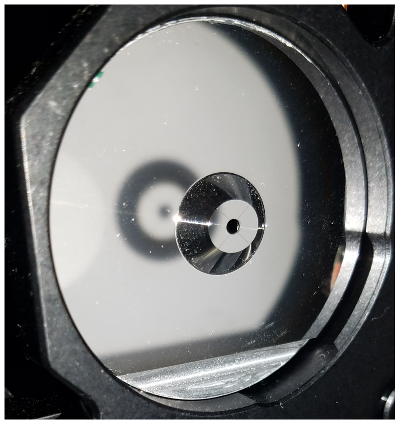

(c) Reflective Magellan mask mounted on the bench

Figure 2.6: Design of the reflective Magellan mask and the final product mounted on the bench

By using geometrical optics rather than anodization techniques to define the edge and features of the mask, the final result was a mask that can be used at any wavelength between 400 and 2000 nm without any limitation on performance except for the minor fluctuations in aluminum's reflectivity across that bandwidth (which remains above 86% across the laser's full wavelength output). To verify the mask design, once the pupil mask was aligned on the testbed, the pupil was relayed to the first conjugate pupil plane, and an image of the beam footprint was taken at 90° incidence with respect to the beam propagation direction. The result was the designed circular Magellan mask with no cropping or vignetting due to beam - mask ellipticity mismatch; this image can be seen in fig 2.13b.

2.1.1.2 Boston Micromachines deformable mirror

The Boston Micromachines Kilo-DM was placed in the second pupil plane in the system (the first relayed pupil plane conjugate to the Magellan mask). This DM is a continuous surface MEMS device with 1020 actuators arranged in a 32 x 32 square grid with ground pins in the four corners. This DM has a 15% interactuator coupling with a pitch of 300 μm. When powered on, the DM has significant sag across the surface. Before it could be used, the DM first had to be flattened and calibrated. This was done predominately by K. Van Gorkom using the Zygo interferometer. The DM was placed in the Zygo's beam, each actuator was poked, and the resulting image of the influence function was measured individually. These influence functions were used to define the model DM created in simulation (see fig 2.7). To flatten the DM using these influence function images, an image of the full DM surface was taken and fit to the influence functions, thereby returning the correct amplitude for each actuator to fit the overall surface shape. This shape with the opposite sign was then applied to the DM, forcing the surface to a flat. This was done iteratively until a flat surface with less than 3.5 nm RMS over the illuminated beam footprint region was reached (Van Gorkom et al., 2018).

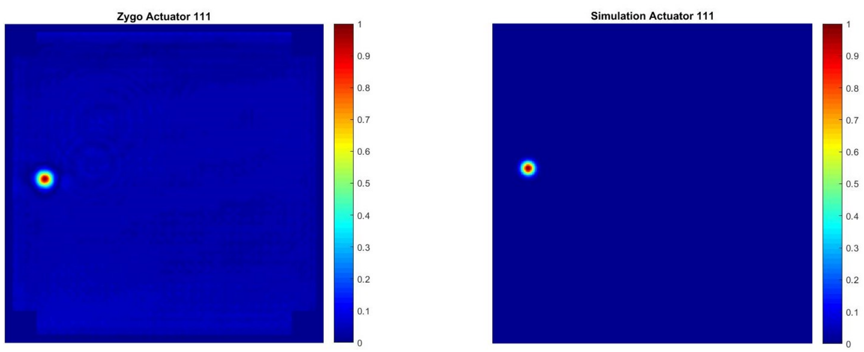

Figure 2.7: Comparison of the Zygo measured and simulated BMC DM influence functions.

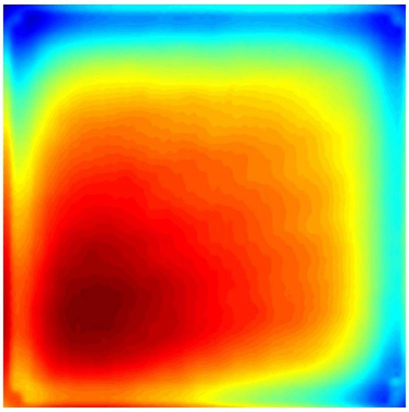

(a) Sag across the surface of the powered, unflattened DM

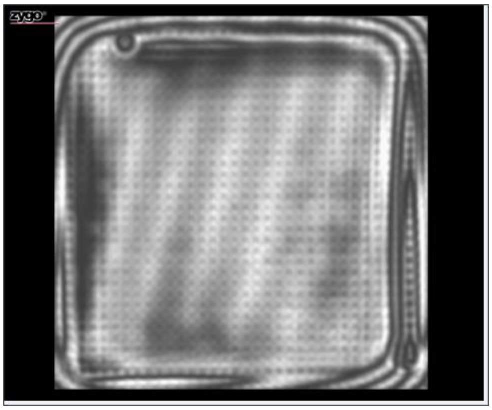

(b) Zygo measurement of the flattened DM surface

Figure 2.8: The BMC DM before and after flattening.

As with the Magellan mask, the beam incident on the DM was angled at 30°, thereby producing the same elongation of the pupil on the DM in the X direction. With 300 μm actuator spacing, the 6.7 mm beam footprint subtended 22 actuators in the Y direction and 25 in the X direction due to the ellipticity. Given that the control radius of the DM is determined by the number of actuators N such that the control radius is equal to $\frac{N}{2}\ \lambda/D$, this set the limiting control radius of the DM to 11 λ/D. Once aligned on the testbed, to determine which actuators were located within the illuminated beam footprint on the DM, each actuator was poked individually and an image was taken of the PSF. The reference image was subtracted, and the change in the PSF for each actuator poke was measured. A threshold was set to select the difference images with the highest signal present, and the corresponding actuators for each of these images was recorded. The resulting image of the beam footprint on the DM seen in fig 2.9 was built by summing together all the influence function images for each of the illuminated actuators detected using this method.

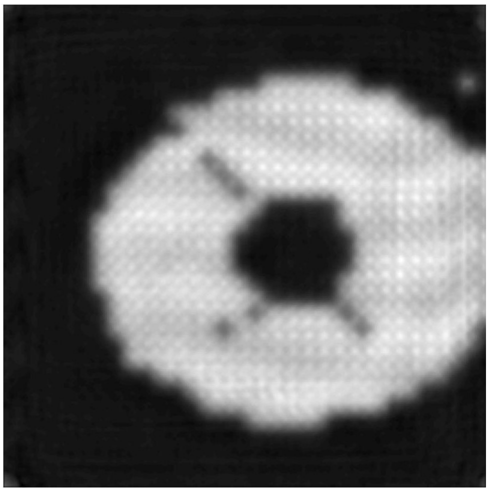

Figure 2.9: Illuminated actuators within the elliptical beam footprint seen on the DM. The shadow of the central obscuration and three of the four spiders can be seen.

For all subsequent use of the DM, commands were sent only to these actuators and one ring of actuators outside the illuminated pupil and one ring of actuators inside the shadow of the secondary obscuration. The oversizing was done to ensure that the full illuminated pupil was active and not being deformed by stationary actuators at the edge of the illuminated region.

It will also be noticed in fig 2.3 that the DM is maintained in a clear acrylic housing. We (myself and J. Knight) designed the housing to provide a humidity controlled environment for the DM. This particular DM is not hermetically sealed, so under high humidity conditions (where "high" is usually defined to be approximately greater than 30%, these devices can arc between actuators on the DM. To ensure this did not happen to the DM, this housing was designed to allow for its cables to run out the back of the box while dry air run through a desiccant was piped in through tubing at the top of the box. An Arduino Uno was used as a hygrometer which monitored the humidity within the box and output measurements every second. This was monitored by MATLAB and Python scripts or by eye by DM operators whenever the DM was in use with safe shutdown procedures in place in case of an increase in humidity. While the acrylic housing was trasparent across the full visible spectrum, it was not designed for high-quality wavefront transmission. The beam entrance into the box was therefore replaced with a custom 10 mm thick UV fused silica window from Thorlabs with $\frac{\lambda}{10}$ transmitted wavefront error at 633 nm. This ensured that the beam quality was not substantially degraded by propagating through low-optical-quality acrylic as it entered and exited the DM enclosure.

2.1.1.3 Vector apodizing phase plate coronagraph

In the first two phases of the MagAO-X instrument, the system coronagraph will be a vAPP similar to the vAPP coronagraph currently in operation at the Magellan Clay Telescope on the existing MagAO system (Otten et al., 2017). The vAPP (Snik et al., 2012) is a coronagraph that takes unpolarized light from the astronomical source and creates two polarized copies of the PSF, each with a 180° D-shaped dark hole that, when combined, yields a 360° high contrast region around the stellar PSF as seen in fig 2.10 (Bos et al., 2018). Between the two polarized science PSFs with dark holes is a copy of the pre-coronagraph system PSF with a peak intensity that is roughly 100x lower than that of the science PSFs. This PSF is the result of an unpolarized leakage term which is not affected by the vAPP.

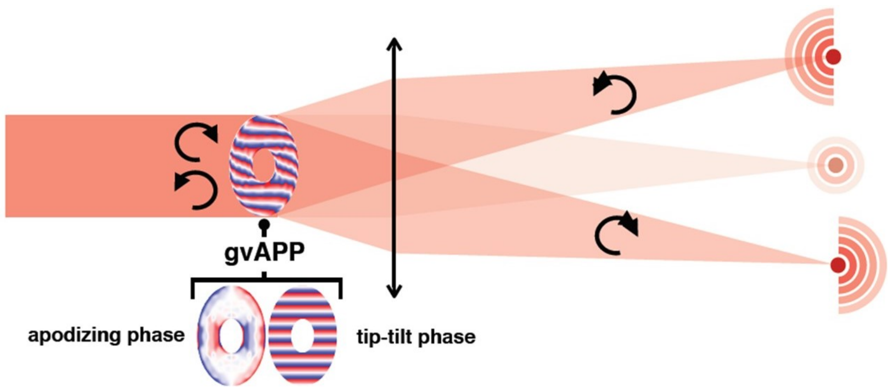

Figure 2.10: Grating vAPP operation (Bos et al., 2018)

For the vAPP in the lab, beyond the science PSFs, the vAPP also creates two sets of low-order modal wavefront sensing (MWFS) PSFs, with one set positively biased and one set negatively biased. These MWFS spots are created by multiplexing multiple mode holograms onto the vAPP coronagraph mask (Wilby et al., 2017). These MWFS PSFs are the signal used for driving the LOWFS closed loop, and they can also be used for optical alignment adjustment. Both uses of the MWFS are addressed in greater detail in Chapter 3.

The vAPP coronagraph in the lab is not one mask, but rather a 2 inch diameter circular plate with seven individual masks inscribed on the substrate. The plate is mounted in a 2 inch rotational mount on a translation stage to allow for easy mask selection and is aligned on the testbed in a pupil plane conjugate to both a Magellan pupil mask and the DM. (fig 2.11).

(a) Testplate phase patterns (b) Mounted testplate

Figure 2.11: Magellan vAPP phase patterns and testplate in the lab

Each mask differs by the outer working angle (OWA) of the dark hole and in the MWFS design. Of the seven masks, six are inscribed with phase patterns producing the two PSFs with dark holes and, in four cases, MWFS PSFs with different modal basis sets. The seventh mask is a simple binary mask of the Magellan pupil with no phase pattern inscribed. Of the masks with MWFS PSFs, one creates only phase diversity spots; one contains the first twelve Zernike polynomials; one contains twenty Zernike modes that have been orthonormalized to the Magellan pupil; and one contains eight Zernike modes that have been orthonormalized to the Magellan pupil plus phase diversity spots. All of these masks and their resulting images can be seen in fig 2.12. The design and operation of the MWFS PSFs are described in further detail in the following chapter.

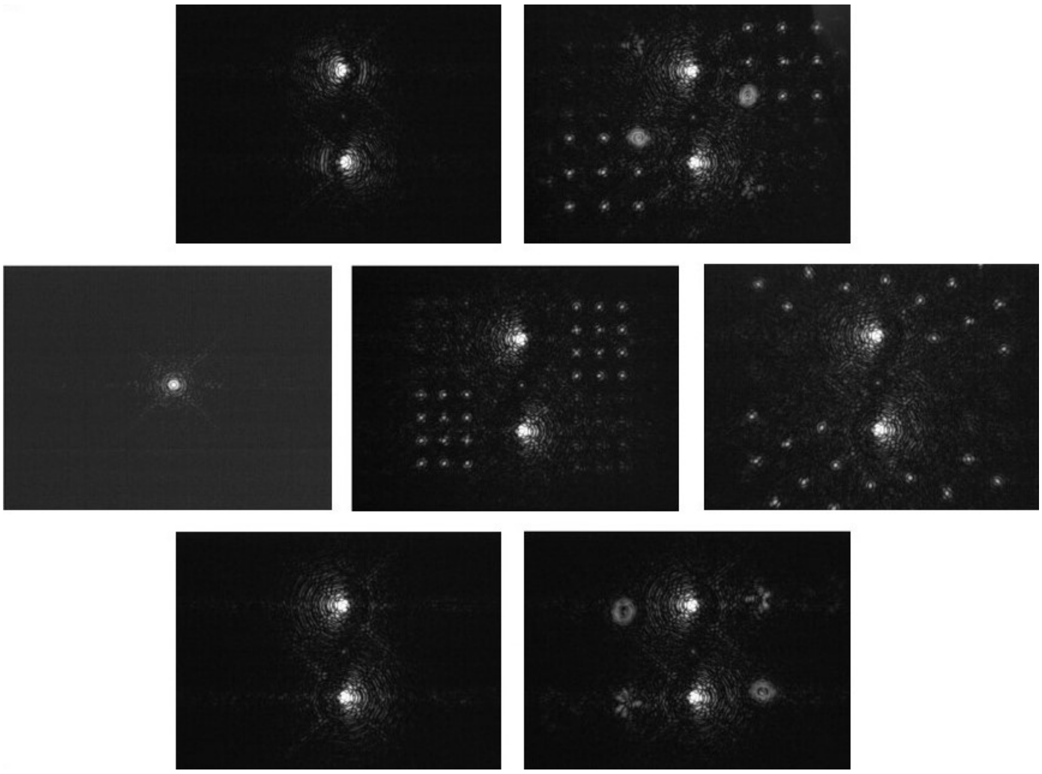

Figure 2.12: The seven vAPP masks and resulting science PSFs, dark holes, and MWFS PSFs on the UA Extreme Wavefront Control Lab's test plate. **Top row**: (*Left*) 2 - 6 λ/D dark holes, no MWFS. (*Right*) 2 - 11 λ/D dark holes, 8 Zernikes orthonormalized to the Magellan pupil + phase diversity MWFS. **Middle row**: (*Left*) No dark holes, no MWFS. (*Center*) 2 - 15 λ/D dark holes, 12 Zernike MWFS. (*Right*) 2 - 11 λ/D dark holes, 20 Zernikes orthonormalized to the Magellan pupil MWFS. **Bottom row**: (*Left*) 2 - 11 λ/D dark holes, no MWFS. (*Right*) 2 - 11 λ/D dark holes, phase diversity MWFS.

For testing wavefront sensing and control algorithms in the lab (see Chapter 5), the 12 Zernike mask shown in the center image of fig 2.12 was implemented on the testbed. For direct comparison to theory, this vAPP was also used for testing the same wavefront sensing algorithms in simulation.

2.1.2 Building and alignment

Up until the coronagraph arm of the testbed, each pupil plane is a one-to-one relay using identical OAP mirrors; a description of the design and operation of these mirrors can be found in Chapter 6. These are the primary powered optics on the testbed responsible for propagating pupil planes to focal planes. To minimize the number of optics required in a system, OAPs are an excellent choice; by being a powered optic that focuses off-axis, an OAP replaces a lens - fold mirror pair by simultaneously bringing the light to focus and sending the beam off to the next optic. They are advantageous over lenses in a broadband system as well since, as mirrors, their performance is achromatic (with the exception of the wavelength dependence of the coating's reflectance). The only issue with OAPs is the level of precision required when aligning them. Due to their parabolic shape, these optics are highly susceptible to astigmatism and coma; without exact alignment of tip/tilt and angle of reflection between the incoming and outgoing beam, these two aberrations dominate the resulting PSF. To achieve this high precision, the PSF following each pair of OAPs can be used to make minute adjustments to remove astigmatism and coma from the final PSF.

To align this testbed, the visible spectrum of the supercontinuum laser without any narrow bandpass filter was used as the source. The first optic in the system post-source is OAP 1. To ensure that this optic was not tipped with respect to the lab bench, it was first aligned in its kinematic tip/tilt mount in front of a collimated helium-neon (HeNe) laser, and the actuators on the back of the mount were adjusted until the outgoing focused beam was level with the testbed. Levelness was determined using a set target observed close to the OAP surface, then far away. This test was done for all optics before they were placed on the testbed to ensure no tipping was induced by each optic. The same test was done with the supercontinuum source and the set test target to ensure that the source itself was also level.

Once OAP 1 was level with the bench, it was placed in front of the supercontinuum source and aligned to send the beam off at a 30° angle with respect to the incoming beam. This OAP collimated the beam coming from the diverging source, so normally a shear plate interferometer would be used to observe the fringes and determine when the beam was collimated (again see Chapter 6 for a discussion on this technique). With a broadband source, a shear plate interferometer could not be used since the fringe pattern visibility washes out with a broadband source. Therefore, to align OAP 1, OAP 2 had to be placed at a distance of twice the OAP focal length ($2f$) away from OAP 1 where it brought the beam to focus. At this focal point (FP1), a camera was placed to observe the PSF, and the two OAPs were then adjusted together until the PSF no longer contained astigmatism or coma, and the energy in the core of the PSF was maximized. Adjusting both OAPs required translation along the beam path to achieve the proper $2f$ distance between the two mirrors, clocking the mirrors (rotating them in their kinematic mounts about the direction of propagation), lateral and height adjustment to center the beam on the center of the OAP, and rotation about the post to ensure that the outgoing beam was at a 30° angle with respect to the incoming beam. After adjustment, the final PSF in the first focal plane was astigmatism and coma free as seen in fig 2.14a.

Following FP1, the beam diverged and was re-collimated with OAP 3, relaying the system entrance pupil (PP1) to the second conjugate pupil of the system (PP2). It should be noted here that, between OAP 1 and OAP 2 at a distance of *1f* from both OAPs is the Magellan pupil mask which defines the entrance pupil of the system at PP1. This pupil is then relayed throughout the system by the OAPs. Therefore, at a distance of *1f* from OAP 3, a one-to-one relayed image of the pupil was formed. A lens system to de-magnify the beam and a camera were temporarily placed in this plane to obtain the image in fig 2.13 showing the re-imaged Magellan pupil mask.

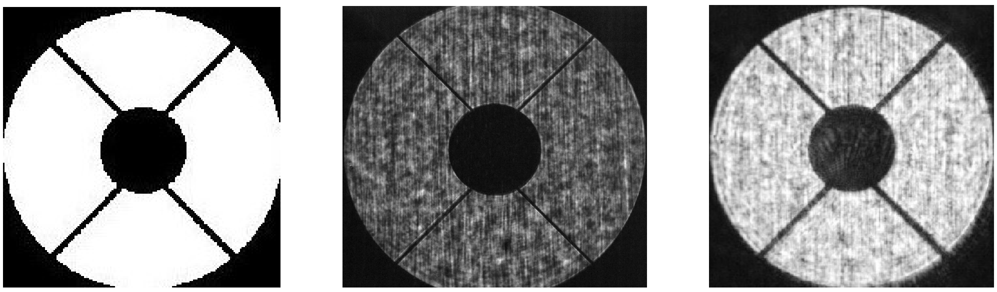

(a) Magellan pupil in simulation

(b) Magellan pupil on the testbed

(c) vAPP coronagraph aligned with Magellan pupil mask

Figure 2.13: Re-imaged pupil planes throughout the optical layout

PP2 is the designated pupil plane for the DM, but for the initial alignment, a flat mirror was used as a place holder. This was done due to the deformed nature of the unpowered DM. Using the DM for initial alignment to ensure good beam quality would have required that the DM be powered on and flattened, which would also mean it needed to be in the humidity-controlled housing. For initial rough-alignment, this was impossible, so a flat was used in its place. Following the temporary flat in PP2, OAP 4 brought PP2 to a focus at FP2, thus ending the front end telescope simulator section of the testbed. A camera was placed at FP2, and OAPs 3 and 4 were adjusted in the same fashion as OAPs 1 and 2 to remove astigmatism and coma from the PSF. The result is shown in fig. 2.14b.

Following FP2, the beam diverges and is collimated by an achromatic doublet relay lens with a 350 mm focal length. This magnifies the beam footprint from 6.7 mm in diameter to 8.6 mm to match the vAPP coronagraph mask size in PP3. Before the vAPP mask was put in place, a 300 mm lens was placed 300 mm behind PP3, bringing the light to focus at FP3. A 100 mm focal length lens to reimage the pupil plane and a camera were then temporarily placed at FP3. With a sharp, in-focus image formed of the conjugate pupils, the vAPP testplate was then mounted and placed into the system and translated along the beam path until its features also came into focus, indicating that it was in a conjugate relayed pupil-plane with the DM plane and the Magellan pupil mask. The vAPP mask chosen for alignment was the simple binary mask without an inscribed phase pattern. The 100 mm focal length lens was then removed, and the final PSF was imaged onto the science camera at FP3 which can be seen in fig 2.14c. It should be noted that the diffraction from the spiders is much more noticeable in FP3 as opposed to FP1 and FP2 because the mask features on the vAPP are oversized to ensure that the vAPP mask becomes the system stop. The larger vAPP spiders therefore results in a stronger spider diffraction pattern.

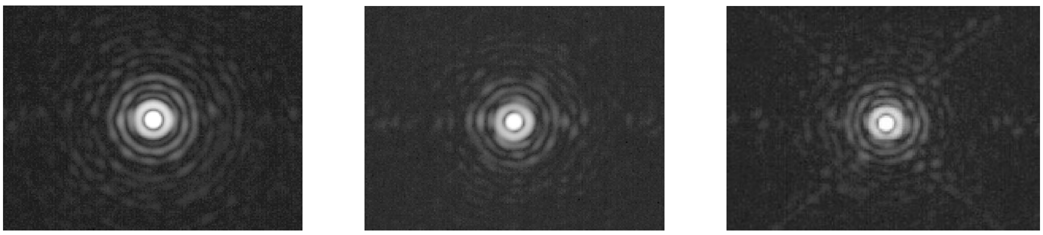

(a) First focal plane (FP1)

(b) Second focal plane (FP2)

(c) Third focal plane (FP3) post-vAPP coronagraph

Figure 2.14: Focal planes throughout the optical layout used for precise alignment

With the system aligned, irises were placed before and after each OAP and lens throughtout the system and aligned with the beam so that, when closed down the beam footprint would be exactly aligned on the center of each iris. The irises are kept open during operation, but can be closed down one at a time to track the beam through the system should any misalignment occur. This method is described in Chapter as a recommendation for use on the MagAO-X system to maintain alignment after transit to the telescope in Chile. With the irises in place, 100 mm relay lens was again placed in front of the camera to form an image of the conjugate pupil planes. The flat in PP2 was then removed and the unpowered DM was placed in the pupil plane. The beam footprint on the irises was then used to determine the correct location and rotation of the DM. The image of the conjugate pupil planes on the science camera also acted as an iris of sorts. By monitoring when light reached the camera and when the pupil mask and vAPP mask images were once again realigned with each other, the DM was precisely aligned to the correct location. When the housing was then placed over the DM, the 10 mm thick window (through which the beam passes twice) induced an optical delay and shifted the beam path, so the DM was slightly translated to compensate for the added thickness.

By using this alignment method, the DM never had to be powered on during alignment. The irises were also kept in the system for future realignment use when an optic in the system inevitably drifted, sagged in its mount, or was moved. The 100 mm len can also be easily shifted in front of the science camera to reimage the conjugate pupil planes to also assist in realignment and to translate the vAPP testplate and align a new vAPP mask in the system.

2.2 The Magellan Extreme Adaptive Optics Instrument (MagAO-X): Instrument overview

The Extreme Wavefront Control Lab is also home to the Magellan extreme adaptive optics (MagAO-X) instrument. As seen in fig 2.1b, MagAO-X is housed in its own cleanroom environment while it is under construction and before it is transported to the Magellan Clay Telescope in Chile. At the telescope, the MagAO-X bench will be placed on a set of floating table legs on the Nasmyth mount as shown in fig 2.15.

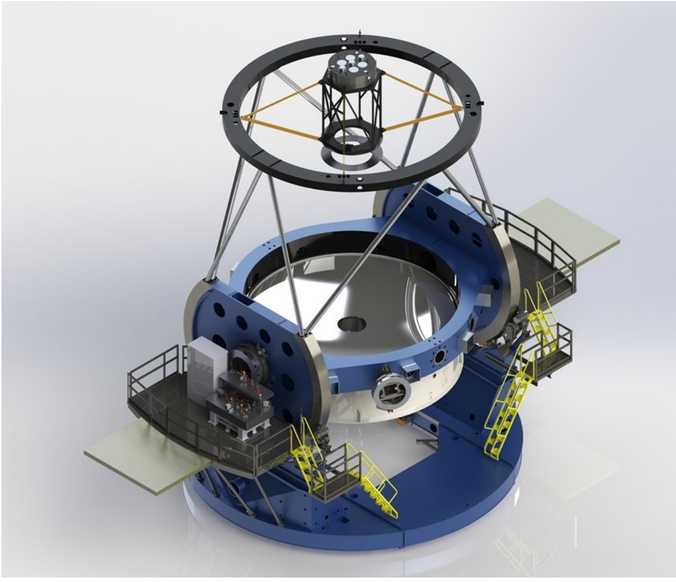

(a) Magellan Clay Telescope

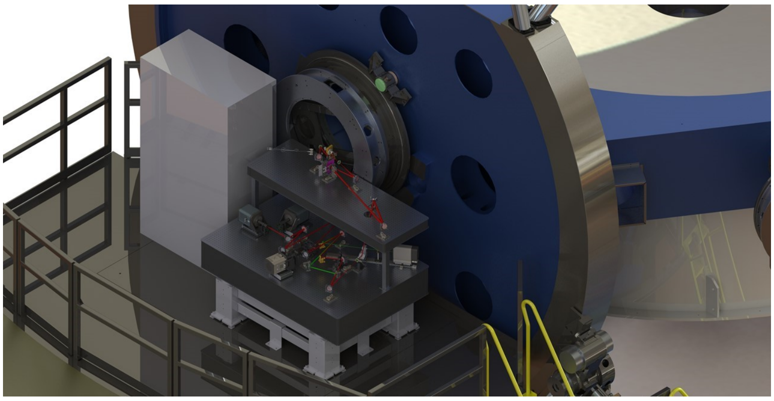

(b) MagAO-X on the Nasmyth platform

Figure 2.15: Rendering of the Magellan Clay Telescope with MagAO-X located on the Nasmyth platform

The instrument is a new extreme adaptive optics (ExAO) system designed for operation in the visible to near-IR which will deliver high contrast-imaging capabilities. Operating in the visible to near-IR, MagAO-X will deliver high Strehl ratios ($\geq$ 70% at Hα), high angular resolution performance (14 - 30 mas) and high-contrast imaging ($\leq 10^{-4}$) between $\sim$1 and 10 λ/D (Males, J. R. and MagAO-X team, 2017). These capabilities will allow for the study of early stages of planet formation, high spectral-resolution images of stellar surfaces, and the potential for taking the first high-contrast direct images of an exoplanet in reflected light.

In the first two phases in MagAO-X's design, the system coronagraph will be a vAPP. Taking into account both the designed contrast the vAPP can ideally deliver and the effects of small-scale aberrations due to Fresnel propagation through all optical surfaces within the instrument, the contrast across the 2 - 15 λ/D dark hole for MagAO-X will be approximately 6 x 10^{-5} before wavefront control (Lumbres et al., 2018) to correct for non-common path (NCP) errors. With wavefront control, the dark hole design contrast of 4 x 10^{-6} can the be reached. The main AO system will be driven by a pyramid wavefront sensor (PyWFS), but to mitigate the impact of quasi-static and non-common path (NCP) aberrations, focal plane wavefront sensing (FPWFS) in the form of low-order wavefront sensing (LOWFS) and spatial linear dark field control (LDFC) will also be employed. These techniques will allow for continuous high-contrast imaging performance at the vAPP's design contrast. LOWFS and LDFC testing on the testbed in the Extreme Wavefront Control Lab with a vAPP coronagraph helped to inform the design of the final MagAO-X vAPP coronagraph and have been instrumental in understanding their expected performance on MagAO-X. The details of these alogorithms as well as the final design choice the MagAO-X vAPP are discussed in Chapters 3 and 5.

CHAPTER 3

Modal Wavefront Sensing and Control

As discussed in the previous chapter, Section 2.1.1.3, the vAPP coronagraph currently in use on the testbed in the UA Wavefront Control Lab is actually a testplate with 7 individual vAPP masks, six of which produce different dark holes and different modal wavefront sensor (MWFS) spots (see fig 3.2). The purpose of these masks in the lab was twofold: (1) to create a dark hole in the lab with which to test dark hole stabilization techniques like linear dark field control (see Chapter 5) and (2) to experiment with the different MWFS spot designs to help inform the final design of the MagAO-X vAPP and validate simulation results. This chapter addresses the simulated and experimental testing of the MWFS spots on the six different vAPP MWFS designs on the vAPP testplate in the UA Wavefront Control Lab.

3.1 Overview of vAPP MWFS operation

The vAPP masks at the UA Wavefront Control Lab are holographic pupil plane elements that serve two functions: they create two 180° dark holes in the science image where light from exoplanets can be detected, and they create two sets of MWFS PSFs spatially separated from the science PSFs in the image plane (Wilby et al., 2017). Each n^{th} PSF in the MWFS is created with a holographic phase pattern $H_n(\xi, \eta)$ that creates a bias with a single mode M_n of amplitude b_n and encodes a specified tilt which places each n^{th} PSF at spatial frequencies $k_{x_n}, k_{y_n} = \frac{x_n}{\lambda F}, \frac{y_n}{\lambda F}$ in the image plane where F is the focal length of the focusing element following the vAPP. The holographic phase pattern for the n^{th} MWFS PSF is therefore defined as

$$H_n(x, y) = |e^{ib_n M_n(\xi,\eta)} \; + \; e^{2\pi i((k_{x_n}\xi + k_{y_n}\eta)}|^2 \tag{3.1}$$

which simplifies to

$$H_n(x, y) = 2 + 2\Re[(e^{2\pi i(k_{x_n}\xi + k_{y_n}\eta)})^* e^{ib_n M_n(\xi,\eta)}] \tag{3.2}$$

where * denotes the complex conjugate operator. From the two conjugate terms comes two separate MWFS PSFs with opposite modal amplitude biases $\pm b_n$. This holographic pattern $H_n(\xi, \eta)$ is encoded on a transmissive pupil plane optic; to create an image at the detector, the hologram is followed by a focusing lens (see fig 3.1).

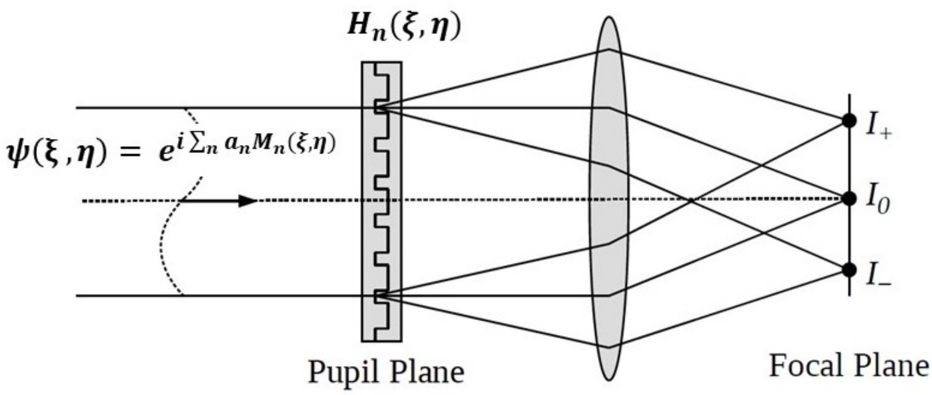

Figure 3.1: Diagram of vAPP operation adapted from Wilby et. al showing the performance of a single-mode hologram $H_n(\xi, \eta)$ in response to an aberrated wavefront $\psi(\xi, \eta)$, and the two oppositiely biased modal PSFs $I_\pm$ it creates in the image plane.

Referring back again to Chapter 1, given the far-field approximation, the resulting image at the detector is then simply the magnitude squared of the Fourier transform of the product of the hologram and the incident wavefront $\psi(\xi, \eta)$

$$I = |\mathcal{F}(H_n(\xi, \eta)\psi(\xi, \eta))|^2. \tag{3.3}$$

The full intensity distribution for a pair of oppositely biased MWFS PSFs $I_{n\pm}$ is

$$I_{n\pm}(x, y) = \delta(x \pm x_n, y \pm y_n) * |\mathcal{F}[\psi(\xi, \eta)]|^2 * |\mathcal{F}[e^{i(a_n \pm b_n)M_n(\xi,\eta)} e^{i \sum_{j \neq n} a_j M_j(\xi,\eta)}]|^2 \tag{3.4}$$

where a_j is the amplitude of the incident wavefront and $*$ is the convolution operator. The δ term gives the the $(\pm x, \pm y)$ location in the image plane of the PSF pairs, the second term is the telescope PSF. Within the the third term, the first exponential represents the wavefront bias, and the second exponential is the inter-modal crosstalk.

To create multiple MWFS PSFs encoded with different modes M_n as seen with the vAPP masks in the lab, multiple holograms are multiplexed onto a single element. This can be done with any low-order modal basis set to create a MWFS that is sensitive to the desired encoded modes. The change in amplitude of these modes can then be monitored to determine the amplitude of a single mode in a given incident aberration; with the MWFS, low-order wavefront sensing (LOWFS) can be done in the image plane.

3.2 Simulating LOWFS with a MWFS

LOWFS is a well-established technique by which jitter, tip, tilt, and other common low-order aberrations such as coma, astigmatism and defocus are sensed using starlight that has been rejected by the coronagraph(Singh et al., 2015; Guyon et al., 2009; Huby et al., 2017; SHI, 2016; Vogt et al., 2011). Traditionally, the signal used to run LOWFS in closed loop has been stellar light rejected at either an intermediate focal plane or at the Lyot stop in a conjugate pupil plane in a Lyot coronagraph (known more commonly as LLOWFS(Singh et al., 2015)) which is then brought to focus at the wavefront sensor camera. One advantage of LOWFS is that is that it does not require light to be diverted from the PSF diffraction core, and therefore there is no loss in the Strehl ratio. With the vAPP coronagraph, the signal used for closed-loop LOWFS is the MWFS PSFs created in the science image plane.

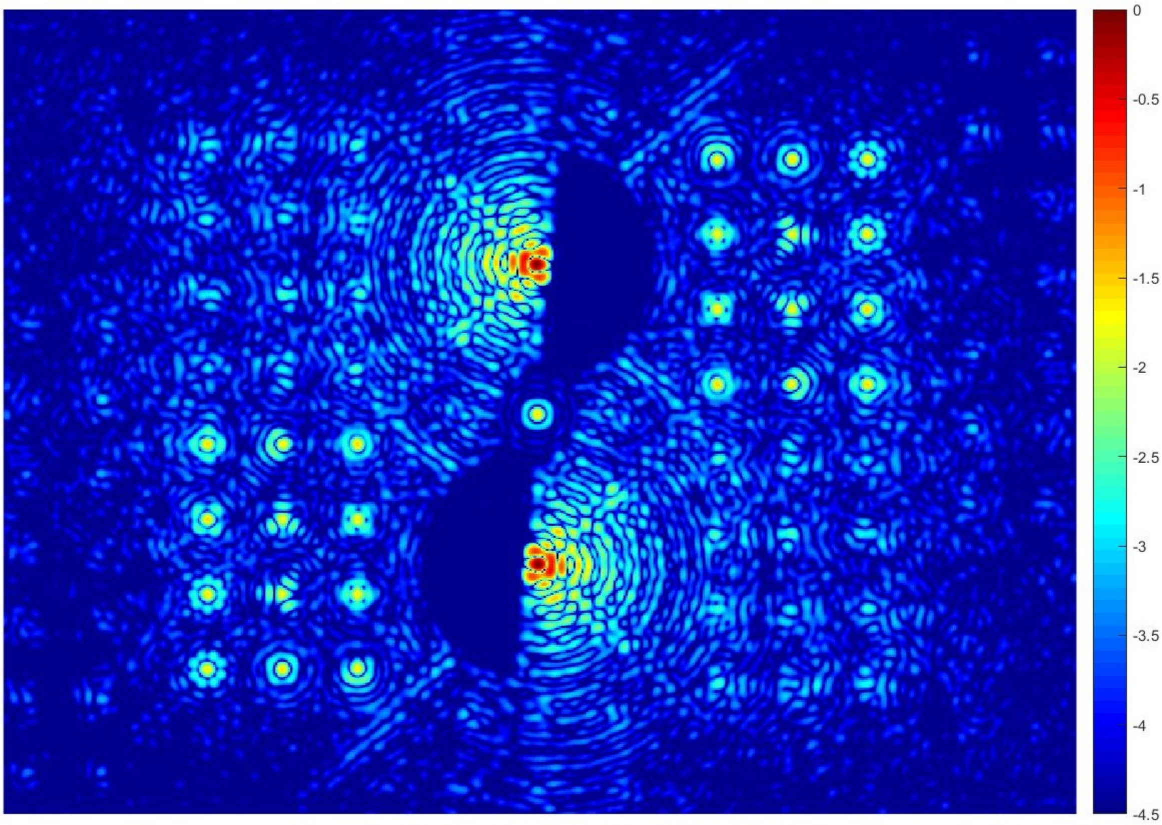

Figure 3.2: Example of the science image delivered by a vAPP coronagraph. Shown here are two science PSFs each with a 2 - 15 λ/D dark hole with an average contrast of $\sim 10^{-5}$. Further out from the dark holes are twelve MWFS PSFs each encoded with a single low-order Zernike mode.

The MWFS PSFs generated by the vAPP are created by encoding the pupil plane vAPP phase mask with the desired modal basis set (Wilby et al., 2017; Doelman et al., 2018). Each MWFS PSF corresponds to one mode. Therefore, for example, the twelve Zernike MWFS set seen in fig 3.2 is encoded with the first twelve Zernikes seen below in fig 3.3.

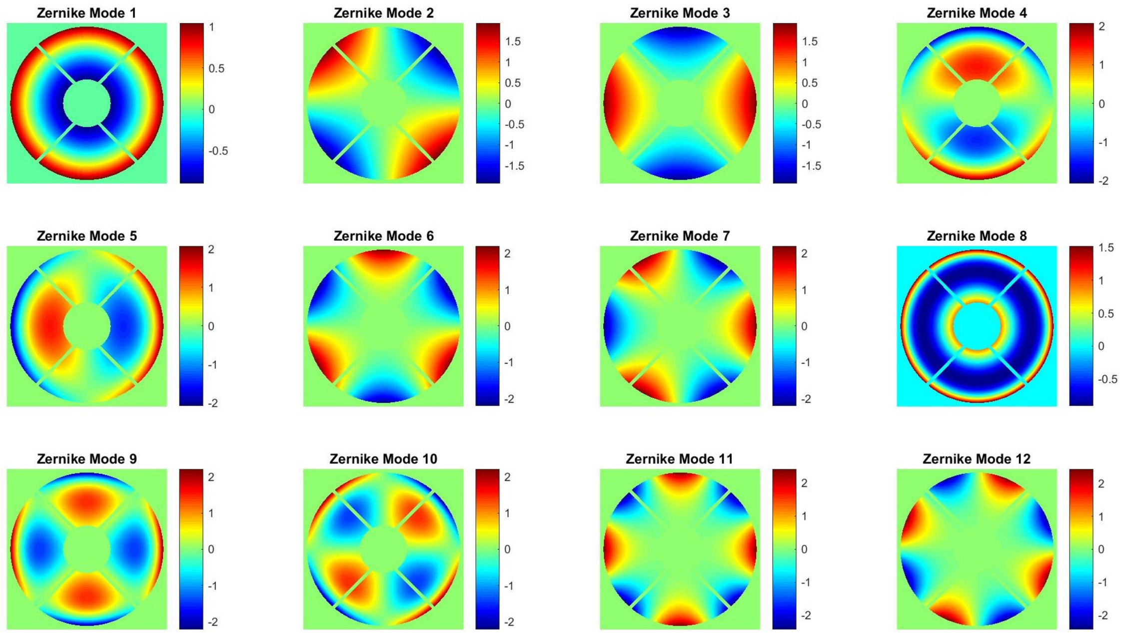

Figure 3.3: The twelve Zernike modal basis set masked by the Magellan pupil and encoded on the vAPP mask to create the twelve Zernike MWFS PSFs seen in 3.2.

To build the response matrix for LOWFS with the vAPP MWFS, tip and tilt and each mode in the MWFS basis set is applied using the DM, and the response of the MWFS spots is recorded. The recorded response for each nth mode is the normalized difference in intensity between the positively biased upper MWFS mode (I_{n+}) and the negatively biased lower MWFS mode (I_{n-}) as dictated by eq. Equation 3.6 (Wilby et al., 2017).

$$I_n = \frac{I_{n+} - I_{n-}}{I_{n+} + I_{n-}} \tag{3.5}$$

An example of the first three Zernike modes and the MWFS signal intensity change resulting from their application on the DM in simulation can be seen in Figure 3.4.

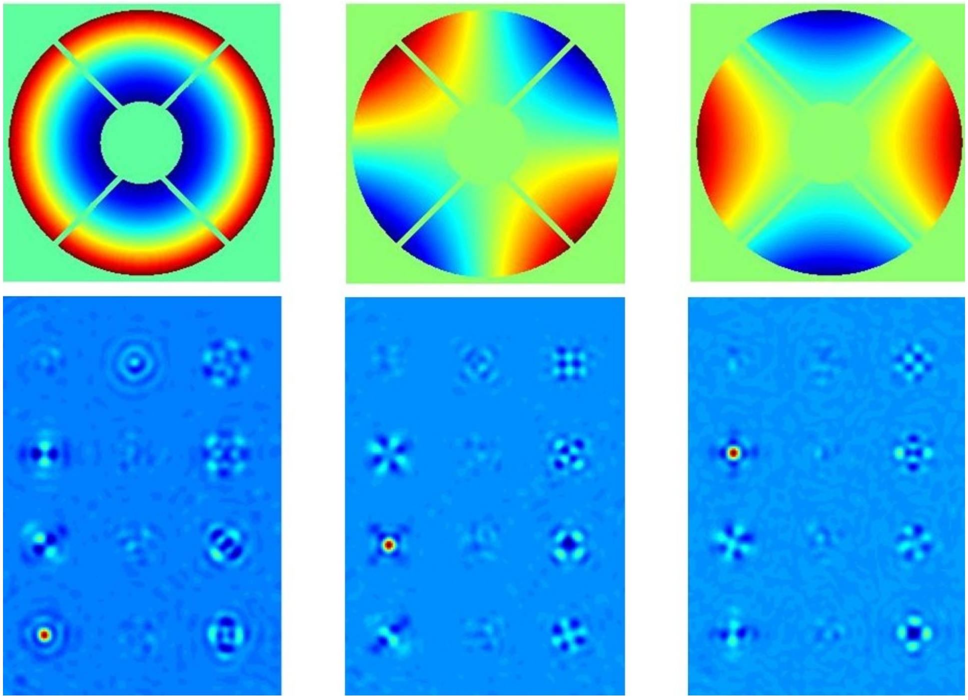

Figure 3.4: The simulated MWFS response to the first three Zernikes used by LOWFS, derived by subtracting the negatively biased lower MWFS PSF set of PSFs from the positively biased upper MWFS set.

This method of LOWFS using the six different vAPP MWFSs delivered by Leiden University has been tested both in simulation and on the testbed at the UA Extreme Wavefront Control Lab testbed to determine the most efficient MWFS design for the MagAO-X instrument. The results of these tests led to the choice of a version of the Zernike MWFS for the final design. For this reason, the following work focuses solely on the results of the Zernike MWFS vAPP coronagraph.

The first step in testing the Zernike MWFS was to characterize the MWFS behavior. The six phase masks on the testplate were experimented with both in simulation and on the bench to determine (1) the regime over which the response of the MWFS PSFs to an applied aberration was linear and (2) the amount of crosstalk between modes. In both simulation and on the testbed, an aberration was injected into the system using the DM, and the calculated correction was applied using the same DM. To compare simulated results to testbed results, a model of the testbed was used in simulation which included a scaled model of the BMC Kilo-DM to match the number of actuators across the DM and the elongated shape of the illuminated beam footprint on the testbed DM due to its angled position relative to the incoming beam.

This was done first in simulation using a model of the vAPP coronagraph and a model of the BMC Kilo-DM in use in the UA Extreme Wavefront Control Lab. Using the DM, tip, tilt, and each of the twelve Zernike polynomials encoded in the MWFS was applied with an amplitude of 100 nm and the normalized response of the MWFS was recorded as previously described. This response matrix G was then inverted and used as the control matrix for the following linearity tests.

To determine the linear response of the MWFS, each aberration was injected into the system with 20 amplitudes ranging from -200 nm to +200 nm with a step size of 22 nm. The amplitude of all aberrations in the basis set a was measured for each n^{th} MWFS mode by fitting the intensity difference image I to the inverted response matrix G^{-1} such that

$$a = G^{-1}I \tag{3.6}$$

The resulting linearity response curves for each aberration are shown in the plots in Figure 3.5.

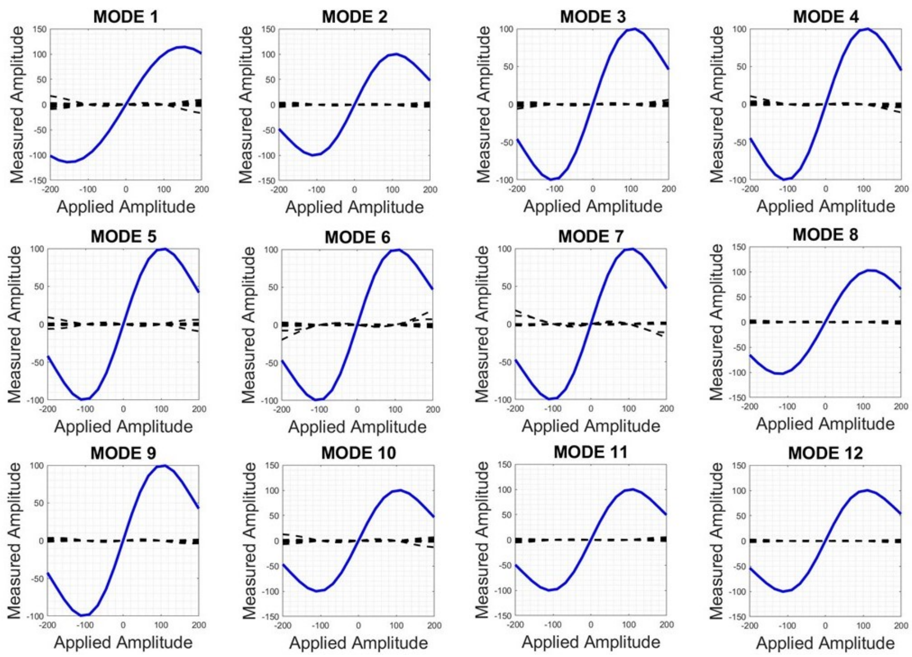

Figure 3.5: Simulated response curves showing the linear response of the MWFS to 12 Zernikes between +/- 100 nm amplitude aberrations. The blue line represents the response of the mode applied, and the dashed black lines represent the response (or crosstalk) of the 11 other modes to the applied mode.

As can been seen in the above figure, each mode has a linear, or at least monotonic, response between +/- 100 nm (plotted in blue). The response of the other modes to the single applied mode or "crosstalk" between the modes is represented by the dashed black lines. It can be clearly seen that, within the linear response regime of each mode, the crosstalk between the other modes is either zero or small enough to be negligible. It is the combination of this monotonic range and negligible crosstalk between modes that has driven this MWFS's selection for the MagAO-X instrument.

To ensure its performance in closed-loop, the Zernike MWFS was tested in simulation. One example presented here in Figure 3.6 shows the injection of a pupil plane aberration with an initial RMS of 113 nm. Using the DM as the corrective element, the simulation converged to a residual wavefront error RMS of 27 nm after 4 iterations. The same tests were implemented in the lab as well, and the results are presented in the following section.

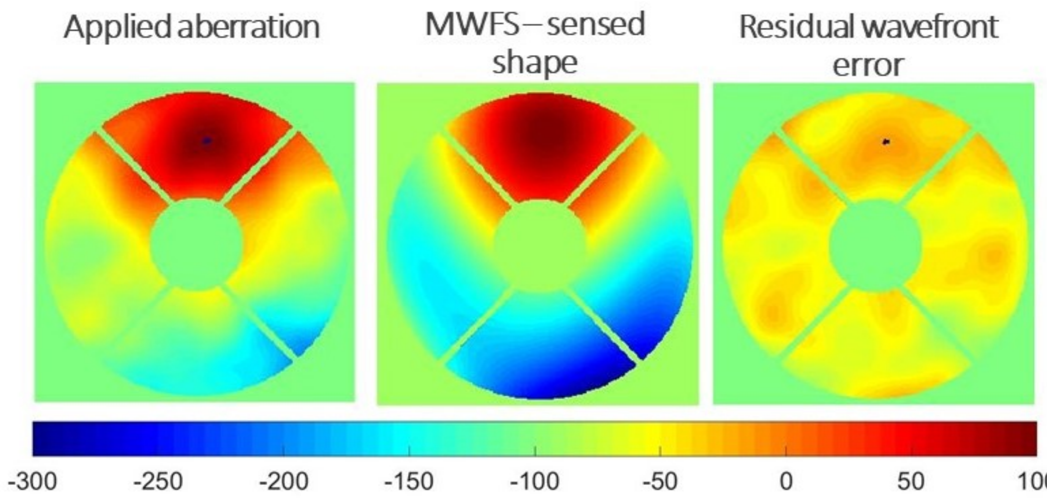

(a) Phase aberration with 113 nm RMS WFE reduced to 27 nm RMS by MWFS-derived DM correction

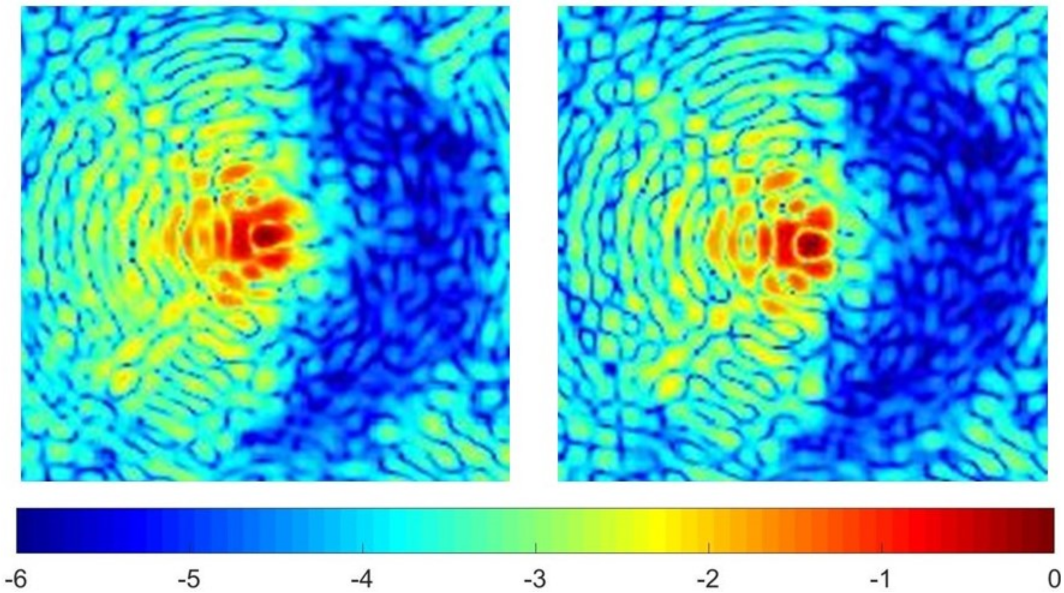

(b) (*Left*) Aberrated PSF and (*Right*) the MWFS corrected

Figure 3.6: LOWFS simulation using 12 Zernike MWFS spots to sense an injected pupil plane aberration and corrected using a model DM. The simulation converged to a residual RMS of 27 nm from an initial 113 nm in 4 iterations.

3.3 Laboratory demonstration of LOWFS with a MWFS

For a direct comparison with the linearity tests performed in simulation, the same test was performed with the twelve Zernike MWFS in the lab.

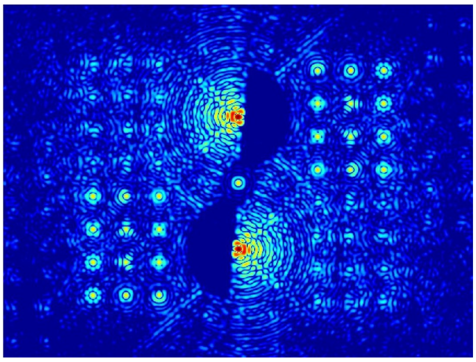

(a) Simulated vAPP image

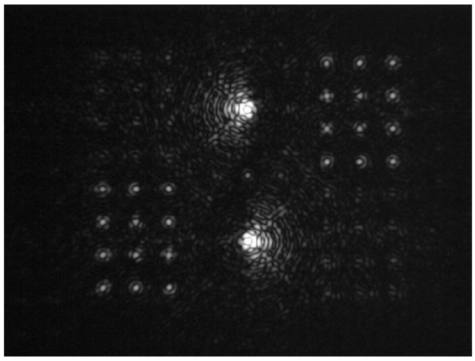

(b) Laboratory vAPP image

Figure 3.7: Comparison of the expected simulated vAPP (log scale) with the 12 Zernike MWFS and the image taken with the same mask in the laboratory (overexposed).

This was done by building a response matrix using the same wavefront sensor area cropping as in simulation and an aberration amplitude of 100 nm. The same aberration amplitudes used in simulation were then applied, and the linear response of each mode and the subsequent crosstalk between modes were recorded in the plots shown in Figure 3.8.

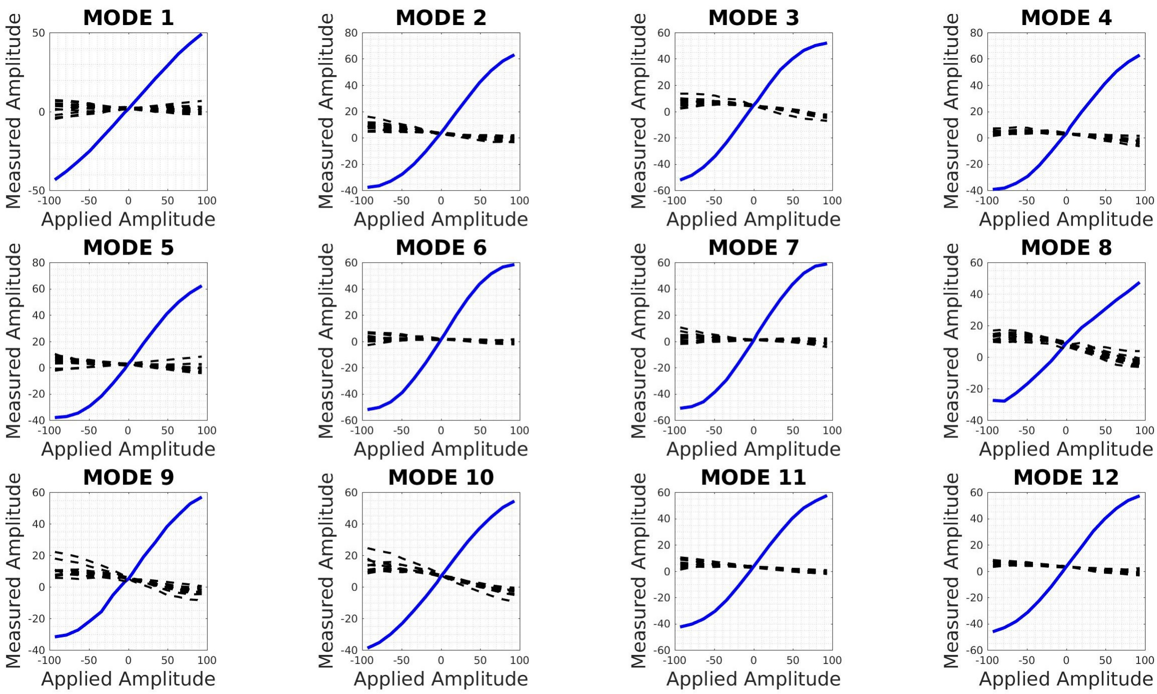

Figure 3.8: Laboratory response curves showing the linear response of the MWFS to 12 Zernikes between +/- 100 nm amplitude aberrations. The blue line represents the response of the mode applied, and the dashed black lines represent the response (crosstalk) of the 11 other modes to the applied mode.

Once again, the response of each mode to itself is plotted in blue, and the crosstalk between the other modes is shown by the dashed black lines. It can be seen that the linear response regime determined in the lab for each mode is between +/-100 nm, thereby matching the results found in simulation. However, the crosstalk between modes as seen in the lab demonstration has increased from the simulation results. It is suspected that this is due both to noise and to slight misalignment in the optical path which induces astigmatism and/or coma upon reflection off the off-axis parabolic mirrors (OAPs). The aberrations resulting from misalignment are sensed by the MWFS and are shown in Figure 3.9, where the MWFS response reveals the presence of defocus and oblique astigmatism.

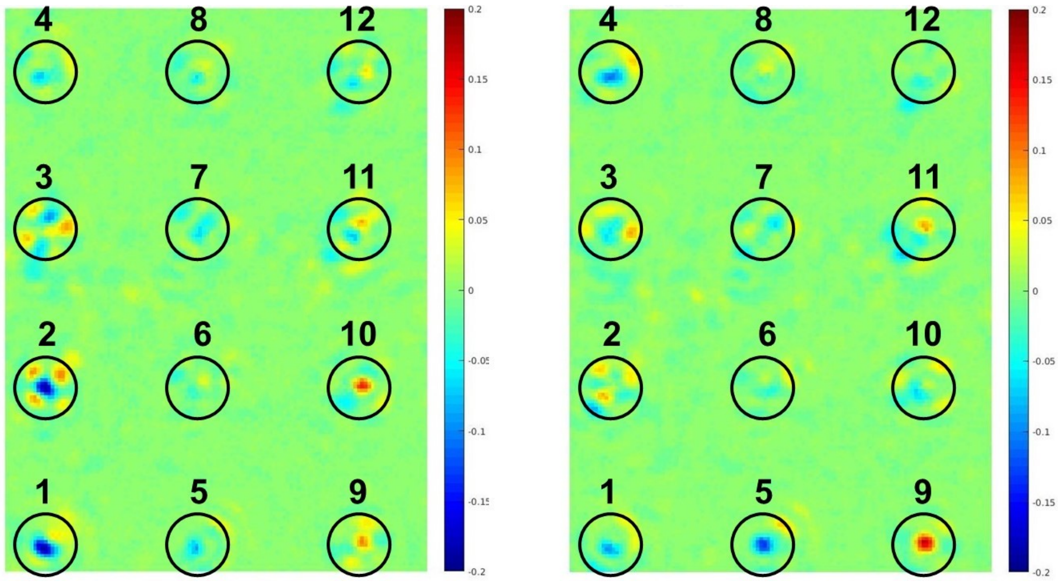

(a) Response to testbed misalignment

(b) Post-alignment correction

Figure 3.9: (*a*) Defocus (1) and astigmatism (2) present on the UA Extreme Wavefront Control Lab testbed due to slight misalignment as seen by the vAPP 12 Zernike MWFS. The two -0.2 amplitude peaks seen in blue corresponds to approximately -0.14 waves of defocus and oblique astigmatism. (*b*) After correction by the DM, the 12 Zernike MWFS shows the removal of the defocus and oblique astigmatism from the optical path but a slight increase in both vertical and horizontal coma (4 and 5). Some vertical secondary astigmatism (9) is also introduced which may be a result of the motion of the beam on the OAP.

Using the 12 Zernike MWFS on the testbed as seen in Figure 3.9, the presence of approximately -0.14 waves of defocus and oblique astigmatism was detected in the optical path due to misalignment. By applying +0.14 waves of both aberrations on the DM, the system alignment was corrected. However, in doing so, some vertical and horizontal coma were also induced. This effect is most likely due to the shifted position of the beam on the final OAP that occurs when applying astigmatism and defocus to the DM. This misalignment on the OAP is the most likely source of the coma seen in the corrected image in Figure 3.9. This interplay between astigmatism and coma is also suspected to be responsible for the greater crosstalk between modes seen in the lab results as compared to the expected modal crosstalk seen in simulation. In spite of the induced coma, the astigmatism and defocus alignment correction increased the Strehl of the science PSFs which can be seen in Figure 3.10 as an increase PSF core definition in both the upper and lower PSFs.

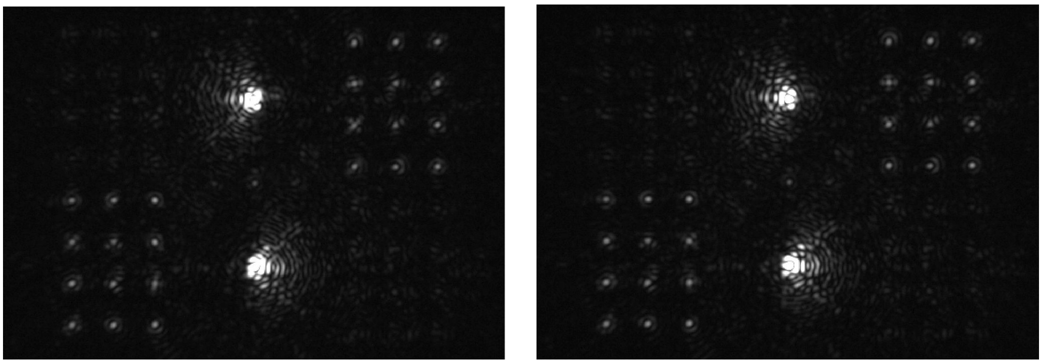

(a) Uncorrected PSFs with astigmatism and defocus present

(b) Corrected PSFs with astigmatism and defocus removed

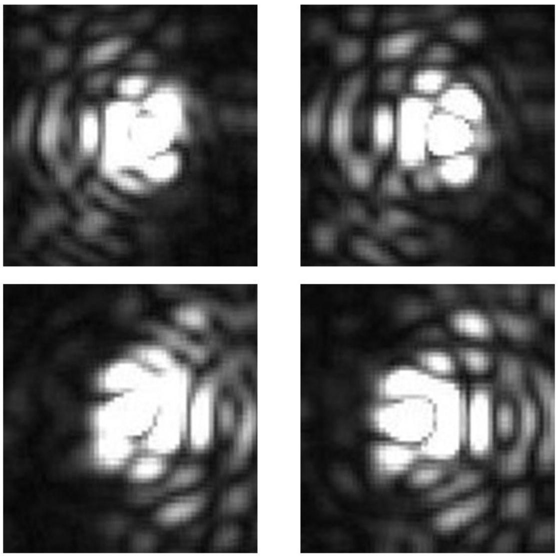

(c) Uncorrected PSFs magnified

(d) Corrected PSFs magnified

Figure 3.10: Lab results showing the DM removal of the oblique astigmatism and defocus sensed by the MWFS.

Following alignment correction, the MWFS was tested in closed-loop in the lab as it was in simulation. The DM was used to inject an aberration into the beam path, and the derived correction was applied using the same DM. Despite the increased crosstalk, the LOWFS loop converged, and in the case demonstrated in fig Figure 3.11, the initial aberration with an RMS of 155 nm was reduced to a residual error with an RMS of 36 nm after 5 iterations.

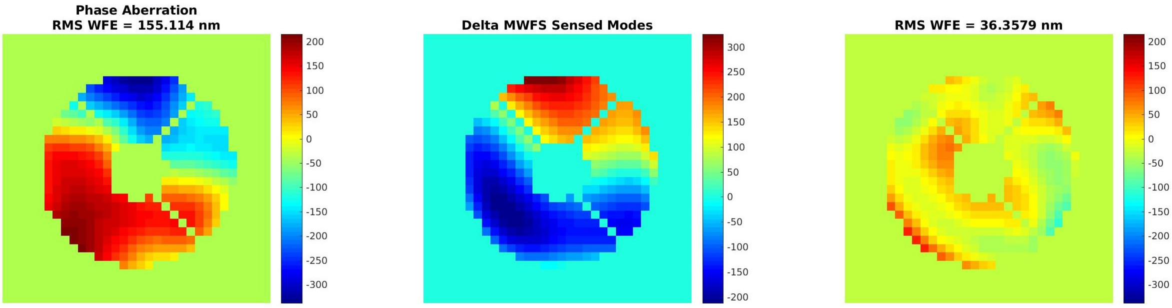

(a) (*Left*) The actuator displacement map of the low-order aberration applied to the DM with an RMS of 155 nm. (*Center*) The LOWFS-derived correction after 5 iterations applied to the DM. (*Right*) The residual wavefront error after correction by the DM with a final RMS of 36 nm.

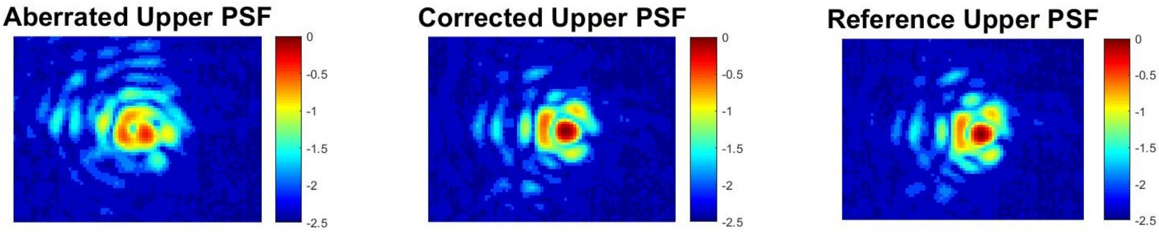

(b) Log_{10} upper vAPP science PSF

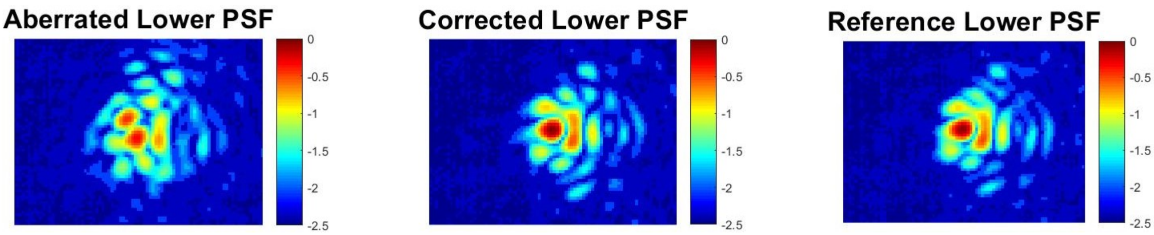

(c) Log_{10} lower vAPP science PSF

Figure 3.11: LOWFS lab results using the 12 Zernike MWFS to sense a 155 nm RMS aberration aberration. The final residual wavefront error after correction was reduced to 36 nm RMS. The science PSFs are shown in their aberrated state (*Left*) and after correction (*Center*) with the unaberrated science PSFs shown for reference (*Right*).

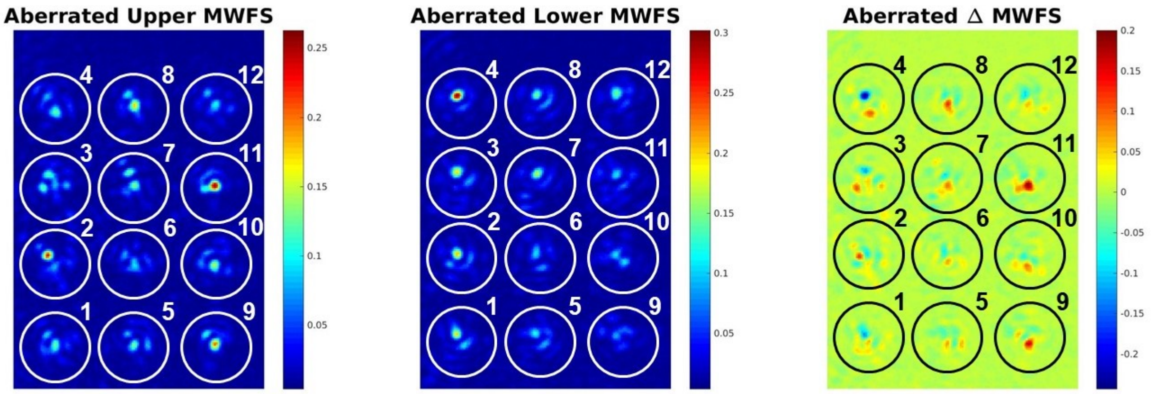

Figure 3.12: The 12 Zernike MWFS response to the 155 nm aberration shown in Figure 3.11. Upper MWFS PSFs (*left*), lower MWFS PSFs (*center*) and the difference of the two sets co-aligned (*right*) to produce the signal used for closed-loop LOWFS.

3.4 MagAO-X vAPP design

The seven mask designs seen in Chapter 2, fig 2.12 were chosen for lab testing to aid in the selection of the final design of the MagAO-X vAPP coronagraph. After testing both in simulation and in the lab, the MagAO-X mask was designed to contain 9 modal wavefront sensor spots encoded with 8 low-order Zernikes that are very commonly induced in optical systems due to misalignment and mounting errors: vertical and oblique astigmatism, vertical and horizontal coma, defocus, vertical and oblique trefoil, and spherical aberration. The ninth MWFS spot was a second defocus term with greater applied amplitude to create a greater defocused PSF with which phase diversity measurements can be made.

The 12 Zernike MWFS discussed earlier was used in the lab for all wavefront control testing in the following chapters, and was therefore tested both in simulation and in the lab. Since the defocused phase diversity MWFS vAPP was also chosen for the final MagAO-X design, tests of its performance in simulation are now included here. An image of this MWFS is shown in fig 3.13.

Linearity plots created for the same 12 Zernike modes are shown in fig 3.14 for the defocused phase diversity spots. Like the Zernike MWFS, the defocused phase diversity spots demonstrated large linear response ranges with minimal crosstalk. Exceptions to the minimal crosstalk can be seen for both astigmatisms and defocus (Zernike modes 2, 3, and 8).

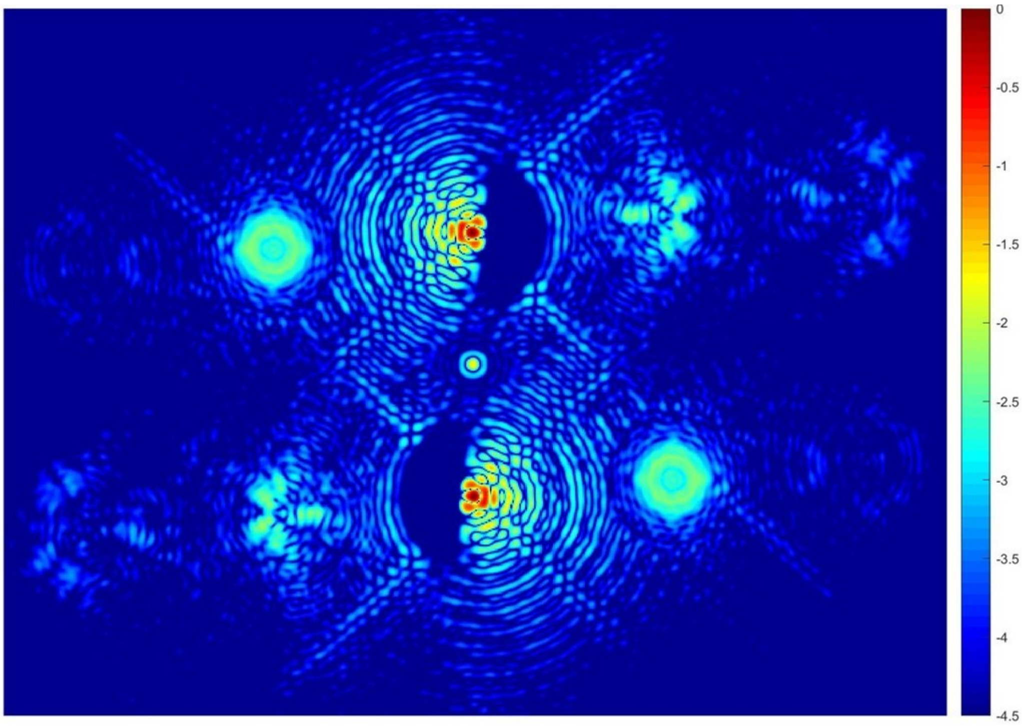

Figure 3.13: The defocused phase diversity MWFS vAPP with dark holes spanning 2 - 11 λ/D. The MWFS spots can be seen in the top left and bottom right. The patterns seen opposite the defocus spots on the other side of the science PSFs are residual ghosts generated by the mask and are not used for LOWFS.

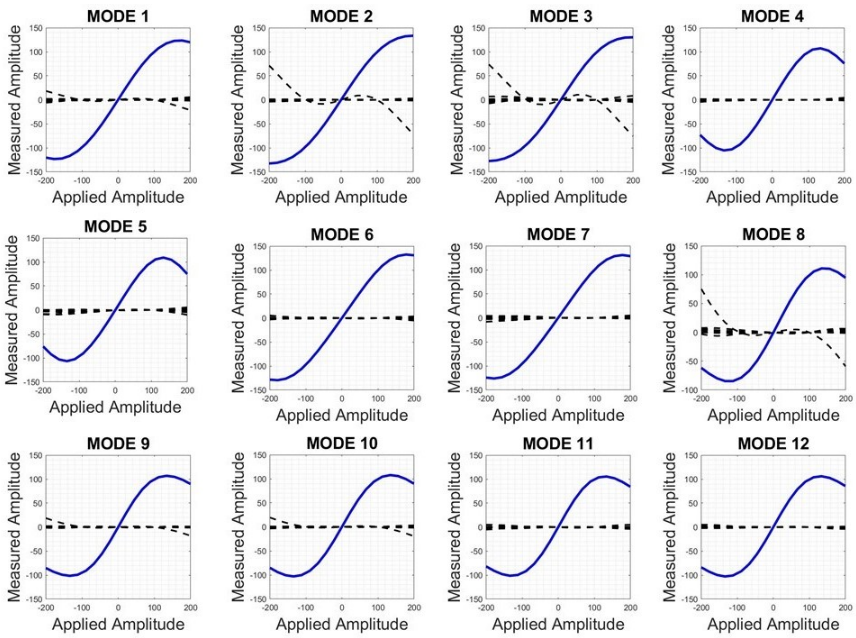

Figure 3.14: Simulated response curves showing the linear response of the defocused phase diversity MWFS to 12 Zernikes between +/- 100 nm amplitude aberrations. The blue line represents the response of the mode applied, and the dashed black lines represent the response (or crosstalk) of the 11 other modes to the applied mode.

As with the 12 Zernike MWFS, each mode has a linear, or at least monotonic, response between +/- 100 nm (plotted in blue). The response of the other modes to the single applied mode or "crosstalk" between the modes is represented by the dashed black lines. It can be clearly seen that, within the linear response regime of each mode, the crosstalk between the other modes is either zero or small enough to be negligible. It is the combination of this monotonic range and negligible crosstalk between modes that has driven this MWFS's selection for the MagAO-X instrument.

An example of its closed-loop performance is presented in figs 3.15 and 3.16 which shows the injection of a pupil plane aberration with an initial RMS of 174 nm. The simulation converged to a residual wavefront error RMS of 34 nm after 3 iterations.

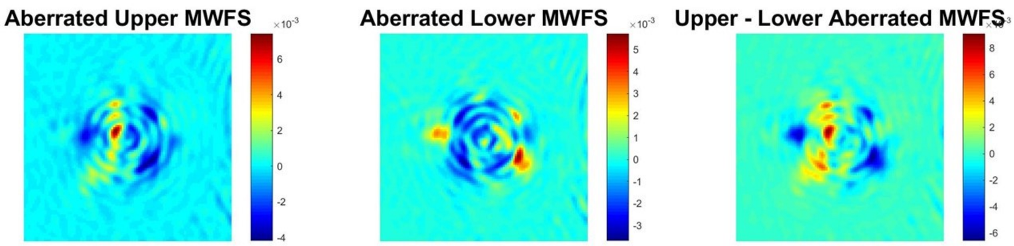

Figure 3.15: The response of the defocused phase diversity spots to the aberration shown in fig 3.16

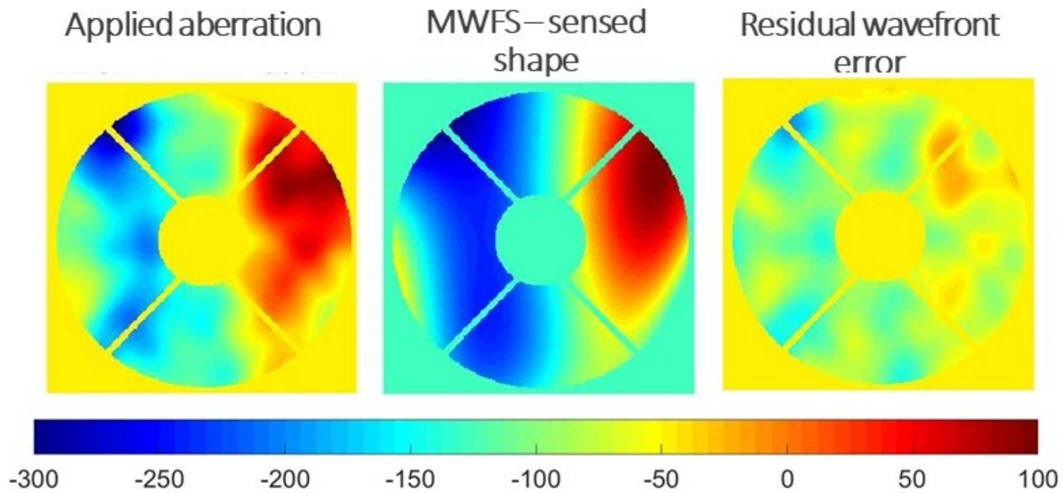

(a) Phase aberration with 113 nm RMS WFE reduced to 27 nm RMS by MWFS-derived DM correction

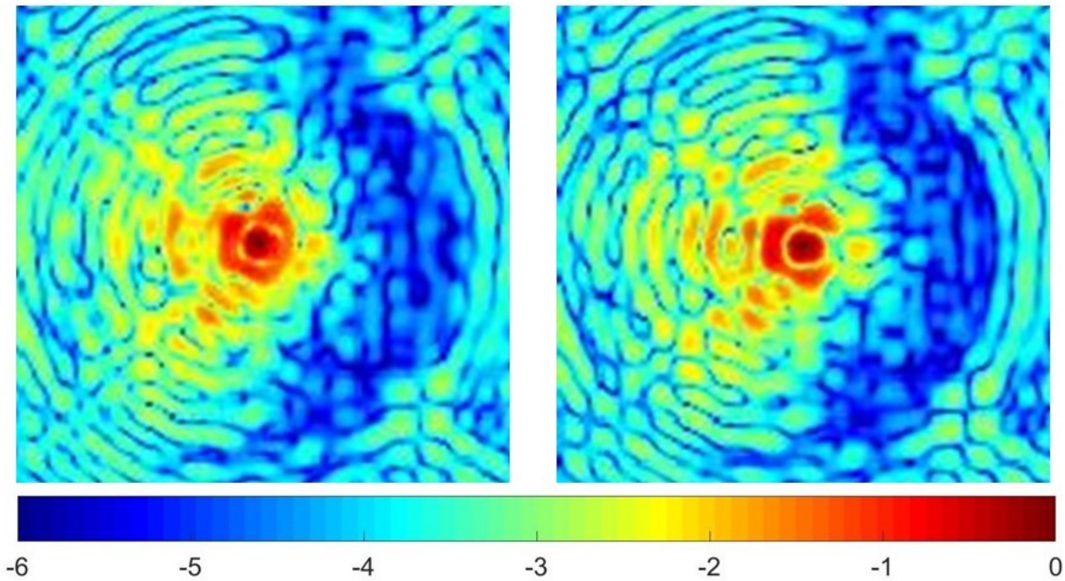

(b) (*Left*) Aberrated PSF and (*Right*) the MWFS corrected

Figure 3.16: LOWFS simulation using a defocused phase diversity spots to sense an injected pupil plane aberration and corrected using a model DM. The simulation converged to a residual RMS of 34 nm from an initial 174 nm in 4 iterations.

This set of defocused spots can be used as a FPWFS with any modal basis set, including mirror modes which will be discussed in Chapter 5, which is why this particular MWFS spot pair was also included in the final MagAO-X design.

After the official design was finalized with the team at Leiden University in the summer of 2018, the mask was manufactured by Imagine Optix, and delivered to the University of Arizona's Extreme Wavefront Control Lab in September 2018 (fig 3.17). Upon arrival, the MagAO-X vAPP was aligned on the testbed to verify its design and performance. Following installation in the beam path, the image shown in fig 3.18a was taken. Comparison with the expected simulated design in fig 3.18b shows that the vAPP performs as expected and will be ready for first light in March 2019.

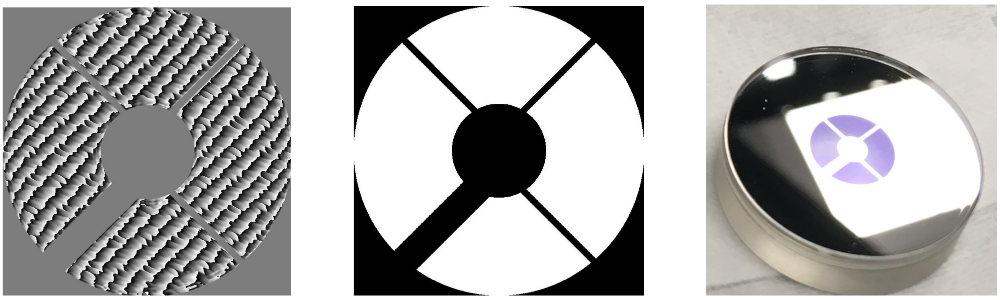

(a) MagAO-X vAPP phase pattern

(b) MagAO-X vAPP binary metal pupil

(c) MagAO-X vAPP coronagraph in the lab

Figure 3.17: Final design of the MagAO-X vAPP coronagraph mask in the lab

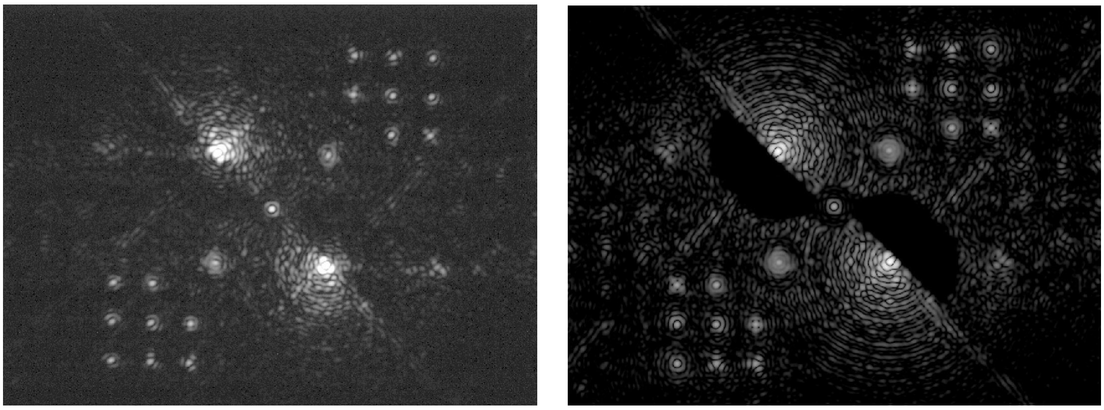

(a) The MagAO-X vAPP on the testbed

(b) The MagAO-X vAPP in simulation

Figure 3.18: Comparison of the MagAO-X vAPP in simulation vs the final mask aligned on the bench at the UA Extreme Wavefront Control Lab. It should be noted in image (a) that the dark hole contrast is lower than in image (b) and shows a distinct streak effect through the dark holes. This is the effect of real optics in the lab vs a perfect simulation environment. In the lab, the OAPs have a high frequency sinusoidal pattern across the optical surface that is a residual of the diamond-turning process by which the OAPs were formed. This sinusoidal residual creates the streak effect through the dark holes. Other residual surface errors from all the optical surfaces on the testbed also compound and decrease the contrast depth across the dark holes to approximately 10^{-3} .

CHAPTER 4

Linear Dark Field Control Theoretical Development

While LOWFS with a MWFS can control low-order aberrations and maintain high Strehl, it cannot, by definition, maintain the high contrast at mid-λ/D separations within the dark hole. The majority of the dark hole expanse is across mid-λ/D separations; within this region, the contrast is limited by mid-spatial frequency aberrations. To control these aberrations and to maintain the initial deep contrast delivered by the coronagraph, we present spatial linear dark field control (LDFC)(Miller et al., 2017).

4.1 Spatial linear dark field control

FPWFS techniques like speckle nulling and EFC that have proven capable of generating a DH with high contrast in the lab have also been under consideration for maintenance of the DH (Cady et al., 2013; Ruffio, 2014; Krist et al., 2016). As a control method, FPWFS presents its own set of challenges given that speckles have a quadratic relationship with aberrations. These techniques also rely on phase diversity measurements of the field at the science detector which require field modulation and multiple images (Give'on et al., 2007; Groff et al., 2015). This field modulation at the science detector, induced by a deformable mirror (DM), throws stellar light back into the DH and disrupts the science measurement. This interruption, which is required to rebuild the DH every time the contrast degrades, fundamentally limits the integration time that can be spent on any given target. The duration of this interruption to the science acquisition is directly related to the contrast of the DH. For deeper contrast, the required exposure time to sense the speckle field increases; therefore, at the 10^{-10} contrast level, multiple images with long exposure times (as high as 90 seconds (Matthews et al., 2017)) can lead to hours of time dedicated solely to maintaining the dark hole, thereby significantly reduces the amount of time that can be spent on observations. The need for modulation, multiple images, and long exposures, consequently makes the use of current speckle nulling methods and EFC non-ideal for continuous maintenance of the DH.

Another technique known as the self-coherent camera (SCC) has been under development as a method for obtaining and maintaining the DH without science acquisition competition (Delorme, J. R. et al., 2016). While SCC does not require modulation, it does still utilize the mixing of some starlight with the DH. Linear dark field control (LDFC) does not require any such mixing of starlight and the DH, and offers a potential solution for overcoming the limitations presented by speckle nulling and EFC. To avoid disrupting the science measurement with field modulation to rebuild the DH, LDFC locks the high contrast state of the field once the DH has been constructed using conventional methods like EFC. Using only one image of the bright field (BF), LDFC freezes the state of the field by sensing and canceling changes in the wavefront that result in speckle formation in the image plane. The ability to maintain the DH with a single image yields a substantial increase in time that can be spent in the observation and analysis of exoplanets and will lead to an overall increase in the number of planets detected and analyzed over the lifetime of an instrument.

4.1.1 Theory

LDFC maintains high contrast without needing to modulate the field and interrupt the science measurement to update the field estimate as is required when using EFC in closed loop. LDFC is a similar algorithm to LOWFS (see Chapter 1) in that it provides a relative wavefront error measurement rather than an absolute phase measurement like electric field conjugation or similar techniques (Groff et al., 2015). To sense the aberrations that degrade the dark hole, spatial LDFC measures the relative changes in intensity of the bright field within the same spatial frequency extent as the dark hole but on the opposite side of the stellar PSF as seen in fig 4.1. LDFC is a common path FPWFS technique with access to mid- and high-spatial frequencies. Instead of sensing only low-order aberrations using a post-coronagraph quadrant method or starlight rejected by the coronagraph like LOWFS, LDFC operates a closed-loop around starlight in the focal plane located outside of the DH.

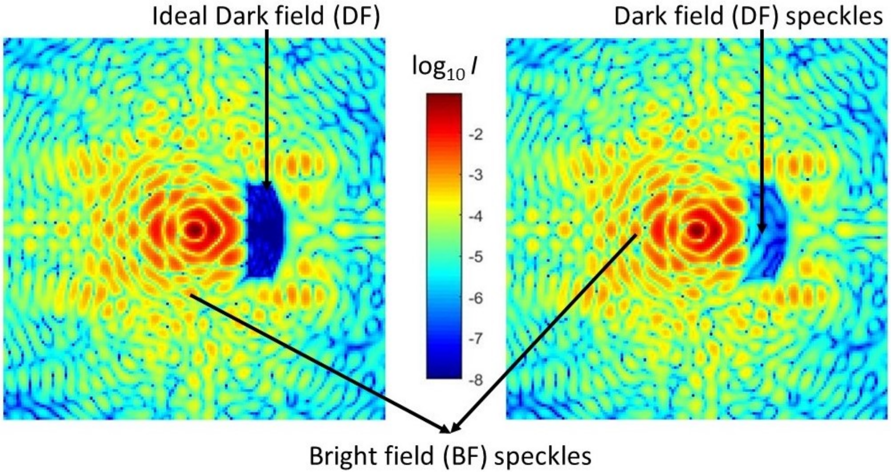

Figure 4.1: Spatial LDFC: 3.5 λ/D x 8.5 λ/D DH created in simulation using conventional EFC (left). Wavefront aberrations produce speckles in the BF and the DH which degrade the DH (right). The change in intensity between the aberrated BF (right) and the ideal BF (left) is used to measure and cancel the speckles in the DH.

Spatial LDFC freezes the state of the DH by using state measurements of light spatially outside of the DH (see fig 4.1). This method uses the linear signal from the strongly illuminated bright field (BF) to measure the change in the image plane intensity and uses that variation to calculate the correction required to return the image to its initial state, thereby stabilizing the DH. Unlike other FPWFS techniques, spatial LDFC does not rely on any induced modulation to derive an estimate of the field to be canceled. Instead, spatial LDFC observes changes in the image intensity with respect to a reference image taken after the DH has been established by conventional speckle nulling methods. This process requires only the reference image and a single image taken at a later time.

Without the need for modulation or multiple images, spatial LDFC does not interrupt the science measurement, it decreases the time necessary to return the DH to its initial high contrast state, and consequently it allows for longer, uninterrupted observing at high contrast. This chapter introduces spatial LDFC as a more efficient alternative to conventional speckle nulling methods for stabilizing the DH. The theory behind spatial LDFC is laid out here in Section 4.1.1, and demonstrations of LDFC's abilities in simulation are shown in Section 4.1.4. Further discussion of the limitations and null space of spatial LDFC is laid-out in Section 4.3.

Spatial LDFC relies on the linear response of the BF to wavefront perturbations that affect both the BF and the DH; this linearity allows for a closed-loop control algorithm directly relating wavefront perturbations to changes in BF intensity. To derive the source of this linear response, we begin with the relationship between an incident wavefront and the resulting image. The complex amplitude of the incident wavefront in a pupil plane E_0 is linearly related to the complex amplitude at the image plane E_t at a given time t. The same linear relationship is true with respect to E_{DM}, the multiplicative complex amplitude introduced by the DM in a conjugate pupil plane, and the complex amplitude at the image plane E_t.

When the changes in optical path length (OPL) induced by the DM are very small such that OPL $\ll 1$, the resulting field E_t at a given time t in the image plane can be written as the sum of the initial pupil plane field E_0 and the small changes in complex amplitude induced in a conjugate pupil plane by the DM (Give'on et al., 2007).

$$E_t \approx E_0 + E_{DM} \tag{4.1}$$

The resulting intensity in the image plane at time t is then given by:

$$I_t = |E_t|^2 \tag{4.2}$$

The total image plane intensity can be written as a sum of three terms: the intensity contribution from the initial pupil field: $|E_0|^2$, the resulting intensity due to phase perturbations induced by the DM: $|E_{DM}|^2$, and the inner product of the initial pupil field and the DM contribution to the complex amplitude:

$$I_t \approx |E_0|^2 + |E_{DM}|^2 + 2\langle E_0, E_{DM} \rangle \tag{4.3}$$

In the DH, the contribution of the initial field to the total intensity is very small, and the total intensity is dominated by the contribution of the DM such that $|E_{DM}|^2 \gg |E_0|^2$, thereby leading to a quadratic dependence of the DH on the DM input. However, in the BF the contribution of the initial field to the total intensity dominates the contribution of the DM:

$$|E_0|^2 \gg |E_{DM}|^2 \tag{4.4}$$

The intensity of the BF at the image plane at time t can therefore be written as a linear function of the complex amplitude contribution of the DM:

$$I_t \approx 2\langle E_0, E_{DM}\rangle + |E_0|^2 \tag{4.5}$$

In eq 4.5, the term $|E_0|^2$ is the reference image I_{ref} taken after the DH has been established. The signal used by spatial LDFC to drive the DH back to its initial state is simply the difference between this reference and a single image I_t taken at time t.

$$\Delta I_t = I_t - I_{ref} \approx 2\langle E_0, E_{DM}\rangle \tag{4.6}$$

This linear response of the BF, ΔI_t, to field perturbations controlled by the DM is shown in fig 4.2 alongside the quadratic response of the DH to the same DM perturbation . In this figure, the BF and DH response to the DM field contribution E_{DM}, is shown in a simulated PSF with a DH established by conventional EFC. A model of a MEMS DM was used to create the DH and then perturb the input wavefront by inducing a positive and negative delay in the optical path with a single actuator. This was done for a range of actuator amplitudes from -0.075 to +0.075 μm (Miller and Guyon, 2016). The resulting intensity response of pixels located in the DH (shown to the left in fig 4.2) is governed by eq 4.3 with the expected quadratic dependence on the field perturbation. The intensity response of the BF (shown to the right in fig 4.2) reveals the predicted linear dependence on the DM-induced field perturbation given by Eq 4.6 .

In closed loop, ΔI_t is small, and the linear approximation holds. However, even when initially closing the loop where ΔI_t is larger, strict linearity is not required, only a monotonic trend. In instances both of strict linearity or of monotonicity, the BF response allows for the construction of a linear servo driven solely by changes in the BF intensity. Unlike EFC and speckle nulling which use modulation to provide an absolute field measurement, LDFC relies on measurements of BF intensity variation in the science image. These intensity variations are used to track and cancel changes in the wavefront that modify both the BF and DH, thereby stabilizing the DH without any disruptions to the science measurement.

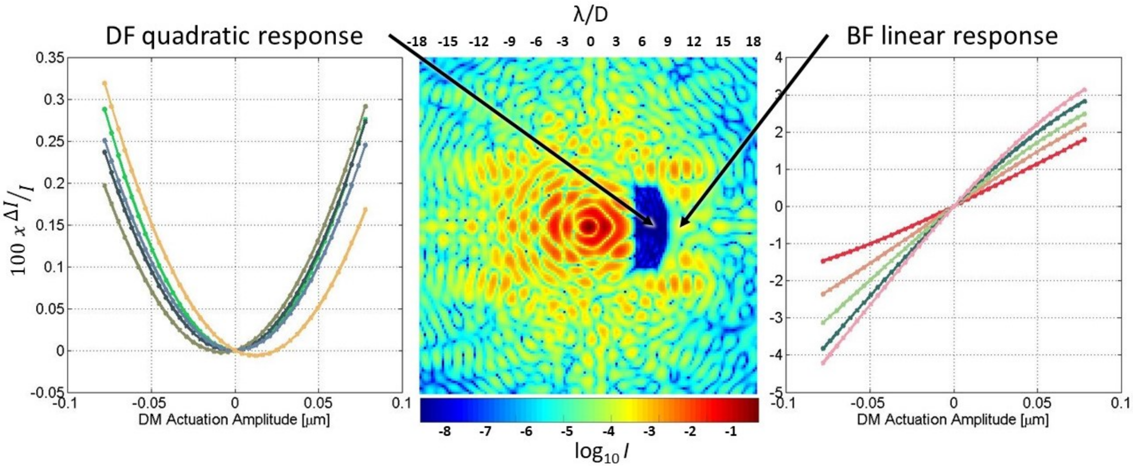

Figure 4.2: The response of the BF and DH to the same range of DM 'poke' amplitudes from -0.075μm to +0.075μm on a single DM actuator. A demonstration of the expected quadratic response of the DH (seen left) and the linear response of the BF (seen right) to the same range of DM poke amplitudes. Each curve in the DH plot is the response of a single pixel in the DH between 7 λ/D and 8 λ/D, and each curve in the BF plot is the response of a single pixel in the BF between 10.5 λ/D and 11.5 λ/D.

4.1.2 Calibration

Given the linear relationship between BF intensity and wavefront, using LDFC to stabilize the DH contrast is faster and more robust than using EFC. EFC requires multiple images to estimate the field, while each iteration of LDFC requires only one image at the science detector to determine how the field has changed with respect to the initial EFC-derived state. Since this image does not require field probing which breaks the science measurement, the LDFC servo operates with a 100% duty cycle. Furthermore, LDFC does not rely on complex field estimates which require a model-based complex phase response matrix that is difficult to measure and verify; instead, LDFC relies only on a DM $\rightarrow$ image calibration that links a set of DM shapes, or basis functions, to changes in intensity in the science image (Guyon et al., February 2015).

For this simulation, the DM influence functions were chosen as the basis functions. The calibration between the image and the basis set was obtained by building a response matrix $\mathcal{M}$ whose columns relate the application of each individual influence function to the responding intensity variation at the science detector. Though modal control (Poyneer and Véran, 2005) does offer performance benefits, especially when it maps with the expected temporal evolution of the wavefront error, such modal control tuning has not been explored at this time. For this work, application of the influence function basis set involved the actuation or 'poking' of one of the k actuators on the DM that lie within the illuminated system pupil. To begin building $\mathcal{M}$, the ideal reference image I_{ref} with dimensions $[n_{pix}$ x $n_{pix}]$ is recorded after the DH has been established using EFC. To fill each of the k columns in $\mathcal{M}$, a single actuator was poked, the resulting perturbed image I_k was measured, and the unperturbed reference image I_{ref} was subtracted off to yield the change in intensity. This was done for all k actuators. The resulting response matrix $\mathcal{M}$ has the dimensions $[n_{pix}^2$ x $k]$.

$$\mathcal{M}[:,k] = I_k - I_{ref} \tag{4.7}$$

The matrix $\mathcal{M}$ records the intensity change of both the BF and DH pixels with respect to each actuator poke. However, spatial LDFC uses only the BF pixels which respond linearly to wavefront perturbations. The selection of these BF pixels relies on multiple parameters including background flux, flux per speckle, detector efficiency, and SNR. Based on these requirements, a threshold was applied to the initial EFC image I_{ref} which selected only the n pixels with intensities greater than or equal to the threshold. The result was an image $I_{ref,n}$ that recorded the initial EFC-state of only the BF pixels. An example of this BF reference image and the corresponding pixel map can be seen in fig 4.3 for a contrast threshold of $10^{-4.5}$.

To build the BF response matrix M, the full response matrix was filtered to include only the n BF pixels with intensities above the threshold such that $M = \mathcal{M}_n$. This filtered response matrix M was used throughout the operation of spatial LDFC.

4.1.3 Closed-loop implementation

To implement LDFC in closed-loop, an image I_t was taken at time t and the same n BF pixels that pass the threshold were recorded in the BF image $I_{t,n}$. The BF reference image $I_{ref,n}$ was then subtracted from the new BF image to track the changes that occurred in the BF with respect to the initial EFC BF reference (see fig 4.4):

$$\Delta I_{t,n} = I_{t,n} - I_{ref,n} \tag{4.8}$$

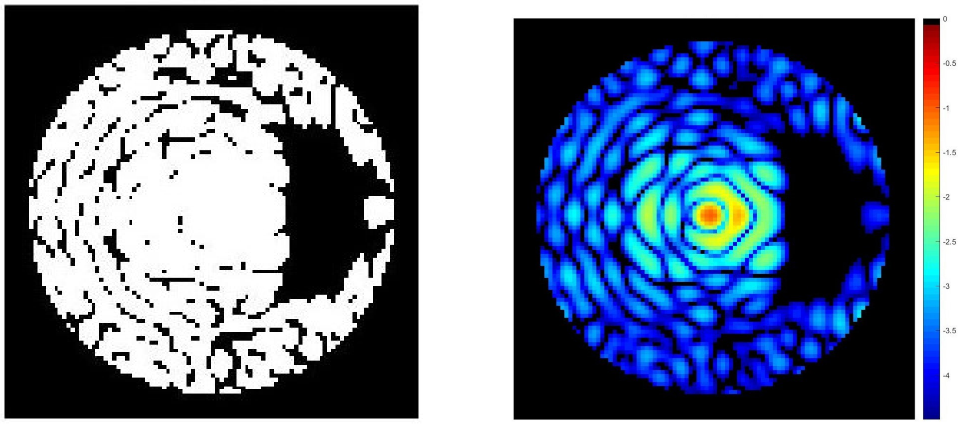

(a) BF pixel mask (b) $I_{ref,n}$

Figure 4.3: Images of the applied BF pixel mask (a) and the $\log_{10}$ masked reference image (b). The binary mask passes only the pixels at or above the contrast threshold (shown in white). In this image, and for the following demonstrations, the contrast threshold was $10^{-4.5}$, and the outer diameter of the masked control area was set to be the control radius of the active area on the DM.

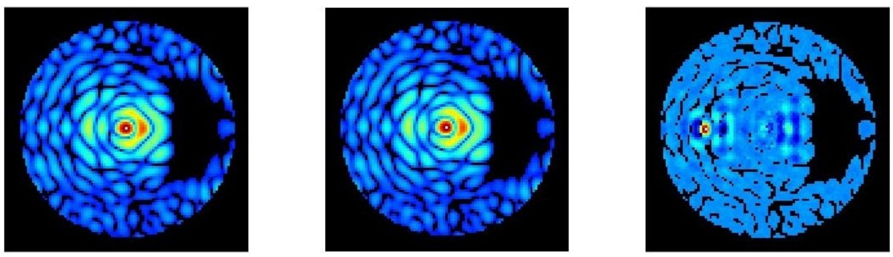

Figure 4.4: Shown here are the BF pixels that are used in the reference (left) and aberrated (center) images to measure the intensity change (right) $\Delta I_{t,n}$ that drives the spatial LDFC control loop to stabilize the DH. In all three images, the 3.5 λ/D x 8.5 λ/D DH can be seen to the right of the PSF core.

This BF intensity change $\Delta\ I_{t,n}$ was fit to the pseudo-inverse of the BF response matrix M, also known as the control matrix, to calculate the DM shape that returned the field to its initial EFC reference state. The DM shape is represented by a vector of individual actuator amplitudes u_t:

$$u_t = -(M^T M)^{-1} M^T\ \Delta I_{t,n} \tag{4.9}$$

This pseudo-inverse of M was implemented by using singular value decomposition (SVD) and applying a threshold to filter out the modes that were not properly sensed by LDFC. For this simulation, the threshold value was chosen based on simulation performance, resulting in the inclusion of 286 out of an initial 398 modes in the pseudo-inversion process. A plot of the singular values of M is shown below in fig 4.5.

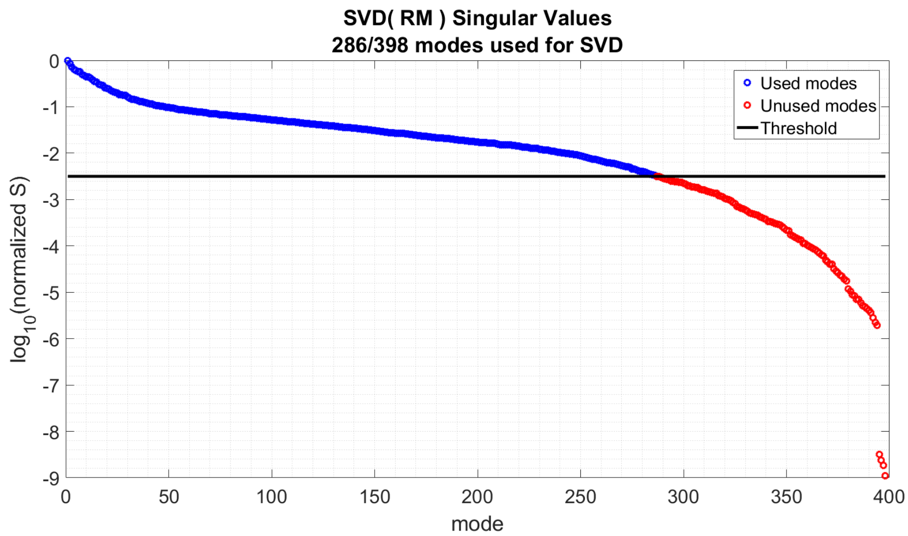

Figure 4.5: Singular values of the spatial LDFC response matrix M showing the applied SVD threshold (black) as well as the modes that were used in the inversion (blue) and the modes that were discarded (red). Out of 398 total modes, 286 were used for the inversion of M in the following simulations.

The response matrix M and subsequent control matrix were measured once and applied in closed loop with an initial gain of 0.6. Once the DH contrast converged to $10^{-7.9}$, the gain was lowered to 0.1 to maintain the correction. The ensuing process of taking an image, calculating the intensity change of the BF from its reference state, and updating the DM was iterated on to actively freeze the science image field in its initial EFC state.

4.1.4 Development in simulation

In simulation, LDFC operates as shown in fig 4.6

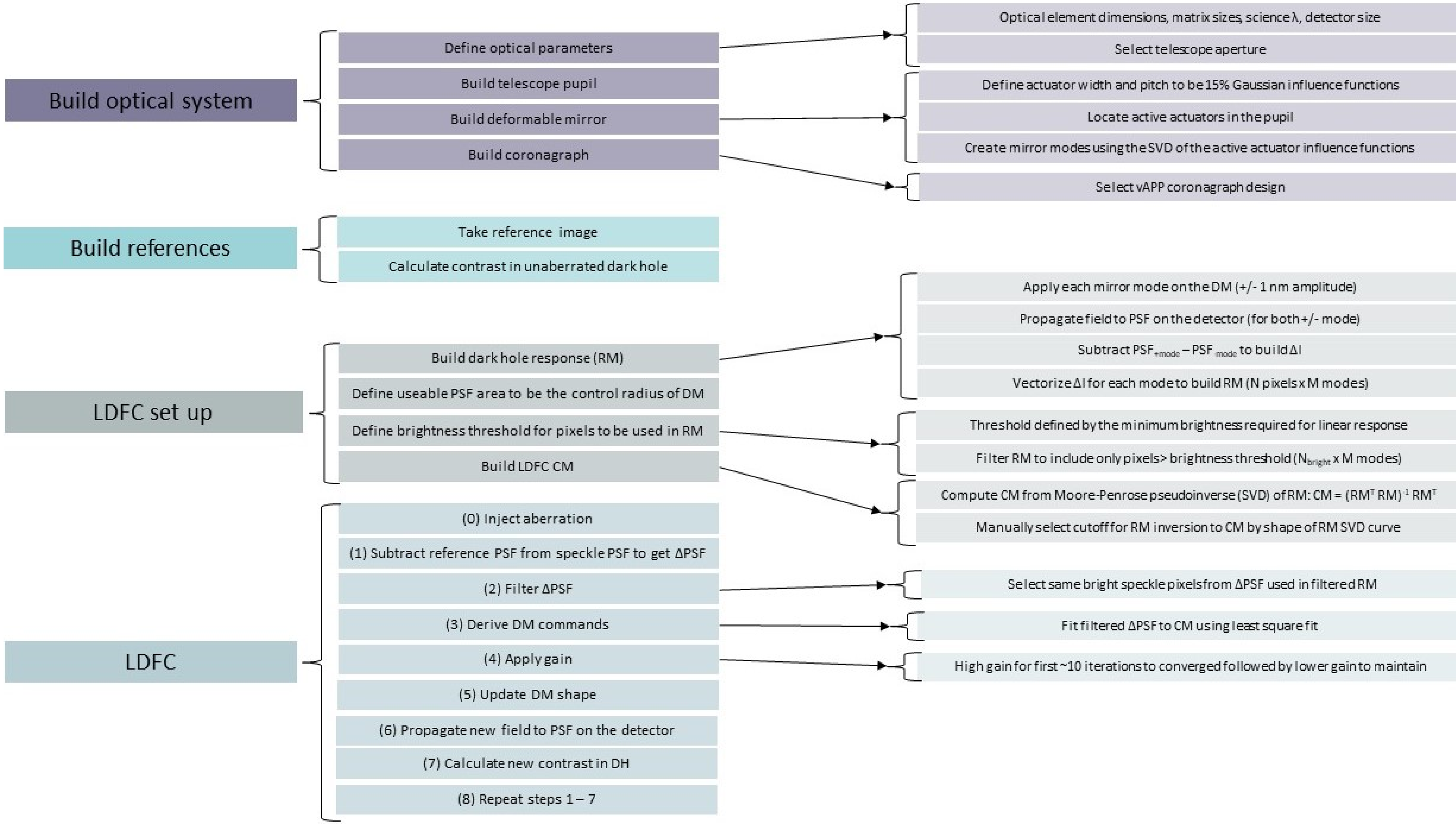

Figure 4.6: LDFC simulation code flow chart

To demonstrate spatial LDFC's ability to maintain the high contrast DH, a 6.5 m telescope system was constructed in simulation which includes a single DM and Lyot coronagraph that removes approximately two orders of magnitudes of stellar light from the final image. The system entrance pupil was a 6.5 m diameter circular, centrally-obscured mask with a 30% central obscuration and 2% spiders (see fig 4.7a). The Lyot coronagraph consists of a Lyot stop undersized by 1% and a focal plane mask with a diameter of 2.44 λ/D. For the system's DM, a model of a Boston Micromachines 1K DM was defined using 1024 actuators sharing a common gaussian influence function and 15% inter-actuator coupling. The diameter of the illuminated pupil projected onto the DM was 6.5 mm, covering approximately 21 actuators and lending an outer working angle (OWA), or control radius of 10.5 λ/D. Sampling at the science detector was 0.24 λ/D per pixel. The source was a magnitude 5 star with sensing done at λ=550 nm (V band) with 10% bandwidth. The total flux at the entrance pupil was 1.82x10^9 photons/second, and this rate was used to embed photon noise in all of the I_t images in eq 4.8. All of these test parameters are listed in Table 4.1.

Stellar magnitude	5
Total flux	1.82x10^9 photons/second
Noise included	photon noise
Exposure time	5 seconds
Source wavelength	550 nm, V band
Source bandwidth	10%
Telescope diameter	6.5 m
Sampling at detector	0.24 λ/D per pixel
# DM actuators used	398, (21 in diameter)
# Bright field pixels used	4535
Bright field contrast threshold	$10^{-4.5}$
Inner working angle (IWA)	2.44 λ/D
Outer working angle (OWA)	10.5 λ/D

Table 4.1: Simulated system parameters used in the following spatial LDFC demonstrations

To build the DH, a standard implementation of EFC (Groff et al., 2015) was used to suppress the stellar light to an average contrast floor of $10^{-7.94}$ within a 3.5 λ/D x 8.5 λ/D region centered at 6.75 λ/D from the PSF core (shown in fig 4.7b). This DH was the ideal reference state for LDFC to maintain, and the intensity image

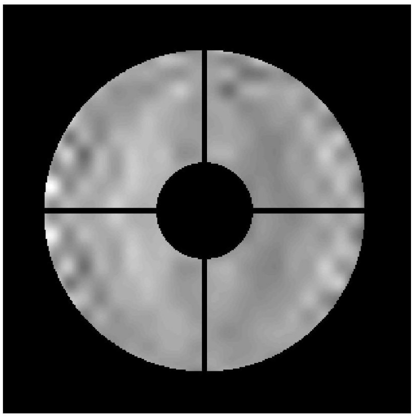

(a) Telescope pupil and DM

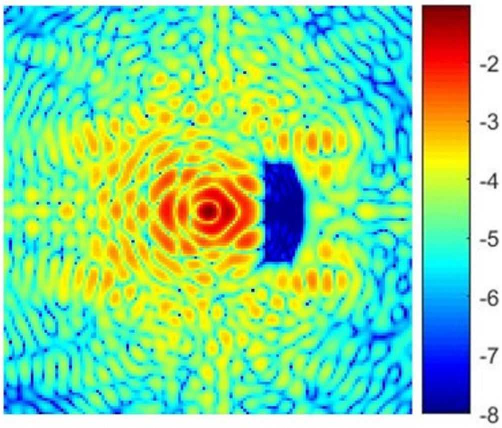

(b) Log_{10} EFC reference image

Figure 4.7: Standard implementation of EFC using a DM with 398 illuminated actuators (a) to create a 3.5 λ/D x 8.5 λ/D DH centered at 6.75 λ/D from the center of the stellar PSF with $10^{-7.94}$ average contrast (b). The peak-to-valley amplitude of the DM to create this dark hole is $\pm$ 0.1 μm.

I_{ref} was saved as the reference image to be used in the LDFC servo to return the DH to its EFC-derived state.

With the DH established, the spatial LDFC algorithm was implemented as described in Section 4.1.3 to maintain the DH in the presence of two separate injected phase aberrations. In the first case, a single speckle pair was induced in the image plane by applying a sine wave phase perturbation in the pupil. For the second case, a random Kolmogorov phase screen was introduced in the pupil creating multiple speckles in the image plane. In both cases, the same optical system, source, and threshold values were kept constant as were all other simulation parameters. The following sections present spatial LDFC's response to these two cases.

4.1.4.1 Sine wave phase perturbation

After the DH was constructed, a spatial sine wave phase perturbation with 6 cycles/aperture was introduced into the pupil plane, forming a speckle at +/- 6 λ/D: one speckle within the DH and one speckle within the BF. The sine perturbation was given a 1 nm peak-to-valley (P-V) amplitude in phase, creating a speckle pair with a maximum magnitude of $10^{-5.0}$ and an average aberrated DH contrast of $10^{-6.90}$. The LDFC control loop was run with a gain of 0.6 until the average DH contrast reached $10^{-7.9}$ at which point the gain was reduced to 0.1 to maintain the correction. The LDFC control loop was allowed to run for 50

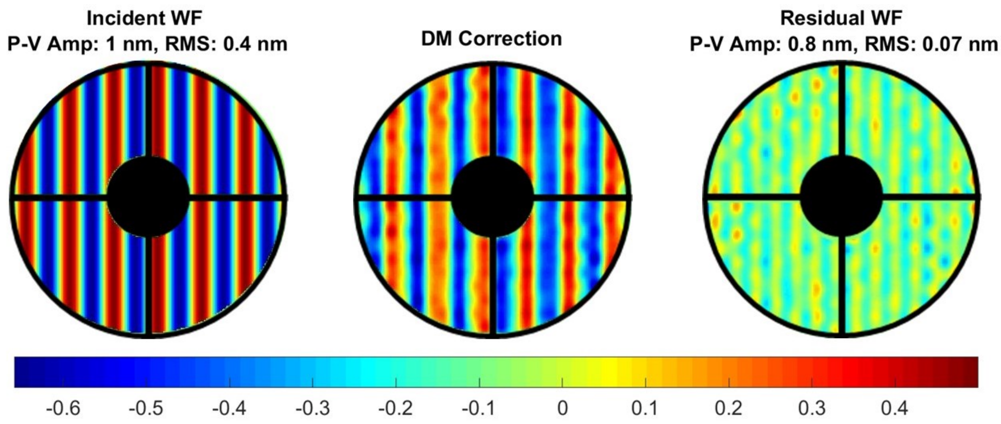

Figure 4.8: The injected 6 cycles/aperture sine wave phase perturbation with a P-V amplitude of 1 nm (left), the DM response derived by LDFC (center) and the final residual wavefront error (right) after 6 iterations. In this case, the residual WFE is dominated by a mode with a frequency of approximately 14 cycles/aperture which falls beyond the spatial frequency limit (10.5 cycles/aperture) the DM can correct. This residual WFE is due to the gaussian shape of the DM's influence functions which cannot perfectly fit the injected sine wave perturbation, thereby leaving a residual sinusoidal pattern. Scale is given in nm.

iterations for this demonstration with convergence occuring after 6 iterations. The results are shown in Table 4.2 and in fig(s) 4.8 - 4.11. It should be noted that, in figs 4.10 and 4.11b, the LDFC-corrected DH contrast occasionally drops below the initial EFC contrast level. This effect is due to noise fluctuations.

EFC DH contrast	$10^{-7.94}$
Speckle magnitude	$10^{-5.0}$
Avg DH contrast with speckle	$10^{-6.90}$
LDFC DH contrast	$10^{-7.94}$
ΔContrast	$10^{-1.04}$
# Iterations to converge	6

Table 4.2: Performance with a sine wave phase: Initial EFC DH average contrast, magnitude of the injected speckle, average contrast of the aberrated DH, average contrast of the DH after LDFC, total change in contrast for one full LDFC loop, and the number of iterations to converge to the EFC contrast floor

4.1.4.2 Kolmogorov phase perturbation

In the first case, the injected aberration created a single speckle in the DH and a corresponding speckle in the BF. To demonstrate spatial LDFC's ability to suppress multiple speckles, a Kolmogorov phase aberration was generated in the pupil plane

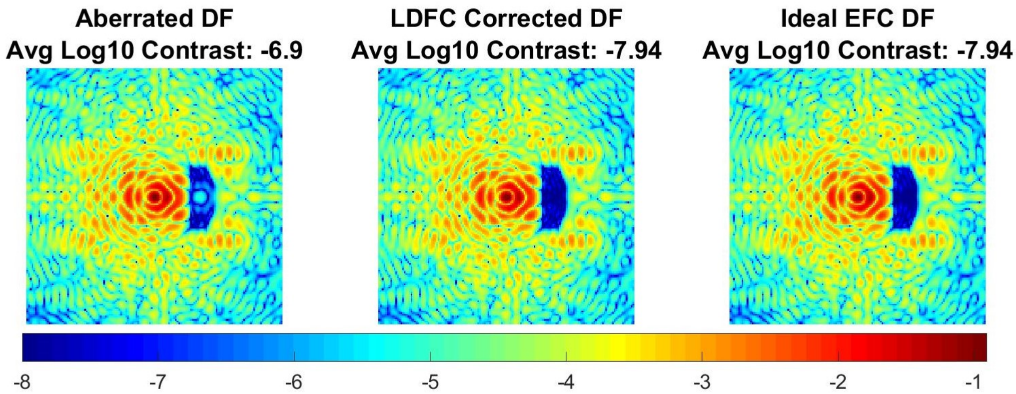

Figure 4.9: The aberrated PSF with a single $10^{-5.0}$ magnitude speckle in the DH with $10^{-6.90}$ average contrast and a matching speckle in the BF, the final LDFC-corrected DH with $10^{-7.94}$ average DH contrast, and the reference EFC-derived DH also with $10^{-7.94}$ average DH contrast. Scale is $\log_{10}$ contrast.

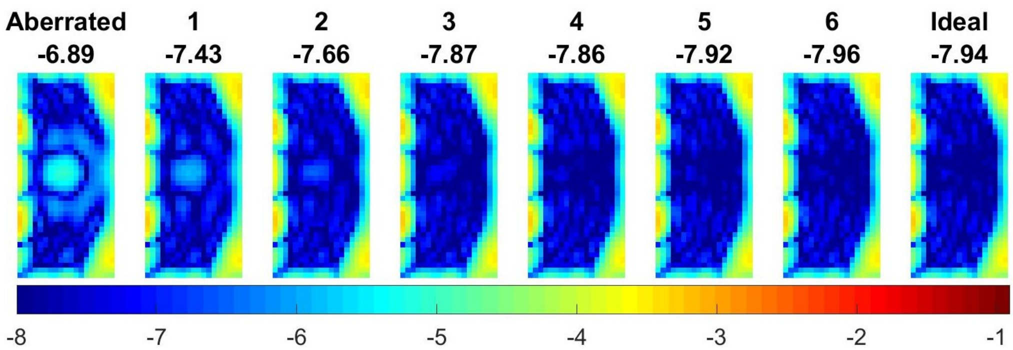

Figure 4.10: Evolution of the DH over the 6 iterations (seen in fig 4.11b) to converge from a degraded DH average contrast of $10^{-6.90}$ with a $10^{-5.0}$ magnitude speckle to the LDFC-corrected DH with $10^{-7.94}$ average contrast. The ideal DH is shown in the final frame for reference. Scale is $\log_{10}$ contrast.

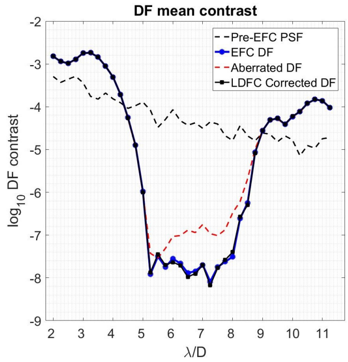

(a) Average contrast across the full DH for the pre-EFC PSF, DH post-EFC (blue), DH post-EFC with injected speckle (red), and the corrected DH post-LDFC (black)

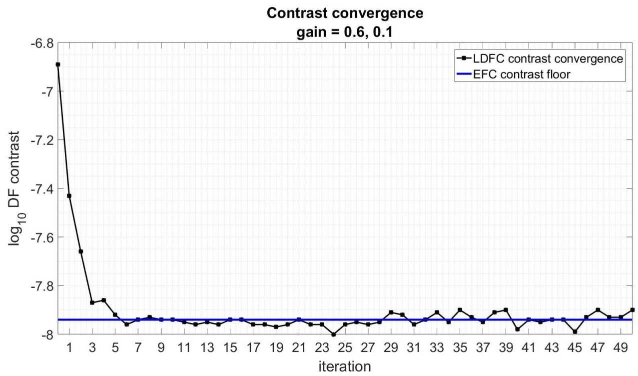

(b) Average DH contrast (black) over 50 iterations showing convergence to the initial EFC contrast (blue) after 6 iterations.

Figure 4.11: Performance of the spatial LDFC servo with a sinusoidal phase perturbation. Gain = 0.6 until the DH contrast reached $10^{-7.9}$. The gain was lowered to 0.1 for the remaining iterations.

instead of a sinusoidal phase perturbation (see fig 4.12). The phase perturbation was given a P-V amplitude of 20.5 nm, creating an aberrated DH with an average contrast of $10^{-6.51}$. The LDFC control loop was again run with a gain of 0.6 until the average DH contrast reached $10^{-7.9}$ at which point the gain was reduced to 0.1 to maintain the correction. The LDFC control loop was allowed to run for 50 iterations for this demonstration with convergence occuring after 6 iterations. The results are shown in Table 4.3 and shown in fig(s) 4.12 - 4.15. As in the previous single speckle demonstration, the LDFC-corrected DH contrast occasionally drops below the initial EFC contrast level in fig 4.15b. This effect is due to noise fluctuations.

EFC DH contrast	$10^{-7.94}$
Avg DH contrast with aberration	$10^{-6.51}$
LDFC DH contrast	$10^{-7.94}$
ΔContrast	$10^{-1.43}$
# Iterations to converge	6

Table 4.3: Performance with Kolmogorov phase: Initial EFC DH average contrast, magnitude of the injected speckle, average contrast of the aberrated DH, average contrast of the DH after LDFC, total change in contrast for one full LDFC loop, and the number of iterations to converge to the EFC contrast floor

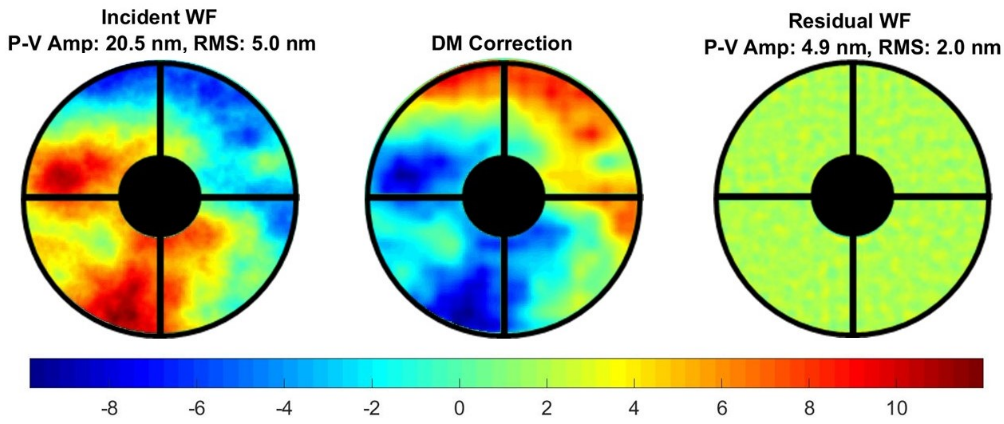

Figure 4.12: The injected Kolmogorov phase perturbation with a P-V amplitude of 20.5 nm (left), the DM response derived by LDFC (center) and the final residual wavefront error (right) after 6 iterations. Scale is given in nm.

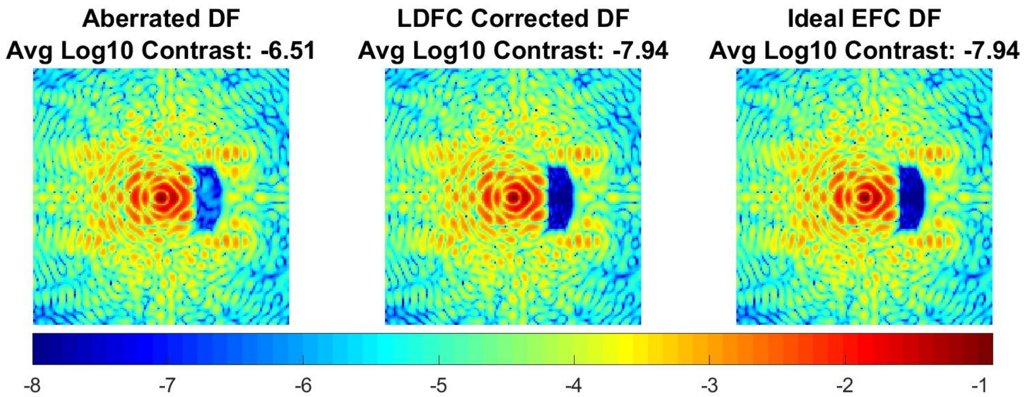

Figure 4.13: The aberrated PSF with multiple speckles in the DH and average DH contrast of $10^{-6.51}$, the final LDFC-corrected DH with $10^{-7.94}$ average DH contrast, and the reference EFC-derived DH with $10^{-7.94}$ average DH contrast. Scale is $\log_{10}$ contrast.

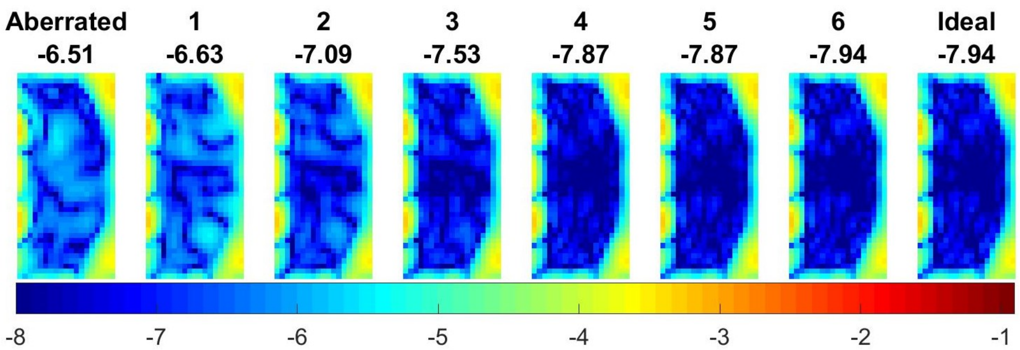

Figure 4.14: Evolution of the DH over the 6 iterations (seen in fig 4.15b) to converge from a degraded DH average contrast of $10^{-6.51}$ to the LDFC-corrected DH with $10^{-7.94}$ average contrast. The ideal DH is shown in the final frame for reference. Scale is $\log_{10}$ contrast.

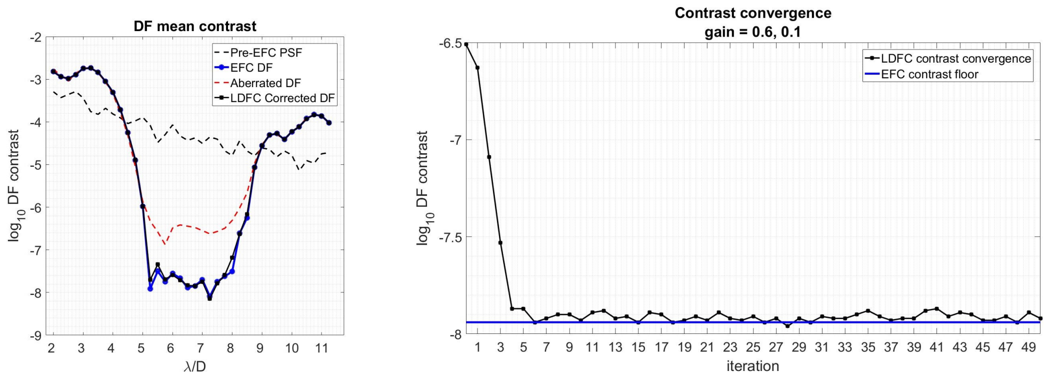

(a) Average contrast across the full DH for the pre-EFC PSF, DH post-EFC (blue), DH post-EFC with injected speckle (red), and the corrected DH post-LDFC (black)

(b) Average DH contrast (black) over 50 LDFC iterations showing convergence to the initial EFC contrast (blue) after 6 iterations.

Figure 4.15: Performance of the spatial LDFC servo with a Kolmogorov phase perturbation. Gain = 0.6 until the DH contrast reached $10^{-7.9}$. The gain was lowered to 0.1 for the remaining iterations.

4.2 Spectral linear dark field control

A potential solution for overcoming spatial LDFC's null space is to operate a separate version of LDFC simultaneously. This second version, known as spectral LDFC, freezes the state of the DH within the control bandwidth by using state measurements of light outside of the control bandwidth. It can also make use of bright speckles outside of the DH (still also outside of the control bandwidth) as long as they do not saturate. This method exploits the fixed wavelength relationships that exist between speckles at different wavelengths that were generated by the same aberration. To first order, this fixed relationship scales the speckle separation linearly with wavelength and scales the complex amplitude inversely with wavelength. The complex amplitude speckle field may also interfere with static chromatic coronagraph residuals due to the coronagraph's finite design bandwidth. These relationships between out-of-band and in-band light allow for the state of the DH within the control band to be monitored and maintained by measurements made of speckles located outside of the spectral control band (Guyon et al., 2018). Since spectral and spatial LDFC rely on a BF signal from separate dimensions, the null spaces of the two forms of LDFC are not expected to overlap. For this reason, concurrent operation of spectral and spatial LDFC can provide a powerful tool for compensating for the separate null spaces of both techniques.

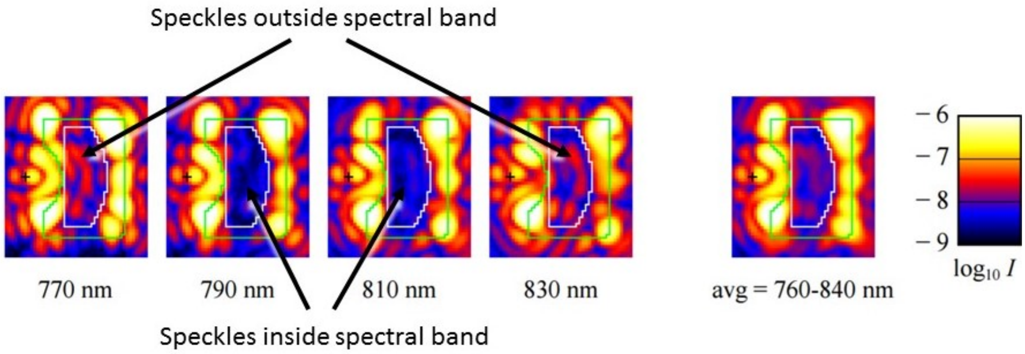

Figure 4.16: Spectral LDFC example: The 7 λ/D x 8 λ/D DH from JPL's High Contrast Imaging Testbed (HCIT) created using a PIAA coronagraph. The DH is shown in four individual spectral channels: two channels within the control bandwidth and two out-of-band channels with speckles used to maintain the DH state within the control bandwidth. Also shown is the average DH over the full 10% bandwidth centered at $\lambda = 800$ nm (Guyon et al., May 2014).

As an example of the BF signal that can be used by spectral LDFC, fig 4.16 shows the DH created using a Phase Induced Amplitude Apodization (PIAA) (Guyon et al., 2006) coronagraph at JPL's High Contrast Imaging Testbed (HCIT). Speckles within the DH are shown at multiple wavelengths, both in-band (the science image) and out-of-band (the signal used by spectral LDFC).

While spectral LDFC was not in operation when this image was taken, this is a clear demonstration of a case in which the in-band DH contrast could be maintained by sensing the speckles that are outside the control bandwidth and applying the appropriate wavelength-scaled correction to cancel the in-band speckles. Further development and analysis of this form of LDFC can be found in an upcoming paper by Guyon et.al. (Guyon et al., 2018).

4.3 Discussion of limitiations and null space

In summary, spatial LDFC acts as an extension of EFC by operating as a servo that can maintain high contrast in the DH during science exposures. Using changes in the BF to provide updates on the state of the field within the DH, spatial LDFC is able to lock the state of the DH after it is established by EFC without relying on field modulation which interrupts the science acquisition and fundamentally limits the exposure time. The substantial increase in uninterrupted observation time spatial LDFC offers makes it a more efficient method than EFC for maintaining deep contrast and will lead to an overall increase in the number of planets detected and analyzed over the lifetime of an instrument. Here we have introduced the mathematical principles behind spatial LDFC and provided demonstrations of its capabilities through numerical simulation.

We have demonstrated here that spatial LDFC is capable of locking the DH contrast at its ideal EFC state using only the BF response to a perturbation in the optical path. However, there are limitations to spatial LDFC and a potential null space which need to be explored. These issues and some potential solutions are addressed below. One significant limiting factor for spatial LDFC is DH symmetry. This technique requires access to a BF that is located spatially opposite the DH. Due to this requirement, spatial LDFC is expected to work only with a non-symmetric DH. However, in the case of a symmetric DH, spectral LDFC offers a possible solution (see Section 4.2). Since spectral LDFC relies on speckles that are located spatially within the DH but outside of the control bandwidth, it is not affected by the lack of a BF spatially opposite the DH. In the case of a much larger DH than the one presented here, spatial LDFC is predicted to still be capable of stabilizing the DH, but it cannot use BF speckles at spatial frequencies higher than those present in the DH to do so.

It should be noted that there are cases to which spatial LDFC can be blind to an aberration. For this technique, the null space consists of wavefront errors that affect the DH without changing the BF. One potential example of this null space is the formation of a speckle on a single side of the focal plane due to the combination of phase and amplitude sine wave aberrations. In such a case, if the speckle falls inside the DH, the BF will not see any modulation and will therefore be unable to sense and correct the aberration. A second potential null space example would consist of an incident phase aberration sine wave with a phase that creates a BF speckle with a phase that is 90^o from the local BF phase. This case may not create a linear signal and would therefore not be corrected by LDFC. It should also be noted that this chapter has specifically explored a system in which aberrations were introduced and corrected by the same DM; in real systems there will be aberrations that occur outside the DM-conjugate pupil plane and subsequently do not correspond exactly to DM authority.

CHAPTER 5

Linear Dark Field Control Validation with a vAPP Coronagraph

LDFC is capable of monitoring low-order aberrations and maintaining high Strehl, but it is more efficient to offload this job to the MWFS as shown in Chapter 3. LDFC is then left to monitor mid-spatial frequency aberrations and maintain the dark hole contrast across the mid-λ/D regime. In the bright field, speckles of a high enough magnitude respond linearly to aberrations in the pupil plane (Miller et al., 2017). This monotonic response allows for closed-loop control of both the bright field and dark hole speckles induced by the same pupil plane aberration.

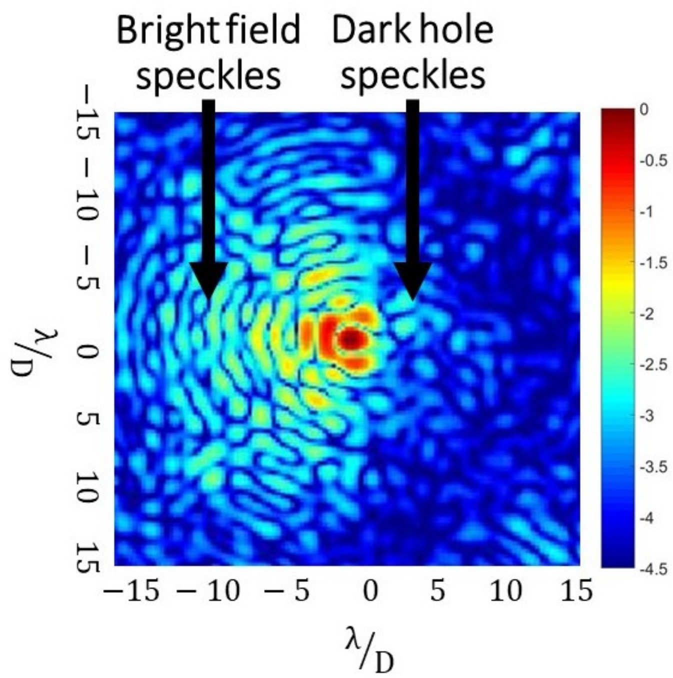

Figure 5.1: The bright field speckles and the corresponding dark hole speckles induced by a mid-spatial frequency pupil plane aberration. The bright field speckles are used to sense the aberration that is simultaneously corrupting the dark hole.

In this chapter, spatial LDFC is demonstrated with a vAPP coronagraph in both simulation and in the lab. The results shown cover three specific cases: (1) using the science image at focus as the WFS, (2) defocusing the science image and using this signal as the WFS, and (3) using the defocused image as the WFS but with a known planet in the bright field. The first two cases were explored both in simulation and in the lab, while the third case was examined only in simulation. In Section 5.1, the test set-up, parameters, calibration, and performance metrics are covered. In Section 5.2, results for these three cases are presented.

5.1 Basic operating principles

5.1.1 Test parameters

For all three cases, the vAPP mask with 12 Zernike MWFS spots and 2 - 15 λ/D dark holes was used, even though these dark holes spanned higher spatial frequencies than could be controlled by the DM. This vAPP was chosen for two reasons: (1) to more easily observe the speckle response to the LDFC correction at the control radius of the DM in simulation, and (2) because the Zernikes MWFS spots allowed for low-order sensing of misalignment errors in the lab that were then compensated for using the DM (see Chapter 3). This low-order correction improved the dark hole contrast at small separations (near 4 λ/D).

Two key differences in the testing done in simulation versus the lab were IWA and initial contrast. In simulation, the dark hole contrast achieved by the vAPP without aberrations was approximately 10^{-5}, and the IWA was set at 2 λ/D. In the lab, both IWA and contrast suffered due to real optics and misalignment. The IWA, even after low-order aberration correction with the MWFS was limited to about 4 λ/D; at smaller separations, the contrast was still dominated by low-order effects. The contrast across the greater extent of the dark hole was limited by mid-spatial frequency aberrations due to optical surface errors (specifically the OAPs). These limited the initial vAPP contrast to approximately 10^{-3} (with some variation across the extent of the dark hole).

5.1.1.1 Building the modal basis functions and response matrix

While similar to LOWFS in principle, rather than using low-order modes for LDFC, mid-spatial frequency modes derived from the influence functions of the DM are used as the modal basis set. These "mirror modes" are chosen such that the spatial frequency content of the basis set matches the spatial extent of the dark hole. The mirror modes were derived by the singular value decomposition (SVD) of the influence function matrix F measured in Chapter 2. Each column in F contains the image of a single DM actuator being "poked" (see fig 2.7); for the 32 x 32 actuator DM in the lab, the dimensions of F for the full DM are $[N_{pixels}$ x 1024]. All 1024 actuators are not illuminated by the relayed pupil (beam footprint) on the DM. Only a select number of actuators $M_{actuators}$ are seen by the optical system. To derive these modes, the influence functions of only the illuminated actuators are used such that F is $[N_{pixels}$ x $M_{actuators}]$ The SVD of F is computed as

$$F = U\Sigma V^* \tag{5.1}$$

where Σ is a $[N_{pixels}$ x $M_{actuators}]$ diagonal matrix, and U and V^* are unitary matrices of sizes $[N_{pixels}$ x $N_{pixels}]$ and $[M_{actuators}$ x $M_{actuators}]$ respectively. The columns of both U and V^* form a set of basis vectors of F. The first $M_{actuators}$ columns in matrix U are each a single mirror mode stored in vector form. Each mode is a linearly independent eigenvector of FF^T. Therefore, for $M_{actuators}$ illuminated on the DM, there are $M_{actuators}$ mirror modes. A sample of the 403 mirror modes used in simulation are shown in fig 5.2.

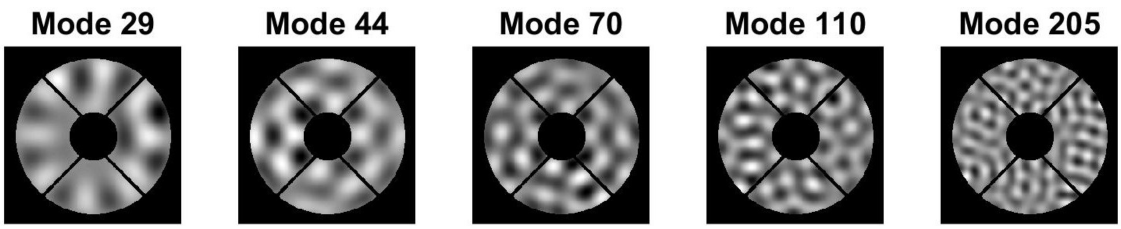

Figure 5.2: A sample of 5 mid-spatial frequency mirror modes used to build the LDFC response matrix. As the mode number increases, so does the spatial frequency content of that mode. Each subsequent mode in the response matrix therefore probes higher spatial frequencies in the image plane.

An advantage of using mirror modes as the modal basis set, particularly for FPWFS, is that, as the mode number increases, so does the spatial frequency content of that mode. Each subsequent mode therefore probes higher spatial frequencies in the image plane. This effect can be seen in figs 5.4 and 5.5. This is not true when using Zernike modes (common in LOWFS) or individual influence functions. By using mirror modes to build the response matrix, the spatial frequencies being controlled can be independently selected. For the following tests in both simulation and in the lab, these mirror modes were used to control the dark hole. In simulation, 403 modes were used in the basis set, but in the lab, the modal basis set was reduced due to limited dynamic range; beyond mode 200, the signal in the outer frequencies began to wash out and was dominated by noise. Increasing the exposure time to capture signal from these modes caused the signal from the lower order modes to saturate. For this reason, the basis set was simply truncated to 200 modes.

In the image plane, the WFS regions were chosen to be circularly symmetric about the center of the upper and lower science PSFs, and the outer extent of these regions was defined by the control radius of the DM; this was done because the DM cannot fit modes with spatial frequency content greater than the control radius, so the response matrix itself does not contain useful information outside this limit; the DM can therefore also not control any aberrations outside of the control radius. Simulated images of the science image at focus and defocused are shown in fig 5.3, as are the WFS regions defined by the DM control radius.

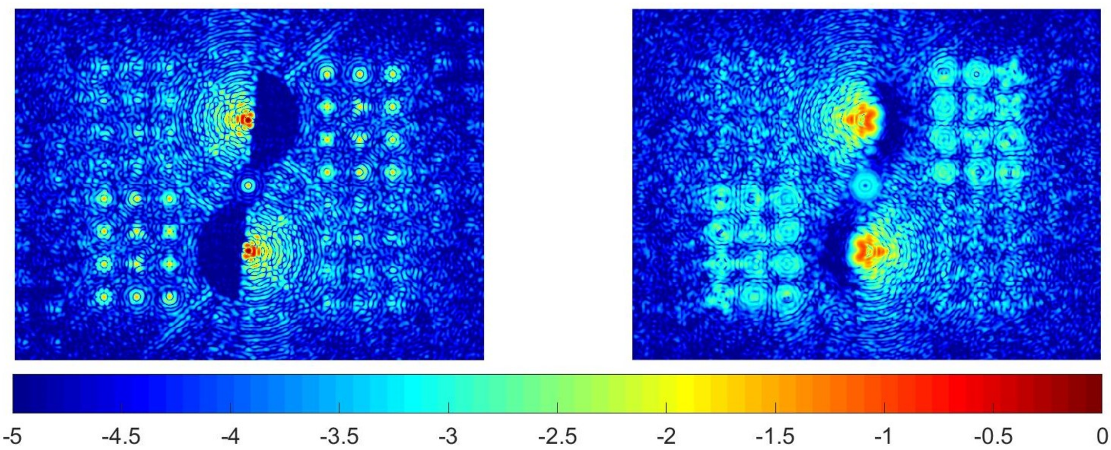

(a) vAPP images at focus and defocused

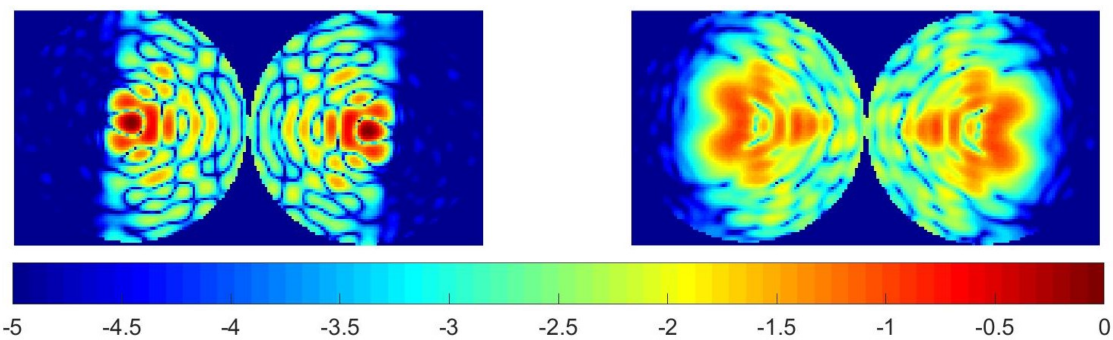

(b) WFS regions defined by the DM control radius at focus and defocused

Figure 5.3: Simulation: The vAPP image at focus and defocused by a 200 nm amplitude phase applied in the pupil plane.

From these images, the bright pixels with a normalized magnitude of 10^{-4} or greater were selected to be kept as part of the WFS response matrix. Recalling eqs 1.15

and 1.16, the response matrix was built in each case by applying each mode on the DM with both a positive amplitude and negative amplitude, and subtracting the resulting PSF images. Images from the simulated response matrix for the at focus and defocused cases can be seen in figs 5.4 and 5.5.

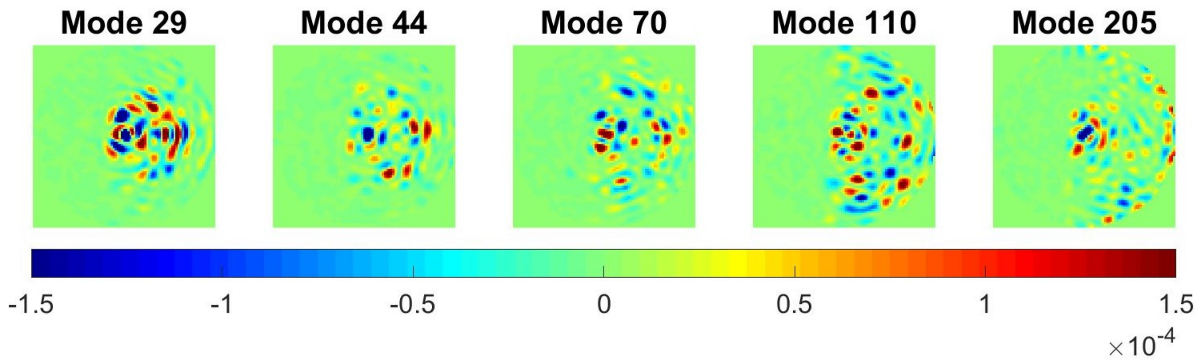

(a) Simulation: At focus

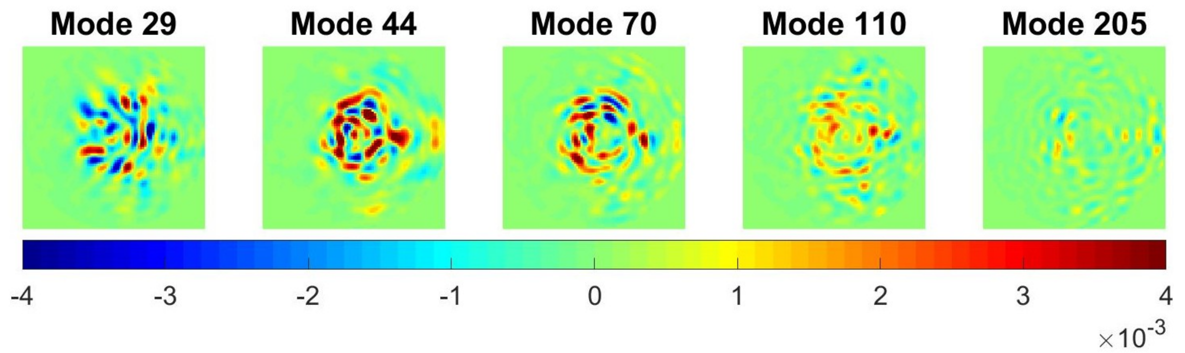

(b) Simulation: Defocused

Figure 5.4: The simulated lower PSF response to the 5 mid-spatial frequency modes in fig 5.2 for both the at focus and defocused cases. As the mode number increases, so does the spatial extent of the mode's response in the focal plane. Higher-numbered modes therefore probe higher frequencies in the PSF.

In the lab, the average contrast of the bright pixels used in the response matrix was approximately 10^{-3} - just above the average dark hole contrast. Pixels within the core were ignored since they saturated for certain modes at the set exposure time. Unlike in simulation, where both PSFs were used in the WFS, only the upper PSF was used in the lab. This choice was not made for a science-based reason, but was done for the sake of time and simplicity; with more time, both PSFs would have been used as the WFS in the lab as well. Example images taken in the lab of the WFS response to 5 modes at focus and defocused can be seen in fig 5.5. The correction derived from only one PSF still resulted in correction on both PSFs.

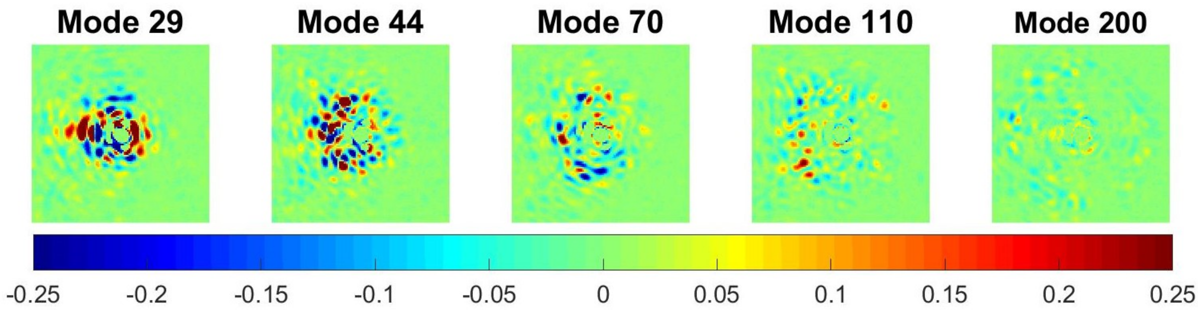

(a) Lab: At focus

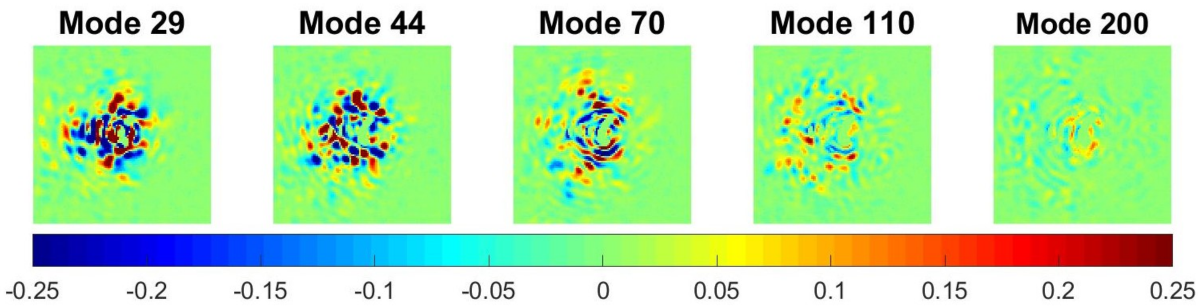

(b) Lab: Defocused

Figure 5.5: The FPWFS response to the 5 mid-spatial frequency modes in fig 5.2 for both the at focus and defocused cases. As the mode number increases, so does the spatial extent of the mode's response in the focal plane. Higher-numbered modes therefore probe higher frequencies in the PSF. In the lab, at a set exposure time that keeps the low-order mode RM images from saturating, the signal from the higher-order modes becomes dominated by noise. This effect is most apparent in the image for mode 200 where the signal is mostly dominated by noise as opposed to the image for mode 29 which is saturated by the stretch of this colorbar.

Recalling eq 4.9, the response matrix is then inverted for use in closed-loop. As the response matrix is overdetermined, it is inverted by pseudoinverse. For this work, the pseudoinverse, RM^+, is computed by SVD

$$RM^+ = V\Sigma^+U^*. \tag{5.2}$$

Using SVD to invert the response matrix allows for the selection of the modes that will be used in the inversion process. The modes used are chosen based on their "weighting" given by the diagonal of the matrix Σ; these weightings are known as the singular values of the response matrix. A mode with a low singular value does not contribute strongly to the reconstruction of the matrix being inverted, and therefore acts as a source of noise if used in the inversion process. To select the cut-off point for the modes used in the inversion, the singular values are plotted as seen in fig 5.6 which shows an example from both simulation and the lab. The

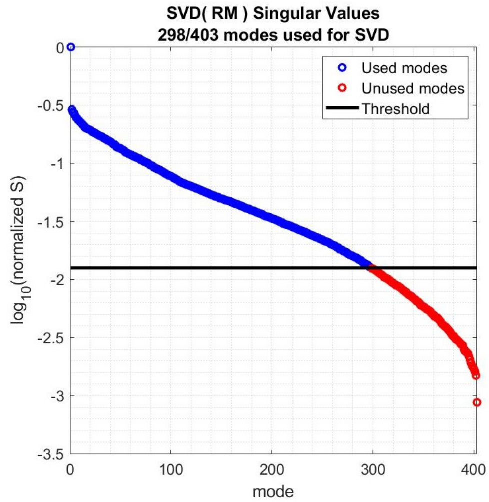

(a) Singular values in simulation: defocused

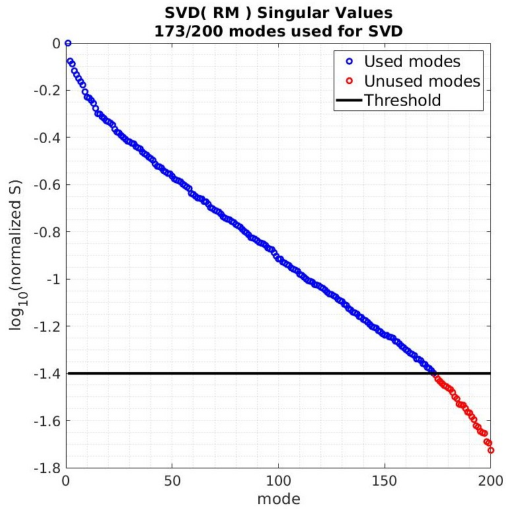

(b) Singular values in the lab: defocused

Figure 5.6: The singular values of the response matrix in both simulation and in the lab for the defocused WFS case. The black line marks the user-defined cut-off point between the modes included in the inversion of the response matrix (blue) and those that were excluded (red). This truncation resulted in the use of 298 modes in simulation and 173 modes in the lab.

SVD limit varies between the lab and simulation cases due to a different number of modes and pixels being used in each case. Selection of modes and pixels used in the lab was driven predominately by saturation issues which were not a problem in simulation.

This inversion process is also addressed in Chapter 4. As a general rule, the cut-off point for the at focus cases was always higher than for the defocused cases (meaning fewer modes were used); this was done because the control loop became unstable with more modes used in the inversion. Most likely, this was due to imperfect filtering of modes that have a non-linear (or at least non-monotonic) response at focus. The response matrix is rebuilt, filtered for bright pixels, and inverted before every LDFC test in both simulation and in the lab.

5.1.1.2 Simulating atmospheric turbulence

To simulate LDFC's performance in the presence of turbulence, temporally correlated Kolmogorov phase time sequences were generated to inject into the telescope pupil. These phase aberrations, ϕ_a, were generated by code written by J. R. Males. This code allowed for the selection of the spatial frequency content of the phase aberration as well as the temporal correlation between each phase step. The spatial PSDs of the aberrations, defined by $\frac{1}{k^\beta}$ and the temporal PSDs, defined as $\frac{1}{f^\alpha}$, were selected to create speckles throughout the full extent of the dark hole with varying levels of temporal correlation.

For spatial frequency content, two cases were chosen: $\beta = 2$ and 3. The $\beta = 2$ case contained higher spatial frequency content than $\beta = 3$, and therfore created speckles at higher spatial frequencies in the image plane. The $\beta = 3$ case was dominated by lower spatial frequency aberrations, thereby generating more speckles closer to the PSF core. For temporal correlation, temporal PSDs were chosen with αs of 4, 3, and 2. For the $\alpha = 4$ case, the individual phase screens were highly correlated, similar to the temporal correlation of frozen flow atmospheric turbulence (Males and Guyon, 2018). In the cases of $\alpha = 3$ and 2, the resulting phase sequences were less temporally correlated and more representative of telescope jitter rather than atmospheric turbulence. In each case, the aberration was injected into the pupil and allowed to evolve over time. A sample of five phase screens from each sequence taken at the same time steps can be seen in figs 5.7 - 5.9.

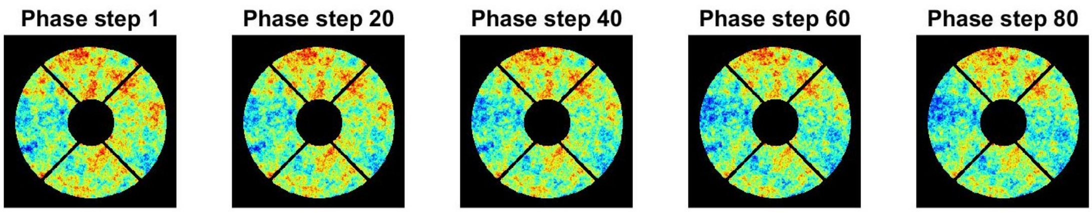

(a) Case 1: $\frac{1}{k^2}$ spatial PSD, $\frac{1}{f^4}$ temporal PSD

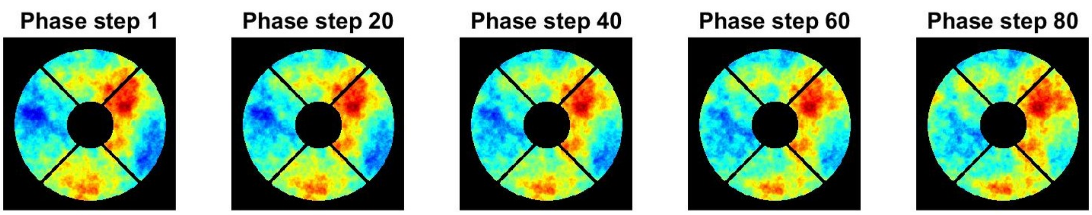

(b) Case 2: $\frac{1}{k^3}$ spatial PSD, $\frac{1}{f^4}$ temporal PSD

Figure 5.7: Simulation: Evolution of a phase aberration in the telescope pupil. Five samples taken from the Kolmogorov phase generated with $\frac{1}{k^\beta}$ spatial frequency content and temporal PSDs given by $\frac{1}{f^4}$. The temporal correlation of this phase sequence is high, similar to the temporal correlation of frozen flow turbulence.

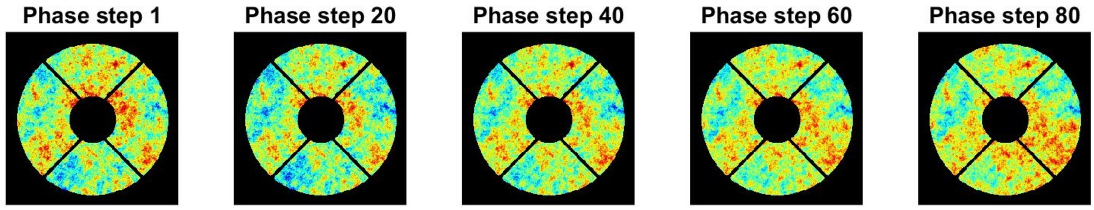

(a) Case 3: $\frac{1}{k^2}$ spatial PSD, $\frac{1}{f^3}$ temporal PSD

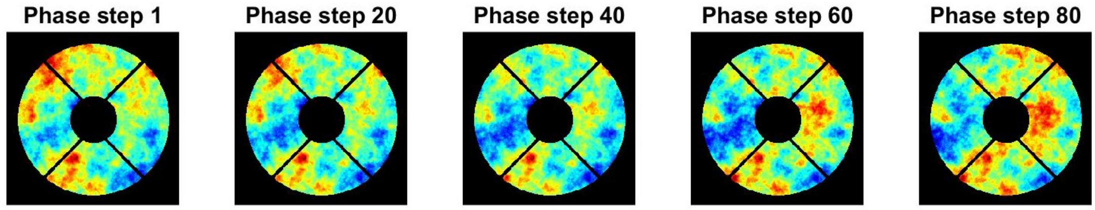

(b) Case 4: $\frac{1}{k^3}$ spatial PSD, $\frac{1}{f^3}$ temporal PSD

Figure 5.8: Simulation: Evolution of a phase aberration in the telescope pupil. Five samples taken from the Kolmogorov phase generated with $\frac{1}{k^\beta}$ spatial frequency content and temporal PSDs given by $\frac{1}{f^3}$. These sequences are less temporally correlated and are more representative of telescope jitter.

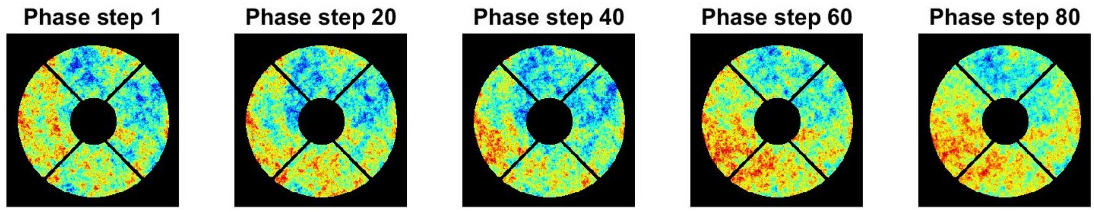

(a) Case 5: $\frac{1}{k^2}$ spatial PSD, $\frac{1}{f^2}$ temporal PSD

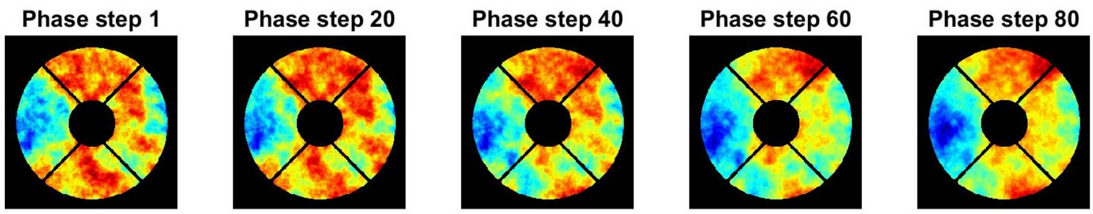

(b) Case 6: $\frac{1}{k^3}$ spatial PSD, $\frac{1}{f^2}$ temporal PSD

Figure 5.9: Simulation: Evolution of a phase aberration in the telescope pupil. Five samples taken from the Kolmogorov phase generated with $\frac{1}{k^\beta}$ spatial frequency content and temporal PSDs given by $\frac{1}{f^2}$. The two cases include phase sequences with $\beta = 2$ and 3. The temporal correlation of the phase sequence is low and is representative of rapidly changing, uncorrelated aberrations like telescope jitter.

In simulation, all of the phase sequences seen in figs 5.7 - 5.9 were tested with LDFC. In the lab however, only cases 1 and 2, with temporal PSD $\frac{1}{f^4}$, were used as they emulated the temporal correlation of frozen flow atmospheric turbulence.

In simulation, the aberration was directly injected into the system pupil plane without using the model DM to create the aberration. Across the simulated pupil, the aberration was composed of a 256 x 256 pixel grid, filling the full simulated pupil clear aperture, thereby allowing for possible speckle generation across the full 2 - 15 λ/D dark hole and well beyond. In the lab, the aberration was injected by writing the phase screen to one channel of the DM; cases 1 and 2 projected onto the DM are shown in fig 5.10. Because of this, the spatial frequency content of the aberrations in the lab were limited by the control radius of the DM. With 22 actuators illuminated across the DM, the applied aberrations created speckles out to $11\lambda/D$. No aberrations were consquently created in the outer extent of the dark hole from 11 - 15 $\lambda/$ in the lab.

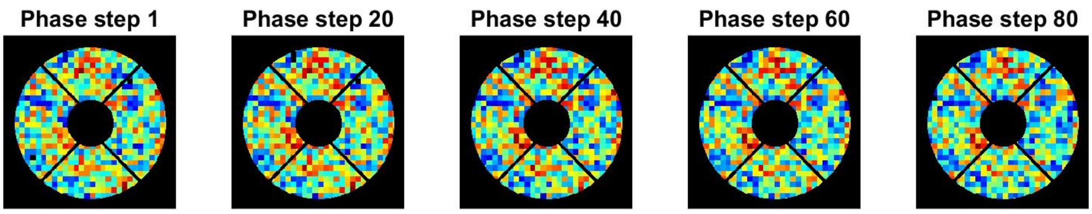

(a) Case 1: $\frac{1}{k^2}$ spatial PSD, $\frac{1}{f^4}$ temporal PSD

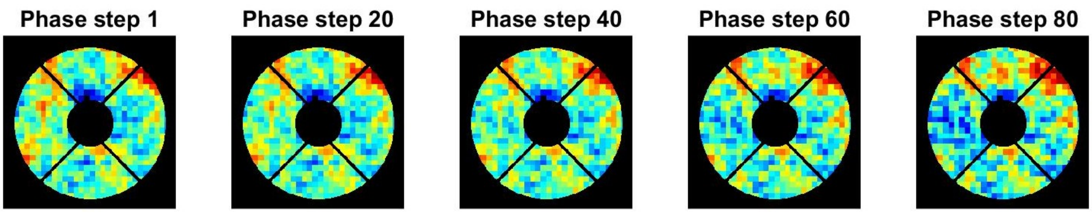

(b) Case 2: $\frac{1}{k^3}$ spatial PSD, $\frac{1}{f^4}$ temporal PSD

Figure 5.10: Lab: Evolution of a phase aberration in the telescope pupil. Five samples taken from the Kolmogorov phase generated with $\frac{1}{k^\beta}$ spatial frequency content and temporal PSDs given by $\frac{1}{f^\alpha}$. The various cases include phase sequences with $\beta = 2$ and 3, and $\alpha = 4$, 3, and 2. For $\alpha = 4$, the temporal correlation of the phase sequence is high, similar to the temporal correlation of frozen flow atmsopheric turbulence. The $\alpha = 2$ and 3 cases are less temporally correlated and are more representative of telescope jitter.

5.1.2 Performance metrics

To evaluate LDFC's ability to stabilize the contrast within the dark hole in both simulation and in the lab, the temporally correlated series of phase aberrations was applied in open-loop and the resulting speckle images and speckle magnitudes were recorded. The same series of phase aberrations were then run again with LDFC running in closed-loop. Two metrics were used to compare the open-loop case to the closed-loop performance: (1) the average contrast in the dark hole and (2) the root mean square (RMS) wavefront error.

5.1.2.1 Average contrast

The primary metric for evaluating LDFC's performance was the average dark hole contrast C given in Chapter 1, eq 1.24

$$C = \frac{I_{DH}}{I_{star}} \tag{5.3}$$

(refer back to Section 1.3 for the full mathematical derivation). To determine LDFC's performance across the dark hole, the dark hole was binned in successive semicircles centered about the PSF core, each with a width of 1 λ/D, thereby changing eq 5.3 to

$$C_{k\frac{\lambda}{D}} = \frac{I_{k\frac{\lambda}{D}}}{I_{star}} \tag{5.4}$$

where $I_{\Delta k\frac{\lambda}{D}}$ is the average irradiance over a 1 λ/D bin beginning at spatial frequency k, and $C_{\Delta k\frac{\lambda}{D}}$ is the contrast within that frequency bin found by normalizing the average irradiance by the peak stellar flux per pixel. In simulation, k runs from 2 to 15 λ/D, while in simulation, k begins at 4 λ/D. This is because, in the lab, limited dynamic range on the cameras caused saturation close to the IWA out to 4 λ/D due to uncorrected low-order aberrations. (Attempts were made to correct these aberrations using the MWFS with some success, but due to misalignment in the system, correction of astigmatism using the DM resulted in the creation of coma. This most likely occured because the DM correction caused the beam to shift, thereby changing the input angle on the final OAP. This correlation between astigmatic correction and coma generation can be seen in Chapter 3, fig 3.9.)

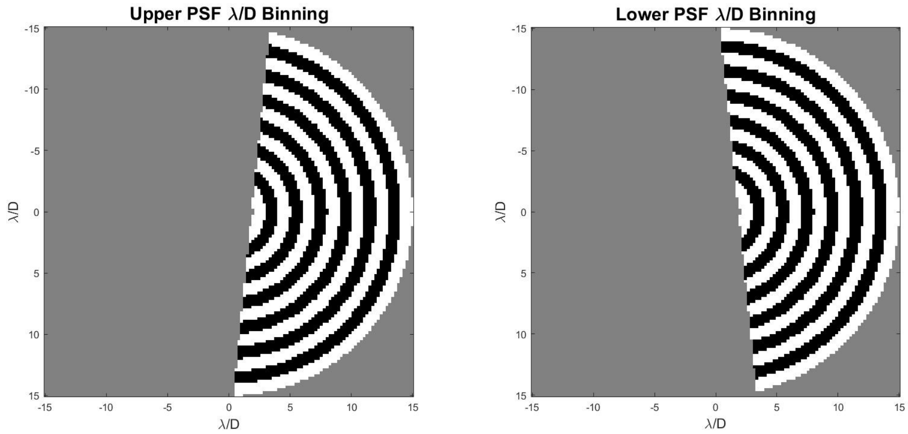

(a) Hemispherical spatial frequency bins for the upper and lower vAPP PSFs with 1 λ/D width

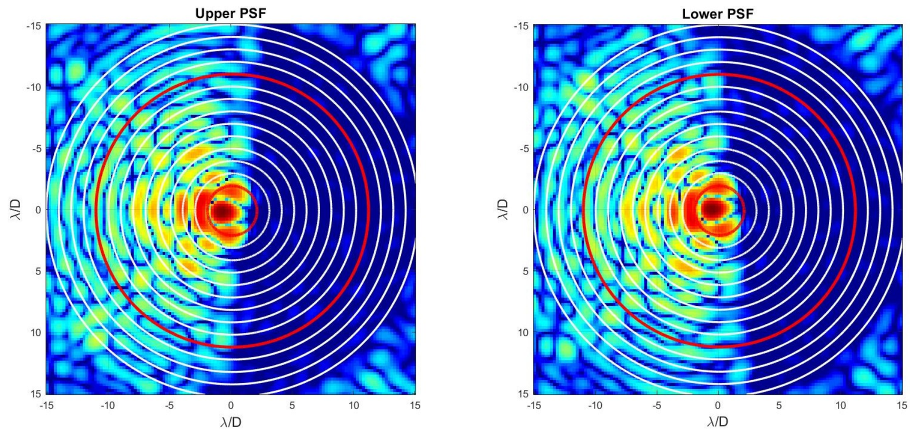

(b) Upper and lower reference vAPP PSFs denoting the 1 λ/D binning

Figure 5.11: Hemispherical masks used for the contrast calculation in 1 λ/D bins and reference PSFs showing the 1 λ/D bins across the full PSF. The red lines denote the inner working angle (IWA) of the vAPP coronagraph and the control radius set by the number of actuators across the DM.

By limiting the ROI to these bins rather than evaluating the full dark hole, we build a more complete picture of how the algorithm performs with respect to spatial frequency. The 1 λ/D binning used in both simulation and in the lab are shown in fig 5.11 with the 12 Zernike vAPP 2 -15 λ/D PSFs in simulation for reference. In fig 5.11a, the red lines denote the IWA of the vAPP coronagraph at 2 λ/D and the OWA defined by the control radius of the DM at 11 λ/D.

Plots showing the contrast in the dark hole across these 1 λ/D bins are shown for each case in this chapter to demonstrate LDFC's ability to stabilize the contrast within the dark hole in the presence of a temporally evolving phase aberration. It should be noted that what is being shown is the stability of the contrast of the dark hole, not the stability of the speckle field. There is a risk that the speckle field may change without causing a change in the average contrast. This will be addressed in future work.

5.1.2.2 Residual wavefront error

Due to calculation errors and a finite number of actuators, the aberrated wavefront is not perfectly "flat" after correction by the DM (i.e. it does not return to a perfect, unaberrated plane wave). However, in closed-loop, the remaining errors across the wavefront, referred to as residual WFE, should converge to a lower value than the inital aberrated wavefront error and remain at that lower value. This behavior can be quantified by calculating the root mean square (RMS) of both the aberrated wavefront and the residual WFE.

To ensure that the LDFC correction converges and "flattens" the aberrated wavefront, the residual WFE, represented by ϕ_Δ, was calculated as the sum of the DM correction ϕ_c and the aberrating phase ϕ_a such that

$$\phi_\Delta = \phi_a + \phi_c. \tag{5.5}$$

The "flatness" of ϕ_Δ was then determined by computing its RMS by

$$\phi_{RMS} = \sqrt{\frac{\sum_{i=1}^{n} \phi_i^2}{n}} \tag{5.6}$$

where n is the number of pixels within the unobscured pupil in simulation. In the lab, since both the aberration and correction are injected by the DM, n is the number of actuators in the illuminated pupil. For comparison of the system performance with and without LDFC, the RMS was calculated for each phase screen in the time sequence ϕ_a in open-loop (without correction) and for the residual WFE ϕ_Δ in closed-loop (with LDFC correction). These results can be seen for each case presented in this chapter.

The RMS metric was not used as the main metric for performance evaluation; it was predominately used to ensure that the loop was not diverging; a rapid increase in ϕ_{RMS} was an early indicator that the loop had become unstable. This metric was of particular use in the lab as the only indicator of loop convergence since the dark hole contrast was calculated in post-processing rather than in real time as it was for simulation.

5.2 Performance analysis

The following results focus on demonstrating spatial LDFC's ability to stabilize the dark hole contrast in the presence of a temporally correlated, evolving phase screen with a temporal PSD given by $\frac{1}{f^4}$. This temporal PSD is similar to the temporal correlation associated with frozen flow atmospheric turbulence, and it will be shown that LDFC is capable of stabilizing the contrast in the presence of this kind of turbulence in simulation as well as in the lab. For a well-rounded analysis of LDFC's performance, results demonstrating LDFC with non-atmospheric turbulence phase aberrations with $\frac{1}{f^3}$ and $\frac{1}{f^2}$ temporal PSDs are included at the end of the chapter as well. The tests are separated into three specific categories as mentioned earlier: (1) using the science image at focus as the WFS, (2) defocusing the science image as the WFS, and (3) using a defocused image as the WFS but with a planet in the bright field. For each case, the injected aberration is a time sequence with 1024 phase steps.

The results are displayed using both performance metrics: average contrast divided into 1 λ/D bins across the dark hole and RMS WFE. For both metrics, the open-loop (no LDFC) case is always plotted in red, and the closed-loop (with LDFC) case plotted in green. For the first two cases, simulation and lab resutls are presented; for the third case with a planet injected into the image, results are only available in simulation.

It is worth noting again that, while the IWA of the coronagraph on the testbed is 2 λ/D as it is in simulation, the exposure time required to image the speckles across the majority of the dark hole is high enough such that the low-order aberrations present near the PSF core and out to approximately 4 λ/D saturate, and the information in that regime is not valid. Therefore, simulation contrast plots begin at the IWA, while lab contrast plots begin at 4 λ/D. Also recalling that, in simulation, the resolution of the injected aberration is set by the matrix size, the aberrations in simulation are capable of creating speckles across the full extent of the 2 -15 λ/D dark hole. On the testbed, the aberration is injected by applying a phase screen on the DM, and therefore the spatial extent of the aberration-induced speckles within the dark hole is limited, just as the LDFC-correction is, to the control radius of the DM. For this reason, simulation results are plotted out to OWA of the dark hole; lab results are plotted only out to the DM control radius. Since the beam diameter and DM model used in simulation replicate the actual beam diameter and DM in the lab, the control radius is set by the illuminated beam diameter across 22 actuators; this sets the greatest controllable spatial frequency in both simulation and the lab to 11 λ/D.

Given that one of the goals of these tests was to predict how LDFC will perform on MagAO-X, the zero magnitude flux for these simulations was set to be 6×10^9 photons/sec, the expected flux at the science camera on the MagAO-X instrument. The simulation cases shown do not include photon noise; they were chosen for display here because they offer an example of the baseline theoretical operation. Tests conducted with photon noise found that, with a 5^{th} magnitude star, both the defocused and at focus cases still convereged when running at 3 kHz - approximately the same speed expected with the PyWFS closed-loop on MagAO-X (Males, J. R. and MagAO-X team, 2017).

This is assuming noise only in the aberrated image; the response matrix and reference are built without noise. This is because theoretically, when taking the reference image and building the response matrix, the exposure time can be made as high as necessary to ensure that the image is not noise dominated. It should be noted also that, while the loop converges at these rates, the performance is still degraded with respect to the noiseless case.

5.2.1 Wavefront sensing with an image at focus

As a FPWFS technique, the ideal scenario for running LDFC would be with the science image at focus. This would allow for real-time correction of the science image while using the science image itself, unmodified, as the WFS. Recalling that the response matrix is built by subtracting the negative mode response from the positive mode response (see eq 1.15), the response matrix can be filtered to exclude pixels that do not respond monotonically to the positive and negative modal inputs.

This removes the pixels within the dark hole that do not respond linearly. Keeping these non-linear and low response pixels in the the response matrix only adds noise in the inversion process when building the command matrix. With the science image used in focus as the WFS, the brightest pixels at the core of the PSF do not respond monotonically, and were therefore excluded from the response matrix as seen in fig 5.12.

(a) Pixels used in simulation

(b) Pixels used in the lab

Figure 5.12: The bright field pixels used in the WFS at focus in simulation and in the lab

It was seen consistently that fewer modes were used in the inversion of the response matrix to stabilize the loop in the at focus cases in comparison to the defocused cases. This could be due to the greater dynamic range across the pixels used in the at focus case; in other words, higher order modes do not contribute as strongly in the at focus case as opposed to the defocused case. The SVD curve for the simulated and lab cases can be seen in fig 5.13 with 293 and 166 modes used in each respective response matrix.

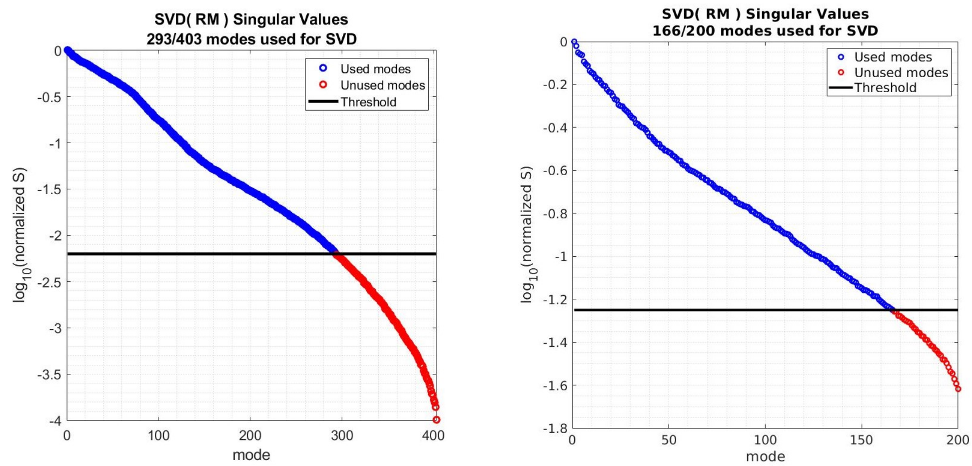

(a) SVD curve in simulation: at focus (b) SVD curve in the lab: at focus

Figure 5.13: The SVD curves for the inversion of the response used in the WFS at focus in simulation and in the lab. After truncation, 293 modes were used in simulation and 166 modes in the lab.

The results for tests both in simulation and in the lab are shown below.

5.2.1.1 Simulation

The injected aberration here has a spatial PSD of $\frac{1}{k^3}$ (see fig 5.7b). The loop here was closed using all 293 modes in the response matrix. Fig 5.14 displays a single time step showing what is occuring in the pupil plane and science image plane simultaneously. It shows the injected aberration, LDFC correction applied to the DM, and the residual WFE after the correction is applied as well as the aberrated (open-loop) dark hole, the closed-loop LDFC corrected dark hole, and the ideal, unaberrated dark hole for comparison.

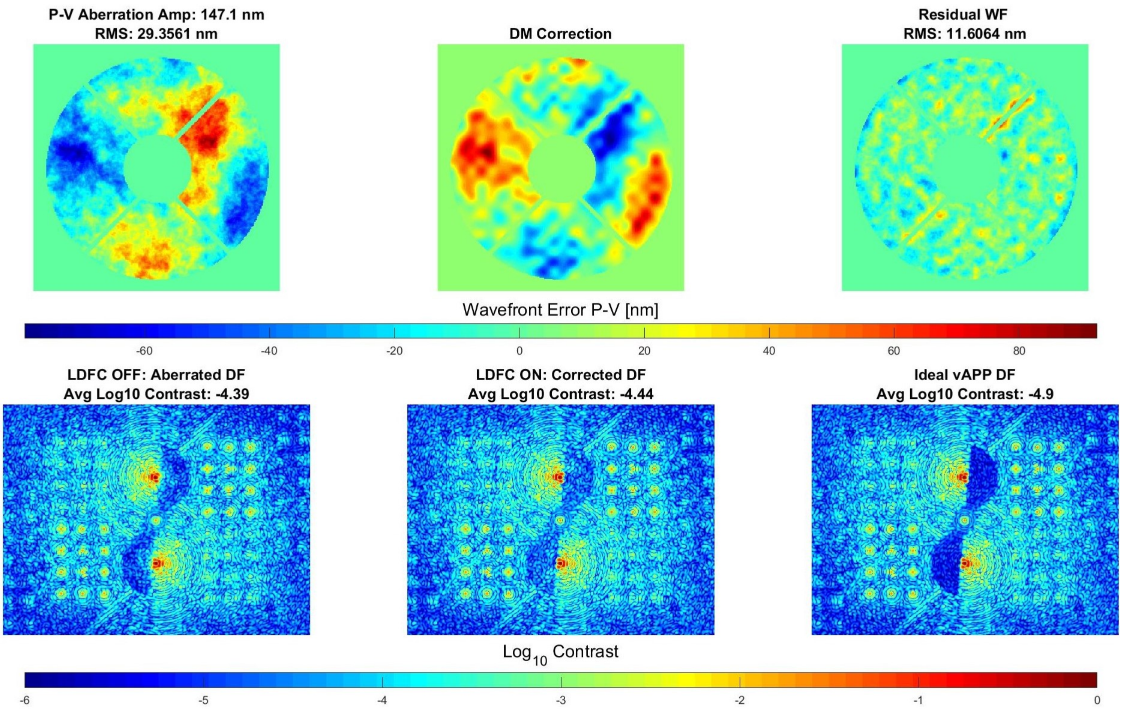

Figure 5.14: Simulation: Single frame showing LDFC running closed-loop. Displayed in the top row is the injected pupil plane phase aberration, the LDFC-derived correction applied on the DM, and the residual wavefront error. In the bottom row is shown the aberrated PSFs with speckles thrown into the dark hole, the LDFC-corrected PSFs, and the ideal unaberrated vAPP PSFs for comparison.

Figs 5.15 - 5.18 display the convergence and stabilization of the dark hole over a 1024 phase screen aberration binned by 1 λ/D hemispherical regions centered about the PSF core (fig. 5.11). Results for the upper and lower dark holes are each plotted separately.

With this $\frac{1}{k^3}$ aberration, lower frequency aberrations dominate, and few speckles are created out past 7 λ/D. LDFC corrects the lower spatial frequency aberrations. At approximately 7 λ/D away from the PSF core, with no high amplitude speckles to correct, LDFC's performance begins to decline, and the difference between the aberrated and corrected cases becomes insignificant. From the control radius at 11 λ/D out to the OWA of the dark hole at 15 λ/D, LDFC itself creates speckles, and the correction becomes worse than the intial aberratio; we suspect this is due to the Gibbs phenomenon. The Gibbs phenomenon is the tendency of Fourier and other eigenfunction series to overshoot or "ring" at discontinuities. This speckle formation at the control radius and beyond is most likely a "ringing" effect at the edge of the control radius which is seen also in dark hole generation with EFC; this can be seen when referring back to figs 4.11a and 4.15a where there is a visible increase in the brighness at the edge of the dark hole that peaks over the intial PSF. This effect will be seen again throughout the results presented for every simulation case.

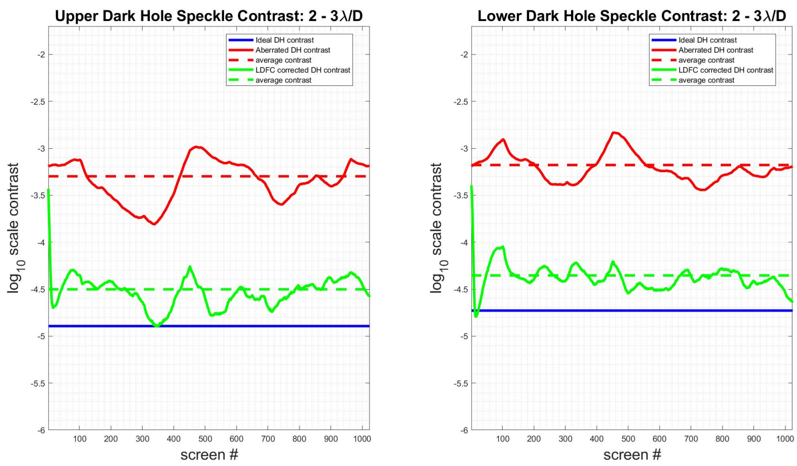

(a) 2 - 3 λ/D

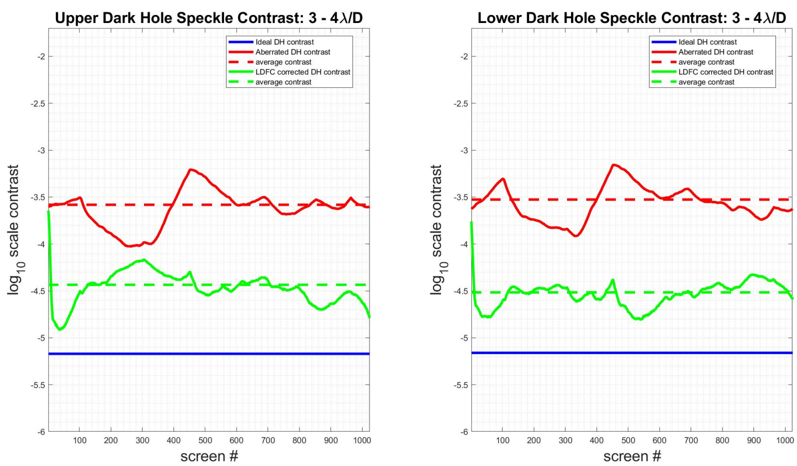

(b) 3 - 4 λ/D

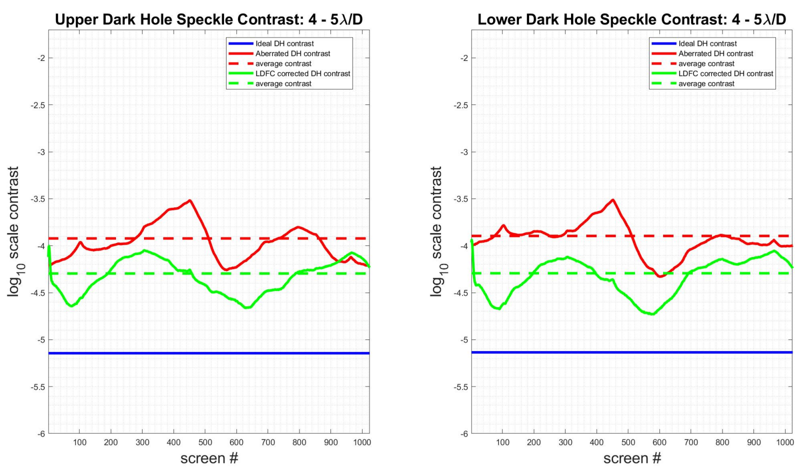

(c) 4 - 5 λ/D

Figure 5.15: Simulation with WFS at focus: Contrast stabilization within 1 λ/D hemispherical bins across 2 - 5 λ/D within the dark hole over a series of 1024 temporally correlated $\frac{1}{f^4}$ phase screens.

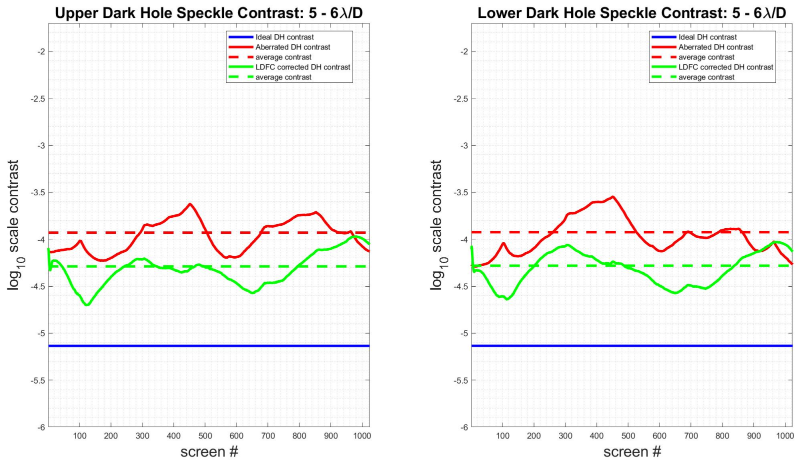

(a) 5 - 6 λ/D

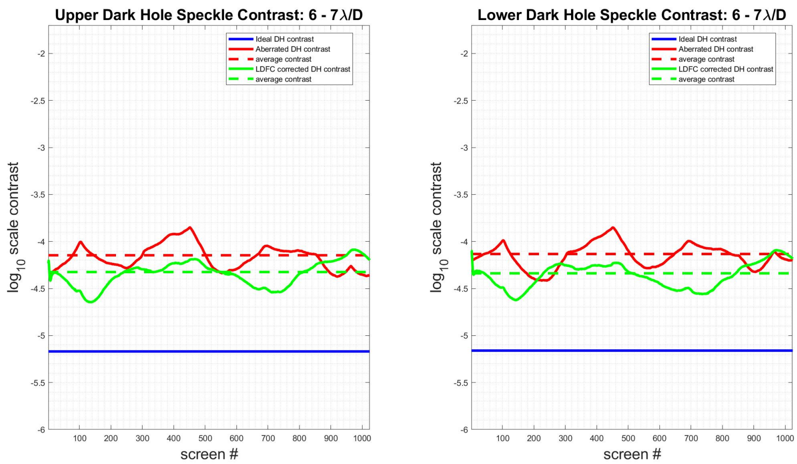

(b) 6 - 7 λ/D

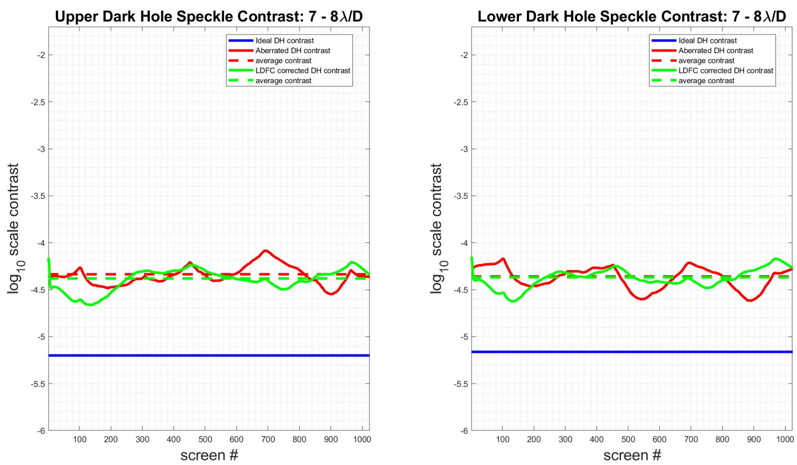

(c) 7 - 8 λ/D

Figure 5.16: Simulation with WFS at focus: Contrast stabilization within 1 λ/D hemispherical bins across 5-8 λ/D within the dark hole over a series of 1024 temporally correlated $\frac{1}{f^4}$ phase screens.

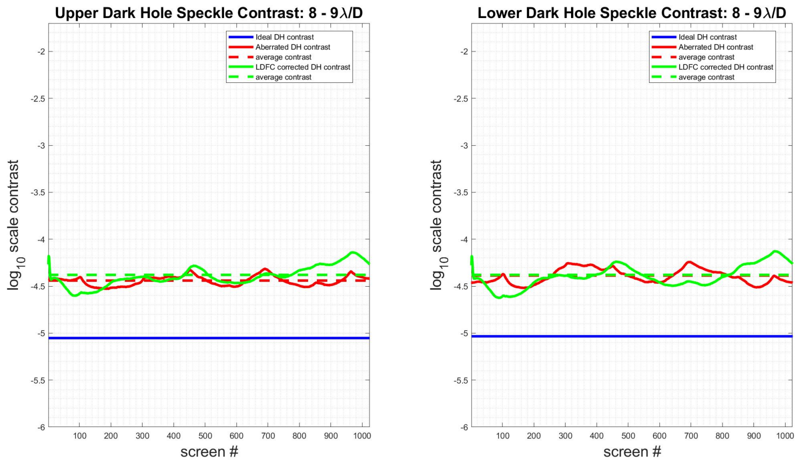

(a) 8 - 9 λ/D

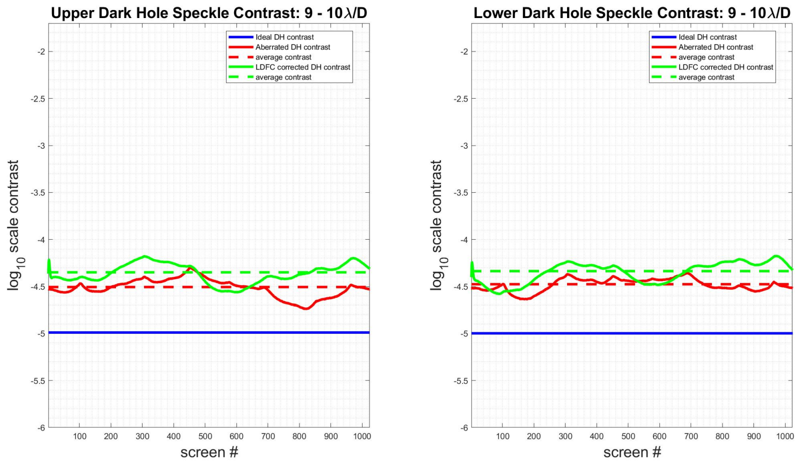

(b) 9 - 10 λ/D

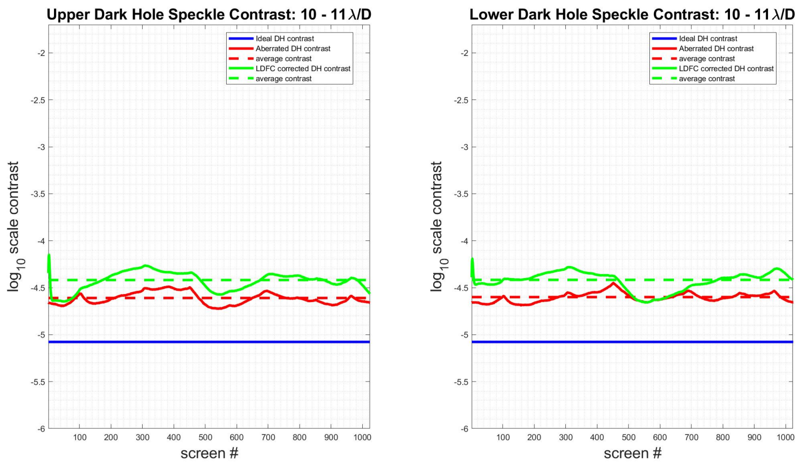

(c) 10 - 11 λ/D

Figure 5.17: Simulation with WFS at focus: Contrast stabilization within 1 λ/D hemispherical bins across 8 - 11 λ/D within the dark hole over a series of 1024 temporally correlated $\frac{1}{f^4}$ phase screens.

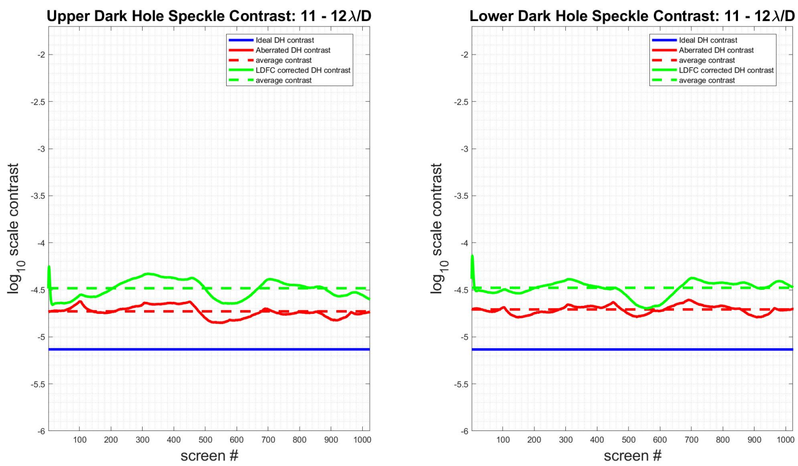

(a) 11 - 12 λ/D

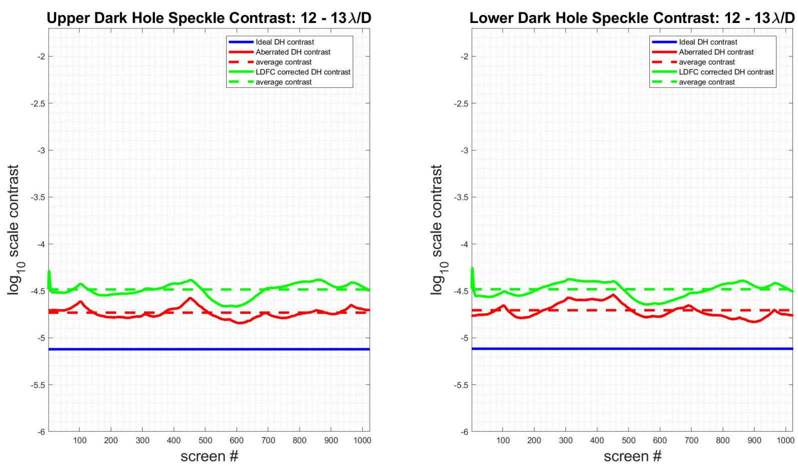

(b) 12 - 13 λ/D

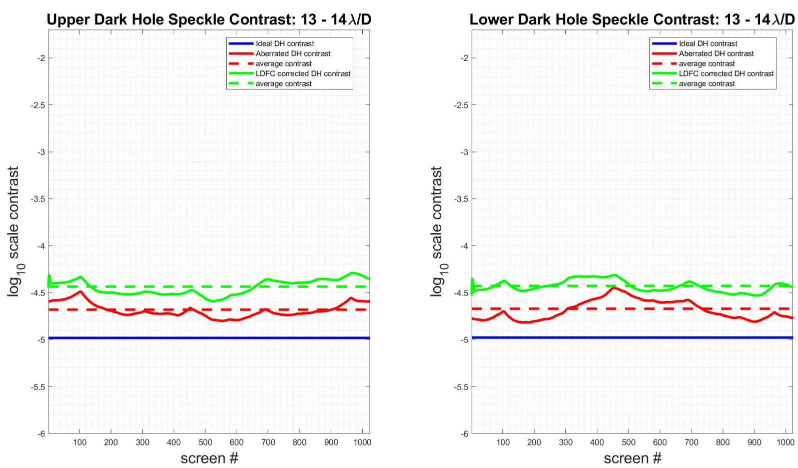

(c) 13 - 14 λ/D

Figure 5.18: Simulation: Contrast stabilization within 1 λ/D hemispherical bins across 11 - 14 λ/D within the dark hole over a series of 1024 temporally correlated $\frac{1}{f^4}$ phase screens.

The following two images display the upper (fig 5.19) and lower (fig 5.20) dark holes at 8 stages as LDFC converges, driving the dark hole contrast back to the initial unaberrated contrast. The images are reference subtracted and masked to only show the dark holes to make the speckle formation and suppression more visible. The red line denotes the 11 λ/D control radius beyond which the DM cannot control speckle formation. While LDFC suppresses speckle formation and stabilizes the contrast within the control radius, outside 11 λ/D, speckles form due to the residual wavefront errors left uncorrected by the DM. It should also be noted that the lower dark hole images have been flipped left to right to match the orientation of the upper dark hole for aesthetic purposes.

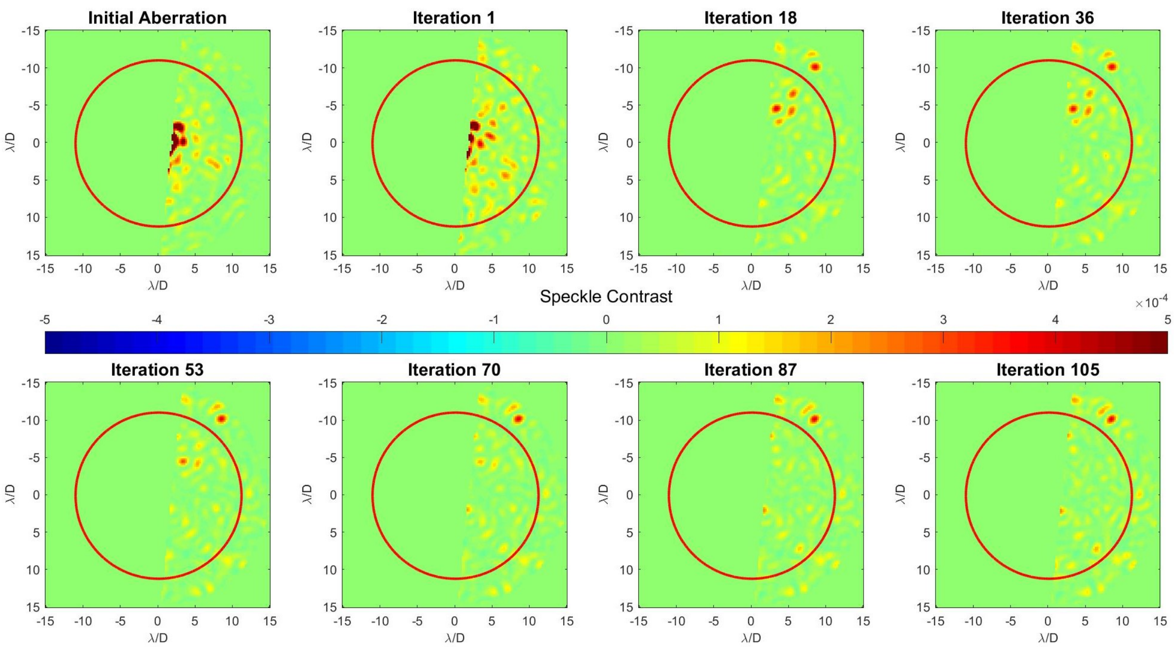

Figure 5.19: Simulated upper dark hole: Convergence back to the initial vAPP contrast level across the 2 - 15 λ/D upper dark hole with the WFS at focus. The red line denotes the control radius of the DM outside of which LDFC throws stellar speckles as it suppresses speckle formation within the control radius. Since this is a reference subtracted image,the colorbar does not represent dark hole contrast; the colorbar represents the log scale amplitude of the residual speckles to demonstrate their decay as the loop converges.

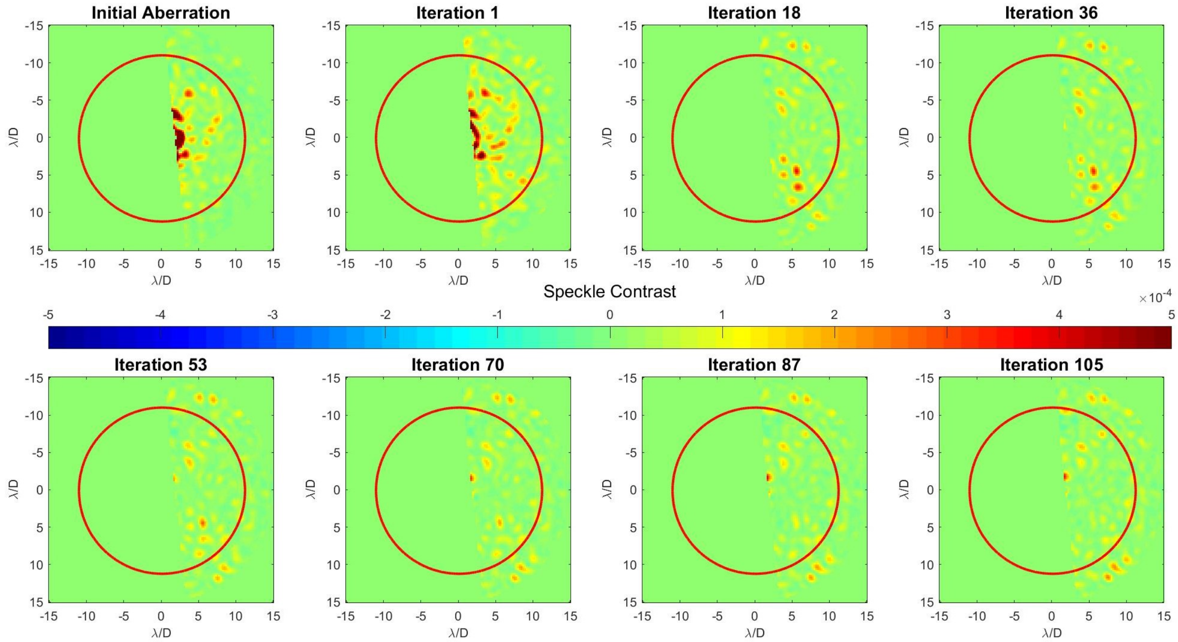

Figure 5.20: Simulated lower dark hole:Convergence back to the initial vAPP contrast level across the 2 - 15 λ/D lower dark hole. The red line denotes the control radius of the DM outside of which LDFC throws stellar speckles as it suppresses speckle formation within the control radius. Since this is a reference subtracted image,the colorbar does not represent dark hole contrast; the colorbar represents the log scale amplitude of the residual speckles to demonstrate their decay as the loop converges.

The second metric used in determining the stability of the LDFC loop is shown in fig 5.21. Here the open-loop RMS WFE of the aberration is plotted in red, and the RMS of residual WFE after correction is plotted in green. While there is variation in the corrected RMS WFE, it is still more stable than the aberrated wavefront.

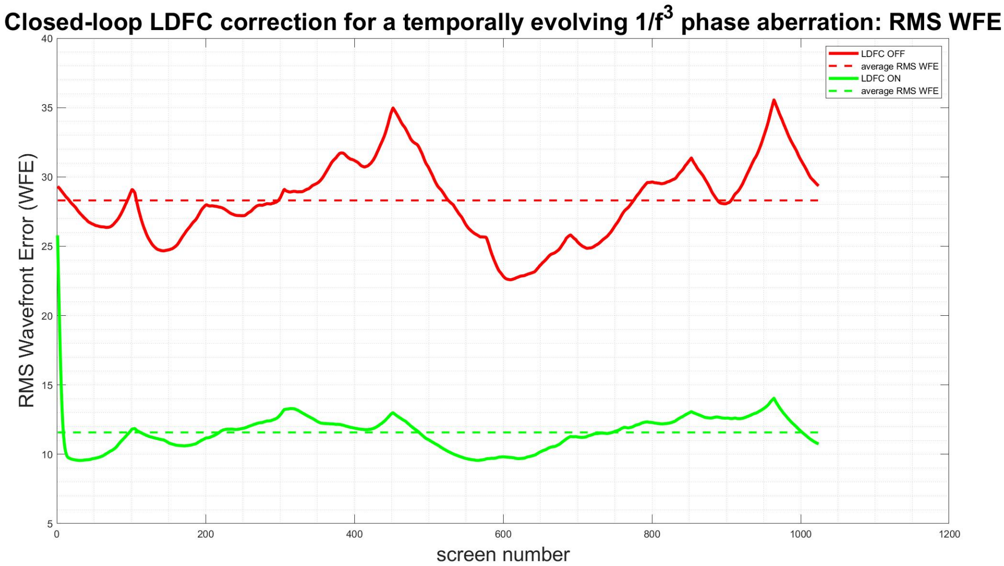

Figure 5.21: RMS WFE for a WFS at focus. Measurements on the y-axis are in nm.

5.2.1.2 Laboratory demonstration

In the lab, an aberration with a spatial PSD of $\frac{1}{k^2}$ was applied on the DM, and the loop was closed with 166 modes. It will be noticed here that only 300 iterations are shown instead of 1024 as seen in all other examples. This is because at approximately phase step 400, the loop diverged. This test was run again with only 100 modes in the response matrix, and the loop remained closed for the full 1024 screen phase sequence but with worse correction; fewer modes yielded less control of the full extent of the dark hole. The RMS WFE for each of these cases can be seen in fig 5.27.

The same aberration was applied multiple times with 166 mode correction, and the loop broke every time. This is most likely due to the presence of at least one "waffle" mode somewhere betwen mode 100 and 166. With more time, this mode could have been identified and removed from the response matrix. For the sake of showing its performance under stable conditions, the following results show the 300 phase steps over which the loop was stable with 166 modes. Dark hole contrast stabilization plots are shown in figs 5.22 - 5.24. Since both the aberration and correction are applied with the DM, both are limited to the 11 λ/D control radius. For this reason, the plots for the lab case shown here only extend to 11 λ/D.

As previously mentioned, in the lab, the initial dark hole contrast suffered due to aberrations induced by the optics; this also resulted in a variation in the initial dark hole contrast with the contrast at its worst near the PSF core. This can be seen in the following plots as the blue line that drifts downward for each successive λ/D bin. However, in each case, the correction remains better than the aberration until approximately 9 λ/D. At this point, the LDFC correction is still a slight improvement in comparison to the aberrated contrast. At 11 λ/D, the DM control radius is reached; given that the DM is used for both the aberration injection as well as the correction, the LDFC correction and aberration overlap at this point where the DM has limited effect.

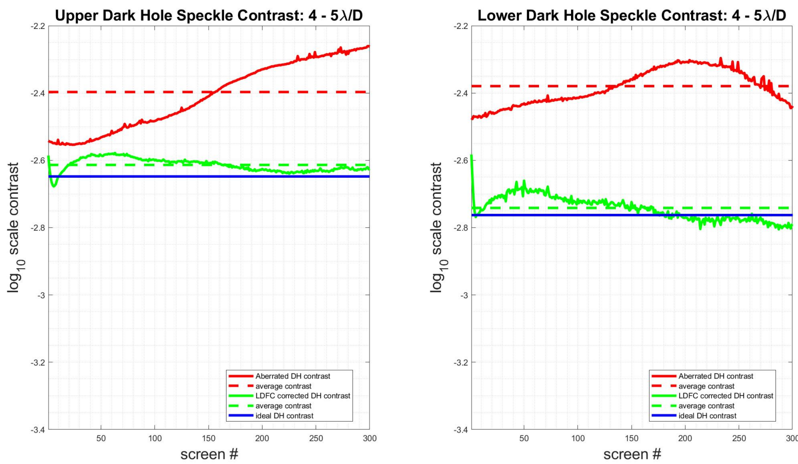

(a) 4 - 5 λ/D

Figure 5.22: Dark hole contrast stabilization across 4 - 5 λ/D with the WFS at focus

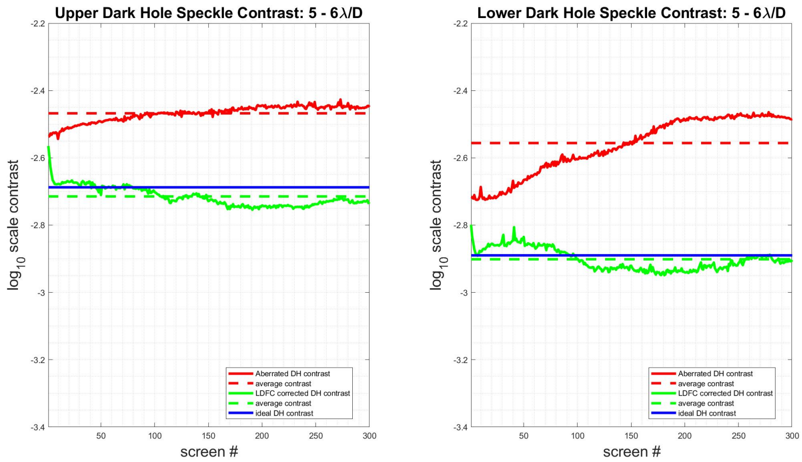

(a) 5 - 6 λ/D

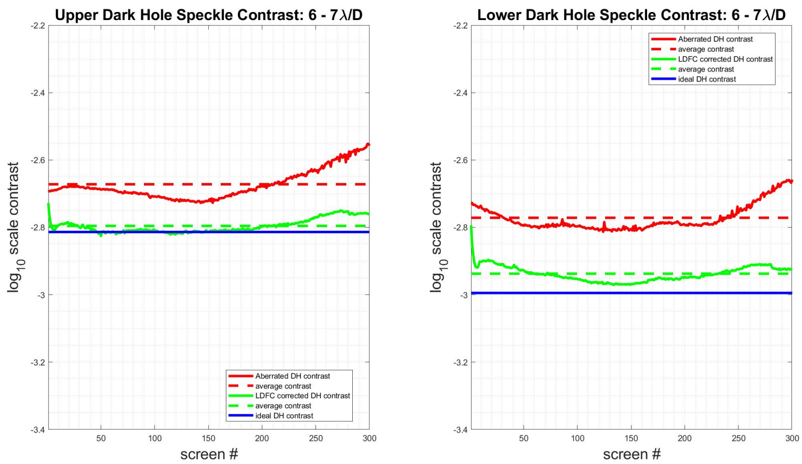

(b) 6 - 7 λ/D

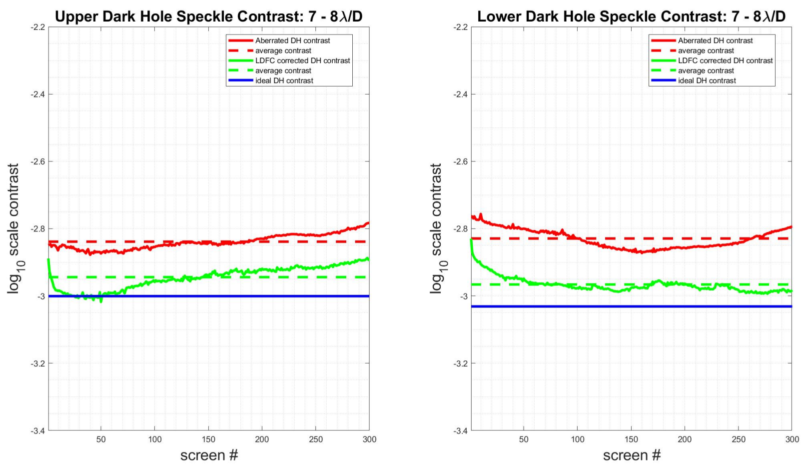

(c) 7 - 8 λ/D

Figure 5.23: Dark hole contrast stabilization across 5 - 8 λ/D with the WFS at focus

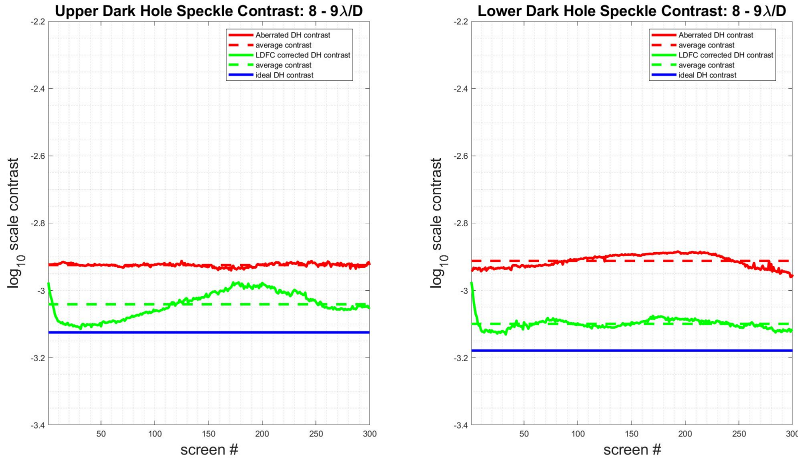

(a) 8 - 9 λ/D

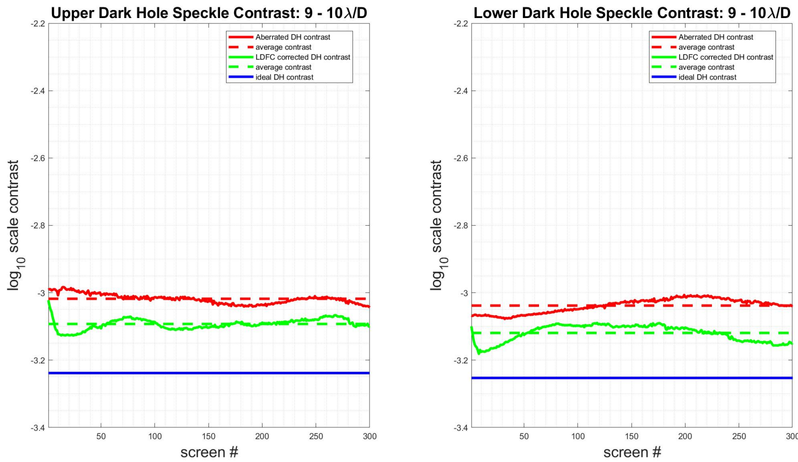

(b) 9 - 10 λ/D

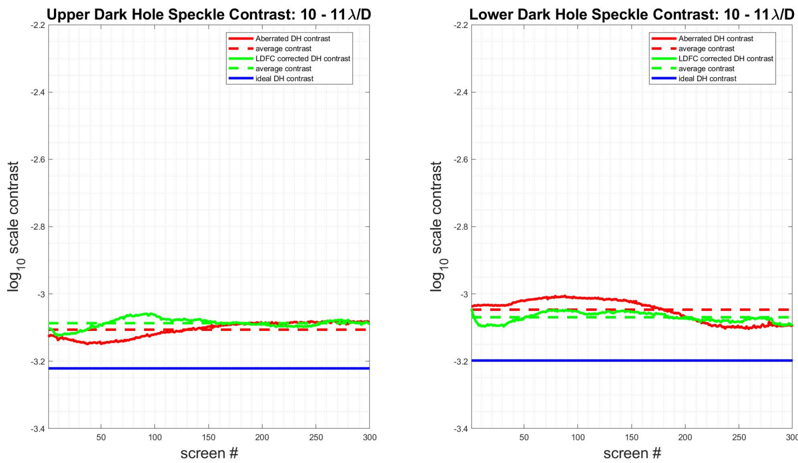

(c) 10 - 11 λ/D

Figure 5.24: Dark hole contrast stabilization across 8 - 11 λ/D with the WFS at focus.

The following two images display the upper (fig 5.25) and lower (fig 5.26) dark holes at 8 stages as LDFC converges, driving the dark hole contrast back to the initial unaberrated contrast. As in simulation, the images are reference subtracted and masked to only show the dark holes to make the speckle formation and suppression more visible. The red line denotes the 11 λ/D control radius beyond which the DM cannot control speckle formation. Since the DM was used both to suppress and create speckles in the lab, no speckles formed outside 11 λ/D in the lab demonstration.

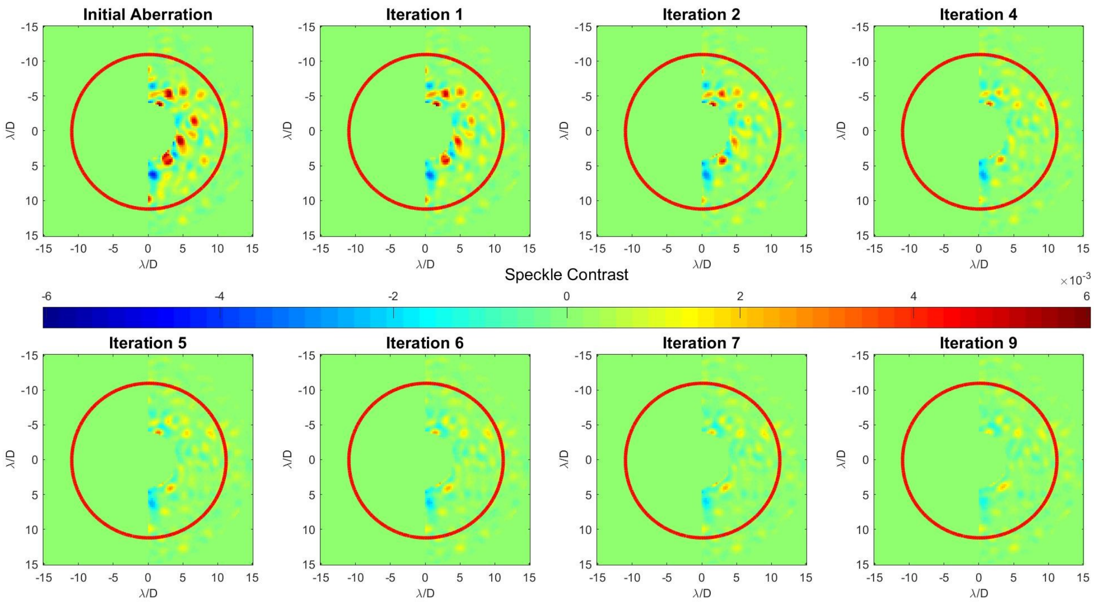

Figure 5.25: Lab upper dark hole:Convergence back to the initial vAPP contrast level across the 4 - 15 λ/D upper dark hole. The red line denotes the control radius of the DM outside of which LDFC throws stellar speckles as it suppresses speckle formation within the control radius. Since this is a reference subtracted image,the colorbar does not represent dark hole contrast; the colorbar represents the log scale amplitude of the residual speckles to demonstrate their decay as the loop converges.

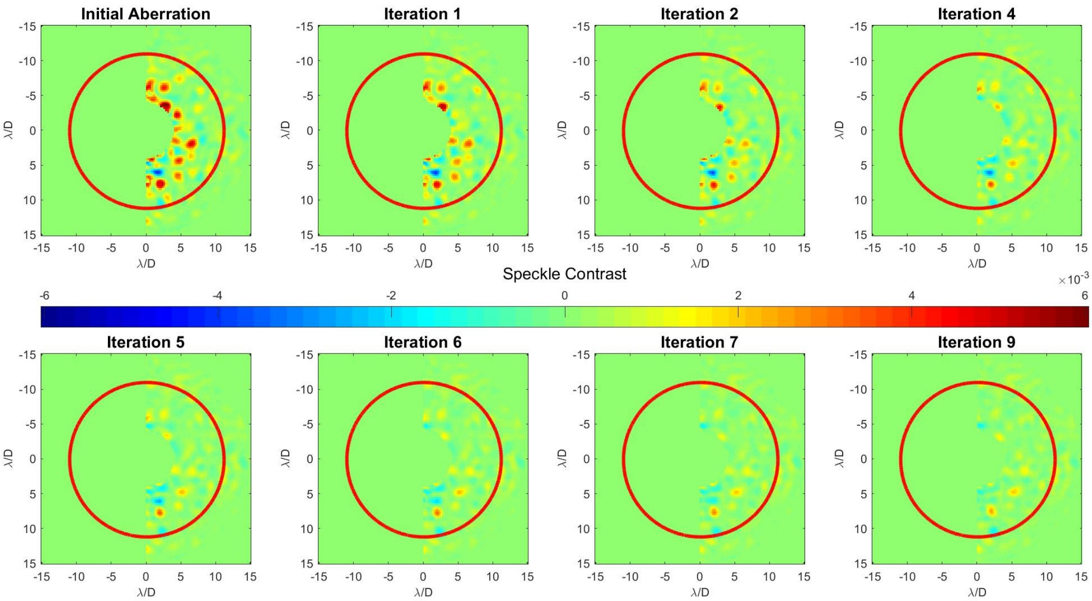

Figure 5.26: Lab lower dark hole:Convergence back to the initial vAPP contrast level across the 4 - 15 λ/D lower dark hole. The red line denotes the control radius of the DM outside of which LDFC throws stellar speckles as it suppresses speckle formation within the control radius. Since this is a reference subtracted image,the colorbar does not represent dark hole contrast; the colorbar represents the log scale amplitude of the residual speckles to demonstrate their decay as the loop converges.

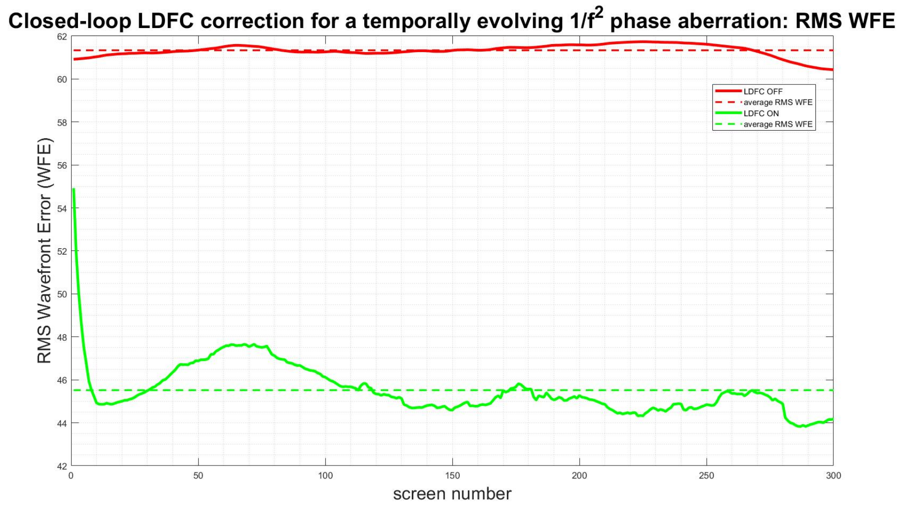

(a) RMS WFE with 166 mode correction for 300 phase screens

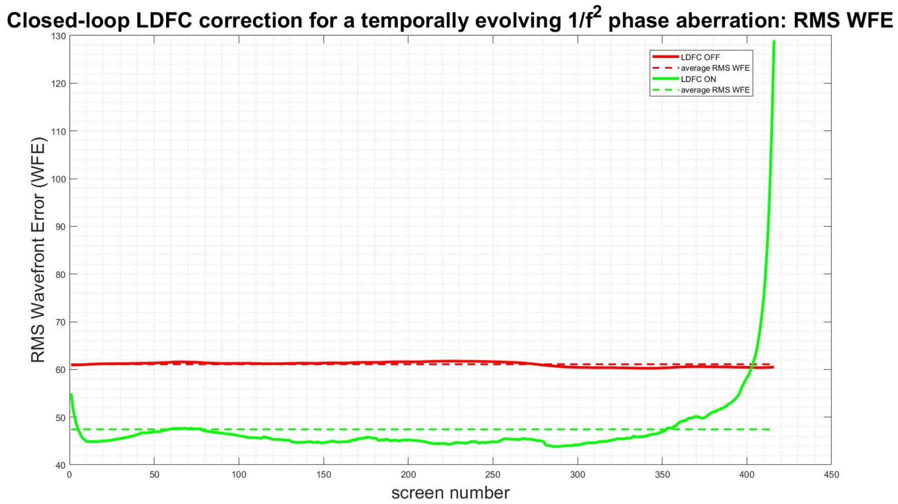

(b) RMS WFE with 166 mode correction for 416 phase screens showing the point at which the loop diverged

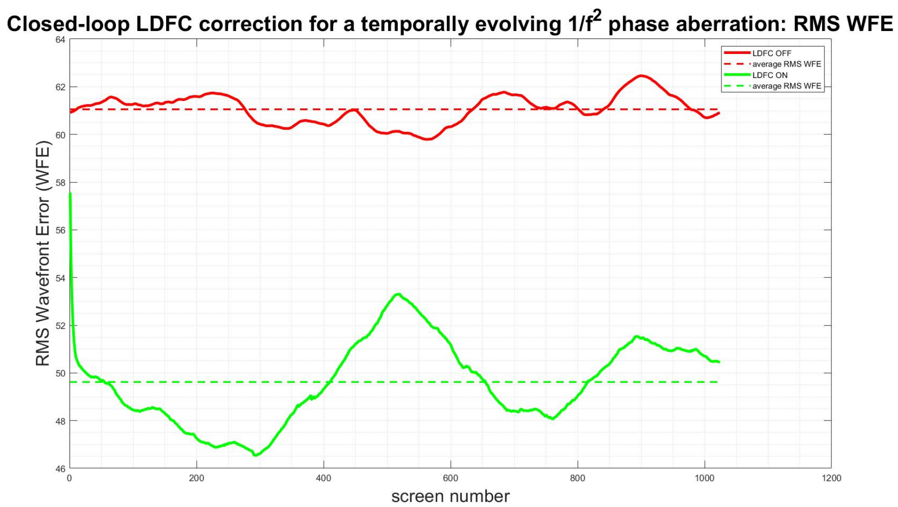

(c) RMS WFE with 100 mode correction

Figure 5.27: RMS WFE for a WFS at focus in the lab showing (a) the RMS WFE while stable with 166 modes, (b) the RMS WFE as the loop diverges, and (c) the stable correction for all 1024 phase steps with only 100 modes. Measurements on the y-axis are in nm.

5.2.2 Wavefront sensing with a defocused image

While using the science image at focus as the WFS is normally the ideal case for also making simultaneous science measurements, defocusing the image for use as the WFS is more advantageous. By defocusing the image, the sign ambiguity of even modes is removed. For example, if the WFS is at focus and the aberration itself is defocus, whether positive or negative, the response at the WFS will look the same; the PSF will grow in size and decrease in intensity. If the WFS is defocused (let's say in the positive direction) and the same defocus aberration is again applied, the positive and negative cases will no longer appear the same. If the defocus aberration is positive, the WFS response will be an even broader, dimmer PSF. If the defocus aberration is negative, the WFS PSF will move back toward focus and become smaller and brighter. In this way, we can now measure both the aberration amplitude as well as the sign of the aberration.

In simulation, a 200 nm amplitude defocus term was introduced into the pupil to produce a defocused image that corresponds to an approximately 2 mm shift from paraxial focus for the f/35 beam at the lab science camera. In the lab, two cameras were used: one with the science image at focus, and one at which the image was defocused by approximately 2mm to match the simulation case. This separation was achieved by placing a 50/50 dichroic beamsplitter right before focus. For the following defocused lab case, the second camera was used.

In simulation, the dynamic range of the pixels in the WFS was not limited as it was in the lab. For this reason, all bright pixels that responded monotonically to the positive and negative application of the modes in the response matrix were used in the simulated, defocused WFS. In the lab, the bright pixels near the PSF core still satured with exposure times that were required to be above the noise floor at the higher spatial frequencies; these pixels were subsequently removed from the response matrix in the lab case. The WFS regions used in the lab and in simulation are shown in fig 5.28.

(a) Pixels used in simulation (b) Pixels used in the lab

Figure 5.28: The bright field pixels used in the defocused WFS in simulation and in the lab

After SVD truncation, 173 modes were used to close the loop in the lab while the full 298 modes were used in simulation. The SVD curves for both cases are shown in fig 5.29.

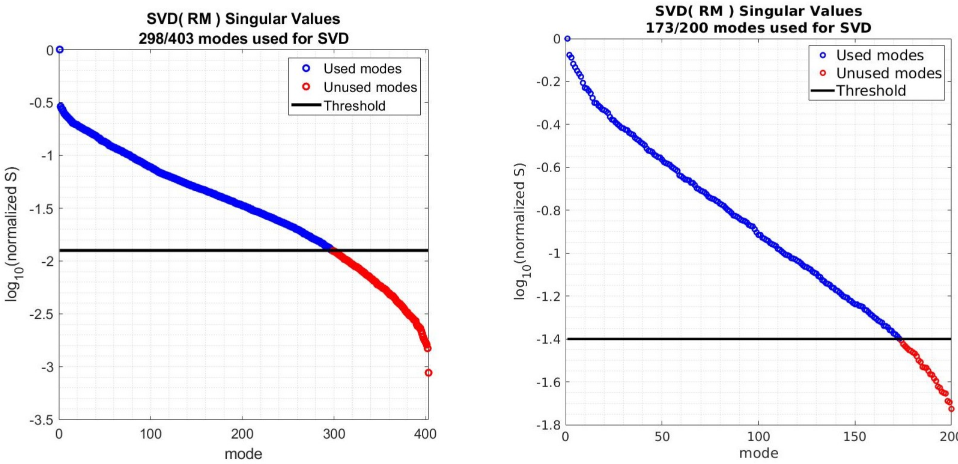

(a) SVD curve in simulation (b) SVD curve in the lab

Figure 5.29: The SVD curves for the inversion of the response used in the defocused WFS in simulation and in the lab. After truncation, 298 modes were used in simulation and 173 in the lab.

The results for tests both in simulation and in the lab are shown below.

5.2.2.1 Simulation

The injected aberration here has a spatial PSD of $\frac{1}{k^2}$ (see fig 5.7a). As for the simulated at focus case, the loop here was closed using 298 modes in the response matrix. Again, fig 5.30 displays a single time step showing what is occuring in the pupil plane and science image plane simultaneously. It shows the injected aberration, LDFC correction applied to the DM, and the residual WFE after the correction is applied as well as the aberrated (open-loop) dark hole, the closed-loop LDFC corrected dark hole, and the ideal, unaberrated dark hole for comparison.

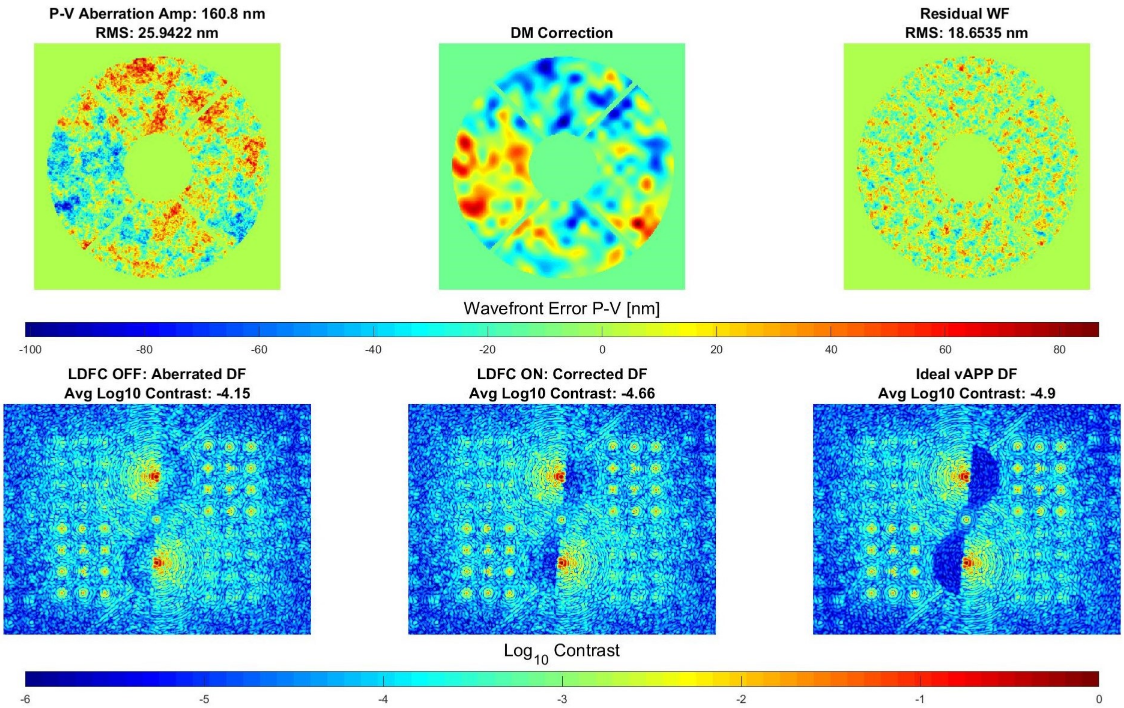

Figure 5.30: Simulation: Single frame taken with LDFC running in closed-loop. Displayed in the top row is the injected pupil plane phase aberration, the LDFC-derived correction applied on the DM, and the residual wavefront error. In the bottom row is shown the aberrated PSFs with speckles thrown into the dark hole, the LDFC-corrected PSFs, and the ideal unaberrated vAPP PSFs for comparison.

Since this aberration in simulation generates speckle across the full extent of the dark hole, it is interesting to see what happens in the dark hole at the control radius of the DM. In fig 5.30, in the center image in the bottom row, the extent of the DM correction is visibly obvious in the dark hole between 11 and 15 λ/D. This speckle formation is most likely again due to the Gibbs phenomenon.

Beyond the control radius at 11 λ/D the DM is incapable of correcting any aberration-induced speckles, and instead forces light within the control radius out to higher spatial frequencies. The "turnover" point, where LDFC no longer corrects the aberration, is obvious in fig 5.33 where the correction begins to degrade as the control radius is reached. After 11 λ/D, the LDFC correction degrades the contrast more than the initial aberration.

Figs 5.31 - 5.34 show LDFC's performance across the full dark hole in the same 1 λ/D bins as in the at focus case. Figs 5.35 and 5.36 display the upper and lower dark holes at 8 stages as LDFC converges, driving the dark hole contrast back to the initial unaberrated contrast. Fig 5.37 shows the stabilization of the RMS WFE in the pupil.

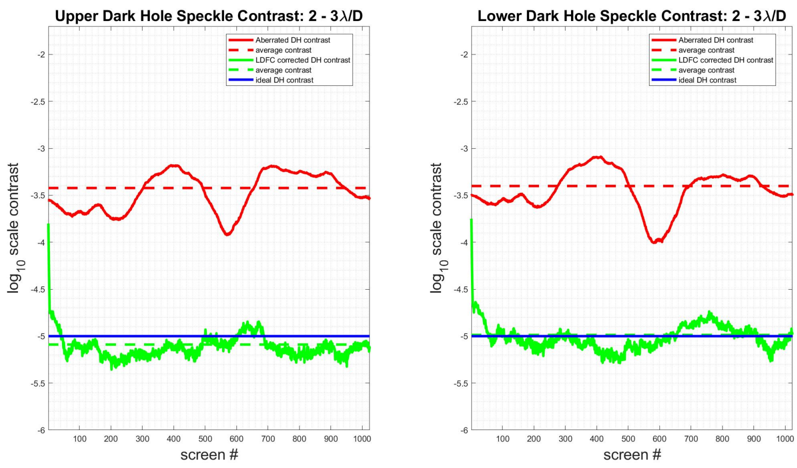

(a) 2 - 3 λ/D

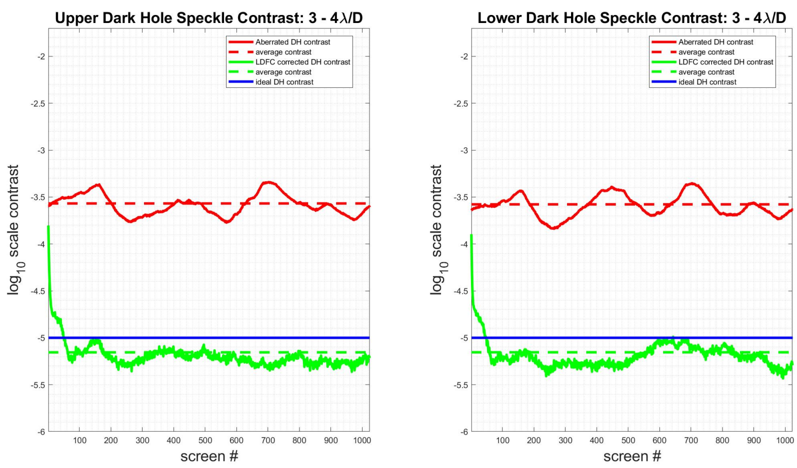

(b) 3 - 4 λ/D

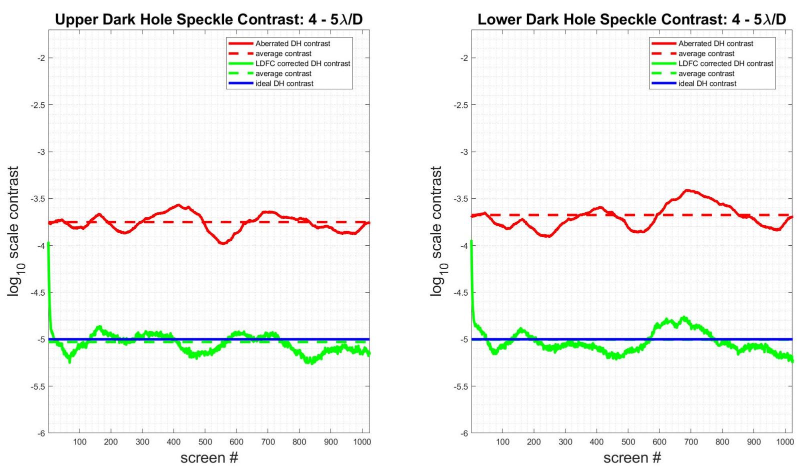

(c) 4 - 5 λ/D

Figure 5.31: Simulation: Contrast stabilization within 1 λ/D hemispherical bins across 2 - 5 λ/D within the dark hole over a series of 1024 temporally correlated $\frac{1}{f^4}$ phase screens.

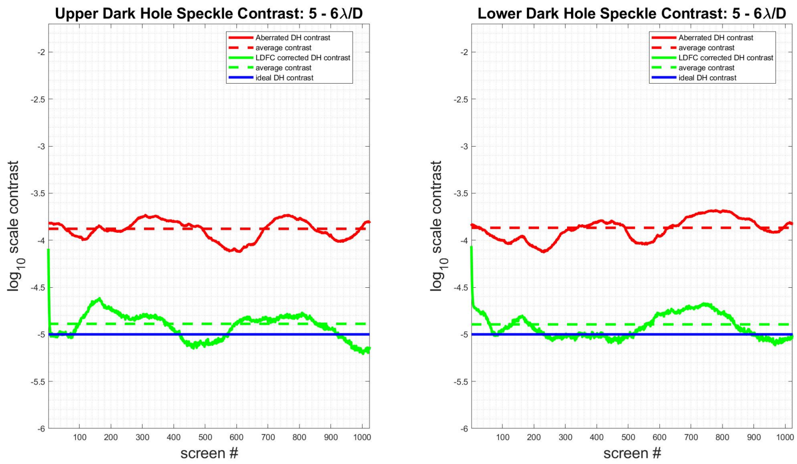

(a) 5 - 6 λ/D

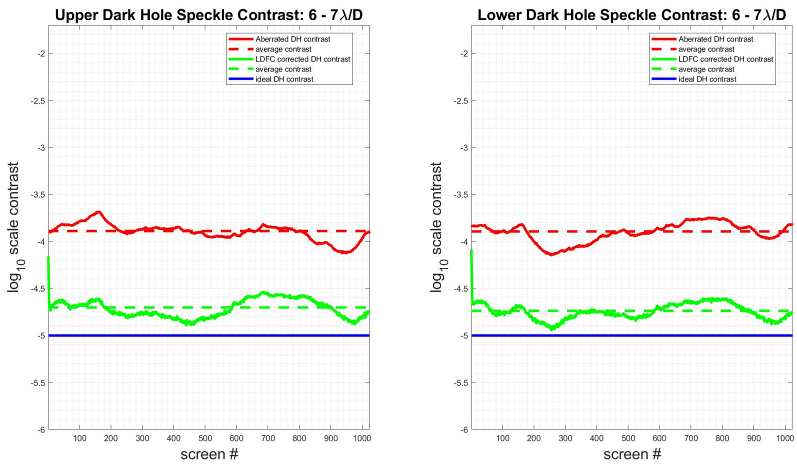

(b) 6 - 7 λ/D

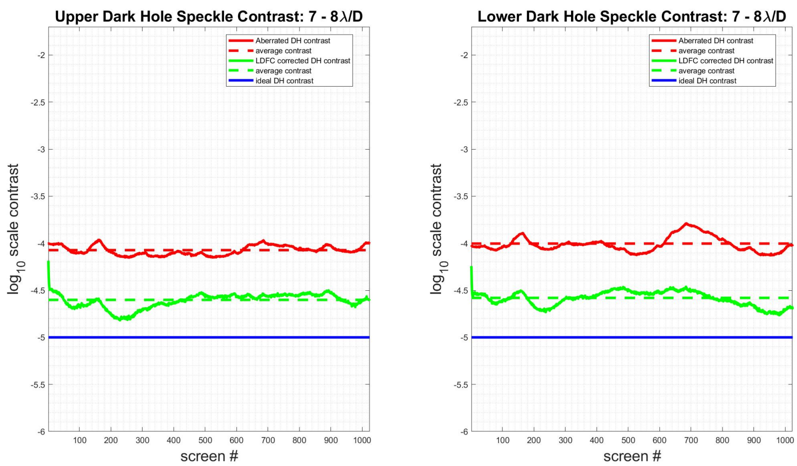

(c) 7 - 8 λ/D

Figure 5.32: Simulation: Contrast stabilization within 1 λ/D hemispherical bins across 5-8 λ/D within the dark hole over a series of 1024 temporally correlated $\frac{1}{f^4}$ phase screens.

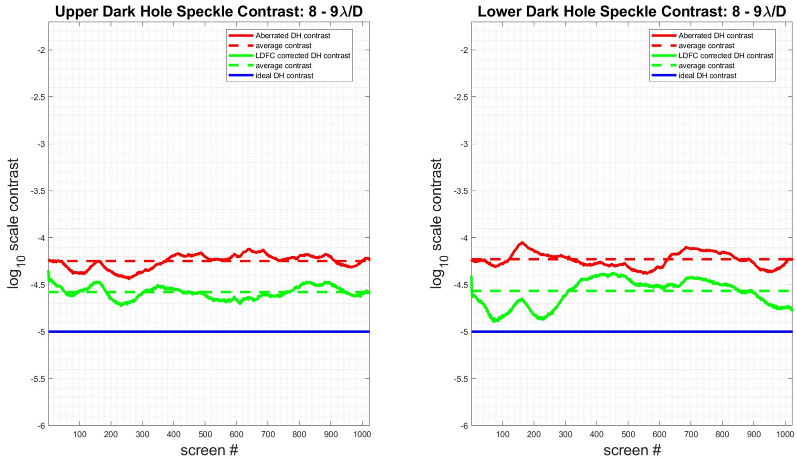

(a) 8 - 9 λ/D

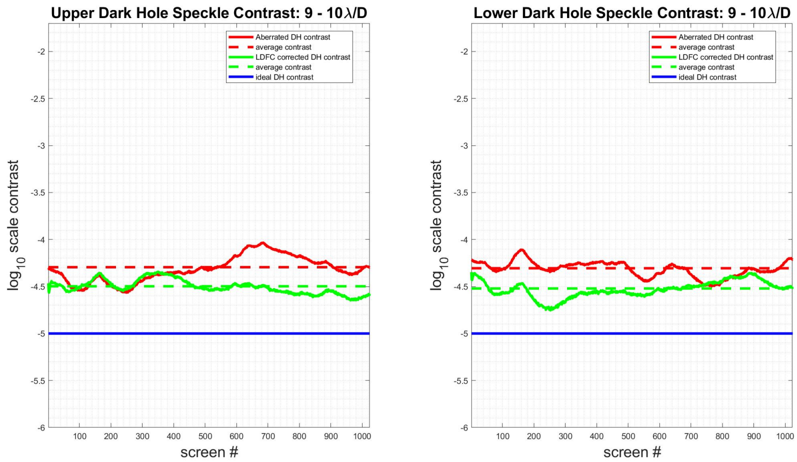

(b) 9 - 10 λ/D

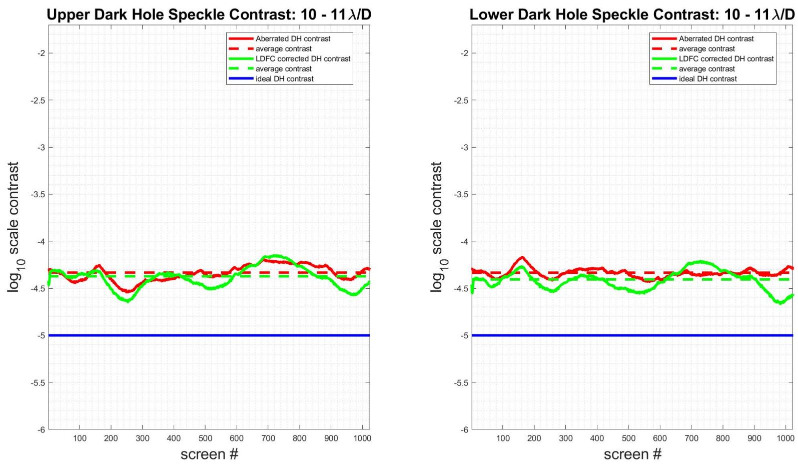

(c) 10 - 11 λ/D

Figure 5.33: Simulation: Contrast stabilization within 1 λ/D hemispherical bins across 8 - 11 λ/D within the dark hole over a series of 1024 temporally correlated $\frac{1}{f^4}$ phase screens.

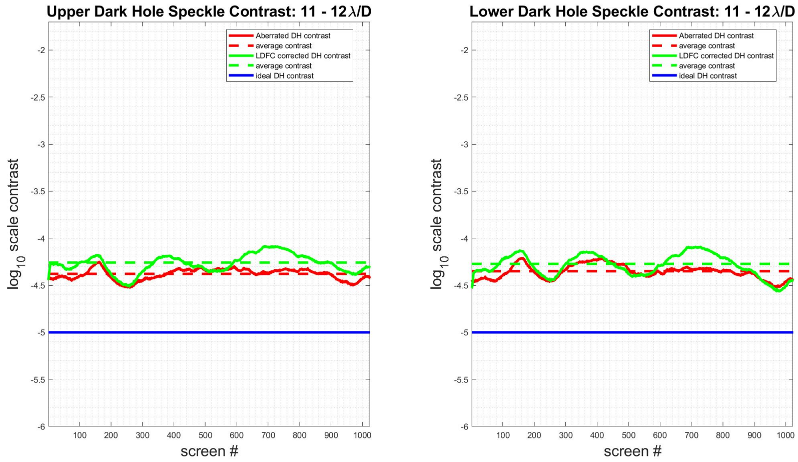

(a) 11 - 12 λ/D

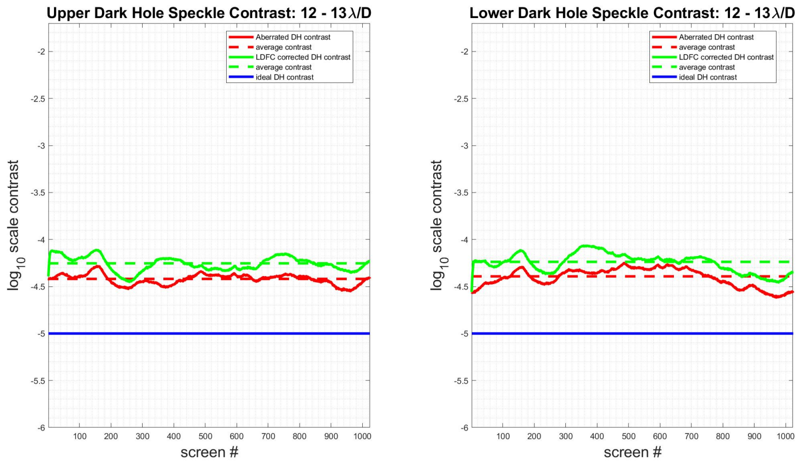

(b) 12 - 13 λ/D

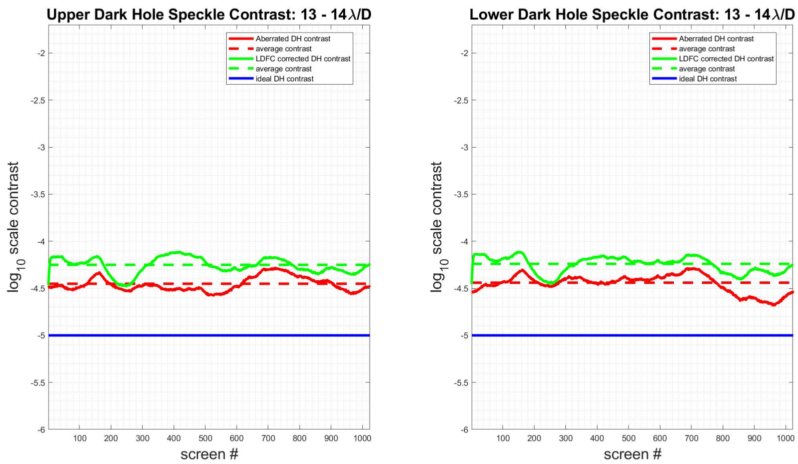

(c) 13 - 14 λ/D

Figure 5.34: Simulation: Contrast stabilization within 1 λ/D hemispherical bins across 11 - 14 λ/D within the dark hole over a series of 1024 temporally correlated $\frac{1}{f^4}$ phase screens.

The images in figs 5.35 and 5.36 are reference subtracted and masked to only show the dark holes to make the speckle formation and suppression more visible. The red line denotes the 11 λ/D control radius beyond which the DM cannot control speckle formation. Here, the spatial extent controlled by LDFC become very obvious. While LDFC suppresses speckle formation and stabilizes the contrast within the control radius, outside 11 λ/D, speckles form due to the residual wavefront errors that are left uncorrected.

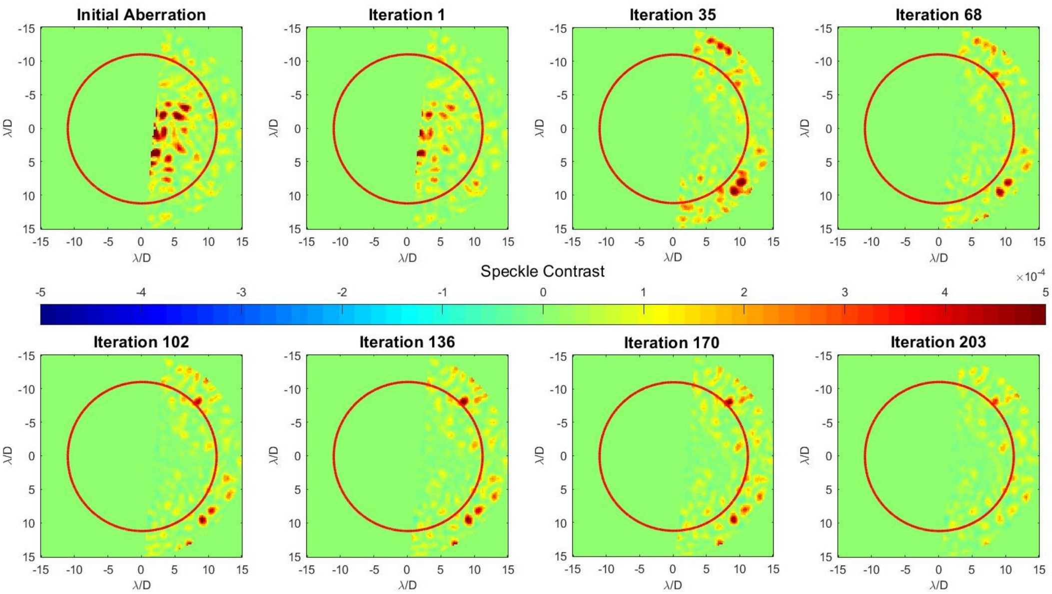

Figure 5.35: Simulated upper dark hole:Convergence back to the initial vAPP contrast level across the 2 - 15 λ/D upper dark hole with the WFS defocused. The red line denotes the control radius of the DM outside of which LDFC throws stellar speckles as it suppresses speckle formation within the control radius. Since this is a reference subtracted image,the colorbar does not represent dark hole contrast; the colorbar represents the log scale amplitude of the residual speckles to demonstrate their decay as the loop converges.

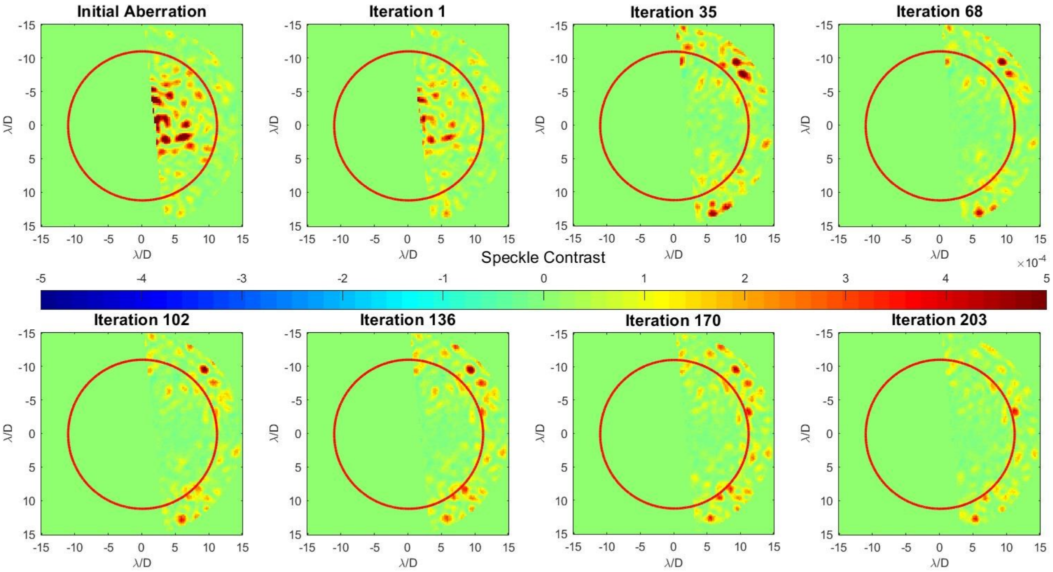

Figure 5.36: Simulated lower dark hole:Convergence back to the initial vAPP contrast level across the 2 - 15 λ/D lower dark hole. The red line denotes the control radius of the DM outside of which LDFC throws stellar speckles as it suppresses speckle formation within the control radius. Since this is a reference subtracted image,the colorbar does not represent dark hole contrast; the colorbar represents the log scale amplitude of the residual speckles to demonstrate their decay as the loop converges.

Figure 5.37: RMS WFE for a defocused WFS. Measurements on the y-axis are in nm.

5.2.2.2 Laboratory demonstration

As with the at focus lab case, an aberration with a spatial PSD of $\frac{1}{k^2}$ was applied on the DM, and the loop was closed with 166 modes. Also previously mentioned, the initial dark hole contrast in the lab suffered due to aberrations induced by the optics; this also resulted in a variation in the initial dark hole contrast with the contrast at its worst near the PSF core. This can be seen in the following plots as the blue line that drifts downward for each successive λ/D bin.

In figs 5.38 - 5.40 , it should be noted that LDFC returns the dark hole to the initial contrast in each bin as well - seen as the green line converges back to the initial blue line or close to it. Also worthy of note is the stabilization of the green LDFC-corrected contrast curve with respect to the red aberrated contrast curve. Out to approximately 9 λ/D, the LDFC correction remains stable without significant oscillation as seen in the aberrated contrast curve. The correction degenerates slightly after 9 λ/D as the DM's control radius is reached. At this point, the LDFC correction is still an improvement in comparison to the aberrated contrast, but there is more variation in the corrected contrast. This is due to higher frequency residual errors that go unsensed or at least uncorrected by the DM which throw speckles out toward the edge of the DM control radius.

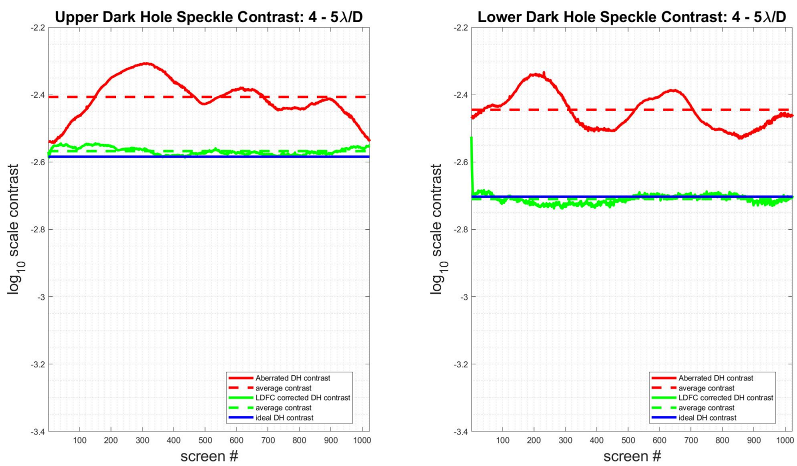

(a) 4 - 5 λ/D

Figure 5.38: Dark hole contrast stabilization across 4 - 5 λ/D with the WFS defocused.

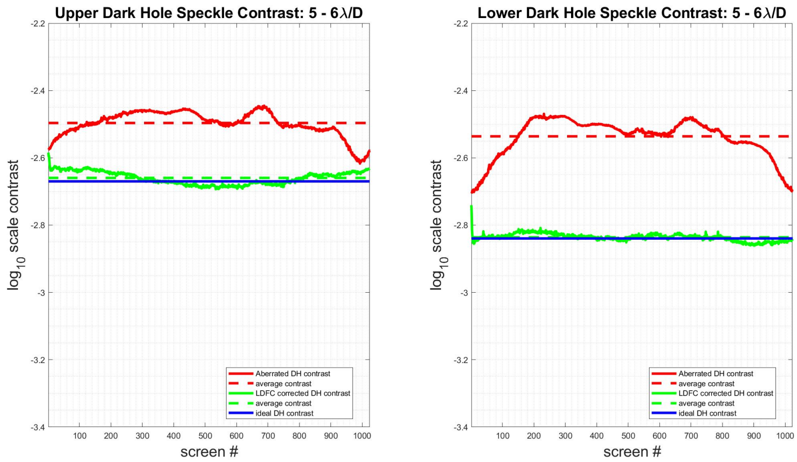

(a) 5 - 6 λ/D

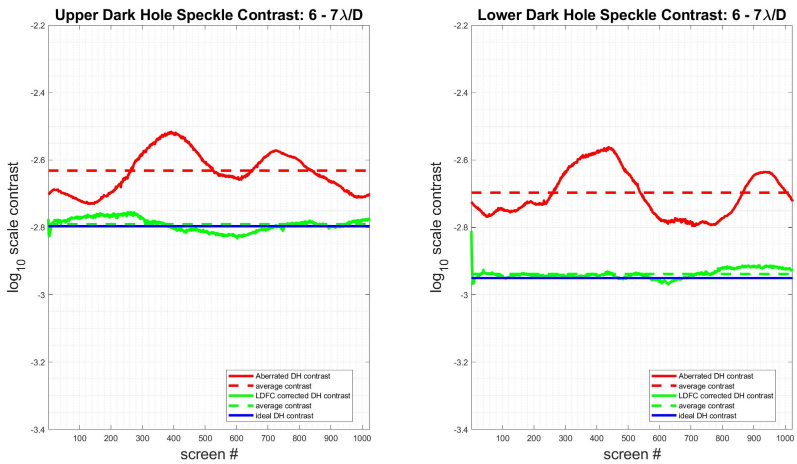

(b) 6 - 7 λ/D

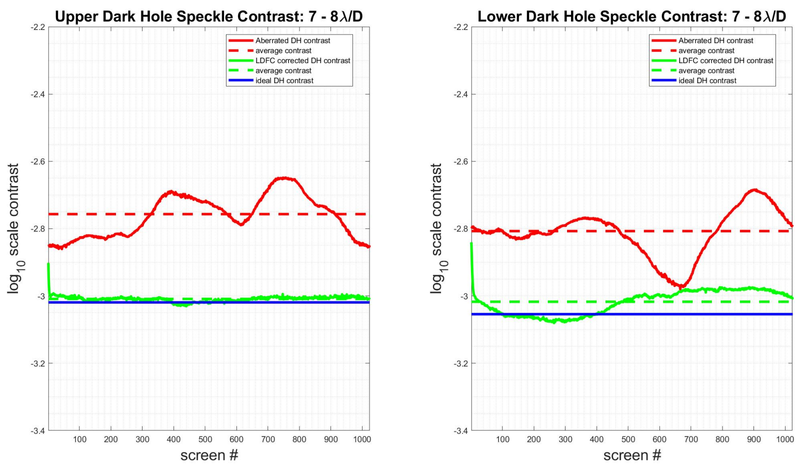

(c) 7 - 8 λ/D

Figure 5.39: Dark hole contrast stabilization across 5 - 8 λ/D with the WFS defocused.

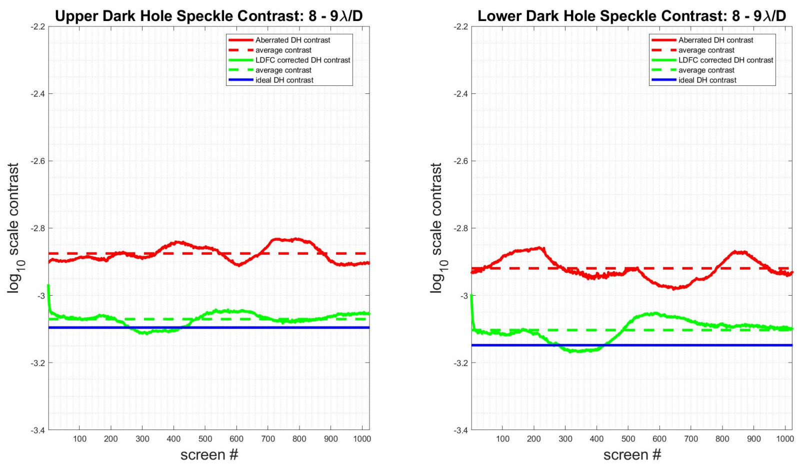

(a) 8 - 9 λ/D

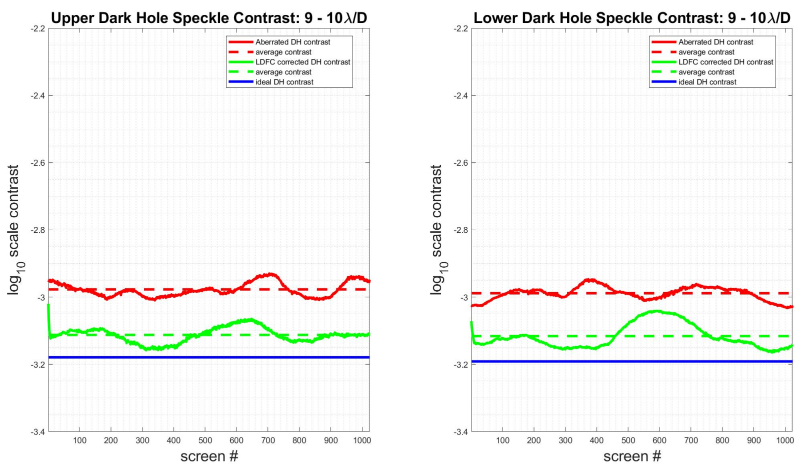

(b) 9 - 10 λ/D

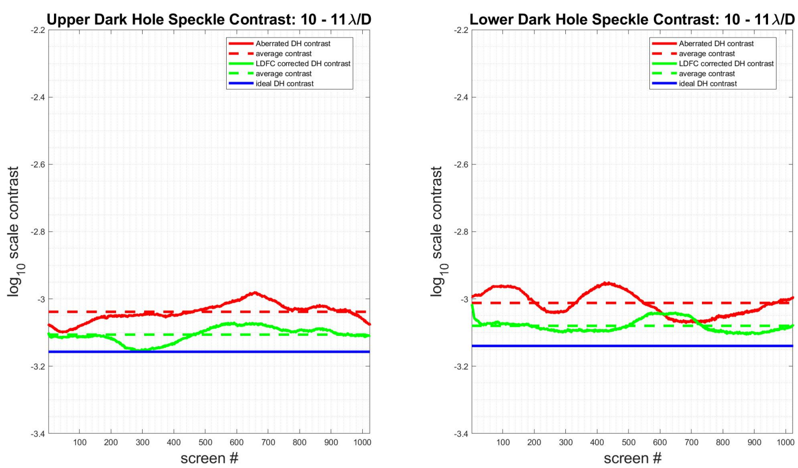

(c) 8 - 11 λ/D

Figure 5.40: Dark hole contrast stabilization across 8 - 11 λ/D with the WFS defocused.

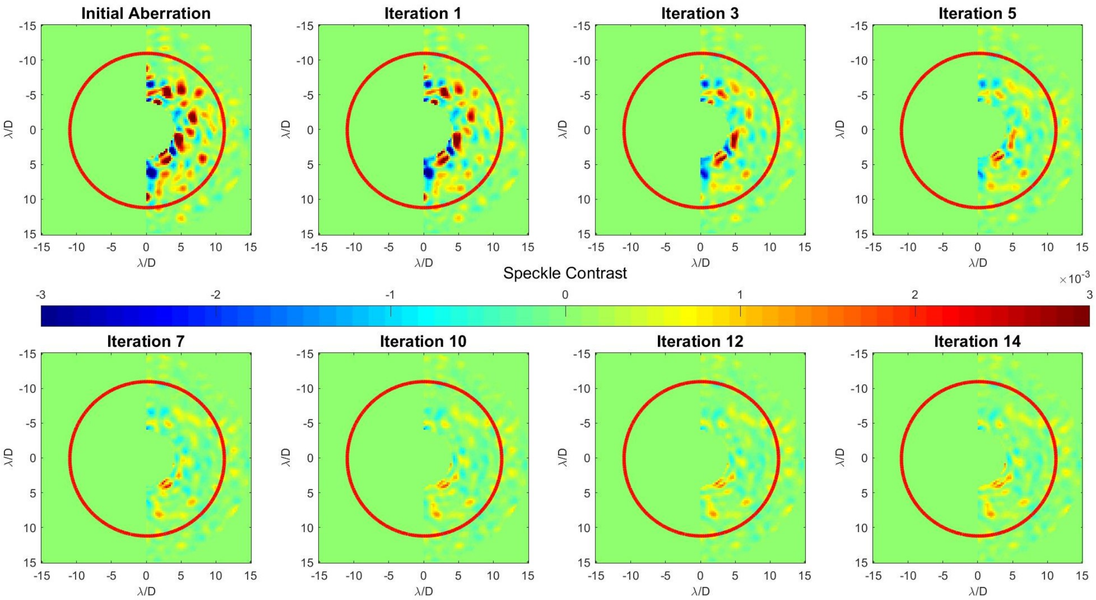

Figure 5.41: Lab upper dark hole:Convergence back to the initial vAPP contrast level across the 4 - 15 λ/D upper dark hole. The red line denotes the control radius of the DM outside of which LDFC throws stellar speckles as it suppresses speckle formation within the control radius. Since this is a reference subtracted image,the colorbar does not represent dark hole contrast; the colorbar represents the log scale amplitude of the residual speckles to demonstrate their decay as the loop converges.

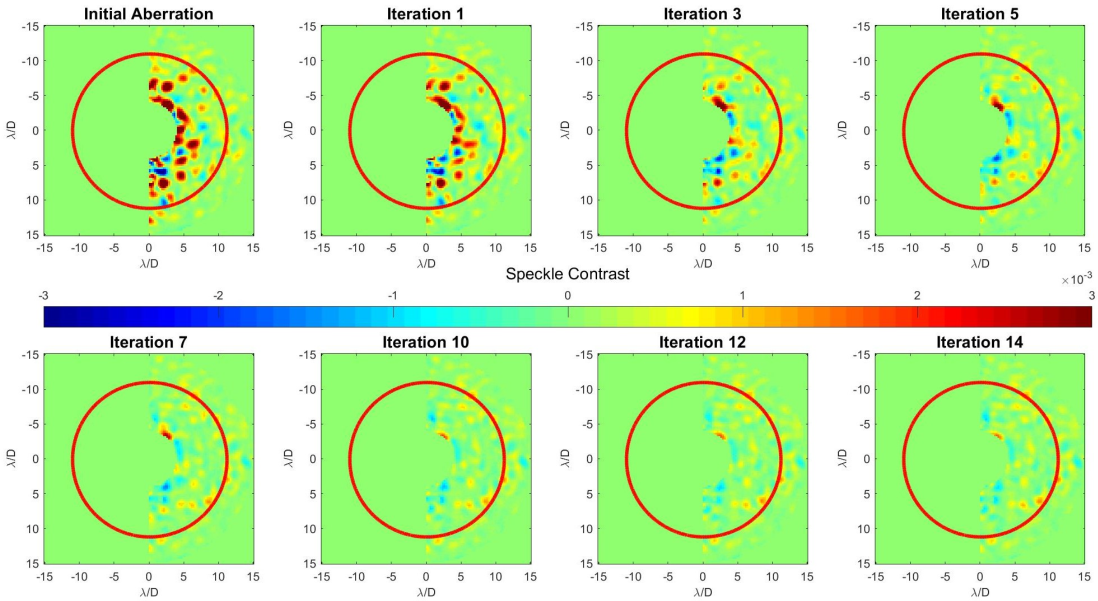

Figure 5.42: Lab lower dark hole:Convergence back to the initial vAPP contrast level across the 4 - 15 λ/D lower dark hole. The red line denotes the control radius of the DM outside of which LDFC throws stellar speckles as it suppresses speckle formation within the control radius. Since this is a reference subtracted image,the colorbar does not represent dark hole contrast; the colorbar represents the log scale amplitude of the residual speckles to demonstrate their decay as the loop converges.

Figure 5.43: RMS WFE for a defocused WFS in the lab. Measurements on the y-axis are in nm.

5.2.3 Wavefront sensing with a planet present

The ultimate goal for LDFC is to maintain the dark hole contrast while observing an exoplanet within the dark hole. However, there may be cases with a single-sided dark hole where the planet falls in the bright field outside of the dark hole and is therefore included in the WFS region. With a vAPP coronagraph, if the planet is in the dark hole in one PSF image, it is in the bright field in the other PSF. This means that, when using the bright field for both PSFs as part of the WFS as was done in simulation for the above cases, the planet image is also in the WFS. This is the case if the response matrix is taken on sky, which would be challenging. To take a reference image and response matrix on sky would require high stability in the image; this means that the main WFS (in most cases a Pyramid WFS), would have to be running simultaneously to maintain the image quality and stability. When applying the modes on the DM to build the LDFC response matrix, the Pyramid WFS will see these modes as well and try to correct them. This means that the commands would have to be sent to the Pyramid WFS as offsets to keep it from registering these modes and attempting correction. This may prove to not be a simple task. Another option would be to build the response matrix with a laser source in a lab environment. The following case explores what happens to LDFC's ability to stabilize the contrast in this scenario when using a defocused WFS.

An aberration was injected into the pupil with a temporal PSD of $\frac{1}{f^4}$ to model atmospheric turbulence and a $\frac{1}{k^2}$ spatial PSD to create speckles across the full dark hole. A planet with a contrast of 10^{-3} was placed at 5 λ/D away from the stellar PSF. The reference image was then taken and the response matrix built; both therefore contained some signal from the planet. Both PSFs were again used as the WFS, and the bright field pixels used in the response matrix were the same as seen in fig 5.28a. Unlike the previous defocused WFS case, this simulation was run with photon noise with a 5^{th} magnitude at 1 kHz. The results are ordered below as in all previous cases.

In fig 5.44, the planet is hidden underneath a halo of speckles in the left image; in the center image where LDFC is running in closed-loop, the planet can be clearly seen in the dark hole of the upper PSF.

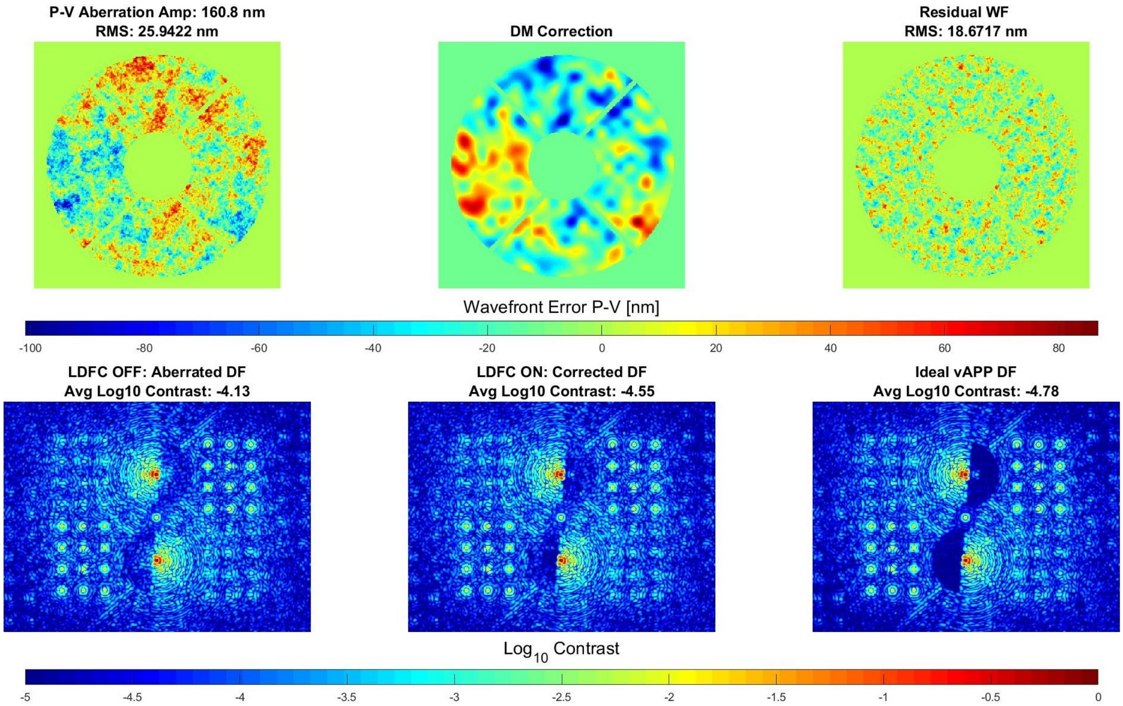

Figure 5.44: Simulation: Single frame taken with LDFC running in closed-loop. Displayed in the top row is the injected pupil plane phase aberration, the LDFC-derived correction applied on the DM, and the residual wavefront error. In the bottom row is shown the aberrated PSFs with speckles thrown into the dark hole, the LDFC-corrected PSFs, and the ideal unaberrated vAPP PSFs for comparison.

The following figs 5.45 - 5.48 show that LDFC's performance does not degrade with the presence of a planet in the bright field when both the response matrix and reference image contain the planet in the bright field as well. LDFC still stabilizes the contrast near the initial contrast out to the DM control radius. The plots for the upper dark hole where the planet is located appear slightly different from previous simulation cases as the planet itself was included in the contrast calculation.

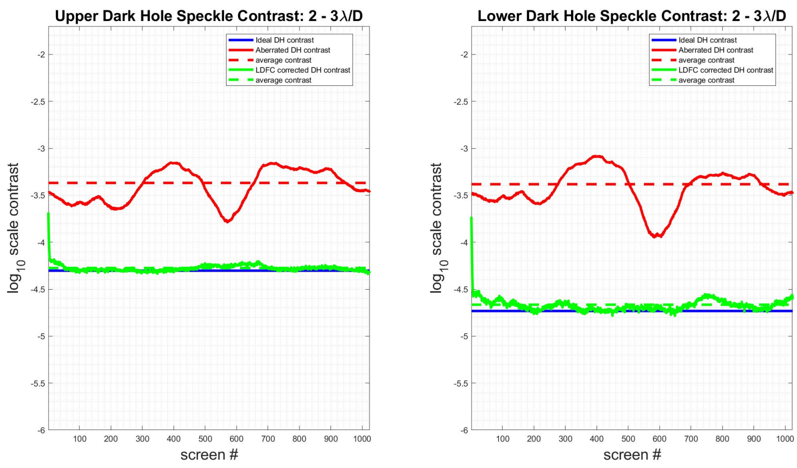

(a) 2 - 3 λ/D

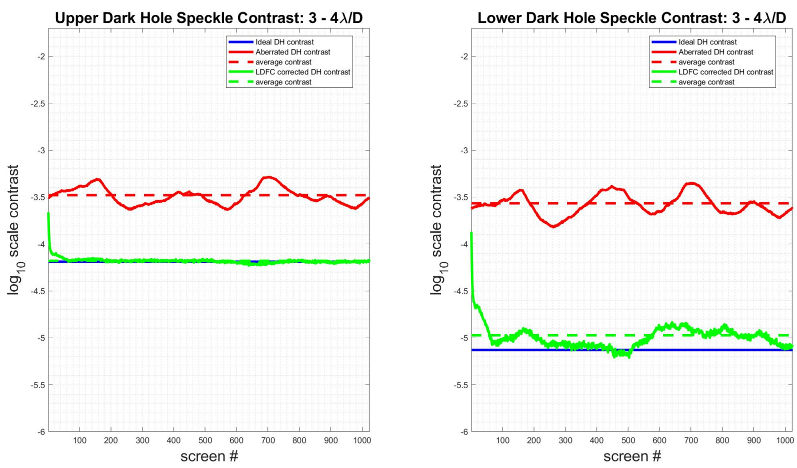

(b) 3 - 4 λ/D

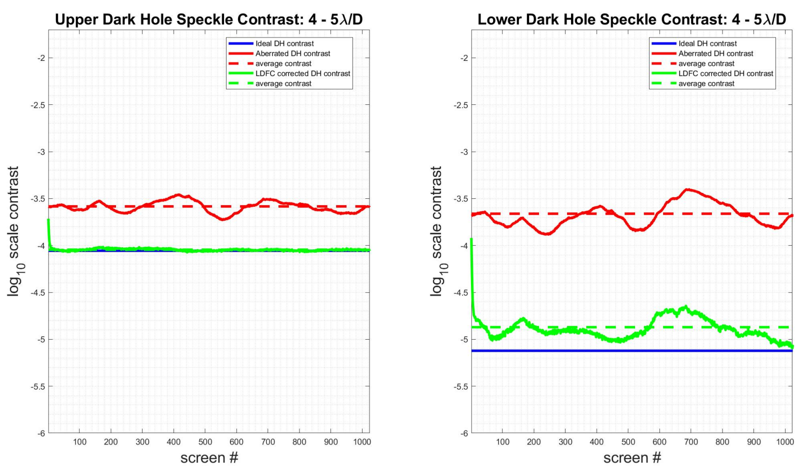

(c) 4 - 5 λ/D

Figure 5.45: Simulation with a planet in the bright field: Contrast stabilization within 1 λ/D hemispherical bins across 2 - 5 λ/D within the dark hole over a series of 1024 temporally correlated $\frac{1}{f^4}$ phase screens.

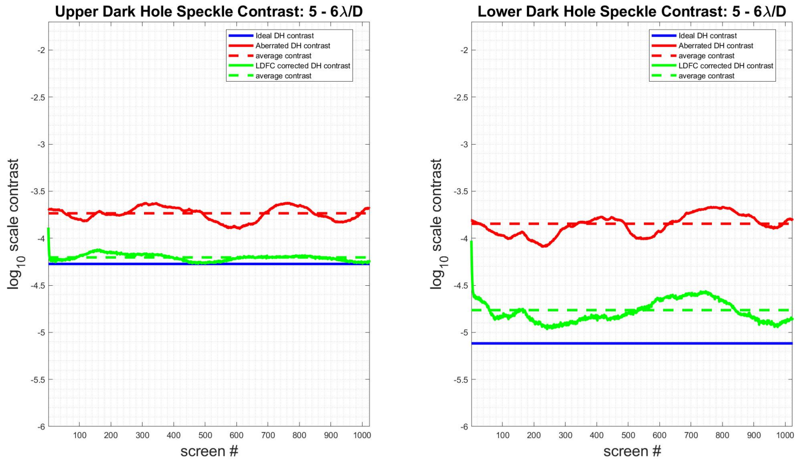

(a) 5 - 6 λ/D

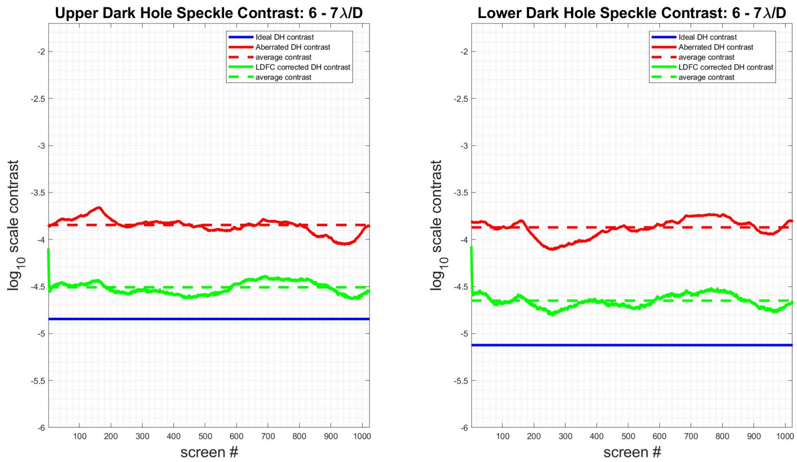

(b) 6 - 7 λ/D

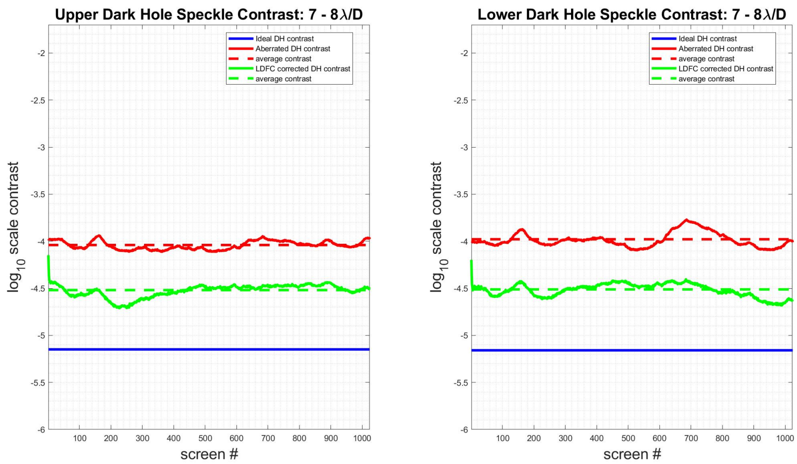

(c) 7 - 8 λ/D

Figure 5.46: Simulation with a planet in the bright field: Contrast stabilization within 1 λ/D hemispherical bins across 5 - 8 λ/D within the dark hole over a series of 1024 temporally correlated $\frac{1}{f^4}$ phase screens.

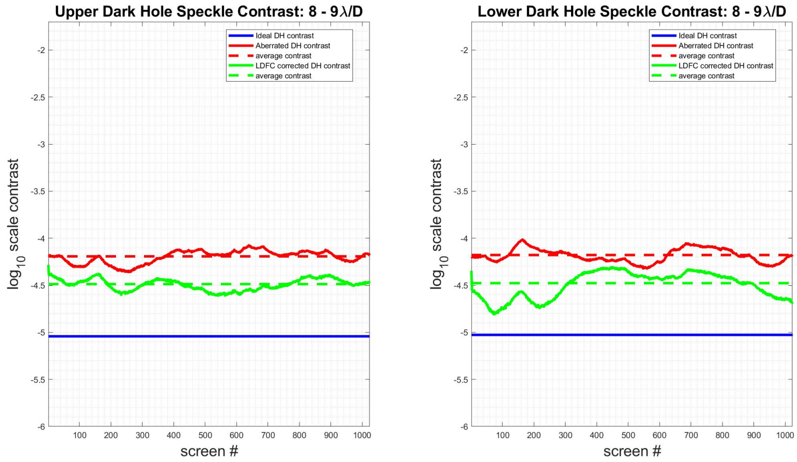

(a) 8 - 9 λ/D

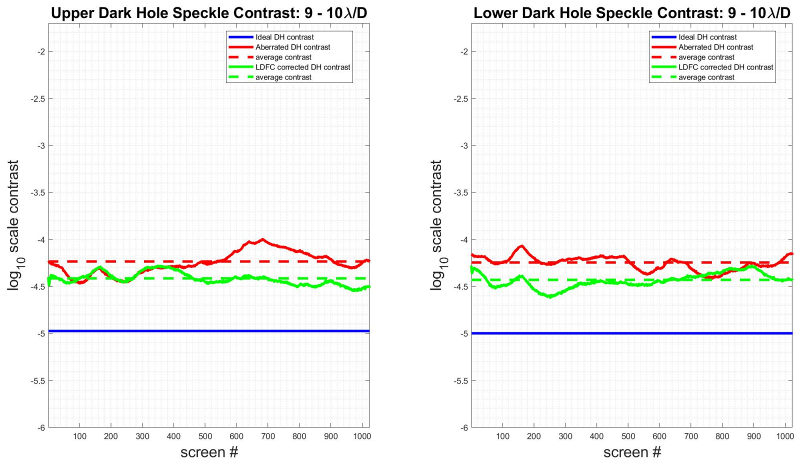

(b) 9 - 10 λ/D

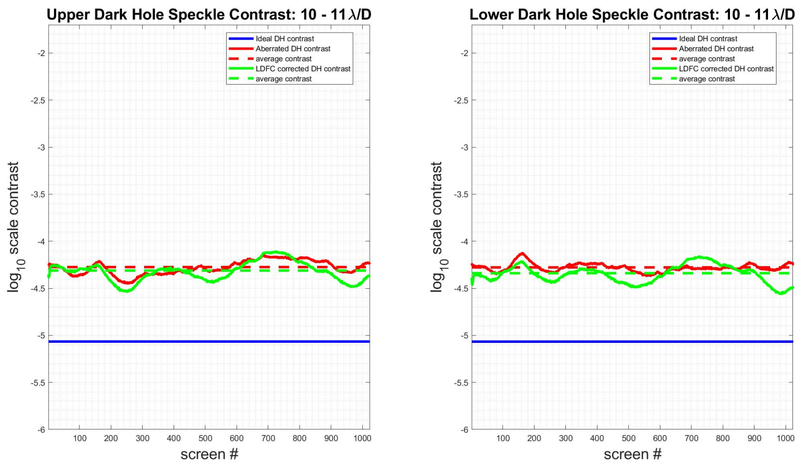

(c) 10 - 11 λ/D

Figure 5.47: Simulation with a planet in the bright field: Contrast stabilization within 1 λ/D hemispherical bins across 8 - 11 λ/D within the dark hole over a series of 1024 temporally correlated $\frac{1}{f^4}$ phase screens.

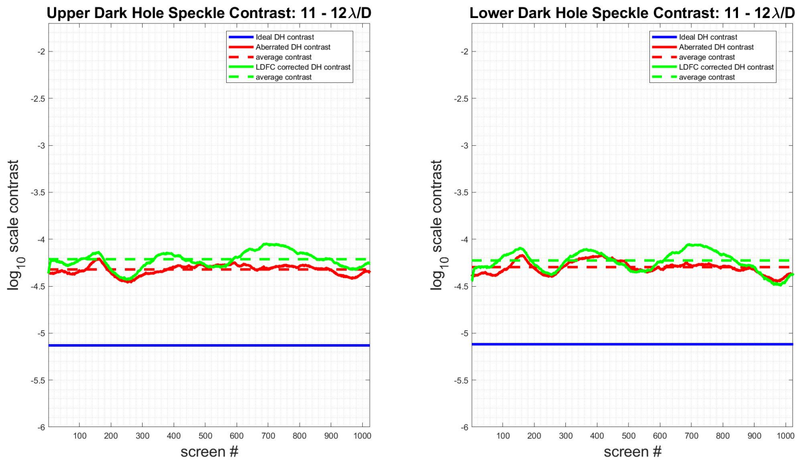

(a) 11 - 12 λ/D

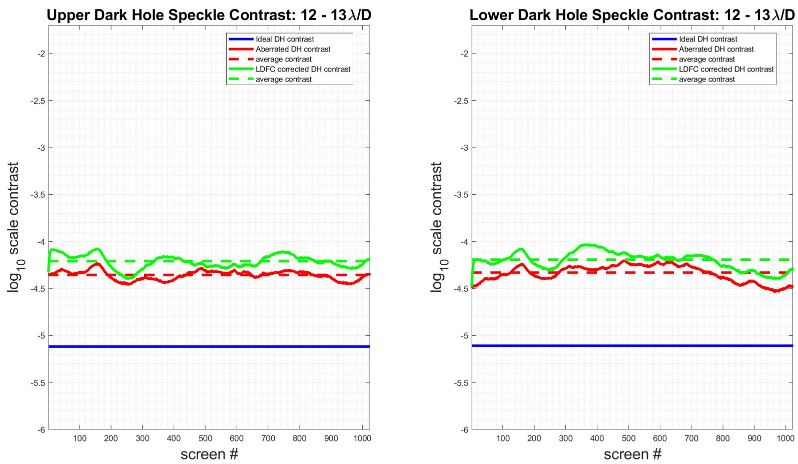

(b) 12 - 13 λ/D

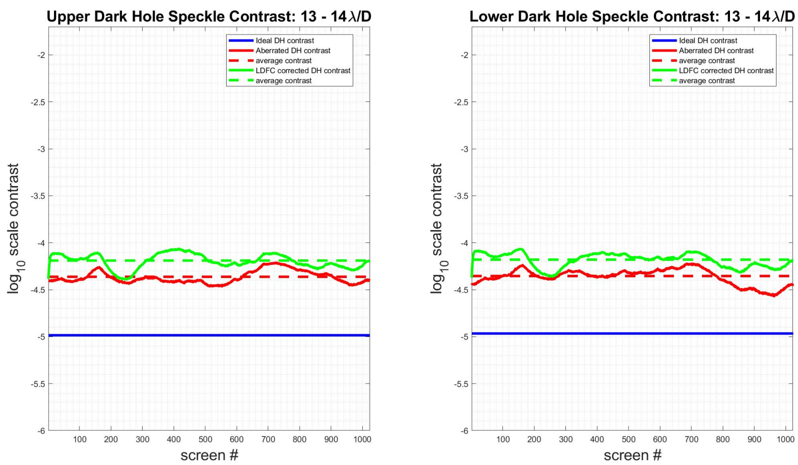

(c) 13 - 14 λ/D

Figure 5.48: Simulation with a planet in the bright field: Contrast stabilization within 1 λ/D hemispherical bins across 11 - 14 λ/D within the dark hole over a series of 1024 temporally correlated $\frac{1}{f^4}$ phase screens.

Figs 5.49 and fig 5.50 again respectively display the upper and lower dark holes at 8 stages as LDFC converges, driving the dark hole contrast back to the initial unaberrated contrast. Since the reference used in this test contains the planet, the images shown here are reference subtracted by a noiseless, unaberrated reference that does not contain the planet to allow for it to be visible in the LDFC-corrected dark hole.

The lower dark hole ref 5.50 in appears the same as in previous cases, but in fig 5.49, the planet becomes visible by frame 37 as LDFC converges. Once LDFC coverges, the dark hole contrast stabilizes, and the speckles remain suppressed throughout the rest of the phase sequence, allowing the planet light to remain above the speckle floor.

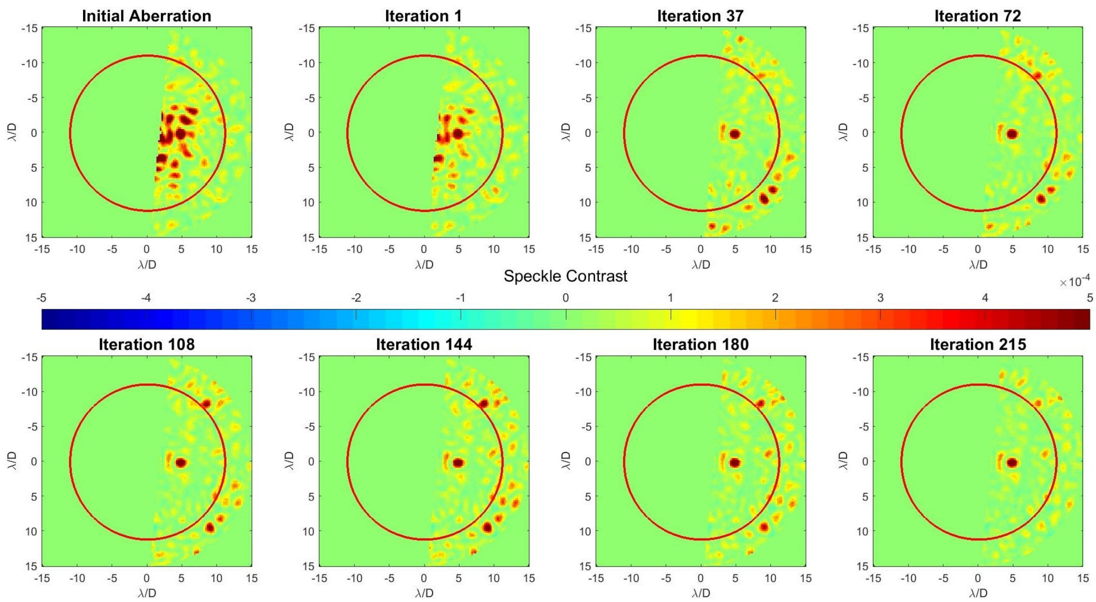

Figure 5.49: Proof that LDFC works! Simulated upper dark hole: Convergence back to the initial vAPP contrast level across the 2 - 15 λ/D upper dark hole with the WFS defocused. The planet becomes clearly visible above the speckles by frame 37 and remains visible throughout the remainder of the sequence. This shows that LDFC is able to maintain the dark hole contrast and suppress speckle formation out to the control radius of the DM, thereby keeping the planet visible in the presence of a temporally evolving phase aberration. It also shows that the response matrix is not adversely affected by the presence of the planet in one of the bright fields used in the WFS. The colorbar represents the log scale amplitude of the planet and the residual speckles to demonstrate their decay as the loop converges.

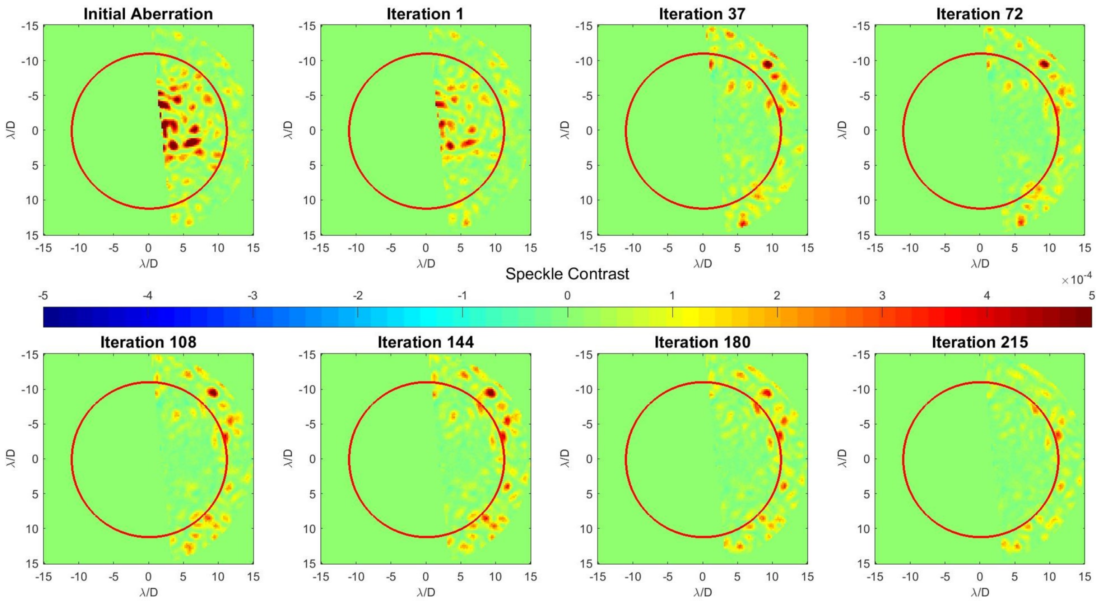

Figure 5.50: Simulated lower dark hole:Convergence back to the initial vAPP contrast level across the 2 - 15 λ/D lower dark hole. The red line denotes the control radius of the DM outside of which LDFC throws stellar speckles as it suppresses speckle formation within the control radius. Since this is a reference subtracted image,the colorbar does not represent dark hole contrast; the colorbar represents the log scale amplitude of the residual speckles to demonstrate their decay as the loop converges.

The RMS WFE in closed-loop compared to open-loop, again showing that LDFC is able to maintain the correction for an aberration with a $\frac{1}{f^4}$ temporal PSD in the presence of photon noise and with a planet in the bright field.

Figure 5.51: RMS WFE for a defocused WFS with a planet. Measurements on the y-axis are in nm.

This simulation specifically explored the case in which the planet was present in both the reference image and the response matrix. It also used both PSFs in the WFS which was defocused. Other cases were also explored in which the planet was not present in either the reference or the response matrix. With the WFS defocused, the very faint signal from the planet was disseminated across many pixels, making its contribution very small. Therefore the algorithm performance did not vary depending on whether or not the planet was present in the response matrix. When the planet was not present in the reference image, however, LDFC did not perform quite as well. However, using both PSFs as the WFS made the algorithm more immune to the absence of the planet in the reference than when using only PSF as the WFS. It should also be kept in mind that the planet in this simulation is roughly 6 magnitudes brighter than any terrestrial planet we expect to find at visible wavelengths; a fainter planet would have even less impact on the reference image and response matrix than the one shown in this simulation.

5.2.4 Performance in non-atmospheric turbulence

For completion, LDFC was also tested under non-atmospheric turbulent conditions represented by phase sequences with temporal PSDs given by $\frac{1}{f^3}$ and $\frac{1}{f^2}$. These cases are less temporally correlated and more representative of noise sources like telescope jitter.

In the case of $\frac{1}{f^3}$ turbulence, LDFC still converged in noiseless conditions as shown in figs 5.52 - 5.57.

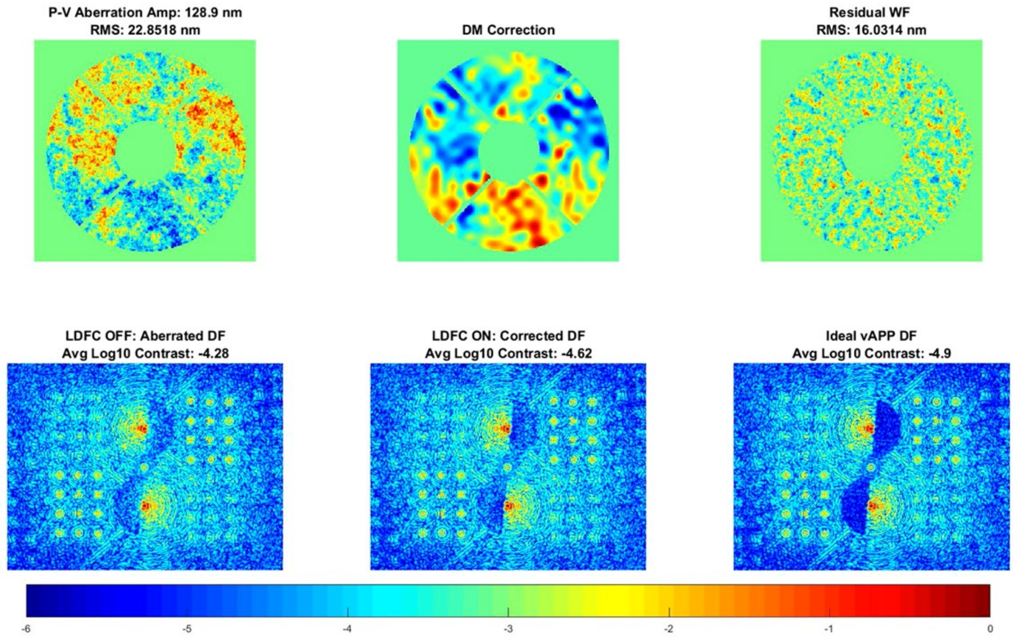

Figure 5.52: Simulation: Single frame taken with LDFC running in closed-loop. Displayed in the top row is the injected pupil plane phase aberration, the LDFC-derived correction applied on the DM, and the residual wavefront error. In the bottom row is shown the aberrated PSFs with speckles thrown into the dark hole, the LDFC-corrected PSFs, and the ideal unaberrated vAPP PSFs for comparison.

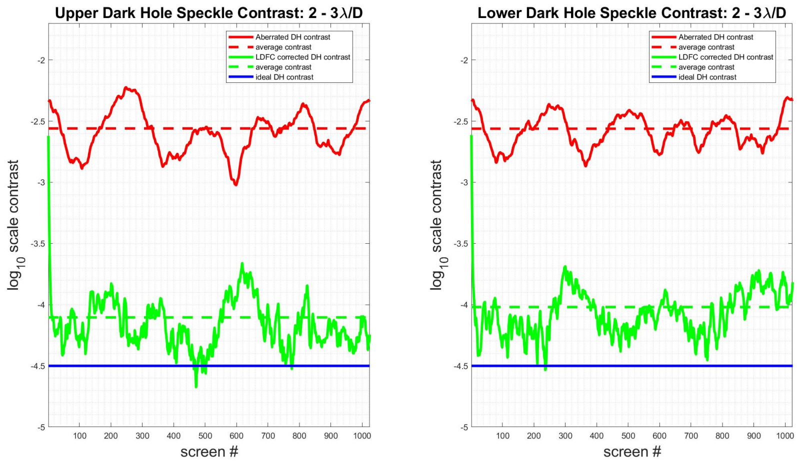

(a) 2 - 3 λ/D

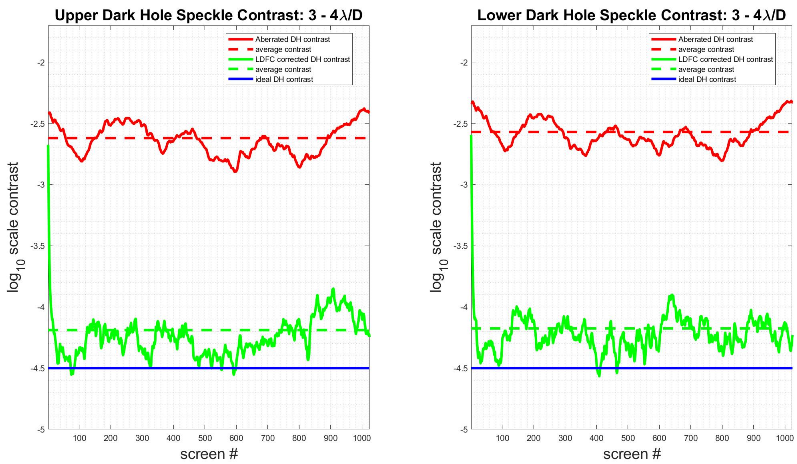

(b) 3 - 4 λ/D

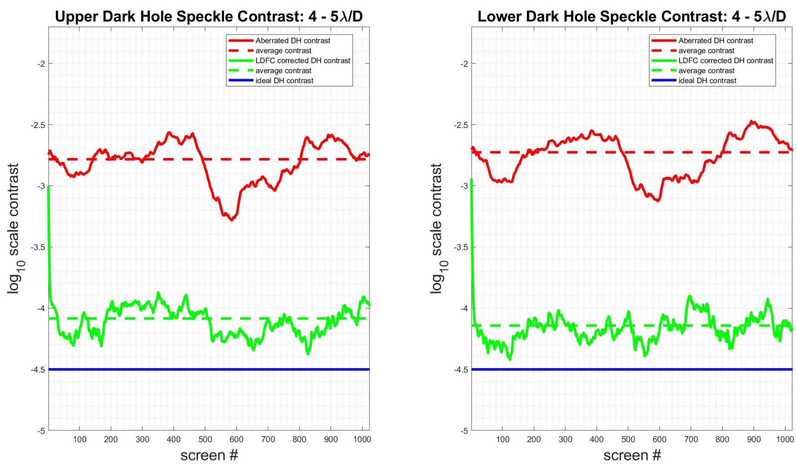

(c) 4 - 5 λ/D

Figure 5.53: Simulation with a $\frac{1}{f^3}$ temporal PSD: Contrast stabilization within 1 λ/D hemispherical bins across 2 - 5 λ/D within the dark hole over a series of 1024 temporally correlated $\frac{1}{f^4}$ phase screens.

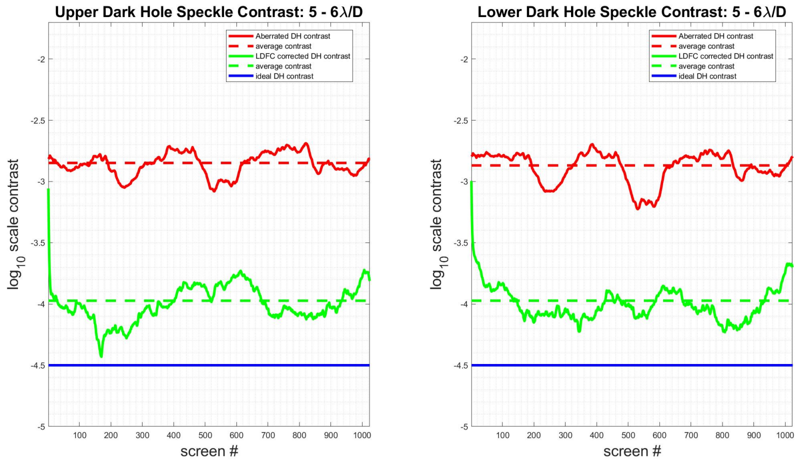

(a) 5 - 6 λ/D

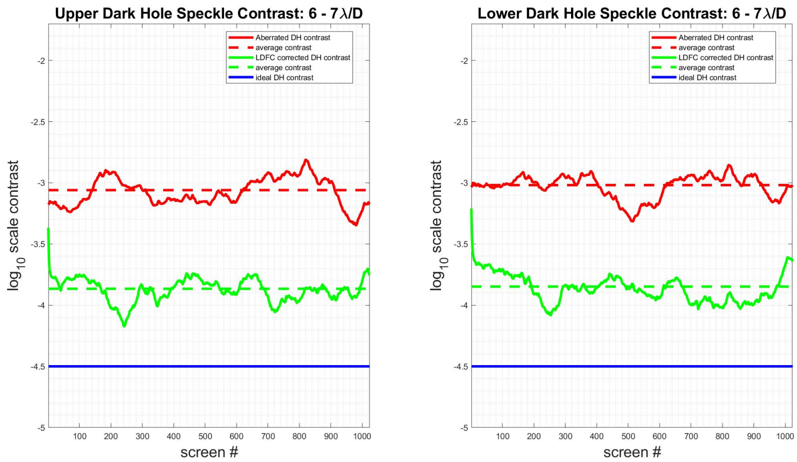

(b) 6 - 7 λ/D

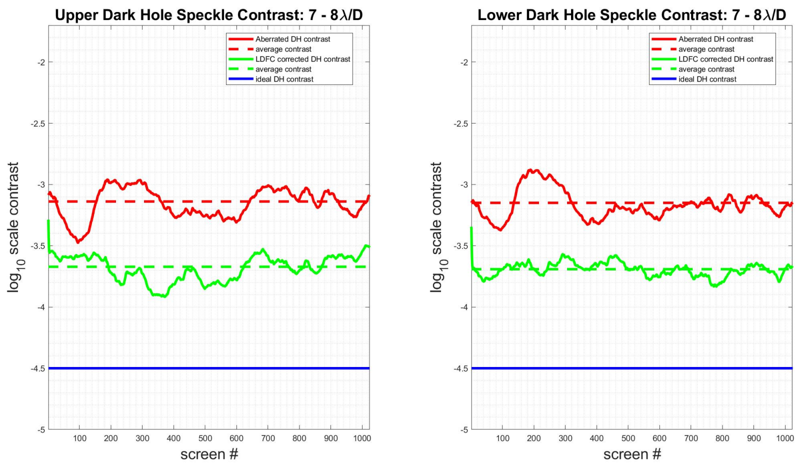

(c) 7 - 8 λ/D

Figure 5.54: Simulation with a $\frac{1}{f^3}$ temporal PSD: Contrast stabilization within 1 λ/D hemispherical bins across 5 - 8 λ/D within the dark hole over a series of 1024 temporally correlated $\frac{1}{f^4}$ phase screens.

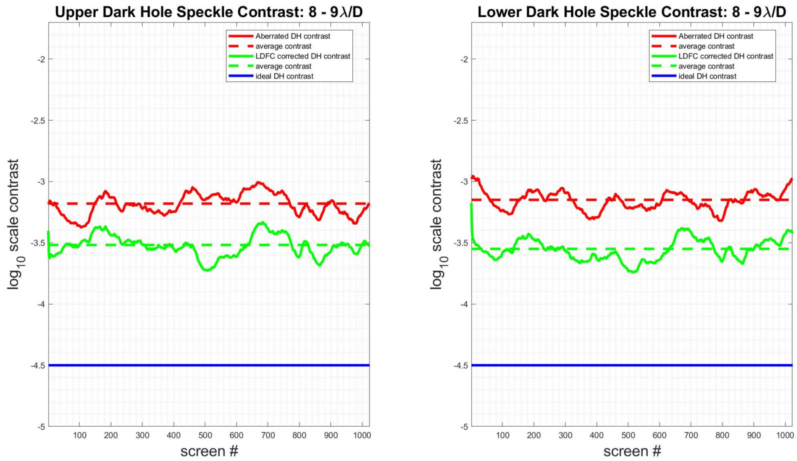

(a) 8 - 9 λ/D

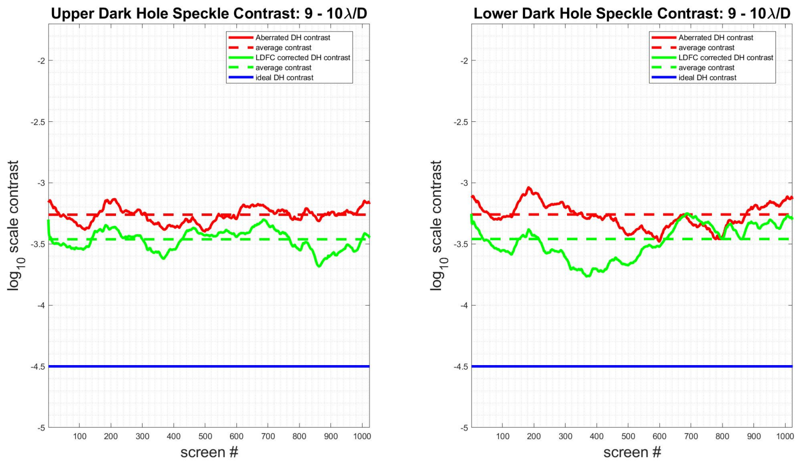

(b) 9 - 10 λ/D

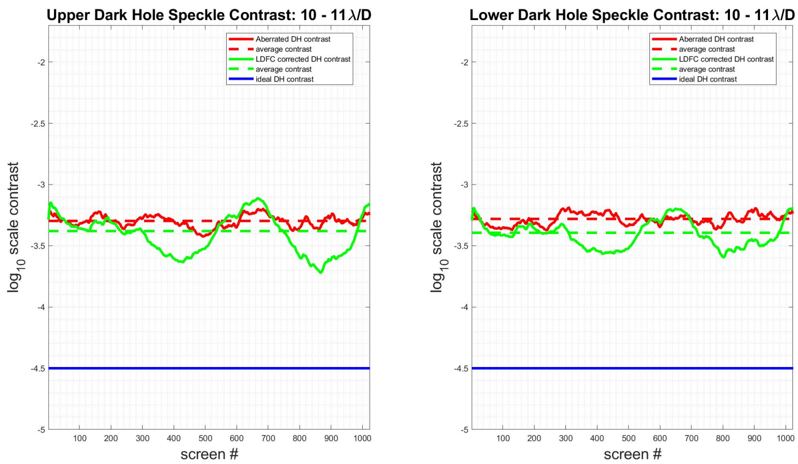

(c) 10 - 11 λ/D

Figure 5.55: Simulation with a $\frac{1}{f^3}$ temporal PSD: Contrast stabilization within 1 λ/D hemispherical bins across 8 - 11 λ/D within the dark hole over a series of 1024 temporally correlated $\frac{1}{f^4}$ phase screens.

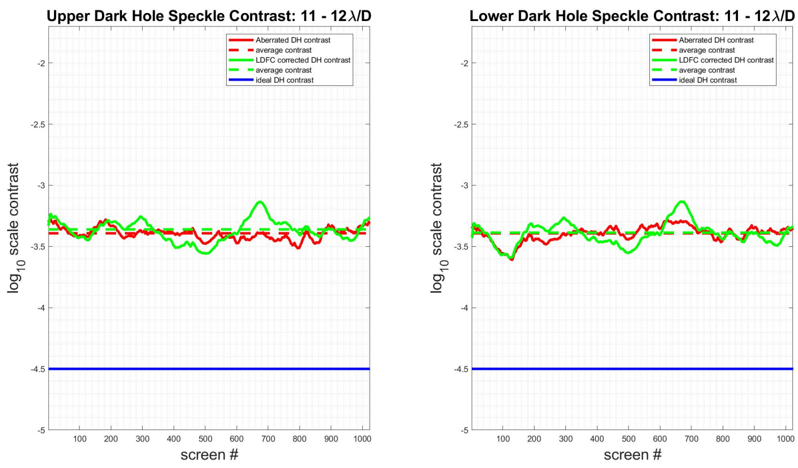

(a) 11 - 12 λ/D

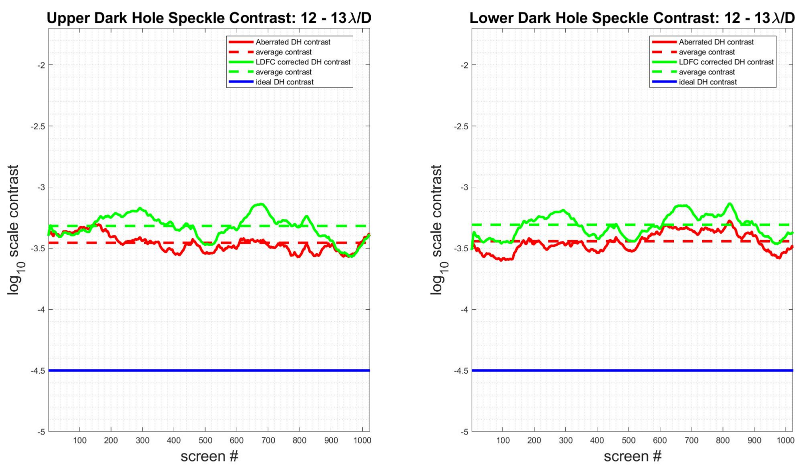

(b) 12 - 13 λ/D

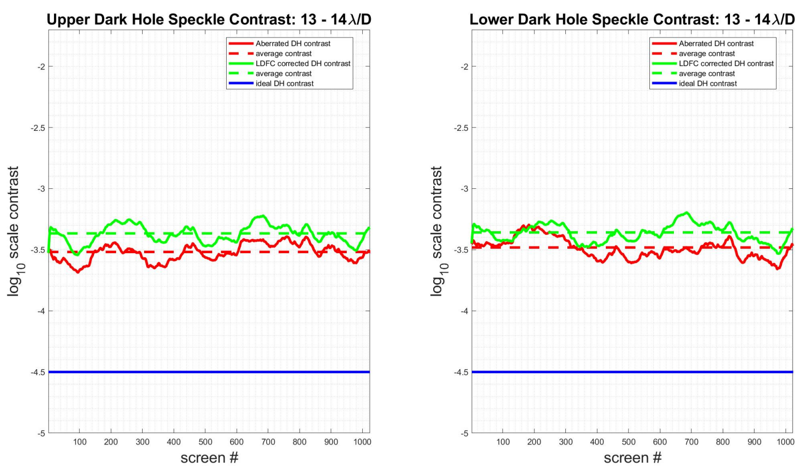

(c) 13 - 14 λ/D

Figure 5.56: Simulation with a $\frac{1}{f^3}$ temporal PSD: Contrast stabilization within 1 λ/D hemispherical bins across 11 - 14 λ/D within the dark hole over a series of 1024 temporally correlated $\frac{1}{f^4}$ phase screens.

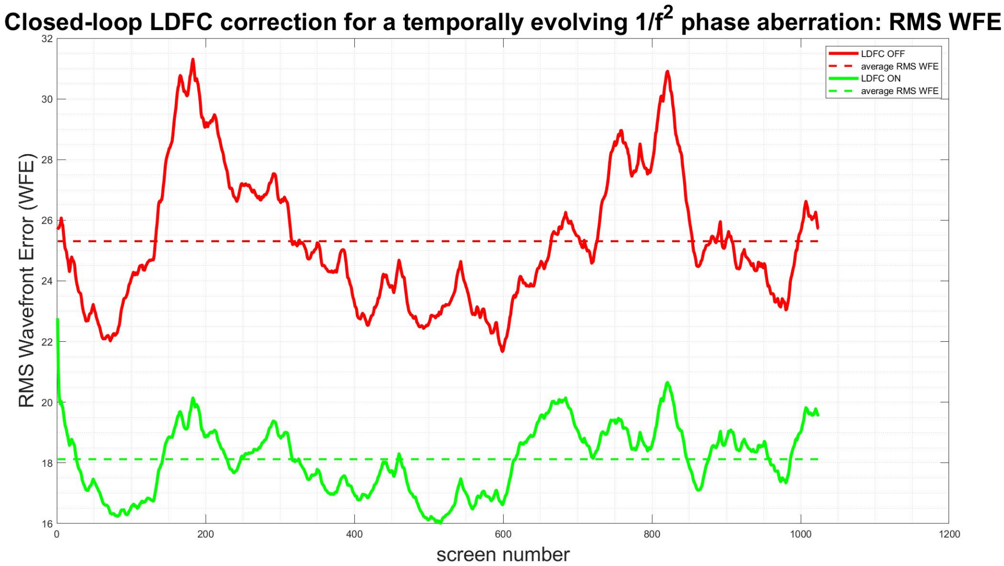

Figure 5.57: RMS WFE for an aberration with a $\frac{1}{f^3}$ temporal PSD. Measurements on the y-axis are in nm.

In the case of a phase aberration with a $\frac{1}{f^2}$ temporal PSD, LDFC converged and remained stable only for the first 200 iterations; after this point, the loop diverged quickly. Multiple tests were done to attempt to keep the loop stable with fewer modes, but the loop still diverged in each case. This behavior was not unexpected since the temporal correlation of the aberration phase sequence was very low. Since the correlation between each individual phase screen was low, the LDC correction applied at the previous step did little to correct the aberration in the next phase step. The loop divergence in this type of scenario is indicative of a common control issue in which the gain is too high. By lowering the gain, it should be possible to stabilize the loop and maintain correction, even in the presence of this phase sequence with low temporal correlation.

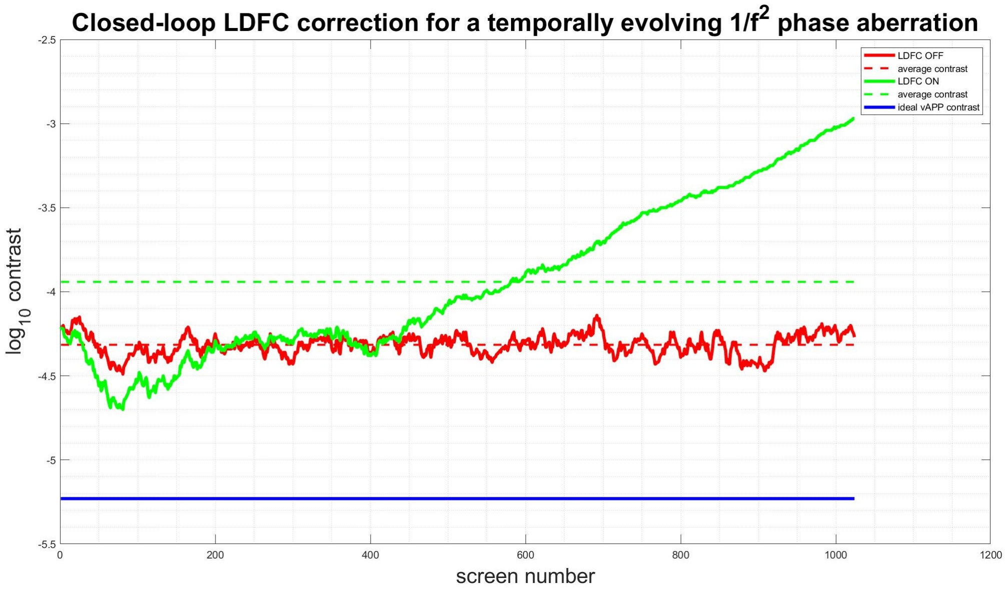

Figure 5.58: The average contrast in closed-loop across the full 2 - 15 λ/D dark hole for an aberration with a $\frac{1}{f^2}$ temporal PSD. LDFC is able to maintain some correction for the first 200 phase steps before diverging due to lack of correlation between phase steps.

CHAPTER 6

MagAO-X Preliminary Design Review

The following chapter is a compilation of the documents I authored for the MagAO-X Preliminary Design Review conducted in April 2017. This chapter covers a wide range of topics including the performance of Lyot low order wavefront sensing on MagAO-X, an overview of some of the hardware including the low-actuator-count ALPAO DM and the off-axis parabolic (OAP) mirrors, and multiple methods for realignment of the instrument post-shipping.

6.1 Lyot Low-Order Wavefront Sensing (LLOWFS)

6.1.1 LOWFS theory

Low-order wavefront sensing (LOWFS) is a coronagraphic wavefront sensing technqiue designed to sense pointing errors and other low-order wavefront aberrations using starlight that would normally just be rejected by the coronagraph. In a Lyot coronagraph, a mask is placed at the focal plane which diffracts starlight outside the geometrical pupil into a downstream pupil plane at which a Lyot mask, an undersized replica of the entrance pupil, is placed. In traditional coronagrahs, starlight is simply blocked by both of these masks, but for LOWFS, that rejected starlight from either the focal plane and the reimaged pupil plane is reflected, respectively, by a reflective focal plane mask (FPM) as well as a reflective Lyot stop, each toward a reimaged focal plane. The resulting PSFs from the starlight rejected by both masks are imaged by separate detectors and used to measure the low-order aberrations. LOWFS is a linear wavefront reconstructor that fits post-AO wavefront residuals to a command matrix built by registering the response of these rejected starlight PSFs to aberrations injected into the system by a deformable mirror (DM). This technique relies on the assumption that if the post-AO wavefront residuals are $\ll 1$ radian rms then the intensity variations in the reflected light are a linear combination of the low-order aberrations occurring upstream of the focal plane mask. LOWFS has been successfully deployed on-sky by the Subaru Coronagraphic

Extreme AO (SCExAO) team, who are contributors to the MagAO-X effort (Singh et al., 2015).

6.1.2 LOWFS for MagAO-X

In the MagAO-X system, a separate LOWFS arm has been designed to sense and correct pointing, tip/tilt, and other low-order modes. Slightly different from the original technique described above, the MagAO-X LOWFS system will use the stellar light leakage term from the vAPP coronagraph (see Section 5.5 Vector apodizing phase plate coronagraph for MagAO-X) as the LOWFS signal. To build the LOWFS control loop around this signal, an ALPAO deformable mirror (DM) with 97 actuators has been selected to be the wavefront corrector to compensate these low-order errors. The MagAO-X instrument will take full advantage of the ability to do wavefront correction with all 97 accessible modes. To do this, LOWFS must be sensitive to all 97 modes; this is accomplished in part by defocusing the LOWFS PSF which broadens the area on the detector over which the modes can be sensed. Due to their smaller uncompensated residual wavefront fitting error (as compared to Zernike modes), mirror modes were chosen to build a 97 mode reconstruction matrix. The following document demonstrates the MagAO-X LOWFS ability to sense and control 97 mirror modes individually and in random combinations, and its ability to use a modal basis set to sense and correct random Kolmogorov phase errors. The reflective Lyot stop PSF was defocused by applying a 100 nm amplitude defocus term in the pupil for these demonstrations.

6.1.3 LOWFS elements

6.1.3.1 Stellar signal

As previously mentioned, the MagAO-X system will rely on the signal from the stellar light leakage term from the vAPP coronagraph (fig 6.1). In terms of spatial frequency sensitivity, the LOWFS control loop built around the response of the light leakage PSF will be similar to both the reflected FPM and reflected Lyot mask cases described previously. This is because the signal from the light leakage term in the vAPP case is not diffracted or blocked by any masks; instead, the stellar leakage PSF is passed directly to a detector, thereby containing both the low and the high spatial frequency content that would be seen by the reflective FPM and Lyot mask cases. The reflective Lyot mask case was chosen for the following demonstrations of LOWFS on MagAO-X as it was under development for use with the PIAACMC, and the underlying principle is the same. The reflective Lyot mask used for these simulations is shown in fig 6.2. The signal from this reflected starlight contains the low, mid, and high spatial frequency content (see Section 6.1.4 for verification) that will be seen with the vAPP stellar leakage PSF.

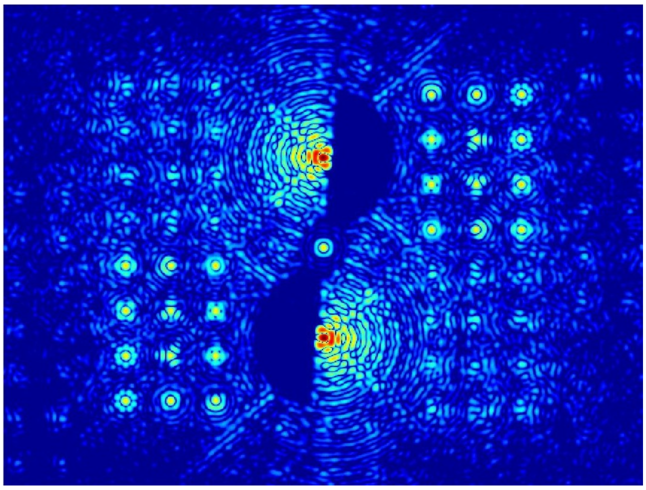

Figure 6.1: LOWFS signal from the vAPP stellar light leakage term (center PSF) shown between the two coronagraphic PSFs.

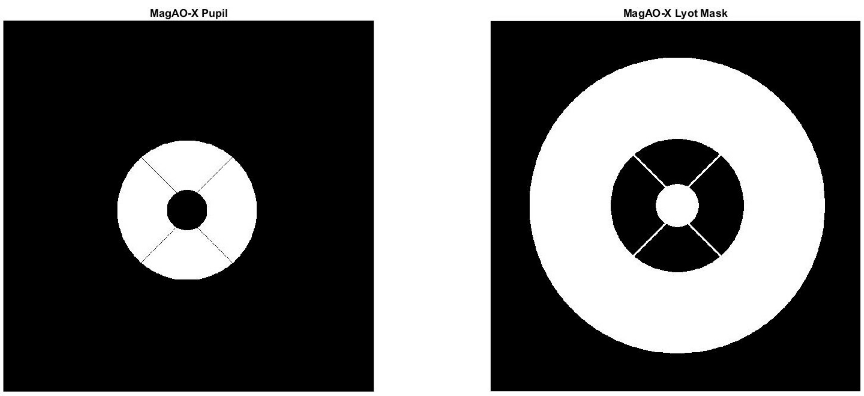

Figure 6.2: MagAO-X masks: Entrance pupil mask (left) and the reflective Lyot stop used for the following LOWFS simulations (right)

6.1.3.2 Deformable mirror

In the MagAO-X LOWFS arm, the low-order aberrations sensed using the starlight reflected by the Lyot mask will be corrected using an ALPAO DM 97-15 (see full spec sheet for this DM below in fig 6.3.). The ALPAO DM is circular and 13.5

mm in diameter and has 97 actuators across the full pupil. This will allow for LOWFS correction with up to 97 individual modes. This DM has been modeled using the mirror's gaussian influence functions for use in the following simulation work demonstrating the MagAO-X LOWFS ability to sense and correct 97 modes.

	DM 69	DM 88	DM 97-08	DM 97-15	DM 241	DM 277	DM 468	DM 820
Number of actuators	69	88	97	97	241	277	468	820
Pupil diameter (mm)	10.5	20.0	7.2	13.5	37.5	24.5	33.0	45.0
Pitch (mm)	1.5	2.5	0.8	1.5	2.5	1.5		
Mirror best flat in close loop	7.0nm RMS (no print through)							
Wavefront tip/tilt stroke (PV)	60µm	40µm	80µm	60µm	40µm	15µm		
Settling time (at +/-10%)	800µs	1.6ms		800µs	1.6ms	500µs		

Figure 6.3: ALPAO DM 97-15 with specifications (ALPAO, 2017).

6.1.4 Sensitivity and correction with 97 mirror modes

To demonstrate the MagAO-X LOWFS ability to sense and correct 97 modes, a mirror mode basis set was derived using Fourier modes. (All 97 modes can be seen in fig 6.4.)

The LOWFS response matrix used in the LOWFS control loop was then constructed using these 97 mirror modes. To build the LOWFS response matrix, each of these individual modes was then applied to the model ALPAO DM, and the PSF formed by the light reflected by the Lyot mask was recorded for each mode. (All 97 PSFs can be seen in fig 6.5)

Each of these PSFs is then reshaped into a single column vector in the LOWFS response matrix. The command matrix used in the LOWFS control loop is then the pseudo-inverse of this response matrix. This command matrix was then used in the following simulations to show the MagAO-X LOWFS ability to sense and control these modes.

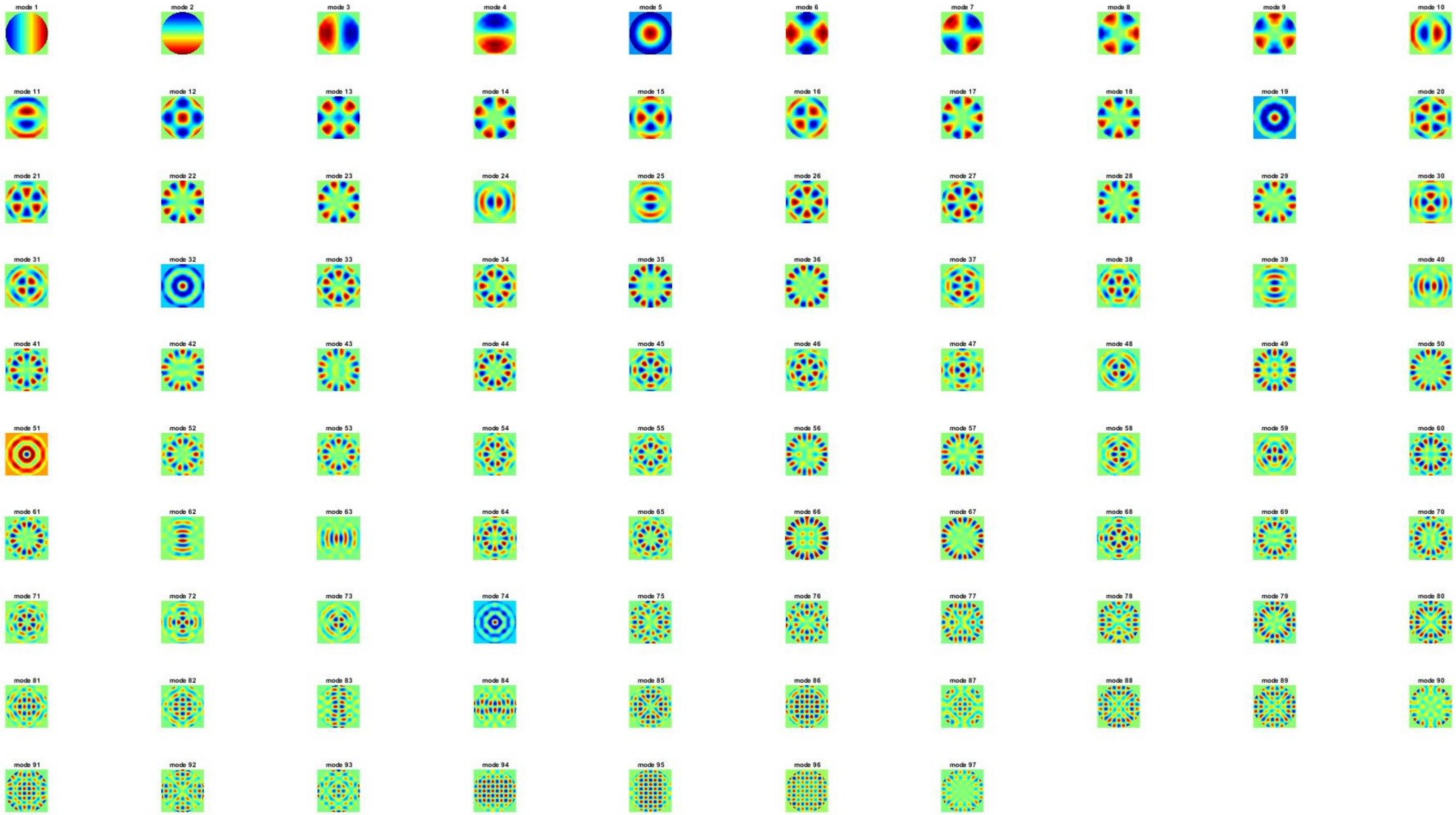

Figure 6.4: Simulation: 97 mirror modes derived from the ALPAO DM influence functions

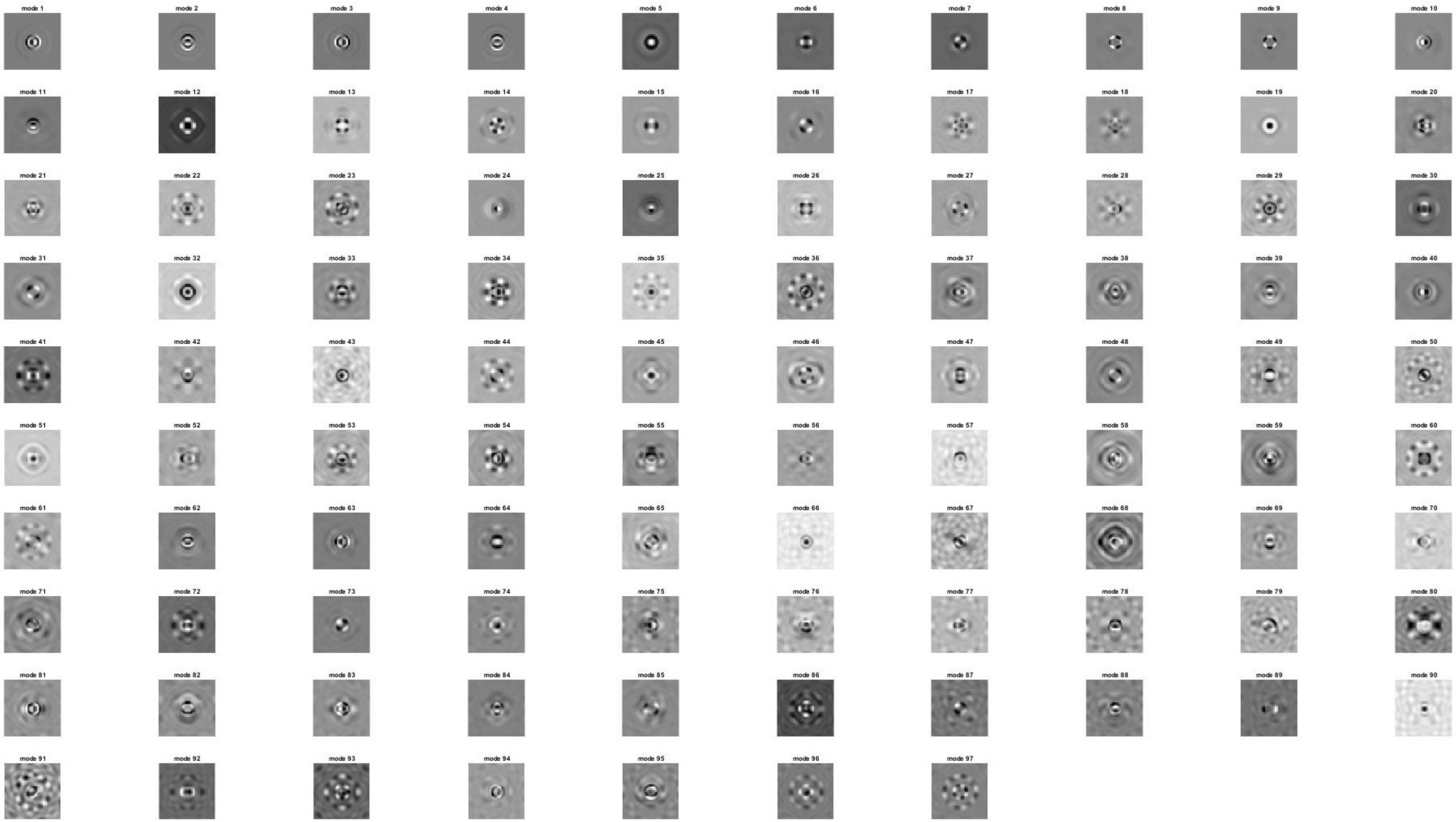

Figure 6.5: Simulation: The LOWFS PSFs for all 97 modes

6.1.4.1 Sensing and correcting individual modes

In the following section, each of the 97 modes shown in fig 6.4 was applied individually to the ALPAO DM model and sensed using the model MagAO-X LOWFS system. Each plot shows the normalized amplitude of the single mode that was applied (in green) and the normalized amplitude of each mode in the LOWFS response (in blue). For this simulation, the LOWFS PSF was defocused by applying a 100 nm amplitude defocus term in the pupil. It should be noted that the LOWFS response to certain modes is noisier than others. This is due to the fact that, for mid-spatial frequencies, there is a tradeoff between coronagraph inner working angle (IWA), transmission at small angles, and LOWFS sensitivity. With a low-IWA coronagraph with good throughput outside of the IWA, LOWFS can only measure a few low-order modes with good sensitivity. Sensitivity to higher-order modes decreases, and the resulting fit to these modes becomes noisier. One way to mitigate this effect is to threshold the number of modes used in the inversion of the response matrix as was shown in previous chapters. This was not done for the following results.

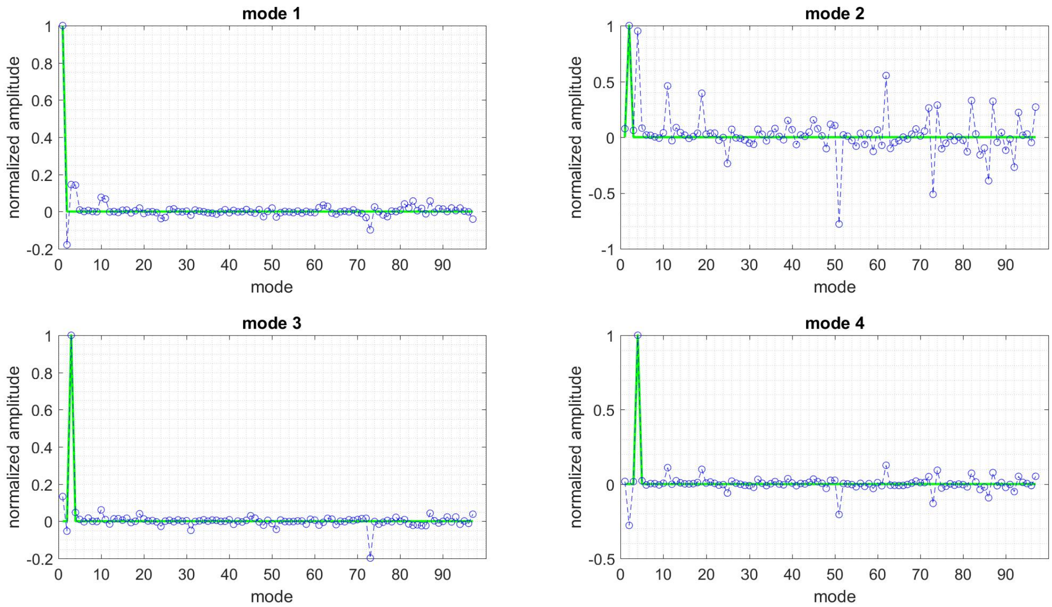

(a) Sensitivity to modes 1 - 4

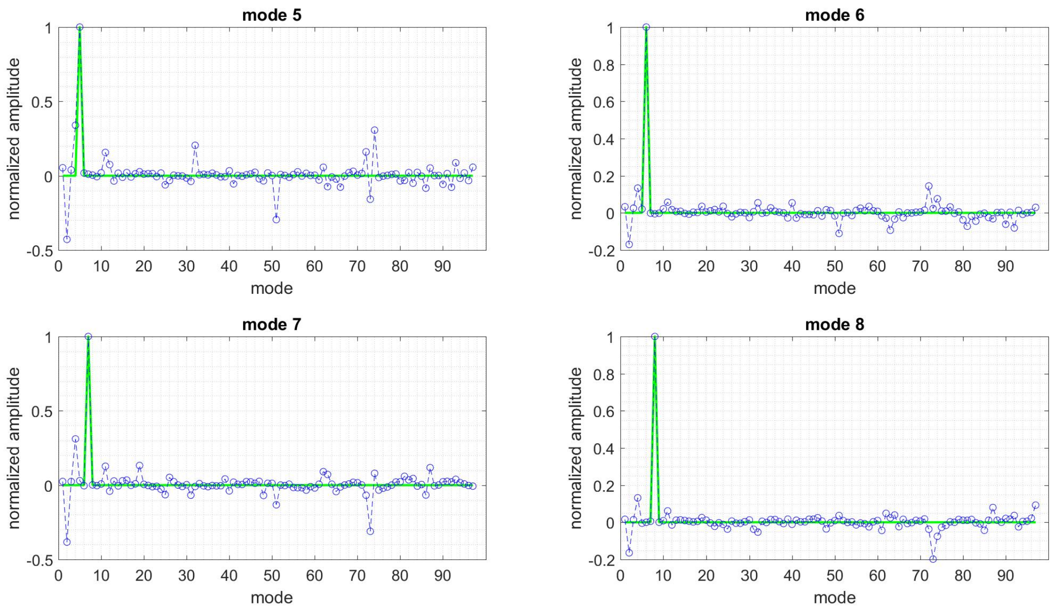

(b) Sensitivity to modes 5 - 8

Figure 6.6: LOWFS response to low-order modes with low spatial frequency content

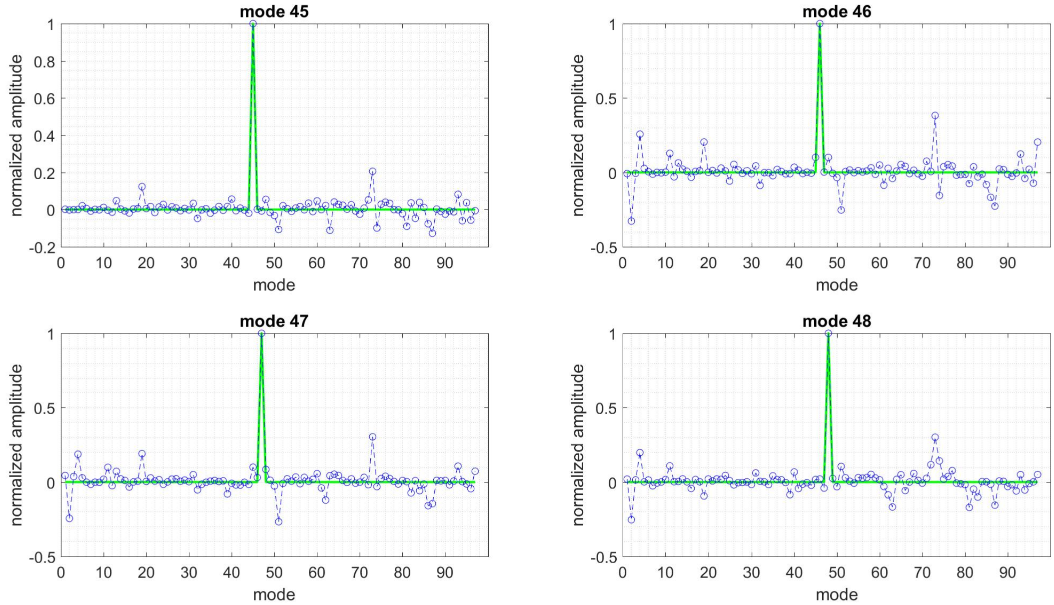

(a) Sensitivity to modes 45 - 48

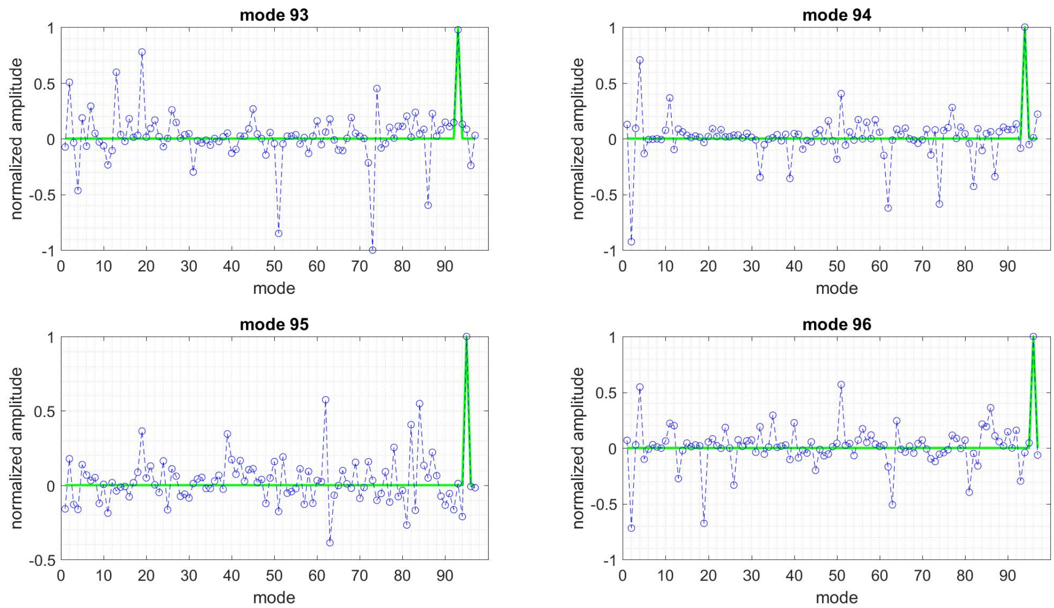

(b) Sensitivity to modes 93 - 96

Figure 6.7: LOWFS response to mid- and high-order modes with mid and high spatial frequency content

6.1.4.2 Sensing and correcting a combination of modes

LOWFS is capable of correcting low-order aberrations within spatial frequency bands to which the technique is sensitive. One demonstration of this ability is shown below. The MagAO-X PSF was aberrated by a random combination of 10 of the 97 modes injected into the pupil and then corrected by LOWFS using the full 97 mode command matrix. In fig 6.8, this 10 mode aberration is shown to the left. The LOWFS response to cancel this aberration is applied to the model ALPAO DM in the center image, and the residual wavefront error after the LOWFS correction is shown to the right.

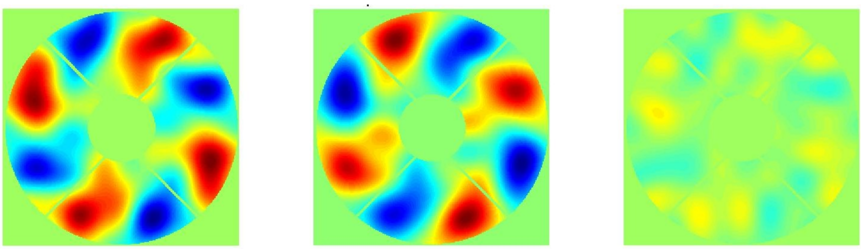

Figure 6.8: Injected 10 mode aberration (left). Applied LOWFS correction (center). Residual phase error after LOWFS (right).

The results from this test are visualized in fig 6.9 by showing the LOWFS PSFs and the PSFs seen at the science detector. In the top row, the defocused LOWFS PSF used for for sensing the aberration in the pupil is shown. The PSF to the left is aberrated by the random 10 mode phase aberration injected into the pupil shown in the left panel of fig 6.8. The PSF to the right is the final LOWFS-corrected PSF after the DM has compensated the injected aberration by applying the shape seen in the center panel of fig 6.8. In the bottom row, the aberrated PSF at the science detector is shown to the left, and the LOWFS-corrected science PSF is shown to the right. The center PSF in the top and bottom rows of fig 6.9 are the differences between the corrected and aberrated LOWFS and science PSFs respectively.

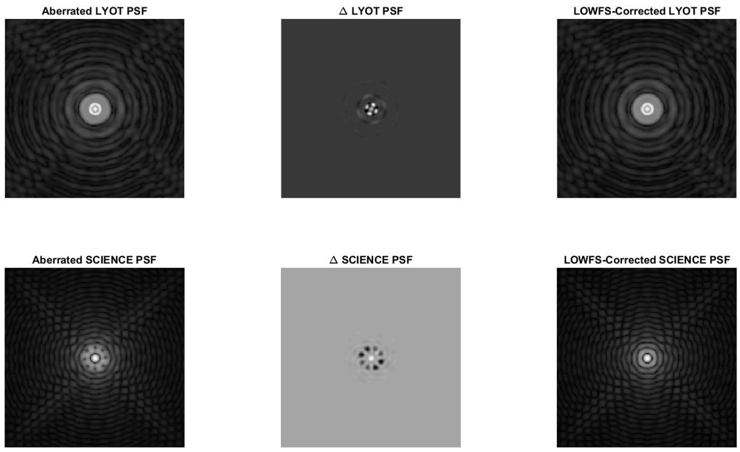

Figure 6.9: Correction of 10 applied random modes using full 97 mode response matrix. Shows the aberrated and corrected LOWFS PSF (top row), and the the aberrated and corrected science PSF (bottom row)

Fig 6.8 shows the normalized amplitudes of the 10 modes in the injected aberration (in green) and the normalized amplitudes of all 97 modes in the LOWFS response to this aberration.

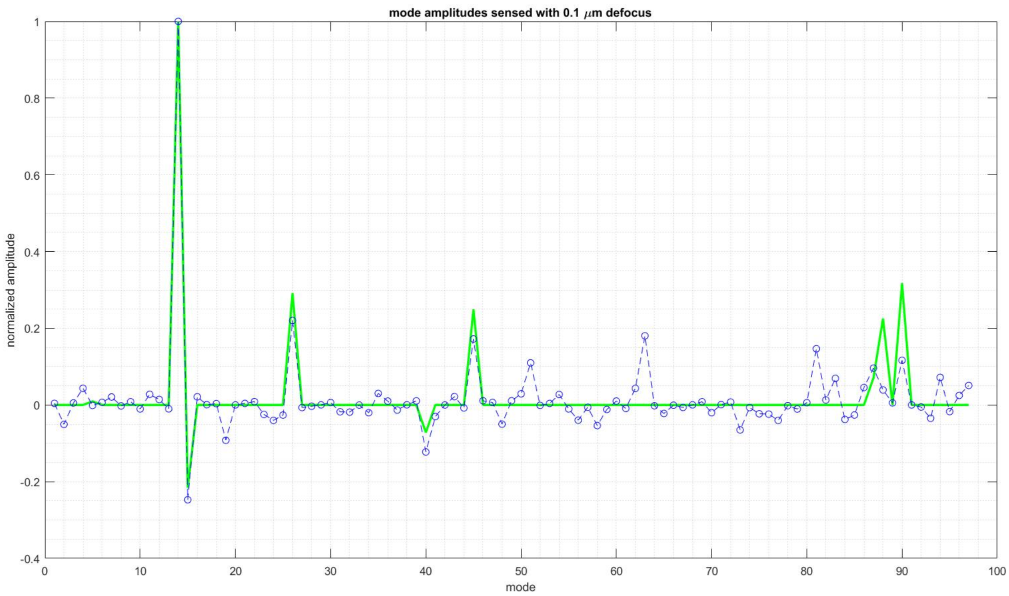

Figure 6.10: The amplitudes of the 10 applied random modes (green) and the amplitude of each mode in the LOWFS response (blue).

6.1.4.3 Sensing and correcting random Kolmogorov phase

In Section 5.1 Optics Specifications, subsection 5.3 Spec comparison, the PSDs for all of the optics in the LOWFS arm of MagAO-X were summed to determine the total power that will be added by the optical surfaces of these noncommon path (NCP) optics. This added power must be actively sensed and corrected by the LOWFS system. To ensure that the correction of this added power due to static and noncommon path (NCP) does not saturate the ALPAO DM, the stroke required to impose these corrections was analyzed (see Section 5.1 Optics Specifications, subsection 5.4 DM stroke). For the highest precision optics with a surface quality of $\lambda/200$, the RMS surface error that must be sensed and corrected by the LOWFS system is 9.6 nm. To prove that the MagAO-X LOWFS system is capable of removing this power, a modified Kolmogorov phase screen with a $\frac{\beta}{k^\alpha}$ PSD was simulated in the system pupil plane to model the combined NCP optics PSD. (In this PSD, k is the spatial frequency, β is a normalization constant, and α is the PSD index.) To model the optical surface PSD, α was chosen to be 2, and the surface precision of the phase screen was set to be 9.6 nm RMS. Using this model, it was then shown that, in the presence of photon noise, the MagAO-X LOWFS system will be capable of sensing and correcting this 9.6 nm RMS optical surface error for multiple stellar magnitudes.

The LOWFS response and correction of the 9.6 nm RMS optical surface error was run for stellar magnitudes 0, 5, 8, 10, and 12 and the frequency at which the LOWFS loop must run to obtain this correction for each stellar magnitude. The LOWFS response matrix was built using the first 20 modes. Results from these tests are shown below.

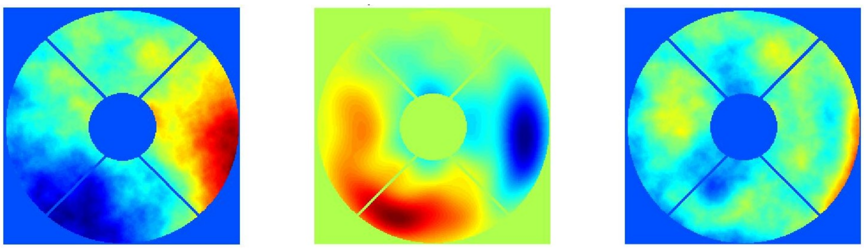

(a) (Left) 9.6 nm RMS optical surface (Center) LOWFS correction applied on ALPAO DM (Right) Residual error after LOWFS correction

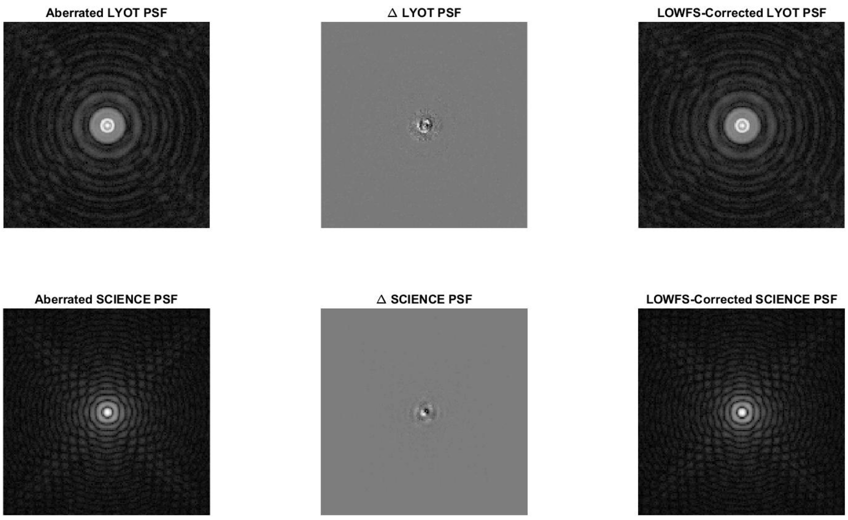

(b) (Top row) LOWFS PSF before and after correction. (Bottom row) Science PSF before and after correction.

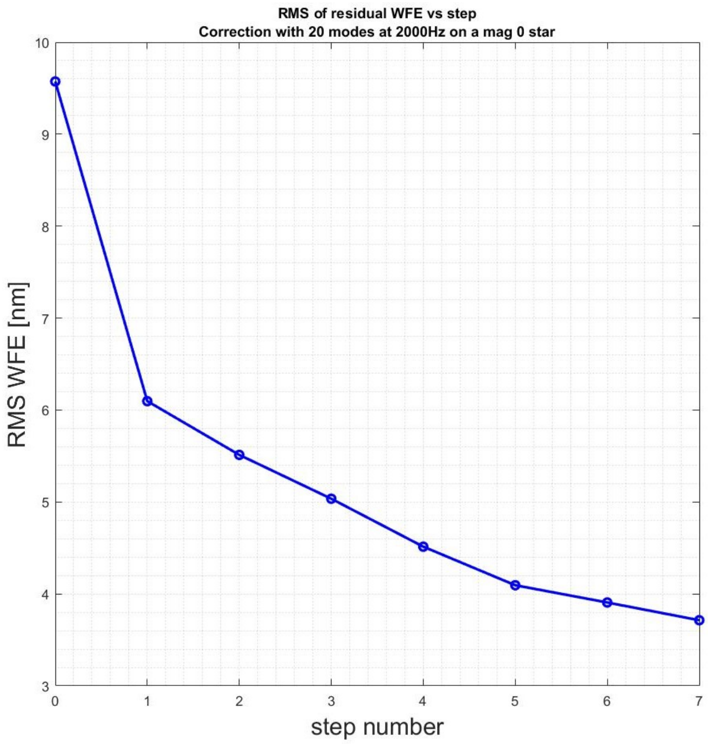

(c) Residual RMS error after LOWFS correction

Figure 6.11: LOWFS correction running at 2 kHz on a 0 magnitude star. Residual error is less than 3.8 nm RMS. Multiple steps were required for convergence; this is most likely due to non-optimized gain and allowing poorly-sensed modes to be used

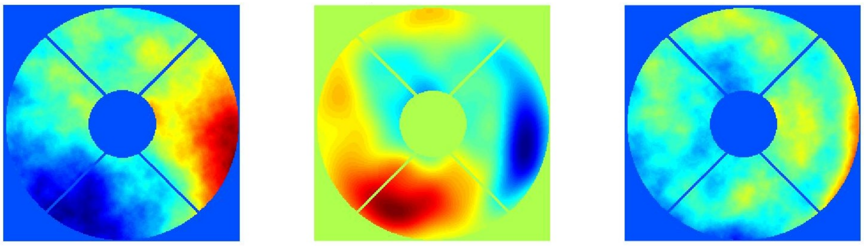

(a) (Left) 9.6 nm RMS optical surface (Center) LOWFS correction applied on ALPAO DM (Right) Residual error after LOWFS correction

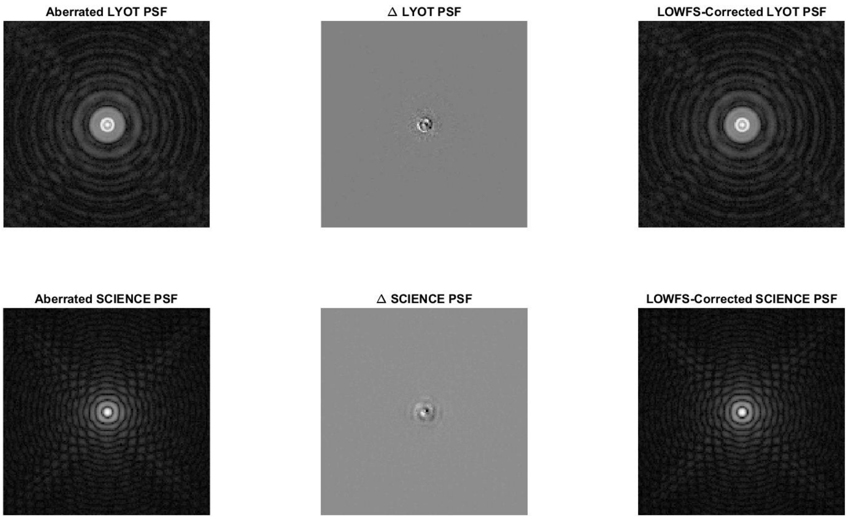

(b) (Top row) LOWFS PSF before and after correction. (Bottom row) Science PSF before and after correction.

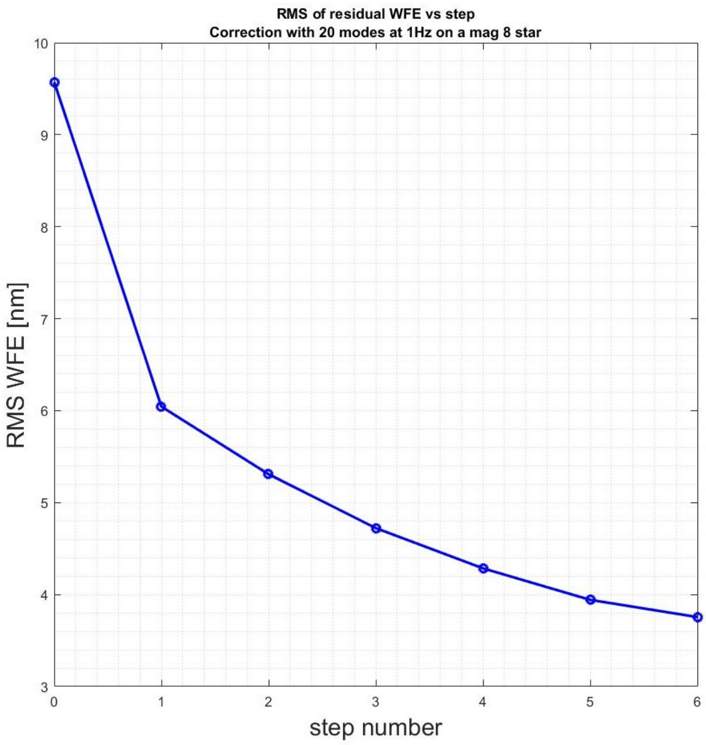

(c) Residual RMS error after LOWFS correction step in nm.

Figure 6.12: LOWFS correction running at 1 Hz on an 8 magnitude star. Residual error is less than 3.8 nm RMS.

Fig 6.13 shows the maximum frequency at which the LOWFS loop can be run for stellar magnitudes 0, 5, 8, 10, and 12 while correcting the 9.6 nm RMS surface error.

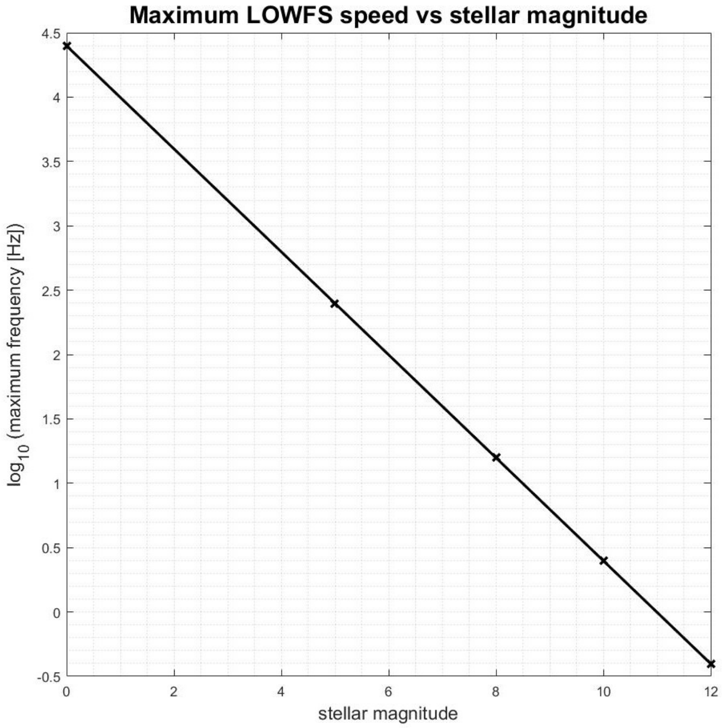

Figure 6.13: Stellar magnitude vs the $\log_{10}$ scale maximum LOWFS frequency for sensing and correcting 9.6 nm RMS surface error. This is with gain = 1. The speed referred to here is simply the inverse of the minimum exposure time required for the loop to converge. It does not include any calculation or lag time and is therefore a theoretical best case.

This plot shows that, for a magnitude 0 star, the maximum frequency at which LOWFS can be run is 25 kHz. For a magnitude 12 start this decreases to 0.4 Hz. For all five stellar magnitudes, LOWFS is capable of sensing and correcting the required 9.6 nm RMS error induced by the NCP optics surface PSD.

6.1.5 Sensing and correcting quadrant piston error

A common problem that has been seen on-sky by multiple observatories is phase-wrapping error that appears as a piston term in wavefront sensor correction. This piston term appears across entire sectors within the entrance pupil that are defined by the projection of the support structures known as 'spiders' in the pupil plane. This piston error is not sensed by the wavefront sensor and causes the correction to walk-off. MagAO-X intends to sense and correct this error using

LOWFS. In the section below, a 50 nm piston error was induced in each of the four MagAO pupil quadrants. LOWFS was then used to sense this piston and suppress it. The injected piston and LOWFS response in each quadrant can be seen in fig 6.14.

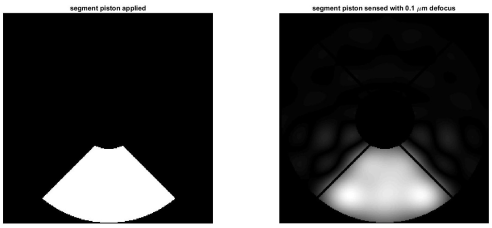

(a) Piston in quadrant 1

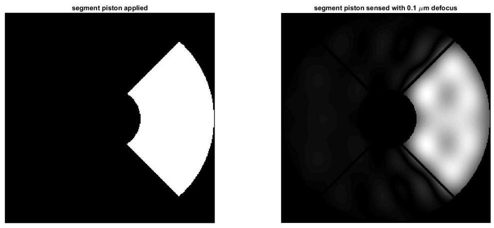

(b) Piston in quadrant 2

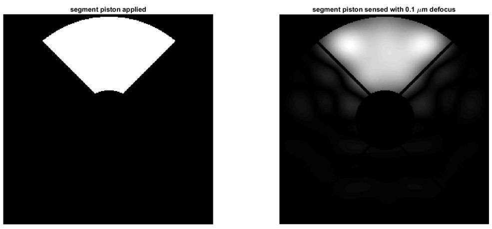

(c) Piston in quadrant 3

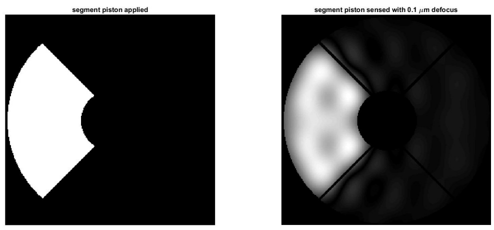

(d) Piston in quadrant 4

Figure 6.14: The applied piston error in each quadrant (left images) and the resulting piston error sensed by LOWFS (right images)

The normalized amplitude of the applied piston (in green) and the normalized amplitue of the LOWFS response to the injected piston (in blue) are shown in fig 6.15.

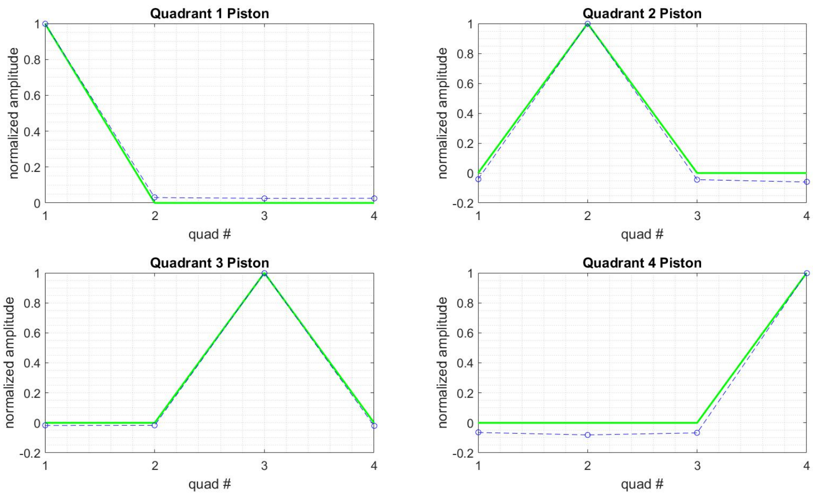

Figure 6.15: The applied piston error in each quadrant (green) and the piston error sensed by LOWFS (blue) for each of the four quadrants

For quadrant 4, the effect of the piston error on the LOWFS PSF (top row) and science PSF (bottom row) can be seen in fig 6.16. The images to the left show the aberration induced in the LOWFS and science PSFs by the piston error, and the right images show the resulting LOWFS corrections.

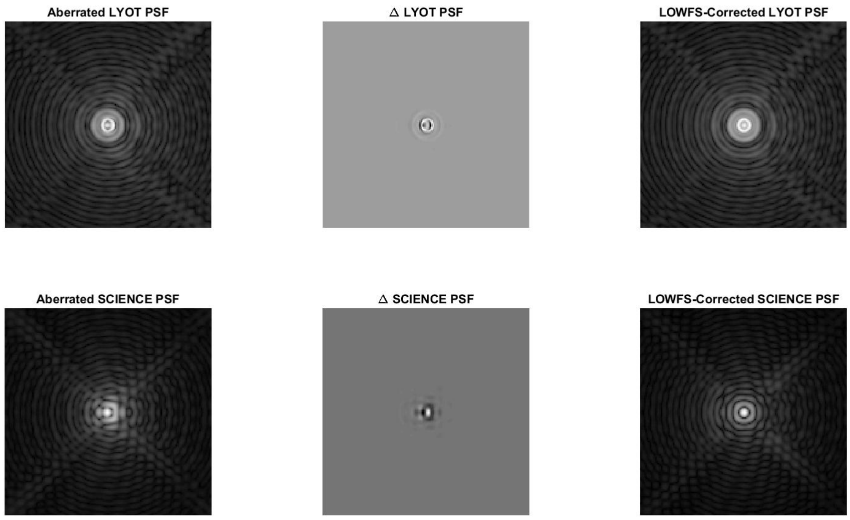

Figure 6.16: Correction of piston in quadrant 4. Shows the aberrated and corrected LOWFS PSF (top row), and the the aberrated and corrected science PSF (bottom row)

These results are a promising indicator that MagAO-X will be capable of sensing and canceling this known piston error using LOWFS.

6.2 Introduction to OAPs

The optics requiring the highest level of precision alignment within the MagAO-X beam path are the off-axis parabolic mirrors (OAPs). OAPs are fundamental to the design of MagAO-X because they are capable of delivering diffraction limited imaging (used to both collimate and focus the incoming beam at different points in the system) while deviating the incoming beam off-axis at a designed reflection angle (see fig 6.17) (Newman, 2013). This deviation provides access to the system focal point without obstruction to the beam. OAPs also have the added benefit of being non-wavelength dependent, meaning they are free of aberration across a broad wavelength range (Optics, 2017). To benefit from the high quality imaging OAPs provide, they must be precisely aligned. Below we discuss plans for initial system alignment as well as a plan to maintain that alignment after moving the

MagAO-X instrument.

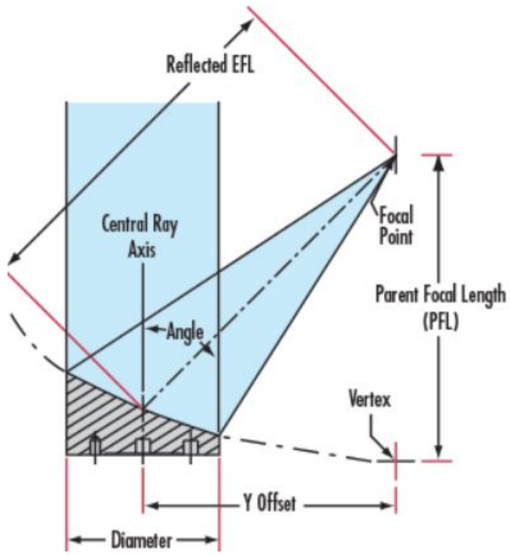

Figure 6.17: OAP diagram demonstrating the ability to focus an incoming collimated beam while deviating the beam off-axis at a designed reflection angle.

6.3 Initial Alignment

6.3.1 Degrees of freedom

OAPs have five degrees of freedom (DOF) accessible to the user for alignment: tip, tilt, translation in height, lateral translation, and translation along the optical path. A sixth degree of freedom key to OAP alignment is the rotation of the OAP around the optical axis; this is also referred to as "clocking". This DOF however, is dealt with by having all OAPs permanently mounted by the manufacturer in the correct orientation before delivery. The remaining five degrees of freedom, however, are very sensitive and require an iterative approach to correctly adjust for ideal alignment.

6.3.2 Mounting

To have access to all five adjustable DOFs, the OAP will be mounted in a kinematic mount with three actuators to allow for tip and tilt. The kinematic mount is placed in an adjustable post holder to allow for height alteration. (It should be noted that OAPs are heavy optics and tend to sink into the adjustable post holders over time; it is therefore crucial that a c-clamp is added to maintain the OAP height after alignment.) For lateral translation and translation along the beam path, the mounted OAP is then placed on two translation stages: one along the beam path and one perpendicular to the beam path. This allows for precise, easy translation of the OAP; these stages will be locked into place after initial alignment. With the optic properly mounted, an iterative approach is used to align the OAP.

6.3.3 Iterative alignment approach

OAP alignment requires a few essential tools: an iris for height verification, as well as a narrowband* spatially-coherent light source and a shear plate interferometer to check for collimation and misalignment-induced optical aberrations. (*Note: the internal source must be narrowband to allow for the use of the shear plate interferometer which uses interference fringes created by a temporally-coherent source to diagnose optical aberrations.) In this section, we layout the steps required to align an OAP in two ways: (1) using an incoming light source that is diverging (so that the OAP collimates the light), and (2) using an incoming light source that is collimated (so that the OAP brings the light to a focus). Recalling that OAPs are used both to focus and collimate light, both alignment schemes will be used to align the MagAO-X instrument since it implements a cascading system of OAPs which will each be aligned one by one in a successive fashion.

6.3.3.1 Aligning to a diverging light source

The following steps describe how to align an OAP to a diverging light source: (Newman, 2013).

1) Verify the angle of the incoming beam

    a. Prior to the first OAP, make sure that the incoming beam is at the desired system height and is propagating parallel to the reference surface (in many cases an optical bench). This can be done by placing two irises set to the system beam height in the beam path: one close to the source and one further down the beam path. The source height and angle with respect to the table can then be adjusted until the beam passes straight through both irises without clipping.

2) Adjust the height of the OAP mount

a. The center of the OAP in the vertical direction should match the center of the beam.

3) Position the OAP

a. Place the horizontal center of the OAP at a distance of one OAP focal length from the light source. Be sure to use the reflected focal length of the OAP, not the parent focal length.

b. Approximate the angle of the OAP to match the designed reflection angle. This can be approximated by eye using a mounted protractor placed in front of the OAP in the beam path such that the incoming and reflected beam pass over the protractor, thereby allowing the user to see the angle between the two beams.

4) Check collimation using a shear plate interferometer

a. Position a shear plate interferometer in the path of the reflected beam. The shear plate will produce straight fringes parallel to the reference line when the beam is perfectly collimated and without aberrations. It is therefore important to orient the reference line towards the incident beam. The angle of the fringes relative to the reference line tells the user about the state of collimation. If the lines are tilted, the beam is defocused, meaning that the OAP must be translated along the beam path. If the fringes are not straight, there is some aberration in the wavefront, which is usually caused by a tilt or de-centering of the OAP. Adjust the tip/tilt and lateral position of the OAP as necessary to achieve straight fringes parallel to the reference line.

5) Check collimation in the orthogonal direction

a. Rotate the shear plate by 90 degrees to check collimation in the tangential or sagittal plane. Make the same adjustments to achieve collimation.

Figure 6.18: Shear plate interferometer showing straight line fringes indicating the light reflecting off of the OAP is collimated and free of aberrations (Newman, 2013).

6) Iterate steps 4 and 5

a. Adjustments of collimation in the two orthogonal planes are not entirely decoupled. When you make an adjustment in one plane, it is likely to affect collimation in the other. Alignment is therefore an iterative process of minor adjustments and checking collimation in both planes. The OAP is well-aligned when the fringes in both directions are straight and parallel to the reference line as shown in fig 6.18 .

7) Check the angle of the output beam

a. The output beam should be parallel to the reference surface, just like the input beam. This can again be done using two irises set at the system beam height: one placed near the OAP and one placed further away. Tilt the OAP until the beam passes straight through both irises.

6.3.3.2 Aligning to a collimated light source

The following steps describe how to align an OAP to a collimated light source: (Newman, 2013)

1) Verify the angle of the incoming beam (same as above)

2) Adjust the height of the OAP mount (same as above)

3) Position the OAP (same as above)

4) Check the image

   a. Look at the focused spot formed by the OAP using a detector. Adjust the angle of the OAP relative to the incoming beam (tilt) to achieve good imaging quality. By adjusting the OAP angles in small increments you can minimize the aberrations observed in the focal plane.

5) Check the angle of the output beam (same as above)

6.3.4 High precision adjustments

Some small residual error can be expected at the end of this alignment scheme given the precision of the above methods. To deal with this residual, a Zygo Verifire interferometer will be placed at the end of the system which will allow for high-precision adjustments of each OAP to be made to fine-tune the alignment. This interferometer ensures reliable "ripple-free" phase measurements in vibration-prone environments, and will allow for small residual errors in the alignment to be removed by small final adjustments made to the OAPs (Zygo, 2017).

6.4 Maintaining Alignment

Initial alignment of the system is crucial, and maintaining the same quality of alignment over time and after shipping the MagAO-X instrument is essential to maintain system performance. Misalignment is expected to occur in shipping, and it is important to minimize the amount of time required to realign the system before going on-sky. We have therefore developed a rough alignment strategy to quickly realign the system.

For maintaining alignment, we propose using three methods: (1) a series of irises placed along the beam path to check for tip/tilt and height variation, (2) an individual reference for each OAP to monitor any changes in the OAP's position with respect to its initial, ideal-alignment orientation, and (3) a series of flip mirrors and cameras to check PSF quality and beam location.

6.4.1 Method 1: Irises

A series of irises will be centered on the beam along the optical path after initial alignment of the instrument and epoxied in place to keep them from moving during shipment (see fig 6.19). The irises will be oversized and fully opened while the instrument is in operation to avoid affecting the beam. For alignment, the irises will be stopped down to check for beam misalignment that will result in clipping by the iris. These irises can be fully epoxied to remain in place, will have no moving parts, and will therefore be the least likely of the three methods to be affected by shipping.

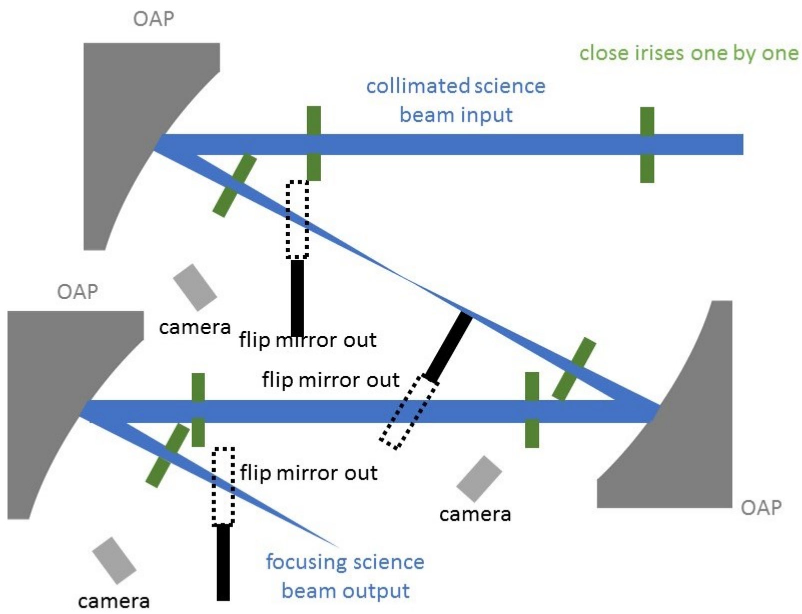

Figure 6.19: Iris method: close down each iris individually in succession down the beam path (with the flip mirrors out of the beam). Misalignment on the iris will give tip/tilt misalignment information for the preceding OAP.

6.4.2 Method 2: Laser/back reflection/camera

The back surface of each OAP will be polished to allow for a 4% reflection off the uncoated back surface. (Note: the OAP mounts are designed to be open in the back, thereby allowing access to the back surface of the optic. For specifics on these mounts, see Section 2.1: Overall Design) A small laser will then be set up and epoxied in place to reflect off the back of the OAP and onto a camera (also epoxied in place with a square post and post holder to avoid rotation in the mount during transit). (See fig 6.20)

The rough alignment maintenance strategy will proceed as follows:

1) Initial alignment of the full optical system

2) Set-up a laser and camera (one of each per OAP) behind each OAP to reflect the laser off the polished back surface of the OAP and onto the camera.

3) For each OAP, take an image of the laser beam footprint with the camera and save as the ideal reference image for each OAP.

4) After shipping, or at any given time after the initial alignment, turn on the laser for each OAP and take an image of the beam footprint on the camera.

5) Measure the shift in position of the beam with respect to the reference image. (See fig 6.21) This will provide information on how the OAP has tipped and tilted since the initial alignment. (Note: these are the two most sensitive DOFs and are therefore the most likely misalignments to occur during shipping. The OAPs will be locked in place in height, in position along the beam path, and laterally with respect to the beam, and will therefore be less likely to move.)

6) Use the actuators on the OAP's kinematic mount to adjust the OAP's tip and tilt to return the beam to its reference position on the camera.

7) To ensure that the OAPs, not the laser/camera system has moved in transit, this procedure will be augmented by iterating on the initial alignment steps 3

- 5, checking the centering of the beam on each OAP, the input and output angle of the beam, and the beam height along the optical train.

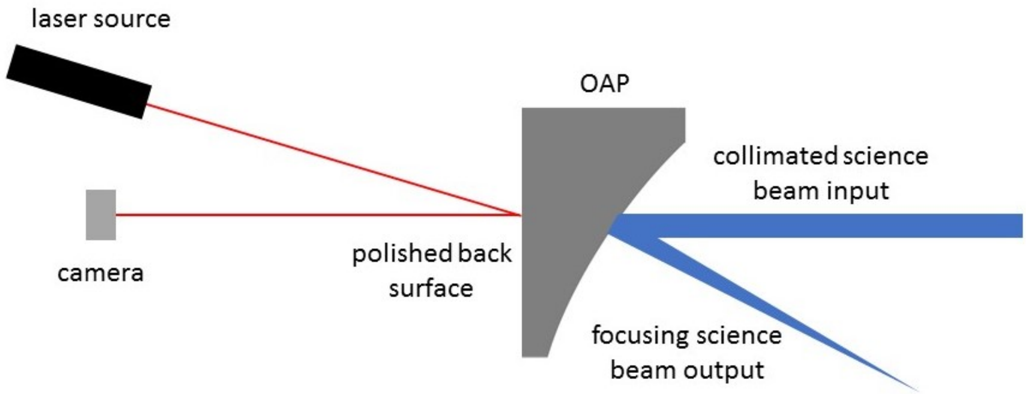

Figure 6.20: OAP layout for rough alignment strategy using a laser reflection of the polished back surface of each OAP reflected back to a camera

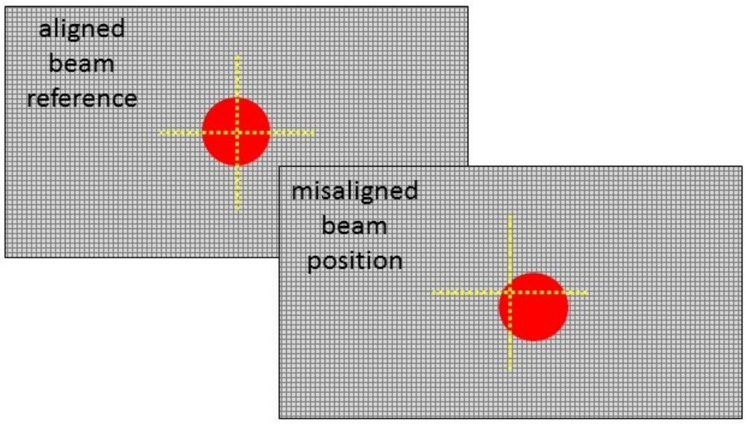

Figure 6.21: Beam displacement used to adjust tip/tilt OAP actuators to realign the OAP

This strategy will bring the OAPs back into alignment. However, OAPs are sensitive optics, so it is possible some residual aberration may remain after this rough alignment. If this is the case, it will be seen in the image quality at the end of the optical system. Smaller, more precise adjustments of the OAPs will then be required to fine tune the final image quality. This can be achieved by checking the beam height throughout the optical system with an iris or target set to the beam height, checking for wavefront aberrations using a shear plate interferometer, and adjusting the OAPs accordingly (see previous section for initial alignment).

6.4.3 Method 3: Flip-mirrors/camera

Flip mirrors will be placed along the optical path after each OAP that will be out of the beam during operation and flipped into the beam, reflecting it back to a camera, one at a time starting at the beginning of the system. In collimated space, the beam footprint location on the camera will be used as in Method 2 to determine any tip/tilt that has been induced on the OAP before it. After OAPs where the light is coming to converging, the camera will be placed at focus. The position of the beam at the camera will be again be used to identify tip/tilt, but the beam at the camera will now be a PSF, the quality of which can be used to more precisely diagnose optical aberrations induced by the preceding OAPs. This method, as well as method 1, has been demonstrated successfully at Subaru Coronagraphic Extreme Adaptive Optics (SCExAO) by Nemanja Jovanovic, whose expertise and on-sky experience have contributed significantly to this alignment scheme.

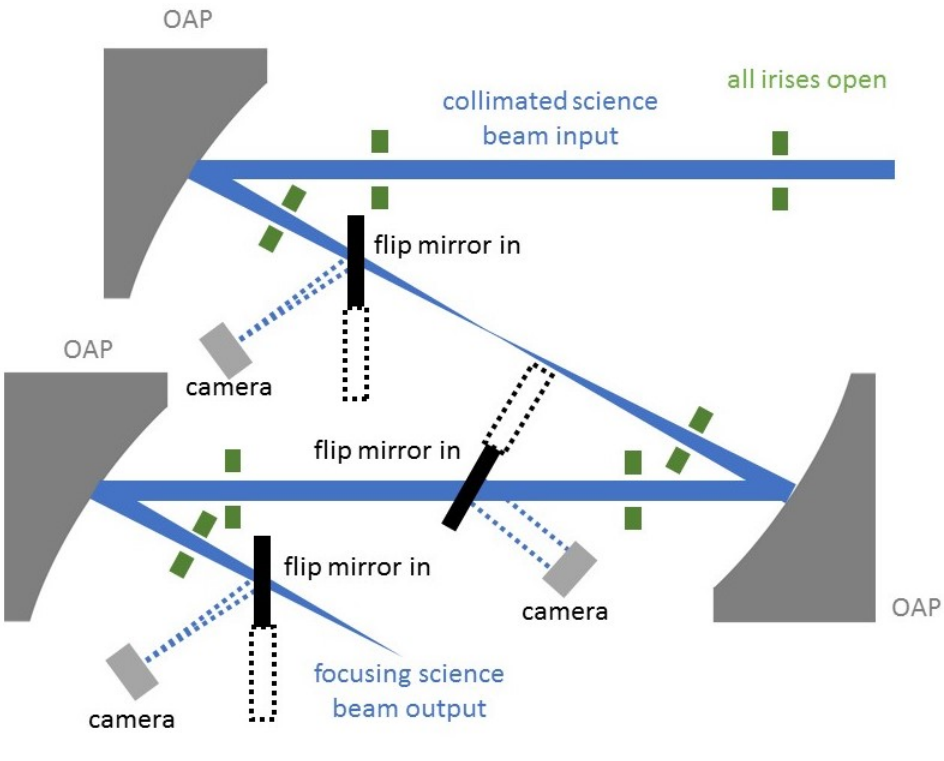

Figure 6.22: Flip mirror method: flip each flip mirror into the beam in succession down the beam path (with the irises fully open). The reflected beam, both collimated and the PSF, will give tip/tilt error information for the preceding OAP, and the PSF will give higher precision error information for the preceding OAP.

6.5 Laser Safety

The internal broadband light source for MagAO-X is a class IIIb Fianium Whitelase micro laser with a total power output > 200mW and a bandwidth of 400 ˘ 2200 nm, with a significant fraction of the total power lying outside of the visible band. Specular reflections as well as direct exposure to this laser can be harmful to the eye. This makes laser safety an important topic for consideration. The upper bench of the MagAO-X instrument is designed to be 1.465 m tall, making it below the average eye level. To further mitigate safety concerns, a near-infrared (NIR) filter will be used to cut off all light past 800 nm, ensuring that all light delivered to the instrument is within the visible spectrum. This filter decreases the total output power being delivered to the instrument to less than 5mW, downgrading it to a class IIIa. This beam will therefore be eyesafe and will allow for personnel to align the instrument without the use of safety goggles. Standard procedure for operating this laser will still include avoiding direct eye exposure to the beam (straight from the source as well as any reflections) by keeping the user's eyes above the level of the beam at all times. Should the NIR filter need to be removed at any time for instrument testing, personnel working on the optical bench will be required to wear laser safety goggles with high OD (optical density) in the laser's peak wavelength regimes. The same Fianium Whitelase micro source that will be used for the MagAO-X bench is currently in use at the University of Arizon's Extreme Adaptive Optics Lab, and the above safety precautions, including procedures and hardware, have been and are currently being successfully implemented.

CHAPTER 7

Conclusions and Future Work

With extremely large telescopes, both on the ground and in space, coming online over the next few decades, the ability to directly image and characterize exoplanets is finally within reach. With state-of-the-art technology, coronagraphs like the vAPP and phase conjugation techniques such as EFC are now capable of creating regions of high contrast within which light from an exoplanet could be visible above the stellar signal at very small separations from the parent star.

In this dissertation, I have shown that we are able to enhance these technologies by including focal plane wavefront sensing techniques, such as modal wavefront sensing and linear dark field control. Modal wavefront sensing allows us to sense and suppress low-order aberrations and therefore maintain small inner working angles. Linear dark field control extends this capability to mid-spatial frequencies by monitoring fluctuations in the bright field outside of the dark hole for aberrations that create speckles in the dark hole that dominate the signal from the exoplanet. By using changes in the bright field to provide updates on the state of the field within the dark hole, linear dark field control is able to lock the high contrast state after it is established without relying on field modulation which interrupts the science acquisition and fundamentally limits the exposure time. Another advantage, specifically of linear dark field control, is that the correction is not affected by non-common path errors.

We have shown in this paper that both modal wavefront sensing and linear dark field control work, not only in simulation but also in the laboratory. Following the findings of this paper, there are several ways in which linear dark field control's performance can be enhanced for on-sky deployment. One obvious way to improve on the results presented here would be to take full advantage of the deformable mirror by fully illuminating the active surface. With more actuators, the control radius increases and allows access to higher spatial frequencies. Alternatively, more actuators could be used to increase and maintain high contrast over a smaller region in the focal plane. Another way to potentially enhance linear dark field control's performance is to vary the gains for different spatial frequency bins in the response matrix. Gain optimization simiilar to that used by the Large Binocular Telescope AO (LBTAO) system could also be beneficial. Finally, different modal basis sets like Fourier or Karhunen-Loeve modes could be used in place of the mirror modes used throughout this work.

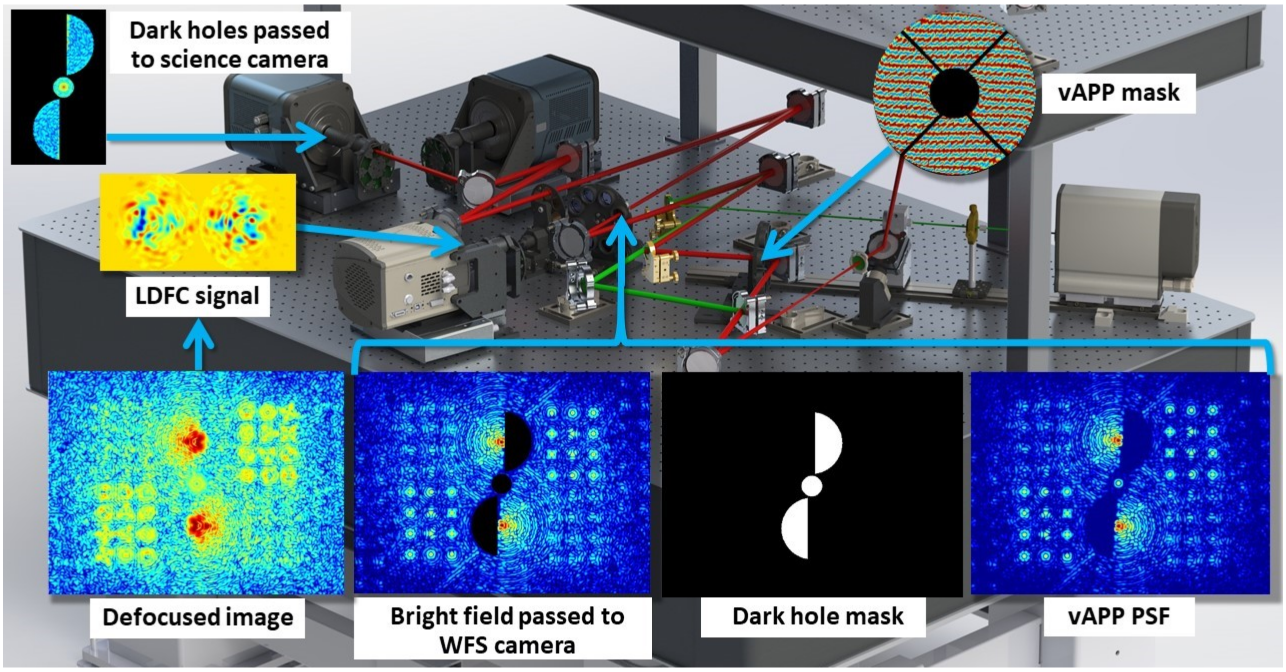

Figure 7.1: Future layout for LDFC and LOWFS using MWFS PSFs on MagAO-X Close et al. (2018)

The next step for both of these techniques is to deploy them on-sky: on MagAO-X in the upcoming year, or even sooner on the Subaru Coronagraphic Extreme Adaptive Optics (SCExAO) instrument. All of the work presented here has been specifically tailored to inform the design and performance of focal plane wavefront sensing techniques that will be deployed on the Magellan Extreme Adaptive Optics Instrument (MagAO-X) in 2019. The current plan for deployment of both modal wavefront sensing and linear dark field control on MagAO-X is to use a binary mask, placed at an intermediate focal plane, which transmits the dark holes to the science camera and reflects the stellar bright field back to a dedicated WFS camera shown in fig. 7.1. This reflected light will contain both the modal wavefront sensor PSFs and the bright field used by linear dark field control. This bright field signal can then be used for low-order wavefront sensing and dark hole stabilization simultaneously by using different regions of the same image as the wavefront sensor for both algorithms. Running both algorithms in the science image will allow for the maintenance of high Strehl as well as high dark hole contrast. The substantial increase in uninterrupted observation time linear dark field control provides over current stabilization methods like EFC will result in an overall increase in the number of planets detected and analyzed over the lifetime of an instrument, thereby bringing the current state of technology one step closer to finding and characterizing another Earth-like planet.

APPENDIX A

Simulation and Laboratory Code

A.1 Testbed model

A.1.1 Master script

```
%MagAOX_Testbed.m
%---------------------------------------------------------------------------
% Author: K.L.Miller [millerk2@email.arizona.edu]               March 2017

% This program simulates the MagAO-X Testbed
%---------------------------------------------------------------------------

%% Testbed Input Parameters
% Option 1: Default Parameters
disp('Default settings:         [0]')
disp('User input parameters:    [1]')
input_options = input(':');
switch(input_options)
    case 0
    disp('-----------------------------------------------------------')
    disp('Using Default Settings')
    disp('* Magellan Pupil')
    disp('* No coronagraph')
    disp('* BMC DM ')
    disp('* 0 deg DM-Beam Angle')
    disp('-----------------------------------------------------------')
    pupilchoice = 0;
    Wavefront = [1 0 0 0 0];
    DefMirror = 0;
    deg = 0;
    coronagraphchoice = 0;
    case 1
% Option 2: User-Set Parameters
    disp('-----------------------------------------------------------')
    disp('Input Testbed Parameters')
    disp('-----------------------------------------------------------')
    % Pupil:
    disp('-------------------------------------------------------------------')
    disp('Pupil Options: ')
    disp('Magellan Pupil (standard) [0]')
    disp('Fat Spider                [1]')
    pupilchoice = input(':');
    % Wavefront:
    disp('-------------------------------------------------------------------')
    disp('Wavefront Options: ')
    disp('(NOTE: Can choose more than one with format [ 1 2 3] in order shown)')
    disp('Clear                     [0]')
    disp('Planet/Star System        [1]')
    disp('Zernike Phase Screen      [2]')
    WF = input(':');
    Wavefront=zeros(1,5);
    Wavefront(WF+1)=1;
    disp('-------------------------------------------------------------------')
    % Deformable Mirror:
    disp('-------------------------------------------------------------------')
    disp('Deformable Mirrors:')
```

```
    disp('Boston Micromachine MEMS (BMC)[0]')
    disp('ALPAO DM                      [1]')
    disp('Iris AO Mirror                [2]')
    disp('All DMs                       [3]')
    DefMirror = input(':');
    disp(' ')
    disp('Angle of DM to incoming beam: ')
    disp('30 degrees on UA testbed')
    deg = input(':');
    disp('-------------------------------------------------------------------')
    % Coronagraph:
    disp('-------------------------------------------------------------------')
    disp('vAPP Coronagraphs:')
    disp('Include vAPP coronagraph?')
    disp('NO                    [0]')
    disp('YES                   [1]')
    coronagraphchoice = input(':');
end

%% Testbed Set Parameters: Units [MM]
% Central Wavelength
lambda=5.5*10^-4;
klam = 2*pi/lambda;
% Focal Length
f=272.24;
% Entrance Pupil Meshgrid (Spatial Domain)
x=linspace(-15,15,1024);dx=x(2)-x(1);[X, Y]=meshgrid(x,x);R=sqrt(X.^2+Y.^2);xsize=size(x,2);
% Frequency Domain
xi=linspace(-1/(2*dx),1/(2*dx),xsize);[XI,ETA]=meshgrid(xi,xi);rho=sqrt(XI.^2+ETA.^2);dxi=xi(2)-xi(1);

%% Camera Parameters
% Camera Dimensions [pixels]
cropX = 150;
cropY = 150;
cropSIZE = cropX*cropY;

% Cropping Size
xcen=xsize/2;ycen=xcen;
xnsize=cropX;ynsize=cropY;

CAMcrop = [cropX cropY cropSIZE xcen ycen];

%% Telescope Pupil
if pupilchoice == 0
    [PUPIL,¬,¬,FullSystemPSF] = CHOOSE_VAPP_MASK(2);
else
    [PUPIL,¬,¬,FullSystemPSF] = CHOOSE_VAPP_MASK(8);
end
DMref = PUPIL;

if deg ≠ 0
    [PUPIL] = angled_matrix_updated(PUPIL,deg,1);
end

%% Clear Aperture
if Wavefront(1) == 1
    NoPhase = ones(xsize,xsize);
else
    NoPhase = 1;
end

%% Planet/Star Wavefront
% Add Planet
if Wavefront(2) == 1
    disp('-------------------------------------------------------------------')
    disp('Planet / star separation: [lambda/D]')
    nld=input(':');
    disp('-------------------------------------------------------------------')
    disp('Planet / star contrast: ')
    ps_ratio=input(':');
    PLANET=ps_ratio.*exp(1i.*-X.*nld);
```

```
else
    PLANET = 0;
end

%% Zernike Polynomials
% Create Zernike Phase Screen
if Wavefront(3) == 1
    ZernMode = apply_Zernike_MultiMode(lambda,r,R,X,Y);
else
    ZernMode = 1;
end

%% CREATE vAPP CORONAGRAPH
if coronagraphchoice == 1
    [EP_vAPP,vAPP_upper,vAPP_lower,FullSystemPSF_vAPP,IWA,OWA] = CHOOSE_VAPP_MASK(0);
end

%% IrisAO DM
if (DefMirror == 2) || (DefMirror == 3)
disp('------------------------------------------------------------')
disp('LOCATING ACTIVE ACTUATORS ACROSS IRIS AO IN EP ')
disp('------------------------------------------------------------')
    IrisAO = create_IrisAO(xsize);
    ActiveDM = 'IRISAO';
else
    IrisAO = 1;
end

%% BMC DM
if (DefMirror == 0) || (DefMirror == 3)
disp('------------------------------------------------------------')
disp('LOCATING ACTIVE ACTUATORS ACROSS BMC IN EP ')
disp('------------------------------------------------------------')
    ActiveDM = 'BMC';
    disp('Use real BMC data: ')
    disp('YES:           [1]')
    disp('NO:            [0]')
    BMC_choice = input(':');
    if BMC_choice == 1
        load locActs_byeye_annular.mat
        locActs = locActs_byeye_annular;
        numActsACTIVE = length(locActs);
        [IFmatACTIVE,BMCflat,¬] = build_real_BMC(0,locActs);
        [BMCflat_reshaped] = angled_matrix_updated(BMCflat,deg,-1);
        BMC = 1;
    else
        [IFmatACTIVE,numActsACTIVE,locActs,¬] = defineBMC_DM(DMref,deg);
        BMC = 1;
    end
else
    BMC = 1;
end

%% ALPAO DM
if (DefMirror == 1) || (DefMirror == 3)
disp('------------------------------------------------------------')
disp('LOCATING ACTIVE ACTUATORS ACROSS ALPAO IN EP ')
disp('------------------------------------------------------------')
    ActiveDM = 'ALPAO';
    [IFmatACTIVE,numActsACTIVE] = defineALPAO2;
    ALPAO = 1;
else
    ALPAO = 1;
end

%% Build Pupil Plane
disp('------------------------------------------------------------')
disp('BUILDING ENTRANCE PUPIL (EP)')
disp('------------------------------------------------------------')
PupilPlane = PUPIL.*IrisAO.*BMC.*ALPAO;
TotalPhase = ZernMode.*NoPhase;
```

```
EP = PupilPlane.*TotalPhase;
EPplanet = EP.*PLANET;
EPangled = angled_matrix(EP,deg,1);

%% Define Active Pupil
disp('-----------------------------------------------------------')
disp('BUILDING DM FLAT ')
disp('-----------------------------------------------------------')
DMflat = reshape(IFmatACTIVE*ones(numActsACTIVE,1),[sqrt(size(IFmatACTIVE,1)),sqrt(size(IFmatACTIVE,1))]);

%% Define DM Control Radius
[DMcolumnMAT,control_radius,lamDperPixel,PixelsPerControlRadius] = ...
      find_DM_control_radius(IFmatACTIVE,FullSystemPSF,locActs);

%% System Parameters Vector
sys_params_mats = cell(1,6);
sys_params_mats{1} = X;
sys_params_mats{2} = Y;
sys_params_mats{3} = PupilPlane;
sys_params_mats{4} = EP;
sys_params_mats{5} = deg;

sys_params = [klam lamDperPixel BMC_choice];
```

A.1.2 Pupil and vAPP coronagraph selection

```
function [EP_vAPP,vAPP_upper,vAPP_lower,FullPSF,IWA,OWA,vAPP_choice] = CHOOSE_VAPP_MASK(vAPP_choice)
%--------------------------------------------------------------------------
% Author: K.L.Miller
% Email: klmiller561@gmail.com
%--------------------------------------------------------------------------
% For a full list of vAPP options and a description of each, use the command:
% [EP_vAPP,vAPP_upper,vAPP_lower,FullPSF,IWA,OWA,vAPP_choice] = CHOOSE_VAPP_MASK(0);
%--------------------------------------------------------------------------
% Reads in vAPP phase fits files, propagates to the image plane, and
% returns the full phase pattern for both coronagraphic PSFs (EP_vAPP) as
% well as the individual phases for the upper and lower coronagraphic
% PSFs (vAPP_upper and vAPP_lower).  Also returns the full system PSF
% including the leakage term (FullPSF), and the inner working angle (IWA)
% and outer working angle (OWA) of the chosen vAPP mask in units of
% lambda/D.  Returns the identification number of the chosen maks
% (vAPP_choice) in case you use the input '0' option and want to remember
% which mask you chose.
%--------------------------------------------------------------------------
if vAPP_choice == 0
    disp('CHOOSE vAPP MASK')
    disp('1 [2,2] 2-15 lambda/D a,b: 12 Zernike MWFS')
    disp('2 [2,3] Pupil only')
    disp('3 [1,2] 2-11 lambda/D: Dark holes only')
    disp('4 [2,1] 2-11 lambda/D b: 20 orthonormal MWFS')
    disp('5 [1,1] 2-11 lambda/D a: Phase diversity MWFS')
    disp('6 [3,1] 2-11 lambda/D a,b: Phase diversity + 8 orthonormal MWFS')
    disp('7 [3,2] 2-6 lambda/D: Dark holes only')
    disp('8 Thick spider pupil design for MagAO-X')
    disp('9 Thick spider MagAO-X vAPP')
    vAPP_choice = input('Mask choice: ');
end

IWA = 2;

if vAPP_choice == 1
    im = fitsread('MagAO-X_1800_vAPP_2-15_a_b_CMWS_square_modeloc_v5.fits');
    OWA = 15;
elseif vAPP_choice == 2
    im = fitsread('MagAO-X_pupil_1800_final.fits');
```

```
    OWA = 0;
elseif vAPP_choice == 3
    im = fitsread('MagAO-X_1800_vAPP_2-11_CMWS.fits');
    OWA = 11;
elseif vAPP_choice == 4
    im = fitsread('MagAO-X_1800_vAPP_2-11_b_CMWS_circle_modeloc_v3.fits');
    OWA = 11;
elseif vAPP_choice == 5
    im = fitsread('MagAO-X_1800_vAPP_2-11_b_CMWS.fits');
    OWA = 11;
elseif vAPP_choice == 6
    im = fitsread('MagAO-X_1800_vAPP_2-11_a_b_CMWS_square_modeloc_v2.fits');
    OWA = 11;
elseif vAPP_choice == 7
    im = fitsread('MagAO-X_1800_vAPP_2-6_CMWS.fits');
    OWA = 6;
elseif vAPP_choice == 8
    im = fitsread('magaox_coronpupil_1720.fits');
    im = flipud(im);
    im = fliplr(rot90(im,1));
    OWA = 0;
elseif vAPP_choice == 9
    im = fitsread('MagAO-X_vAPP_1720_final_v2.fits');
    im = fliplr(rot90(im,1));
    OWA = 15;
end
%------------------------------------------------------------------------
% DEFINE NEW SIZE FOR PUPIL
new_size = 229;
%------------------------------------------------------------------------
% DEFINE PUPIL
if (vAPP_choice == 8) || (vAPP_choice == 9)
    pupil = fitsread('magaox_coronpupil_1720.fits');
    pupil = flipud(pupil);
    pupil = fliplr(rot90(pupil,1));
else
    pupil = fitsread('MagAO-X_pupil_1800_final.fits');
end
%------------------------------------------------------------------------
% RESIZE AND ZERO PAD PUPIL AND vAPP
% Resizes the zero-padded pupil to create a final PSF with a pixel sampling
% of ¬ 0.24 lambda/D per pixel (10 pixels across the PSF core)
Pupil = resize_and_zero_pad_matrix(pupil,1024,new_size/1800);
vAPP_phase = resize_and_zero_pad_matrix(im,1024,new_size/1800);
%------------------------------------------------------------------------
% CREATE vAPP PHASE
EP_vAPP = Pupil.*(exp(1i.*vAPP_phase)+exp(-1i.*vAPP_phase));
vAPP_upper = Pupil.*exp(1i.*vAPP_phase);
vAPP_lower = Pupil.*exp(-1i.*vAPP_phase);
%------------------------------------------------------------------------
% SET CAMERA SIZE
cropX = 640;
cropY = 480;
xcen = 512;
ycen = 512;

% Fourier propagation of the full phase to the image plane
% (Scale factor = 1 should be dx for correct Fourier coeff scaling)
h = fourierProp(EP_vAPP,1);
PSF = h.*conj(h);
PSF_cam = imcrop(PSF,[(xcen-cropX/2) (ycen-cropY/2) (cropX-1) (cropY-1)]);

% Unpolarized leakage term that is roughly 1/100th the intensity of the coronagraphic PSFs
leakage = (10^-2);
hleakage = fourierProp(Pupil,1);
PSFleakage = (hleakage.*conj(hleakage)).*leakage;
PSFleakage_cam = imcrop(PSFleakage,[(xcen-cropX/2) (ycen-cropY/2) (cropX-1) (cropY-1)]);

% Sums the coronagraphic PSFs and leakage term together in intensity
% (Makes the approximation that all three PSFs are fully incoherent with one another)
FullPSF = fliplr(PSF_cam + PSFleakage_cam);
```

```
figure;imagesc(log10(normIM(FullPSF)));axis off;daspect([1 1 1]);colormap jet;colorbar;caxis([-4.5 ...
      0]);title(['vAPP Mask ',num2str(vAPP_choice)])
```

A.1.3 Deformable mirror generation

```
function [BMC_IFmatACTIVE,numActs,locActs,BMCmask] = defineBMC_DM(pupil,deg)
%% Define Full DM
x = linspace(-1,1,size(pupil,1));
[X,Y]=meshgrid(x,x);
center_points = zeros(size(pupil));

numActsInPupil = 22;
d = normIM(pupil(:,size(pupil,2)/2));
fd = find(d,1,'first');
ld = find(d,1,'last');
pupilDia = ld-fd+1;
k1 = 1;
k2 = round(pupilDia/numActsInPupil);
k=k1:k2:size(pupil);
center_points(k,k) = 1;

rBMC = 0.315;
BMCmask=(X<rBMC).*(X>-rBMC).*(Y<rBMC).*(Y>-rBMC);

%% Full DM
ActuatorMaskFULL = (BMCmask.*center_points);
[mFULL,nFULL] = find(ActuatorMaskFULL == 1);
numActsFULL = length(mFULL);

%% Define Influence Functions
width = 0.0003;
if deg ≠ 0
    gaus = exp(-(((X.*cosd(deg)).^2)+(Y.^2))./width);
else
    gaus = exp(-((X.^2)+(Y.^2))./width);
end

%% Gaussian Influence Function Response Matrix

A0 = (10^-6); % (10^-6) mm or (10^-3) um or 1 nm
IFcube = zeros(size(X,1),size(X,2),numActsFULL);
for i = 1:length(mFULL)
    IFcube(:,:,i) = circshift((A0.*gaus),[mFULL(i)-(numActsFULL/2),nFULL(i)-(numActsFULL/2)]);
end

IFmat = zeros(size(pupil,1)*size(pupil,2),numActsFULL);
for j = 1:numActsFULL
        IFmat(:,j) = reshape(IFcube(:,:,j),[size(pupil,1)*size(pupil,2),1]);
    disp(j)
end

%% Active DM
if deg ≠ 0
    [pupilangled] = angled_matrix_updated(pupil,deg,1);
    PupilMask = normIM(pupilangled);
else
    PupilMask = normIM(pupil);
end
ActuatorMask = (BMCmask.*center_points.*PupilMask);

[m,n] = find(ActuatorMask == 1);
numActs = length(m);

%% Return Location of Active Actuators
lFULL = zeros(length(mFULL),2);
```

```
for i = 1:length(lFULL)
    lFULL(i,:)=[mFULL(i) nFULL(i)];
end

l = zeros(length(m),2);
for i = 1:length(l)
    l(i,:)=[m(i) n(i)];
end

lcompare = ismember(lFULL, l, 'rows');
locActs = find(lcompare ==1);

%% Builds Influence Function Matrix for Active Actuators
BMC_IFmatACTIVE = IFmat(:,locActs);

end
```

A.2 Linear Dark Field Control

A.2.1 Master script

```
% LDFC_MagAOX_Defocused_modal_selection.m
%--------------------------------------------------------------------------
% Author: Kelsey L. Miller                                        June 2018
% Contact: millerk2@email.arizona.edu
%--------------------------------------------------------------------------
% LDFC: Linear Dark Field Control Simulation
% Adds photon noise
% Simulates linear dark field control on a dark hole created by any
% selected vAPP coronagraph
%--------------------------------------------------------------------------
close all;clearvars;clc
todaysdate = date;

%% ADD REQUIRED DIRECTORIES

%% CALL/BUILD OPTICAL SYSTEM
%------------------------------------------------------------------------
disp('---------------------------------------------------------------------------')
disp('INITIALIZING SYSTEM')
disp('---------------------------------------------------------------------------')
% System Parameters
    MagAOX_Testbed

    PupilPlaneCrop = imcrop(PupilPlane,[(xcen-243/2) (ycen-243/2) (243-1) (243-1)]);
    disp(['DM CONTROL RADIUS: ',num2str(control_radius),' lambda/D'])
    disp(['LAMBDA/D PER PIXEL: ',num2str(lamDperPixel),' lambda/D'])

    if PLANET ≠ 0
        disp('Use PLANET in Reference Image?')
        disp('NO           [0]')
        disp('YES          [1]')
        planetREFchoice = input(':');
        disp(' ')
        disp('Use PLANET in Response Matrix?')
        disp('NO           [0]')
        disp('YES          [1]')
        planetRMchoice = input(':');
    end

%% vAPP CORONAGRAPH SELECTION
    if pupilchoice == 0
        [EP_vAPP,vAPP_upper,vAPP_lower,RefPSF0,IWA,OWA,vAPP_choice] = CHOOSE_VAPP_MASK(0);
    else
```

```
        [EP_vAPP,vAPP_upper,vAPP_lower,RefPSF0,IWA,OWA,vAPP_choice] = CHOOSE_VAPP_MASK(9);
    end

%% ADD DEFOCUS TO vAPP STOP IMAGE
% Pull out defocus term
    load ZERNmat.mat
    AmpDefocus = 200; %distance in nm (e.g. 10^3 = 1 micron of defocus)
    if AmpDefocus == 0
        defocustitle = 'atFocus';
    else
        defocustitle = 'Defocused';
    end
    defocus = AmpDefocus.*reshape(ZERNmat(:,3).*(10^-6),[1024,1024]);
    Defocus = exp(1i.*klam.*2.*defocus);
    clearvars ZERNmat

%% NOISE
    noisechoice = 1;
    LoopFrequency_Hz = 1000;
    ΔT = 1/LoopFrequency_Hz; %seconds

%% SET FLUX
disp('---------------------------------------------------------------------------')
disp('SETTING FLUX')
disp('---------------------------------------------------------------------------')
    Dpupil_m = 6.5; % Telescope pupil diameter [meters]
    lambda_um = lambda*10^3; % Central wavelength converted from mm to um
    bandwidth_um = 0.1*lambda_um; % 10% bandwidth
    stellarMAG = 5;%[0 5 8 10 12]
    [flux_factor,Flux,BAND_NAME] = scale_flux(PupilPlane,stellarMAG,ΔT,lambda_um,bandwidth_um,Dpupil_m);
    EP_Flux = EP.*flux_factor./sqrt(3);% The division by sqrt(3) is a scale factor to compensate for the vAPP
    EPplanet_Flux = EPplanet.*flux_factor./sqrt(3);
    PSFscalefactor = 1;

%% DEFINE DARK HOLE AND WFS REGIONS
disp('---------------------------------------------------------------------------')
disp('DEFINING DF AND WFS REGIONS')
disp('---------------------------------------------------------------------------')

% Define DF and WFS regions
    CAMcrop = [640 480 640*480 512 512];
    [DHwindowCROP,DHwindowUP,DHwindowLOW,windowCROP]=define_DF_area_vAPP(RefPSF0,X,CAMcrop,lamDperPixel,IWA,...
control_radius);

    upper_Ybeg = find(windowCROP(1:round(size(windowCROP,1)/2),round(size(windowCROP,2)/2))==1,1,'first');
    upper_Yend = find(windowCROP(1:round(size(windowCROP,1)/2),round(size(windowCROP,2)/2))==1,1,'last');

    lower_Ybeg = ...
          (480/2)+find(windowCROP(round(size(windowCROP,1)/2):end,round(size(windowCROP,2)/2))==1,1,'first');
    lower_Yend = lower_Ybeg + abs(upper_Yend - upper_Ybeg);

    windowCROP_upper = windowCROP(upper_Ybeg:upper_Yend,:);
    windowCROP_lower = windowCROP(lower_Ybeg:lower_Yend,:);

    upper_Xbeg = find(windowCROP_upper(round(size(windowCROP_upper,1)/2),:)==1,1,'first');
    upper_Xend = find(windowCROP_upper(round(size(windowCROP_upper,1)/2),:)==1,1,'last');

    lower_Xbeg = find(windowCROP_lower(round(size(windowCROP_lower,1)/2),:)==1,1,'first');
    lower_Xend = find(windowCROP_lower(round(size(windowCROP_lower,1)/2),:)==1,1,'last');


%% CREATE REFERENCES
disp('---------------------------------------------------------------------------')
disp('BUILDING REFERENCES')
disp('---------------------------------------------------------------------------')

% Reference star without defocus (coronagraph)
    REFfield = PupilPlane;

    [SCIstar_PSFref] = VAPP_PROPAGATOR(REFfield,vAPP_upper,vAPP_lower,EP_Flux);
    [SCIplanet_PSFref] = VAPP_PROPAGATOR(REFfield,vAPP_upper,vAPP_lower,EPplanet_Flux);
```

```
    SCI_PSFref = SCIstar_PSFref + SCIplanet_PSFref;

    SCI_maxStar = max2(SCI_PSFref);
    im0 = log10(abs(normIM(SCI_PSFref)));

% Reference star with defocus (coronagraph)
    [PSFstarref] = VAPP_PROPAGATOR(REFfield,vAPP_upper,vAPP_lower,EP_Flux.*Defocus);
    [PSFplanetref] = VAPP_PROPAGATOR(REFfield,vAPP_upper,vAPP_lower,EPplanet_Flux.*Defocus);
    PSFref = PSFstarref + PSFplanetref;
    maxStar = max2(PSFref);

% DF metric
    DH = SCI_PSFref.*DHwindowCROP;
    DH_avg_contrast = mean2(log10(abs(DH(DH≠0)./SCI_maxStar)));

% Select, normalize, and combine reference WFS regions
    if ((PLANET ≠ 0) & (planetREFchoice == 0))
        PSFrefWindow = windowCROP.*PSFstarref;
    else
        PSFrefWindow = windowCROP.*PSFref;
    end
    upper_wfs = PSFrefWindow(upper_Ybeg:upper_Yend,upper_Xbeg:upper_Xend);
    lower_wfs = PSFrefWindow(lower_Ybeg:lower_Yend,lower_Xbeg:lower_Xend);
    WFSref = normIM(horzcat(lower_wfs,upper_wfs));

    WFScropSIZE = size(WFSref,1)*size(WFSref,2);

    WFS_positions = [upper_Ybeg upper_Yend lower_Ybeg lower_Yend upper_Xbeg upper_Xend lower_Xbeg ...
         lower_Xend,WFScropSIZE];

% Image scaling factors
    cminLOG = floor(DH_avg_contrast);
    cmaxLOG = max2(log10(abs(PSFref./maxStar)));

%% MODAL BASIS SELECTION
% Basis set options
disp(' ')
disp('Select modal vs zonal control: ')
disp('Influence functions  (zonal):             [0]')
disp('Zernike Polynomials  (modal):             [1]')
disp('Karhunen-Loeve Modes (modal):             [2]')
disp('DM Mirror Modes (modal)     :             [3]')
MODEchoice = input(':');
disp(' ')

% INFLUENCE FUNCTIONS
if MODEchoice == 0
    MODEmatACTIVE = IFmatACTIVE;
    numMODES = size(MODEmatACTIVE,2);

% ZERNIKE POLYNOMIALS
elseif MODEchoice == 1
    if strcmp(ActiveDM(1:3),'ALP') == 1
        [MODEmatACTIVE,numZERNfull] = project_modes_on_IF_mat('ZERNmatACTIVE_ALPAO',IFmatACTIVE);
    elseif strcmp(ActiveDM(1:3),'BMC') == 1
        [MODEmatACTIVE,numZERNfull] = project_modes_on_IF_mat('ZERNmatACTIVE_BMC',IFmatACTIVE);
    end
     % Optional truncation
    disp(['Use how many of the total ',num2str(numZERNfull),' Zernike polynomials: '])
    disp('For all modes:            [0]')
    ZERNchoice = input(':');

    if ZERNchoice == 0
        numMODES = numZERNfull;
    else
        numMODES = ZERNchoice;
        MODEmatACTIVE = MODEmatACTIVE(:,1:numMODES);
    end

% KARHUNEN-LOEVE MODES
elseif MODEchoice == 2
```

```
    if strcmp(ActiveDM(1:3),'ALP') == 1
        [MODEmatACTIVE,numKLfull] = project_modes_on_IF_mat('KLmat97ACTIVE_ALPAO',IFmatACTIVE);
    elseif strcmp(ActiveDM(1:3),'BMC') == 1
        [MODEmatACTIVE,numKLfull] = project_modes_on_IF_mat('KLmat97ACTIVE_BMC',IFmatACTIVE);
    end

    % Optional truncation
    disp(['Use how many of the total ',num2str(numKLfull),' KL modes: '])
    disp('For all modes:            [0]')
    KLchoice = input(':');

    if KLchoice == 0
        numMODES = numKLfull;
    else
        numMODES = KLchoice;
        MODEmatACTIVE = MODEmatACTIVE(:,1:numMODES);
    end

% DM MIRROR MODES
elseif MODEchoice == 3
    [DM_MODEmatACTIVE,DMmodes] = build_DM_mirror_modes(IFmatACTIVE,PUPIL);
    MODEmatACTIVE = normIM(DM_MODEmatACTIVE).*(10^-6);
    numMODES = size(MODEmatACTIVE,2);
end
MODEmatACTIVE_FULL = MODEmatACTIVE;

%% OPTION TO CHOOSE FEWER CONTROLLED MODES FOR TIME_ALPHA = 2 CASE
lowestMODE = 1;highestMODE = size(MODEmatACTIVE_FULL,2);
MODEmatACTIVE = MODEmatACTIVE_FULL(:,lowestMODE:highestMODE);
numMODES = size(MODEmatACTIVE,2);

%% BUILD RESPONSE MATRIX (RM)
disp('--------------------------------------------------------------------------')
disp('BUILDING RESPONSE MATRIX & DETERMINE LINEARITY')
disp('--------------------------------------------------------------------------')
% Response matrix
    pokeAmp  = 1;
% Determine pixel linearity
    EPcell = cell(1,2);
    EPcell{1} = EP_Flux;
    if ((PLANET ≠ 0) & (planetRMchoice == 1))
        EPcell{2} = EPplanet_Flux;
    else
        EPcell{2} = 0;
    end
    [weighted_pixel_map,RM_FULL] = ...
         determine_linearity(pokeAmp,MODEmatACTIVE_FULL,EPcell,PupilPlane,AmpDefocus,Defocus,vAPP_upper,...
vAPP_lower,WFSref,klam,WFS_positions,windowCROP,PSFscalefactor);

%% OPTION TO CHOOSE FEWER CONTROLLED MODES FOR TIME_ALPHA = 2 CASE
RM = RM_FULL(:,lowestMODE:highestMODE);

% DISPLAY RESPONSE MATRIX
figure;
for i = 1:numMODES
    imagesc(reshape(RM(:,i),[size(WFSref,1) size(WFSref,2)]));axis off;daspect([1 1 1])
    colormap jet;colorbar;title(['mode ',num2str(i),'/',num2str(numMODES)]);
    drawnow;
end

%% BUILD COMMAND MATRIX
disp('--------------------------------------------------------------------------')
disp('BUILDING LINEAR DARK FIELD CONTROL (LDFC) COMMAND MATRIX')
disp('--------------------------------------------------------------------------')
% % Set BF pixel threshold
    pixelthresh = -2.5;%-4 for at focus;%-2.5;for defocused
% Build LDFC control matix
    [LDFC_CM,mWINDOW,windowSIZE,SVDmodes] = ...
         Build_Weighted_LDFC_Command_Matrix(RM,numMODES,WFSref,weighted_pixel_map,pixelthresh);
    LDFC_CM = pokeAmp.*LDFC_CM;
    LDFCmap = zeros(size(WFSref));
```

```
    LDFCmap(mWINDOW) = 1;
    figure;imagesc(LDFCmap);axis off;daspect([1 1 1]);colormap gray

%% LOAD TIME-EVOLVING PHASE SCREENS
disp('Choose phase cube: ')
disp('1/f^2, time alpha 2    [1]')
disp('1/f^3  time alpha 2    [2]')
disp(' ')
disp('1/f^2, time alpha 3    [3]')
disp('1/f^3  time alpha 3    [4]')
disp(' ')
disp('1/f^2, time alpha 4    [5]')
disp('1/f^3  time alpha 4    [6]')
abchoice = input(':');
if abchoice == 1
    load oneoverf_squared_1024x1024_timealpha_2.mat
    abname = '1_fsquared_phase';
    timealpha = '2';
elseif abchoice == 2
    load oneoverf_cubed_1024x1024_timealpha_2.mat
    abname = '1_fcubed_phase';
    timealpha = '2';
elseif abchoice == 3
    load oneoverf_squared_1024x1024_timealpha_3.mat
    abname = '1_fsquared_phase';
    timealpha = '3';
elseif abchoice == 4
    load oneoverf_cubed_1024x1024_timealpha_3.mat
    abname = '1_fcubed_phase';
    timealpha = '3';
elseif abchoice == 5
    load oneoverf_squared_1024x1024.mat
    abname = '1_fsquared_phase';
    timealpha = '4';
elseif abchoice == 6
    load oneoverf_cubed_1024x1024.mat
    abname = '1_fcubed_phase';
    timealpha = '4';
end
KolPhaseCube = normIM(cnoise_padded);

%% CREATE / CHECK FOR DIRECTORY
if noisechoice == 1
    filename = ...
         char(horzcat('TEST_Simulation_LDFC_',abname,'_timealpha',timealpha,'_IWA_',num2str(IWA),'lamD_','OWA_',...
num2str(OWA),'lamD_',defocustitle));
elseif noisechoice == 0
    filename = ...
         char(horzcat('TEST_Simulation_LDFC_',abname,'_timealpha',timealpha,'_IWA_',num2str(IWA),'lamD_','OWA_',...
num2str(OWA),'lamD_',defocustitle,'_NOISELESS'));
end

dircheck = exist(filename,'dir');

%% INJECT PHASE ABERRATION
disp('--------------------------------------------------------------------------')
disp('INJECTING PHASE ABERRATION')
disp('--------------------------------------------------------------------------')
% Define number of phase screens
    NumShifts = size(KolPhaseCube,3);
% BUILD KOLMOGOROV PHASE SCREEN
    % LOW SPATIAL FREQUENCIES
    %     [KolPhase,¬]=apply_Kolmogorov(2*10^2,xsize,50,10^-4,10^200,klam,11/3,0);
    % MID SPATIAL FREQUENCIES
    %     [KolPhase,¬]=apply_Kolmogorov(1*10^2,xsize,50,10^-4,10^-3,klam,11/3,0);
    %     KolPhase = exp(1i.*KolPhaseCube(:,:,1));
    %     freq = 30;%39
    %     Amp = 2;%2
    %     KolPhase = exp(1i.*((Amp.*klam.*(10^-6)).*sin(freq.*X./(2.*r))));
% Measure injected phase screen [nm]
%     MaxAbAmpNM = max2(angle(KolPhase).*PupilPlane.*(10^6)/klam);
```

```
%     MinAbAmpNM = min2(angle(KolPhase).*PupilPlane.*(10^6)/klam);
%     [¬,PV_nm] = RMS_PV_calculator(angle(KolPhase).*(10^6)/klam,PupilPlane);
%     disp(['P-V amplitude: ',num2str(PV_nm),' nm'])

%% SAVE OPTIONS
disp('---------------------------------------------------------------------------')
disp('MAKE LDFC PUPIL/PSF MOVIE?')
disp('---------------------------------------------------------------------------')
disp('NO        [0]')
disp('YES       [1]')
moviechoice = input(':');
disp('---------------------------------------------------------------------------')
disp('CHOOSE THE PLOTS TO BE SAVED:')
disp('---------------------------------------------------------------------------')
if moviechoice == 1
disp('LDFC PUPIL/PSF MOVIE       [0]')
end
disp('FULL DARK HOLE CONTRAST    [1]')
disp('PUPIL PLANE RMS WFE        [2]')
disp('CONTRAST BY lambda/D BINS  [3]')
disp('DARK HOLE SPECKLES         [4]')
disp('LDFC CONVERGENCE PLOTS     [5]')
plotsavechoice = input(':');

%% BEGIN LDFC CLOSED-LOOP
disp('---------------------------------------------------------------------------')
disp('BEGINNING LINEAR DARK FIELD CONTROL (LDFC) MAIN LOOP')
disp('---------------------------------------------------------------------------')

% INITIALIZE PARAMETERS
gain = 0.6;
gain1 = gain;
gain2 = 0.4;
gaincounter = 15;
aTOTAL = 0;
loopcounter = 0;
LDFCimages = zeros(480,640,NumShifts);
ABimages = zeros(480,640,NumShifts);
LDFCcontrast = zeros(1,NumShifts);
ABcontrast = zeros(1,NumShifts);
DHmetric = zeros(1,NumShifts);
looptimer = zeros(1,NumShifts);
RMS_EP = zeros(1,NumShifts);
RMS_WFE = zeros(1,NumShifts);

%-------------------------------------------------------------------------
% (0) MAKE LDFC PUPIL/PSF MOVIE
%-------------------------------------------------------------------------
if sum(ismember(plotsavechoice,0)) == 1
    if dircheck == 7
        cd(filename)
    else
        mkdir(filename)
        cd(filename)
    end
    filename_video = horzcat(filename,char('.avi'));
    v = VideoWriter(filename_video);
    open(v);
end

% -----------------------------------------------------------------------
% BEGIN PHASE SCREEN SHIFTING LOOP
% -----------------------------------------------------------------------
for i = 1:NumShifts
    loopcounter = loopcounter + 1;
% Preallocate counters and vectors
        numLoops = 1;%4;%10;
        tryagain = zeros(1,10000);
        LDFCcounter = 0;
        convergencecounter = zeros(1,numLoops);
        DH_LDFC_avg_contrast = 0;
```

```
        state = 0;
% Set contrast convergence condition
        condition = round(abs(DH_avg_contrast)-0.1,2);
        DFcontrast = -condition;
% Inject speckle into DH
        KolPhase = exp(1i.*KolPhaseCube(:,:,i));
        PhaseAberration = KolPhase;
% DH EFC PSF aberrated by PhaseAberration
        AbField = REFfield.*PhaseAberration;
        [AbstarPSF] = VAPP_PROPAGATOR(AbField,vAPP_upper,vAPP_lower,EP_Flux.*Defocus);
        [AbplanetPSF] = VAPP_PROPAGATOR(AbField,vAPP_upper,vAPP_lower,EPplanet_Flux.*Defocus);
        AbPSF = AbstarPSF + AbplanetPSF;
        if  noisechoice == 1
            AbPSF = add_photon_noise(AbPSF,ΔT);
        end
% Aberrated science image without defocus
        [SCIstar_AbPSF] = VAPP_PROPAGATOR(AbField,vAPP_upper,vAPP_lower,EP_Flux);
        [SCIplanet_AbPSF] = VAPP_PROPAGATOR(AbField,vAPP_upper,vAPP_lower,EPplanet_Flux);
        SCI_AbPSF = SCIstar_AbPSF + SCIplanet_AbPSF;
        if  noisechoice == 1
            SCI_AbPSF = add_photon_noise(SCI_AbPSF,ΔT);
        end
% ------------------------------------------------------------------------
% BEGIN LDFC CORRECTION LOOP
% ------------------------------------------------------------------------
    while LDFCcounter < numLoops
        LDFCcounter = LDFCcounter + 1;
% Gain
        if loopcounter > gaincounter
            gain = gain2;
        end
% Take new aberrated PSF image
        if loopcounter == 1
            PSF = AbPSF;
        else
            PSF = LDFC_PSF;
        end
% Apply window
        PSFcropWINDOW = PSF.*windowCROP;
% --------BEGIN TIMER---------
tic
% ----------------------------
% Select, normalize, and combine WFS regions
        ab_upper_wfs = PSFcropWINDOW(upper_Ybeg:upper_Yend,upper_Xbeg:upper_Xend);
        ab_lower_wfs = PSFcropWINDOW(lower_Ybeg:lower_Yend,lower_Xbeg:lower_Xend);
        WFSab = horzcat(ab_lower_wfs,ab_upper_wfs);
% Calculate normalized intensity change
        ΔWFS = normIM(WFSab) - normIM(WFSref);
% Select and vectorize BF pixels (probes) from ΔImage
        LDFC_Probe = ΔWFS(mWINDOW)';
%-------------------------------------------------------------------
% Same as above, but more obvious what's happening
%     ΔImageVec = reshape(ΔImage,[size(ΔImage,1)*size(ΔImage,2),1]);
%     LDFC_Probe = ΔImageVec(mWINDOW');
%-------------------------------------------------------------------
% Derive actuator strokes by fitting BF pixels to LDFC control matrix
        aLDFC = - (LDFC_CM*LDFC_Probe).*gain;
% Update actuator strokes on each iteration
        aTOTAL = aTOTAL + aLDFC;
% Build DM command
        DMcommand = MODEmatACTIVE*aTOTAL;
% --------END TIMER---------
looptimer(loopcounter) = toc;
% --------------------------
% Apply actuator commands to DM
        LDFC_DMshape = reshape(DMcommand,[sqrt(length(MODEmatACTIVE)),sqrt(length(MODEmatACTIVE))]);
% Resulting LDFC correction field
        LDFCcorrection = exp(1i.*2.*klam.*LDFC_DMshape);
        LDFCfield = LDFCcorrection.*AbField;
% DH LDFC correction PSF
        [LDFCstar_PSF] = VAPP_PROPAGATOR(LDFCfield,vAPP_upper,vAPP_lower,EP_Flux.*Defocus);
```

```
        [LDFCplanet_PSF] = VAPP_PROPAGATOR(LDFCfield,vAPP_upper,vAPP_lower,EPplanet_Flux.*Defocus);
        LDFC_PSF = LDFCstar_PSF + LDFCplanet_PSF;
        if  noisechoice == 1
            LDFC_PSF = add_photon_noise(LDFC_PSF,∆T);
        end
% LDFC science image without defocus
        [SCIstar_LDFC_PSF] = VAPP_PROPAGATOR(LDFCfield,vAPP_upper,vAPP_lower,EP_Flux);
        [SCIplanet_LDFC_PSF] = VAPP_PROPAGATOR(LDFCfield,vAPP_upper,vAPP_lower,EPplanet_Flux);
        SCI_LDFC_PSF = SCIstar_LDFC_PSF + SCIplanet_LDFC_PSF;
        if  noisechoice == 1
            SCI_LDFC_PSF = add_photon_noise(SCI_LDFC_PSF,∆T);
        end
% -----------------------------------------------------------------------
% CHECK TO ENSURE LDFC LOOP IS CONVERGING ON EFC DF SOLUTION
% -----------------------------------------------------------------------
% Pre-LDFC average DF contrast (mag)
        if LDFCcounter == 1
            DH_AB_ROI = SCI_AbPSF.*DHwindowCROP;
            DH_AB_avg_contrast = mean2(log10(abs(DH_AB_ROI(DH_AB_ROI≠0)./(max2(SCI_AbPSF)))));
            DH_AB0 = round(DH_AB_avg_contrast,2);
            ABcontrast(loopcounter) = DH_AB0;
            tryagain(1) = 0;
            DHmetric(1) = -DH_AB0;
        end

% Post-LDFC average DF contrast (mag)
        DH_LDFC_ROI = SCI_LDFC_PSF.*DHwindowCROP;
        DH_LDFC_avg_contrast = mean2(log10(abs(DH_LDFC_ROI(DH_LDFC_ROI≠0)./max2(SCI_LDFC_PSF))));

% Current LDFC state
        LDFCcontrast(loopcounter) = round(DH_LDFC_avg_contrast,2);
        state = round(abs(DH_LDFC_avg_contrast),2);
        if (state ≥ condition)
            convergencecounter(LDFCcounter) = 1;
        end
% Record contrast
%         contrast(LDFCcounter+1) = -state;
% Post-LDFC contrast improvement (∆ mag)
        Delta_Contrast = state - DH_AB0;
% DF contrast improvement metric
        DHmetric(LDFCcounter+1) = state;
        DeltaMetric = (DHmetric(LDFCcounter+1)) - (DHmetric(LDFCcounter));
        Improvement = DHmetric(LDFCcounter) - abs(DH_AB0);
        disp([num2str(loopcounter),'/',num2str(NumShifts),'  contrast = ',num2str(DHmetric(LDFCcounter+1))])
% Saves LDFC PSF and actuator commands if DF contrast is NOT improving to re-fit with new CM
        if (DeltaMetric > 0)
            tryagain(LDFCcounter+1) = 0;
        elseif (DeltaMetric < 0) && ((condition - state) > 0.6)
            tryagain(LDFCcounter+1) = 1;
        end
% -----------------------------------------------------------------------
% VISUALIZE RESULTS
% -----------------------------------------------------------------------
        EPcrop = imcrop((angle(PhaseAberration).*PupilPlane.*(10^6)/klam),[(xcen-243/2) (ycen-243/2) (243-1) ...
            (243-1)]);
        EPcrop = PupilPlaneCrop.*(EPcrop - mean2(EPcrop(EPcrop≠0)));
        [RMS_EP(loopcounter),¬] = RMS_PV_calculator(EPcrop,PupilPlaneCrop);
        [¬,PV_nm] = RMS_PV_calculator(angle(KolPhase).*(10^6)/klam,PupilPlane);

        CORRECTIONcrop = imcrop((LDFC_DMshape.*PupilPlane.*(10^6)*2),[(xcen-243/2) (ycen-243/2) (243-1) ...
            (243-1)])-mean2(EPcrop);
        CORRECTIONcrop = PupilPlaneCrop.*(CORRECTIONcrop - mean2(CORRECTIONcrop(CORRECTIONcrop≠0)));

        RESIDUALcrop = imcrop(angle(LDFCfield).*PupilPlane.*(10^6)/klam,[(xcen-243/2) (ycen-243/2) (243-1) ...
            (243-1)]);
        RESIDUALcrop = PupilPlaneCrop.*(RESIDUALcrop - mean2(RESIDUALcrop(RESIDUALcrop≠0)));
        [RMS_WFE(loopcounter),PV_WFE] = RMS_PV_calculator(RESIDUALcrop,PupilPlaneCrop);

if sum(ismember(plotsavechoice,0)) == 1
        figure(4);
        subplot(2,3,1);imagesc(EPcrop);axis off;axis square;colormap jet;title({['Incident WF ...
```

```
                ',num2str(loopcounter),'/',num2str(NumShifts)],['P-V Aberration Amp: ',num2str(round(PV_nm,1)),' ...
                nm'],['RMS: ',num2str(RMS_EP(loopcounter)),' nm']},'FontSize',12);drawnow;
        subplot(2,3,2);imagesc(CORRECTIONcrop);axis off;axis square;colormap jet;title('DM ...
                Correction','FontSize',12);drawnow;
        subplot(2,3,3);imagesc(RESIDUALcrop);axis off;axis square;colormap jet;caxis([min2(EPcrop) ...
                max2(EPcrop)]);title({'Residual WF ',['RMS: ',num2str(RMS_WFE(loopcounter)),' ...
                nm']},'FontSize',12);drawnow;

        B = colorbar('southoutside');
        set(B, 'Position', [.145 0.52 0.745 .02]) %([left bottom width height])
        set(get(B,'title'),'string','Wavefront Error P-V [nm]','FontSize',14);

        subplot(2,3,4);imagesc(log10(abs(normIM(SCI_AbPSF))));title({'LDFC OFF: Aberrated DF',['Avg Log10 ...
                Contrast: ',num2str(ABcontrast(loopcounter))]},'FontSize',12);axis off;daspect([1 1 ...
                1]);caxis([cminLOG cmaxLOG]);colormap jet;drawnow;
        subplot(2,3,5);imagesc(log10(abs(normIM(SCI_LDFC_PSF))));title({'LDFC ON: Corrected DF',['Avg Log10 ...
                Contrast: ',num2str(LDFCcontrast(loopcounter))]},'FontSize',12);axis off;daspect([1 1 ...
                1]);caxis([cminLOG cmaxLOG]);colormap jet;drawnow;
        subplot(2,3,6);imagesc(log10(abs(normIM(SCI_PSFref))));title({'Ideal vAPP DF',['Avg Log10 Contrast: ...
                ',num2str(-condition)]},'FontSize',12);axis off;daspect([1 1 1]);caxis([cminLOG ...
                cmaxLOG]);colormap jet;drawnow;

        C = colorbar('southoutside');
        set(C, 'Position', [.145 0.05 0.745 .02]) %([left bottom width height])
        set(get(C,'title'),'string','Log_1_0 Contrast','FontSize',14);

        % MAKE MOVIE
        set(gcf, 'Position', get(0, 'Screensize'));
        frame = getframe(gcf);
        writeVideo(v,frame);

        if i == NumShifts
            set(gcf, 'Position', get(0, 'Screensize'));
            filename_jpg = 'LDFC_final_frame_example.jpg';
            filename_fig = 'LDFC_final_frame_example.fig';
            set(gcf, 'Position', get(0, 'Screensize'));
            cd(filename)
            saveas(gcf,filename_jpg,'jpg')
            saveas(gcf,filename_fig,'fig')
        end

end
%--------------------------------------------------------------------------

        LDFCimages(:,:,loopcounter) = SCI_LDFC_PSF;
        ABimages(:,:,loopcounter) = SCI_AbPSF;

    end
    disp(' ')
end
% MAKE MOVIE
if sum(ismember(plotsavechoice,0)) == 1
    close(v);
end
%-------------------------------------------------------------------------
%% (1) PLOT FULL DARK HOLE CONTRAST
%-------------------------------------------------------------------------
disp(['average time per iteration: ',num2str(mean(looptimer(looptimer≠0))*(10^3)),'millisec'])

figure;
plot(ABcontrast,'-r','LineWidth',3);
hold on;plot(mean(ABcontrast).*ones(size(LDFCcontrast)),'r','LineWidth',2);
hold on;plot(LDFCcontrast,'-g','LineWidth',3);
hold on;plot(mean(LDFCcontrast).*ones(size(LDFCcontrast)),'g','LineWidth',2)
hold on;plot(DFcontrast.*ones(size(LDFCcontrast)),'b','LineWidth',3)
xlabel('screen number','FontSize',20);ylabel('log_1_0 contrast','FontSize',20);grid minor;
legend('LDFC OFF','average contrast','LDFC ON','average contrast','ideal vAPP contrast');
if strcmp(abname,'1_fcubed_phase') == 1
    title('Closed-loop LDFC correction for a temporally evolving 1/f^3 phase aberration','FontSize',24)
elseif strcmp(abname,'1_fsquared_phase') == 1
    title('Closed-loop LDFC correction for a temporally evolving 1/f^2 phase aberration','FontSize',24)
```

```
end

if sum(ismember(plotsavechoice,1)) == 1
    if dircheck == 7
        cd(filename)
    else
        mkdir(filename)
        cd(filename)
    end
    filename_jpg = horzcat(filename,char('.jpg'));
    filename_fig = horzcat(filename,char('.fig'));
    set(gcf, 'Position', get(0, 'Screensize'));
    saveas(gcf,filename_jpg,'jpg')
    saveas(gcf,filename_fig,'fig')
end
contrastmin = find(LDFCcontrast(1:300) == min(LDFCcontrast(1:300)),1,'first');
%-------------------------------------------------------------------------

%------------------------------------------------------------------------
%% (2) PLOT PUPIL PLANE RMS WFE
%------------------------------------------------------------------------
figure;
plot(RMS_EP,'-r','LineWidth',3);
hold on;plot(mean(RMS_EP).*ones(size(RMS_EP)),'--r','LineWidth',2);
hold on;plot(RMS_WFE,'-g','LineWidth',3);
hold on;plot(mean(RMS_WFE).*ones(size(RMS_WFE)),'--g','LineWidth',2)
xlabel('screen number','FontSize',20);ylabel('RMS Wavefront Error (WFE)','FontSize',20);grid minor;
legend('LDFC OFF','average RMS WFE','LDFC ON','average RMS WFE');
if strcmp(abname,'1_fcubed_phase') == 1
    title('Closed-loop LDFC correction for a temporally evolving 1/f^3 phase aberration: RMS WFE','FontSize',24)
elseif strcmp(abname,'1_fsquared_phase') == 1
    title('Closed-loop LDFC correction for a temporally evolving 1/f^2 phase aberration: RMS WFE','FontSize',24)
end

if sum(ismember(plotsavechoice,2)) == 1
    if dircheck == 7
        cd(filename)
    else
        mkdir(filename)
        cd(filename)
    end
    filename_jpg = horzcat(filename,char('_RMS_WFE.jpg'));
    filename_fig = horzcat(filename,char('_RMS_WFE.fig'));
    set(gcf, 'Position', get(0, 'Screensize'));
    saveas(gcf,filename_jpg,'jpg')
    saveas(gcf,filename_fig,'fig')
end

%------------------------------------------------------------------------
%% (3) PLOT CONTRAST BY lambda/D BINS
%------------------------------------------------------------------------
if noisechoice == 1
    if (PLANET ≠ 0)
        SCI_PSFref_noise = add_photon_noise(SCIstar_PSFref,ΔT);
        SCIwithplanet_PSFref_noise = add_photon_noise(SCI_PSFref,ΔT);
    else
        SCI_PSFref_noise = add_photon_noise(SCI_PSFref,ΔT);
    end
    maxStar_noise = max2(SCI_PSFref_noise);
else
    if (PLANET ≠ 0)
        SCI_PSFref_noise = SCIstar_PSFref;
        SCIwithplanet_PSFref_noise = SCI_PSFref;
    else
        SCI_PSFref_noise = SCI_PSFref;
    end
    maxStar_noise = maxStar;
end

contrast_logscale_factor = 1/maxStar_noise;
numSCREENS = loopcounter;
```

```
%-----------------------------------------------------------------------
% CROP DATA
%------------------------------------------------------------------------
xcenUPPER = 318+4;
ycenUPPER = 152;

xcenLOWER = 319-1;
ycenLOWER = 332;

cropdim = 130;

if (PLANET ≠ 0)
    Ref_UPPERplanet = imcrop(SCIwithplanet_PSFref_noise,[(xcenUPPER-cropdim/2) (ycenUPPER-cropdim/2) ...
          (cropdim-1) (cropdim-1)]);
    Ref_LOWERplanet = fliplr(imcrop(SCIwithplanet_PSFref_noise,[(xcenLOWER-cropdim/2) (ycenLOWER-cropdim/2) ...
          (cropdim-1) (cropdim-1)]));
end

Ref_UPPER = imcrop(SCI_PSFref_noise,[(xcenUPPER-cropdim/2) (ycenUPPER-cropdim/2) (cropdim-1) (cropdim-1)]);
Ref_LOWER = fliplr(imcrop(SCI_PSFref_noise,[(xcenLOWER-cropdim/2) (ycenLOWER-cropdim/2) (cropdim-1) ...
      (cropdim-1)]));

ABERRATED_CUBE_UPPER = zeros(cropdim,cropdim,loopcounter);
ABERRATED_CUBE_LOWER = zeros(cropdim,cropdim,loopcounter);
LDFC_CUBE_UPPER = zeros(cropdim,cropdim,loopcounter);
LDFC_CUBE_LOWER = zeros(cropdim,cropdim,loopcounter);

for i = 1:numSCREENS
    ABERRATED_CUBE_UPPER(:,:,i) = imcrop(ABimages(:,:,i),[(xcenUPPER-cropdim/2) (ycenUPPER-cropdim/2) ...
          (cropdim-1) (cropdim-1)]);
    ABERRATED_CUBE_LOWER(:,:,i) = fliplr(imcrop(ABimages(:,:,i),[(xcenLOWER-cropdim/2) (ycenLOWER-cropdim/2) ...
          (cropdim-1) (cropdim-1)]));
    LDFC_CUBE_UPPER(:,:,i) = imcrop(LDFCimages(:,:,i),[(xcenUPPER-cropdim/2) (ycenUPPER-cropdim/2) ...
          (cropdim-1) (cropdim-1)]);
    LDFC_CUBE_LOWER(:,:,i) = fliplr(imcrop(LDFCimages(:,:,i),[(xcenLOWER-cropdim/2) (ycenLOWER-cropdim/2) ...
          (cropdim-1) (cropdim-1)]));
end
%------------------------------------------------------------------------
% CREATE MASK
%------------------------------------------------------------------------
% pixel scale: 1 pixel = 0.23 lambda/D or 4 pixels = 1 lambda/D
pixelscale = 0.23;
x = linspace(-1,1,cropdim);
[X,Y] = meshgrid(x,x);
R = sqrt(X.^2 + Y.^2);
DHLimit = 0.2;
numBINS = OWA - IWA; % Returns 1 lambda/D bins
IWA_pixels = IWA/pixelscale;
OWA_pixels = OWA/pixelscale;
lamDbins = linspace(IWA,OWA,numBINS+1);
lamDbins_pixels = linspace(IWA_pixels,OWA_pixels,numBINS + 1);
r = 2.*lamDbins_pixels./cropdim;
mask_UPPER = zeros(cropdim,cropdim,numBINS);
mask_LOWER = zeros(cropdim,cropdim,numBINS);
for i = 1:numBINS
   mask_UPPER(:,:,i) = (abs(R<r(i+1))-abs(R<r(i))).*circshift((X>(DHLimit.*Y.*-cosd(60))),[0 8]).*(X>0.01);
   mask_LOWER(:,:,i) = (abs(R<r(i+1))-abs(R<r(i))).*circshift((X>(DHLimit.*Y.*cosd(60))),[0 8]).*(X>0.01);
end
%----------------------MASK FOR PLOTTING----------------------------------
mask_UPPER_TOTAL = zeros(size(mask_UPPER,1),size(mask_UPPER,2));
mask_LOWER_TOTAL = zeros(size(mask_UPPER,1),size(mask_UPPER,2));
for i = 1:numBINS
    if (mod(i,2) == 1)
        amp = 1;
    else
        amp = -1;
    end
    mask_UPPER_TOTAL = mask_UPPER_TOTAL + amp.*mask_UPPER(:,:,i);
    mask_LOWER_TOTAL = mask_LOWER_TOTAL + amp.*mask_LOWER(:,:,i);
end

```

```matlab
mask_UPPER_TOTAL = mask_UPPER_TOTAL.*circshift((X>(DHLimit.*Y.*-cosd(60))),[0 8]);
mask_LOWER_TOTAL = mask_LOWER_TOTAL.*circshift((X>(DHLimit.*Y.*cosd(60))),[0 8]);

numticks = 7;
figure;
subplot(1,2,1);imagesc(mask_UPPER_TOTAL);axis square;colormap gray
xticks(linspace(1, cropdim, numticks));xticklabels(linspace(-15 , 15 , ...
      numticks));xlabel('\lambda/D','FontSize',14)
yticks(linspace(1, cropdim, numticks));yticklabels(linspace(-15 , 15 , ...
      numticks));ylabel('\lambda/D','FontSize',14)
title('Upper PSF \lambda/D Binning','FontSize',18)
subplot(1,2,2);imagesc(mask_LOWER_TOTAL);axis square;colormap gray
xticks(linspace(1, cropdim, numticks));xticklabels(linspace(-15 , 15 , ...
      numticks));xlabel('\lambda/D','FontSize',14)
yticks(linspace(1, cropdim, numticks));yticklabels(linspace(-15 , 15 , ...
      numticks));ylabel('\lambda/D','FontSize',14)
title('Lower PSF \lambda/D Binning','FontSize',18)

figure;
subplot(1,2,1);imagesc(real(log10(normIM(Ref_UPPER))));axis square;colormap jet;title('Upper ...
      PSF','FontSize',14);caxis([-5 0]);grid on
xticks(linspace(1, cropdim, numticks));xticklabels(linspace(-15 , 15 , ...
      numticks));xlabel('\lambda/D','FontSize',14)
yticks(linspace(1, cropdim, numticks));yticklabels(linspace(-15 , 15 , ...
      numticks));ylabel('\lambda/D','FontSize',14)
drawcircle_color(linspace(IWA,OWA,numBINS+1)./pixelscale,'w',cropdim,cropdim,0,0,2);
drawcircle_color([2 11]./pixelscale,'r',cropdim,cropdim,0,0,3);
subplot(1,2,2);imagesc(real(log10(normIM(Ref_LOWER))));axis square;colormap jet;title('Lower ...
      PSF','FontSize',14);caxis([-5 0]);grid on
xticks(linspace(1, cropdim, numticks));xticklabels(linspace(-15 , 15 , ...
      numticks));xlabel('\lambda/D','FontSize',14)
yticks(linspace(1, cropdim, numticks));yticklabels(linspace(-15 , 15 , ...
      numticks));ylabel('\lambda/D','FontSize',14)
drawcircle_color(linspace(IWA,OWA,numBINS+1)./pixelscale,'w',cropdim,cropdim,0,0,2);
drawcircle_color([2 11]./pixelscale,'r',cropdim,cropdim,0,0,3);

%-------------------------------------------------------------------------
% DARK HOLE COUNTS
%-------------------------------------------------------------------------
cminCONTRAST = -6;
cmaxCONTRAST = -1.7;

DH_REF_U = zeros(1,numBINS);
DH_REF_L = zeros(1,numBINS);

DH_ABERRATED_UPPER_COUNTS = zeros(numBINS,numSCREENS);
DH_LDFC_UPPER_COUNTS = zeros(numBINS,numSCREENS);
DH_ABERRATED_LOWER_COUNTS = zeros(numBINS,numSCREENS);
DH_LDFC_LOWER_COUNTS = zeros(numBINS,numSCREENS);

for j = 1:numBINS
    if (PLANET ≠ 0)
        DH_REF_U(j) = mean2(Ref_UPPERplanet(mask_UPPER(:,:,j) == 1)).*contrast_logscale_factor;
        DH_REF_L(j) = mean2(Ref_LOWERplanet(mask_LOWER(:,:,j) == 1)).*contrast_logscale_factor;
    else
        DH_REF_U(j) = mean2(Ref_UPPER(mask_UPPER(:,:,j) == 1)).*contrast_logscale_factor;
        DH_REF_L(j) = mean2(Ref_LOWER(mask_LOWER(:,:,j) == 1)).*contrast_logscale_factor;
    end
    for i = 1:numSCREENS

        im_AB_U = abs(ABERRATED_CUBE_UPPER(:,:,i));
        im_LDFC_U = abs(LDFC_CUBE_UPPER(:,:,i));
        im_AB_L = abs(ABERRATED_CUBE_LOWER(:,:,i));
        im_LDFC_L = abs(LDFC_CUBE_LOWER(:,:,i));

        DH_ABERRATED_UPPER_COUNTS(j,i) = mean2(im_AB_U(mask_UPPER(:,:,j) == 1)).*contrast_logscale_factor;
        DH_LDFC_UPPER_COUNTS(j,i) = mean2(im_LDFC_U(mask_UPPER(:,:,j) == 1)).*contrast_logscale_factor;
        DH_ABERRATED_LOWER_COUNTS(j,i) = mean2(im_AB_L(mask_LOWER(:,:,j) == 1)).*contrast_logscale_factor;
        DH_LDFC_LOWER_COUNTS(j,i) = mean2(im_LDFC_L(mask_LOWER(:,:,j) == 1)).*contrast_logscale_factor;
    end
end
```

```
for j = 1:numBINS
        figure;
        subplot(1,2,1)
        plot(log10(DH_REF_U(j).*ones(1,numSCREENS)),'b','LineWidth',3);hold on
        plot(log10(DH_ABERRATED_UPPER_COUNTS(j,:)),'r','LineWidth',3);hold on
        plot(log10(mean(DH_ABERRATED_UPPER_COUNTS(j,:)).*ones(1,numSCREENS)),'--r','LineWidth',3);hold on
        plot(log10(DH_LDFC_UPPER_COUNTS(j,:)),'g','LineWidth',3);hold on
        plot(log10(mean(DH_LDFC_UPPER_COUNTS(j,:)).*ones(1,numSCREENS)),'--g','LineWidth',3);hold on
        grid minor;
        xlabel('screen #','FontSize',18);ylabel('log_1_0 scale contrast','FontSize',18)
        title(['Upper Dark Hole Speckle Contrast: ',num2str(lamDbins(j)),' - ...
             ',num2str(lamDbins(j+1)),'\lambda/D'],'FontSize',18)
        legend('Ideal DH contrast','Aberrated DH contrast','average contrast','LDFC corrected DH ...
             contrast','average contrast','Location','best')
        xlim([1 numSCREENS]);
        ylim([cminCONTRAST cmaxCONTRAST])

        subplot(1,2,2)
        plot(log10(DH_REF_L(j).*ones(1,numSCREENS)),'b','LineWidth',3);hold on
        plot(log10(DH_ABERRATED_LOWER_COUNTS(j,:)),'r','LineWidth',3);hold on
        plot(log10(mean(DH_ABERRATED_LOWER_COUNTS(j,:))).*ones(1,numSCREENS),'--r','LineWidth',3);hold on
        plot(log10(DH_LDFC_LOWER_COUNTS(j,:)),'g','LineWidth',3);hold on
        plot(log10(mean(DH_LDFC_LOWER_COUNTS(j,:))).*ones(1,numSCREENS),'--g','LineWidth',3);hold on
        grid minor;
        xlabel('screen #','FontSize',18);ylabel('log_1_0 scale contrast','FontSize',18)
        title(['Lower Dark Hole Speckle Contrast: ',num2str(lamDbins(j)),' - ...
             ',num2str(lamDbins(j+1)),'\lambda/D'],'FontSize',18)
        legend('Ideal DH contrast','Aberrated DH contrast','average contrast','LDFC corrected DH ...
             contrast','average contrast','Location','best')
        xlim([1 numSCREENS]);
        ylim([cminCONTRAST cmaxCONTRAST])
        if sum(ismember(plotsavechoice,3)) == 1
            set(gcf, 'Position', get(0, 'Screensize'));
            filename_jpg = horzcat(filename,'_',num2str(lamDbins(j)),'_',num2str(lamDbins(j+1)),'lamD',...
char('_contrast_stabilization.jpg'));
            filename_fig = horzcat(filename,'_',num2str(lamDbins(j)),'_',num2str(lamDbins(j+1)),'lamD',...
char('_contrast_stabilization.fig'));
            set(gcf, 'Position', get(0, 'Screensize'));
            cd(filename)
            saveas(gcf,filename_jpg,'jpg')
            saveas(gcf,filename_fig,'fig')
        end
end

%-------------------------------------------------------------------------
%% (4) PLOT DARK HOLE SPECKLES
%-------------------------------------------------------------------------
if sum(ismember(plotsavechoice,4)) == 1
       if dircheck == 7
        cd(filename)
    else
        mkdir(filename)
        cd(filename)
    end
    filename_video = horzcat(filename,char('_SPECKLE_VIDEO.avi'));
    v = VideoWriter(filename_video);
    open(v);
end
cmax = max2(sum(mask_UPPER,3).*contrast_logscale_factor.*((ABERRATED_CUBE_UPPER(:,:,1)) - (Ref_UPPER)));
cmin = -cmax;

 numticks = 7;

 figure;
for i = 1:numSCREENS
    subplot(1,4,1);imagesc(sum(mask_UPPER,3).*contrast_logscale_factor.*((ABERRATED_CUBE_UPPER(:,:,i)) - ...
          (Ref_UPPER)));daspect([1 1 1]);caxis([cmin cmax]);title({[num2str(i),'/',num2str(numSCREENS)],'Upper ...
          Dark Hole','Aberrated'},'FontSize',14);
    xticks(linspace(1, cropdim, numticks));xticklabels(linspace(-15 , 15 , ...
          numticks));xlabel('\lambda/D','FontSize',14)
    yticks(linspace(1, cropdim, numticks));yticklabels(linspace(-15 , 15 , ...
```

```
            numticks));ylabel('\lambda/D','FontSize',14)
    drawcircle_color(11./pixelscale,'r',cropdim,cropdim,0,0,2)
    subplot(1,4,2);imagesc(sum(mask_UPPER,3).*contrast_logscale_factor.*((LDFC_CUBE_UPPER(:,:,i)) - ...
            (Ref_UPPER)));daspect([1 1 1]);caxis([cmin cmax]);title({'Upper Dark Hole','LDFC - ...
            Corrected'},'FontSize',14);
    xticks(linspace(1, cropdim, numticks));xticklabels(linspace(-15 , 15 , ...
            numticks));xlabel('\lambda/D','FontSize',14)
    yticks(linspace(1, cropdim, numticks));yticklabels(linspace(-15 , 15 , ...
            numticks));ylabel('\lambda/D','FontSize',14)
    drawcircle_color(11./pixelscale,'r',cropdim,cropdim,0,0,2);
    subplot(1,4,3);imagesc(sum(mask_LOWER,3).*contrast_logscale_factor.*((ABERRATED_CUBE_LOWER(:,:,i)) - ...
            (Ref_LOWER)));daspect([1 1 1]);caxis([cmin cmax]);title({'Lower Dark Hole','Aberrated'},'FontSize',14);
    xticks(linspace(1, cropdim, numticks));xticklabels(linspace(-15 , 15 , ...
            numticks));xlabel('\lambda/D','FontSize',14)
    yticks(linspace(1, cropdim, numticks));yticklabels(linspace(-15 , 15 , ...
            numticks));ylabel('\lambda/D','FontSize',14)
    drawcircle_color(11./pixelscale,'r',cropdim,cropdim,0,0,2);
    subplot(1,4,4);imagesc(sum(mask_LOWER,3).*contrast_logscale_factor.*((LDFC_CUBE_LOWER(:,:,i)) - ...
            (Ref_LOWER)));daspect([1 1 1]);caxis([cmin cmax]);title({'Lower Dark Hole','LDFC - ...
            Corrected'},'FontSize',14);
    xticks(linspace(1, cropdim, numticks));xticklabels(linspace(-15 , 15 , ...
            numticks));xlabel('\lambda/D','FontSize',14)
    yticks(linspace(1, cropdim, numticks));yticklabels(linspace(-15 , 15 , ...
            numticks));ylabel('\lambda/D','FontSize',14)
    drawcircle_color(11./pixelscale,'r',cropdim,cropdim,0,0,2);
    g = colorbar('southoutside','Position',[0.13 0.1 0.78 0.03],'FontSize',14);colormap jet;
    set(get(g,'title'),'string','Speckle Contrast','FontSize',14);

    if sum(ismember(plotsavechoice,4)) == 1
        set(gcf, 'Position', get(0, 'Screensize'));
        frame = getframe(gcf);
        writeVideo(v,frame);
    end
    clf
end
if sum(ismember(plotsavechoice,4)) == 1
    close(v);
end

%-------------------------------------------------------------------------
%% PLOT DARK HOLE CONVERGENCE
%-------------------------------------------------------------------------
 cmax = max2(sum(mask,3).*contrast_logscale_factor.*((ABERRATED_CUBE_UPPER(:,:,1)) - (AB_ref_UPPER)));
 cmin = -cmax;

numticks = 7;
n_conv_screens = 8;
screennumber = round(linspace(1,contrastmin,8));

%--------------------------UPPER LDFC CUBE------------------------------
for i = 1:n_conv_screens
    figure(28);
    if i == 1
        subplot(2,n_conv_screens/2,1);imagesc(sum(mask_UPPER,3).*contrast_logscale_factor.*...
((ABERRATED_CUBE_UPPER(:,:,1)) - (Ref_UPPER)));daspect([1 1 1]);caxis([cmin cmax]);title('Initial ...
     Aberration','FontSize',14);
    else
        subplot(2,n_conv_screens/2,i);imagesc(sum(mask_UPPER,3).*contrast_logscale_factor.*...
((LDFC_CUBE_UPPER(:,:,screennumber(i-1))) - (Ref_UPPER)));daspect([1 1 1]);caxis([cmin ...
     cmax]);title(['Iteration ',num2str(screennumber(i-1))],'FontSize',14);
    end
    xticks(linspace(1, cropdim, numticks));xticklabels(linspace(-15 , 15 , ...
            numticks));xlabel('\lambda/D','FontSize',10)
    yticks(linspace(1, cropdim, numticks));yticklabels(linspace(-15 , 15 , ...
            numticks));ylabel('\lambda/D','FontSize',10)
    drawcircle_color(11./pixelscale,'r',cropdim,cropdim,0,0,2)
end
    h = colorbar('southoutside','Position',[0.13 0.47 0.78 0.03],'FontSize',10);
    set(get(h,'title'),'string','Speckle Contrast','FontSize',14);
    colormap jet;
if sum(ismember(plotsavechoice,5)) == 1
```

```
        set(gcf, 'Position', get(0, 'Screensize'));
        filename_jpg = horzcat(filename,char('_DH_CONVERGENCE_LDFC_upper.jpg'));
        filename_fig = horzcat(filename,char('_DH_CONVERGENCE_LDFC_upper.fig'));
        set(gcf, 'Position', get(0, 'Screensize'));
        cd(filename)
        saveas(gcf,filename_jpg,'jpg')
        saveas(gcf,filename_fig,'fig')
end

%---------------------------LOWER LDFC CUBE--------------------------------
for i = 1:n_conv_screens
    figure(30);
    if i == 1
        subplot(2,n_conv_screens/2,1);imagesc(sum(mask_LOWER,3).*contrast_logscale_factor.*...
((ABERRATED_CUBE_LOWER(:,:,1)) - (Ref_LOWER)));daspect([1 1 1]);caxis([cmin cmax]);title('Initial ...
     Aberration','FontSize',14);
    else
        subplot(2,n_conv_screens/2,i);imagesc(sum(mask_LOWER,3).*contrast_logscale_factor.*...
((LDFC_CUBE_LOWER(:,:,screennumber(i-1))) - (Ref_LOWER)));daspect([1 1 1]);caxis([cmin ...
     cmax]);title(['Iteration ',num2str(screennumber(i-1))],'FontSize',14);
    end
    xticks(linspace(1, cropdim, numticks));xticklabels(linspace(-15 , 15 , ...
         numticks));xlabel('\lambda/D','FontSize',10)
    yticks(linspace(1, cropdim, numticks));yticklabels(linspace(-15 , 15 , ...
         numticks));ylabel('\lambda/D','FontSize',10)
    drawcircle_color(11./pixelscale,'r',cropdim,cropdim,0,0,2)
end
    k = colorbar('southoutside','Position',[0.13 0.47 0.78 0.03],'FontSize',10);
    set(get(k,'title'),'string','Speckle Contrast','FontSize',14);
    colormap jet;
if sum(ismember(plotsavechoice,5)) == 1
        set(gcf, 'Position', get(0, 'Screensize'));
        filename_jpg = horzcat(filename,char('_DH_CONVERGENCE_LDFC_lower.jpg'));
        filename_fig = horzcat(filename,char('_DH_CONVERGENCE_LDFC_lower.fig'));
        set(gcf, 'Position', get(0, 'Screensize'));
        cd(filename)
        saveas(gcf,filename_jpg,'jpg')
        saveas(gcf,filename_fig,'fig')
end


%% WRITE DATA TO FILE
cd(filename)

fileID = fopen('DATA_PARAMETERS.txt','w');
fprintf(fileID,todaysdate,' \r\n');
fprintf(fileID,' \r\n');
fprintf(fileID,' \r\n');
if (PLANET ≠ 0)
    if (planetREFchoice == 0)
        fprintf(fileID,'Planet NOT in reference image \r\n');
    else
        fprintf(fileID,'Planet in reference image \r\n');
    end
        if (planetRMchoice == 0)
        fprintf(fileID,'Planet NOT in response matrix \r\n');
    else
        fprintf(fileID,'Planet in response matrix \r\n');
        end
end
fprintf(fileID,' \r\n');
fprintf(fileID,'Noise choice: ');
if (noisechoice == 0)
    fprintf(fileID,'NOISELESS \r\n');
else
    fprintf(fileID,'WITH PHOTON NOISE \r\n');
end
fprintf(fileID,' \r\n');
fprintf(fileID,'Spatial frequency content: ');
fprintf(fileID,abname,'\r\n');
fprintf(fileID,' \r\n');
```

```
fprintf(fileID,' \r\n');
fprintf(fileID,'Correlation time alpha: ');
fprintf(fileID,timealpha,'\r\n');
fprintf(fileID,' \r\n');
fprintf(fileID,' \r\n');
fprintf(fileID,'Stellar magnitude: ');
fprintf(fileID,'%d\r\n',stellarMAG);
fprintf(fileID,' \r\n');
fprintf(fileID,'Loop frequency [Hz]: ');
fprintf(fileID,'%d\r\n',LoopFrequency_Hz);
fprintf(fileID,' \r\n');
fprintf(fileID,'Exposure time [seconds]: ');
fprintf(fileID,'%e\r\n',ΔT);
fprintf(fileID,' \r\n');
fprintf(fileID,'WFS defocus [nm]: ');
fprintf(fileID,'%d\r\n',AmpDefocus);
fprintf(fileID,' \r\n');
fprintf(fileID,'Pixel threshold [log10]: ');
fprintf(fileID,'%d\r\n',pixelthresh);
fprintf(fileID,' \r\n');
fprintf(fileID,'Number of control modes: ');
fprintf(fileID,'%d\r\n',numMODES);
fprintf(fileID,' \r\n');
fprintf(fileID,'Gains: ');
fprintf(fileID,'%f %f\r\n',gain1);
fprintf(fileID,'%f %f\r\n',gain2);
fprintf(fileID,' \r\n');
fprintf(fileID,' \r\n');
fprintf(fileID,'IWA [lambda/D]: ');
fprintf(fileID,'%d\r\n',IWA);
fprintf(fileID,' \r\n');
fprintf(fileID,'OWA [lambda/D]: ');
fprintf(fileID,'%d\r\n',OWA);
fprintf(fileID,' \r\n');
fprintf(fileID,'Max log scale speckle contrast: ');
fprintf(fileID,'%e\r\n',cmax);
fprintf(fileID,' \r\n');
fprintf(fileID,'Pupil phase PV [nm]: ');
fprintf(fileID,'%g\r\n',PV_nm);
fprintf(fileID,' \r\n');
fprintf(fileID,'Number of screens: ');
fprintf(fileID,'%d\r\n',numSCREENS);
fclose(fileID);
```

A.2.2 Response matrix generation

```
function [weighted_pixel_map,RM] = ...
      determine_linearity(pokeAmp,MODEmatACTIVE,EPcell,PupilPlane,AmpDefocus,Defocus,vAPP_upper,...
vAPP_lower,WFSref,klam,WFS_positions,windowCROP,PSFscalefactor)
disp('-------------------------------------------------------------------')
disp('DETERMINING PIXEL LINEARITY')
disp('-------------------------------------------------------------------')

%% BUILD POSITIVE & NEGATIVE RESPONSE MATRICES
numMODES = size(MODEmatACTIVE,2);
A = pokeAmp;
% Applies positive mode shape on the DM and returns the response PSF - reference PSF
[RMpos,¬,¬] = ...
      Build_vAPP_Response_Matrix_Defocused(A,MODEmatACTIVE,EPcell,PupilPlane,Defocus,vAPP_upper,vAPP_lower,...
WFSref,klam,numMODES,WFS_positions,windowCROP,PSFscalefactor,0,0);
% Applies negative mode shape on the DM and returns the response PSF  - reference PSF
[RMneg,¬,¬] = ...
      Build_vAPP_Response_Matrix_Defocused(-A,MODEmatACTIVE,EPcell,PupilPlane,Defocus,vAPP_upper,vAPP_lower,...
WFSref,klam,numMODES,WFS_positions,windowCROP,PSFscalefactor,0,0);
% Subtracts the negative response PSF fro the positive response PSF
```

```matlab
RM = (RMpos + normIM(reshape(WFSref,[size(WFSref,1)*size(WFSref,2),1]))) - (RMneg  + ...
      normIM(reshape(WFSref,[size(WFSref,1)*size(WFSref,2),1])));

%% DISPLAY LINEAR MAPS FOR EACH MODE
% Looks for monotonic relationship for each mode (a negative response for
% the negative mode and a positive response for the positive mode) in each
% pixel in the WFS image.  If the pixel response is monotonic, the pixel is
% given a value of 1, 0 otherwise
linearmap = zeros(size(WFSref));
linearmapsum = zeros(size(WFSref));
for i = 1:numMODES
    impos = reshape(RMpos(:,i),[size(WFSref,1),size(WFSref,2)]);
    imneg = reshape(RMneg(:,i),[size(WFSref,1),size(WFSref,2)]);

for j = 1:size(impos,1)*size(impos,2)
    if (impos(j) > 0) && (imneg(j) < 0)
        linearmap(j) = 1;
    elseif (impos(j) < 0) && (imneg(j) > 0)
        linearmap(j) = 1;
    else
        linearmap(j) = 0;
    end
end
    linearmapsum = linearmapsum+linearmap;
end

%% APPLY LINEARITY THRESHOLD
disp('--------------------------------------------------------------------')
disp('BUILDING WEIGHTED PIXEL MAP')
disp('--------------------------------------------------------------------')
% Sum of the binary images for each modal response normalized by the number
% of modes in the response matrix.  Any pixel with a value of 1 here always
% has a monotonic response, a pixel with a value of zero is never
% monotonic, a pixel with a value of 0.5 responds monotonically to half the
% modes in the reponse matrix, etc.
imsum = linearmapsum;
weighted_pixel_map = imsum./numMODES;

figure;
imagesc(weighted_pixel_map);axis off;daspect([1 1 1]);colormap gray;colorbar;title(['weighted linearity map: ...
      +/-',num2str(A),'nm',' with ',num2str(AmpDefocus),' nm defocus'])
end
```

```matlab
function [RM,WFS_PSF,WFSref] = ...
      Build_vAPP_Response_Matrix_Defocused(pokeAmp_nm,IFmatACTIVE,EPcell,PupilPlane,Defocus,vAPP_upper,vAPP_lower,...
WFSref,klam,numActs,WFS_positions,windowCROP,PSFscalefactor,noisechoice,expTIME)
%% Cropping Parameters
upper_Ybeg = WFS_positions(1);
upper_Yend = WFS_positions(2);
lower_Ybeg = WFS_positions(3);
lower_Yend = WFS_positions(4);
upper_Xbeg = WFS_positions(5);
upper_Xend = WFS_positions(6);
lower_Xbeg = WFS_positions(7);
lower_Xend = WFS_positions(8);
WFScropSIZE = WFS_positions(9);

EP_Flux = EPcell{1};
EPplanet_Flux = EPcell{2};


%% Create RM
        RM = zeros(WFScropSIZE,numActs);

        Amp = pokeAmp_nm;%IFmatACTIVE amplitude == 1 nm == 10^-6 um
        DMpokeMAT = Amp.*IFmatACTIVE;
```

```
%          figure;
        for i = 1:numActs
            % Poke Actuator
            DMpoke = reshape(DMpokeMAT(:,i),[sqrt(length(IFmatACTIVE)),sqrt(length(IFmatACTIVE))]);

            % Actuator Poke in Phase in Pupil
            PUPILpoke = exp(1i.*klam.*2.*DMpoke).*PupilPlane;

            % Propagate to Image Plane
            [PSFstar_POKE] = VAPP_PROPAGATOR(PUPILpoke,vAPP_upper,vAPP_lower,EP_Flux.*Defocus).*PSFscalefactor;
            [PSFplanet_POKE] = ...
                 VAPP_PROPAGATOR(PUPILpoke,vAPP_upper,vAPP_lower,EPplanet_Flux.*Defocus).*PSFscalefactor;
            PSF_POKE = PSFstar_POKE + PSFplanet_POKE;

           if noisechoice == 1
                PSF_POKE = add_photon_noise(PSF_POKE,expTIME);
            end

            % Apply window
            PSF_POKE_WINDOW = PSF_POKE.*windowCROP;

            % Select, normalize, and combine WFS regions
            upper_wfs = PSF_POKE_WINDOW(upper_Ybeg:upper_Yend,upper_Xbeg:upper_Xend);
            lower_wfs = PSF_POKE_WINDOW(lower_Ybeg:lower_Yend,lower_Xbeg:lower_Xend);
            WFS_PSF = horzcat(lower_wfs,upper_wfs);

            % Calculate normalized intensity change
            DELTA_PSF = normIM(WFS_PSF) - normIM(WFSref);

            % Fill RM Matrix
            RM(:,i) = reshape(DELTA_PSF,[WFScropSIZE,1]);
        end
end
```

A.3 Electic Field Conjugation

A.3.1 Master script

```
%EFC_with_vAPP.m
%--------------------------------------------------------------------------
% Author: K.L.Miller [millerk2@email.arizona.edu]              March 2018
% Returns an aberrated single-sided vAPP dark hole to it's initial state
% using EFC by using full knowledge of the fields at the image plane
% Works with any DM and rebuilds the complex response matrix (G)
% every time the code is run.
%--------------------------------------------------------------------------

%% Field Estimation Choice
disp('Use field estimation or known fields?')
disp('Use known fields:    [0]')
disp('Estimate fields:     [1]')
estimate_field = input(':');

%% Call MagAO-X Parameters and Elements
MagAOX_Testbed
EP0 = EP;
[CM_IFmatACTIVE,¬] = pinvN_choose_thresh(IFmatACTIVE);

%% Phase Error
[KolPhase,¬]=apply_Kolmogorov(1.5*10^2,xsize,1,5*10^-5,1*10^-3,klam,11/3,0);
figure;imagesc((angle(KolPhase)./klam).*(10^6));axis off;axis square;colormap jet;colorbar;title('Optical ...
     aberration surface map: scale [nm]')

```

```
%% Create vAPP Dark Hole
vAPP_choice = 0;
[¬,vAPP_upper,vAPP_lower,FullPSF,IWA,OWA] = CHOOSE_VAPP_MASK(vAPP_choice);
EP_vAPP = EP;
EP = KolPhase.*EP0;
sys_params_mats{4} = EP;
PSFchoice = 'upper';

%% Define Window for EFC (Region of Interest)
[FullPSF] = VAPP_PROPAGATOR(1,vAPP_upper,vAPP_lower,PUPIL);
[RefPSF,xcen,ycen] = vAPP_IMAGE_CENTERING_CHOICE(FullPSF,CAMcrop,PSFchoice,1);
CAMcrop(4) = xcen;
CAMcrop(5) = ycen;
[DHwindow]=define_DF_area_vAPP_OneSided_DF_choose_area(IWA,OWA,lamDperPixel,CAMcrop,PSFchoice);

windowVECTOR = reshape(DHwindow,[cropSIZE,1]);
winPIXEL = find(windowVECTOR);

% Complex Window Vector
windowVECTORfull = vertcat(windowVECTOR,windowVECTOR);

%% Reference Star (w/o Aberration)
[PSFstar] = VAPP_PROPAGATOR(1,vAPP_upper,vAPP_lower,PUPIL);
maxStar = max(max(PSFstar));

[PSFstarcrop] = vAPP_IMAGE_CENTERING_CHOICE(PSFstar,CAMcrop,PSFchoice,0);
DHideal = log10(PSFstarcrop./maxStar);
DHidealmeanIntensity = mean2(DHideal(DHwindow==1));

cmin = DHidealmeanIntensity;
cmax = 0;

stellar_plotting_params = [cmin cmax maxStar];

%% Create Reference PSF (w/ Aberration)
[PSFab] = VAPP_PROPAGATOR(EP,vAPP_upper,vAPP_lower,PUPIL);
[OldPSFcrop] = vAPP_IMAGE_CENTERING_CHOICE(PSFab,CAMcrop,PSFchoice,0);

DH0 = log10(OldPSFcrop./maxStar);
DH_AB_meanIntensity = mean2(DH0(DHwindow==1));
figure;imagesc(DH0);axis off;axis square;colormap jet;colorbar;caxis([-5 0]);title(['Aberrated DH Contrast: ...
      ',num2str(DH_AB_meanIntensity)])

%% Build Response and Control Matrices
[G,CMfull] = build_G_matrix_vAPP(IFmatACTIVE,vAPP_upper,vAPP_lower,...
sys_params_mats,klam,CAMcrop,PSFchoice);

%% Filter Control Matrix
CM = CMfull(:,(windowVECTORfull == 1));

%% Electric Field Conjugation (EFC)
% Probe specs
    % Spatial frequencies in image plane
    numColumns = 26;
    A = linspace(1,numColumns,numColumns);
    % Probe size in X and Y in spatial frequencies
    wx = 1;
    wy = 50;
    b = 0;

% Initialize loop
    % Set Gain
    gain = 2;
    gain0 = gain;
    % Initialize dark hole metric
    DHmetric = DH_AB_meanIntensity;
    % Initialize DM actuators
    aTOTAL = zeros(size(IFmatACTIVE,2),1);
    % Initialize contrast vector
    contrast = zeros(1,100000);
    contrast(1) = mean2(DH0(DHwindow==1));
```

```
    % Reset loop counter
    LoopCounter = 0;

disp('-------------------------------------------------------------------')
disp('Probing Field & Building E Estimate')
disp('-------------------------------------------------------------------')
disp('Loop 0')
disp(['DH Metric: ',num2str(contrast(1))])
disp(' ')

while round(DHmetric,1) > -4.9
    LoopCounter = LoopCounter + 1;
    [C] = pick_probe_amplitude(DHmetric);
    disp(['probe amplitude = ',num2str(C)])
    probe_specs = [wx wy C b];

    if LoopCounter == 1
        Field = EP;
    end

    if (LoopCounter > 1)
        if ((contrast(LoopCounter)-contrast(LoopCounter - 1)) > 0)
            gain = gain0;
            disp(['Choosing lower gain: ',num2str(gain)])
        end
        if ((abs(contrast(LoopCounter))-abs(contrast(LoopCounter - 1))) < 0.05) && ...
              ((contrast(LoopCounter)-contrast(LoopCounter - 1)) < 0)
            gain = gain + 0.5;
            disp(['Choosing higher gain: ',num2str(gain)])

            disp('Rebuilding G with DM shape and E-field estimate')
            [G,CMfull] =build_G_matrix_vAPP_with_E_estimate(FieldCorrection,IFmatACTIVE,vAPP_upper,vAPP_lower,...
sys_params_mats,klam,CAMcrop,PSFchoice);
            CM = CMfull(:,(windowVECTORfull == 1));
        end
    end

    if estimate_field == 1
% Estimation of Complex E Field
        plot_choice = 1;
        [E,EfullREAL,EfullIMAG,probeCUBE_pos,probeCUBE_neg] = ...
              Field_Estimation_with_vAPP_FOR_BENCH(Field,vAPP_upper,vAPP_lower,locActs,IFmatACTIVE,CM_IFmatACTIVE,...
G,winPIXEL,CAMcrop,sys_params,sys_params_mats,stellar_plotting_params,PSFchoice,probe_specs,A,plot_choice);
% Plotting for Visual Verification of E Field Estimate
        [H_REAL,H_IMAG] = VAPP_PHASE_PROPAGATOR(Field,vAPP_upper,vAPP_lower,PUPIL);
        [hREAL] = vAPP_IMAGE_CENTERING_CHOICE(H_REAL,CAMcrop,PSFchoice,0);
        [hIMAG] = vAPP_IMAGE_CENTERING_CHOICE(H_IMAG,CAMcrop,PSFchoice,0);

        cminR = min2(DHwindow.*hREAL);cmaxR = max2(DHwindow.*hREAL);
        cminI = min2(DHwindow.*hIMAG);cmaxI = max2(DHwindow.*hIMAG);

        cminRE = min2(EfullREAL);cmaxRE = max2(EfullREAL);
        cminIE = min2(EfullIMAG);cmaxIE = max2(EfullIMAG);

        figure(12);
        im1 = DHwindow.*hREAL;
        im2 = DHwindow.*hIMAG;
        im3 = EfullREAL;
        im4 = EfullIMAG;
        subplot(2,2,1);imagesc(im1);axis off;daspect([1 1 1]);colormap jet;caxis([cminR ...
              cmaxR]);colorbar;title('R(Field)');drawnow
        subplot(2,2,2);imagesc(im2);axis off;daspect([1 1 1]);colormap jet;caxis([cminI ...
              cmaxI]);colorbar;title('I(Field)');drawnow
        subplot(2,2,3);imagesc(im3);axis off;daspect([1 1 1]);caxis([cminRE cmaxRE]);colormap ...
              jet;colorbar;title('Estimated R(Field)');drawnow
        subplot(2,2,4);imagesc(im4);axis off;daspect([1 1 1]);caxis([cminIE cmaxIE]);colormap ...
              jet;colorbar;title('Estimated I(Field)');drawnow
    else
% Known Complex E Field
        [H_REAL,H_IMAG] = VAPP_PHASE_PROPAGATOR(Field,vAPP_upper,vAPP_lower,PUPIL);
        [hREAL] = vAPP_IMAGE_CENTERING_CHOICE(H_REAL,CAMcrop,PSFchoice,0);
```

```
        [hIMAG] = vAPP_IMAGE_CENTERING_CHOICE(H_IMAG,CAMcrop,PSFchoice,0);
        Efull = vertcat(reshape((hREAL),[cropSIZE,1]),reshape((hIMAG),[cropSIZE,1]));
        E = Efull(windowVECTORfull == 1);
    end

if LoopCounter == 1
    disp('---------------------------------------------------------------')
    disp('Building Dark Hole')
    disp('---------------------------------------------------------------')
end

% Calculate Actuator Amplitudes
    a = - (CM*E).*gain;
    aTOTAL = a + aTOTAL;

% Build DM Response
    DMshape = reshape(IFmatACTIVE*aTOTAL,[sqrt(length(IFmatACTIVE)),sqrt(length(IFmatACTIVE))]);
    if deg ≠ 0
        [DMshape] = angled_matrix_updated(DMshape,deg,-1);
    end

% Propagate Field to Image Plane
    FieldCorrection = exp(1i.*2.*klam.*DMshape);
    Field = FieldCorrection.*EP;
    [PSF] = VAPP_PROPAGATOR(Field,vAPP_upper,vAPP_lower,PUPIL);
    [PSFcrop] = vAPP_IMAGE_CENTERING_CHOICE(PSF,CAMcrop,PSFchoice,0);

% Dark Hole Metric
DH = log10(PSFcrop./maxStar);
DHmeanIntensity = mean2(DH(DHwindow==1));
DHmetric = DHmeanIntensity;

contrast(LoopCounter+1) = DHmetric;
disp(['Loop ',num2str(LoopCounter)])
disp(['DH Metric: ',num2str(DHmetric)])
disp(' ')

% Show Dark Hole & DM shape
DMcrop = imcrop(DMshape.*(10^3).*PupilPlane,[(512-256/2) (512-256/2) (256-1) (256-1)]);
figure(13);
subplot(1,2,1);imagesc(DMcrop);axis off;axis square;colormap jet;colorbar;caxis([min2(DMcrop) ...
      max2(DMcrop)]);title(['DM shape ',num2str(LoopCounter)]);drawnow
subplot(1,2,2);imagesc(log10(PSFcrop./maxStar));axis off;axis square;colormap jet;colorbar;caxis([cmin ...
      cmax]);title(['log_1_0 DF contrast: ',num2str(DHmetric)]);drawnow

if LoopCounter ≥ length(contrast)
    break
end
end

%% Cropping and Plotting
%Plot First and Final PSFs
figure;
npoints = 35;
nticks = (npoints - 1)/2;
subplot(1,2,1);imagesc(log10(OldPSFcrop./maxStar));axis square;caxis([cmin cmax]);colormap ...
      jet;title({'Aberrated',['log_1_0 contrast = ',num2str(contrast(1))]},'FontSize',16);drawnow
set(gca,'XTick',(0:size(OldPSFcrop,2)/nticks:size(OldPSFcrop,2)) );set(gca,'XTickLabel', ...
round(linspace(-round(size(OldPSFcrop,2)/2*lamDperPixel),round(size(OldPSFcrop,2)/2*lamDperPixel),nticks)));
set(gca,'YTick',(0:size(OldPSFcrop,2)/nticks:size(OldPSFcrop,1)) );set(gca,'YTickLabel',...
round(linspace(-round(size(OldPSFcrop,2)/2*lamDperPixel),round(size(OldPSFcrop,2)/2*lamDperPixel),nticks)));
xlabel('\lambda/D','FontSize',12);ylabel('\lambda/D','FontSize',12)

subplot(1,2,2);imagesc(log10(PSFcrop./maxStar));axis square;caxis([cmin cmax]);colormap jet;title({'After ...
      EFC',['log_1_0 contrast = ',num2str(DHmetric)]},'FontSize',16);drawnow
set(gca,'XTick',(0:size(PSFcrop,2)/nticks:size(PSFcrop,2)) );set(gca,'XTickLabel', ...
      round(linspace(-round(size(PSFcrop,2)/2*lamDperPixel),round(size(PSFcrop,2)/2*lamDperPixel),nticks)));
set(gca,'YTick',(0:size(PSFcrop,2)/nticks:size(PSFcrop,1)) ...
      );set(gca,'YTickLabel',round(linspace(-round(size(PSFcrop,2)/2*lamDperPixel),...
round(size(PSFcrop,2)/2*lamDperPixel),nticks)));
xlabel('\lambda/D','FontSize',12);ylabel('\lambda/D','FontSize',12)
```

```
colorbar('southoutside')

figure;imagesc(log10(PSF./maxStar));axis off;daspect([1 1 1]);caxis([cmin cmax]);colormap jet;title({'After ...
      EFC',['log_1_0 contrast = ',num2str(DHmetric)]},'FontSize',16)

% Show Final DM Shape
cminDM = mean2(DMcrop)-5*std2(DMcrop);cmaxDM = mean2(DMcrop)+5*std2(DMcrop);
figure;
imagesc(DMcrop);axis off;axis square;colormap jet;colorbar;title('Applied DM Shape ...
      [\mum]','FontSize',20);caxis([cminDM cmaxDM])
disp(' ')

c = find(contrast,1,'last');contrastPLOT = contrast(1:c);
figure;
plot(contrastPLOT,'-*k','LineWidth',3);hold ...
      on;plot(ones(size(contrastPLOT)).*DHidealmeanIntensity,'b','LineWidth',3)
grid minor;axis square;xlabel('Iteration Number','FontSize',14),ylabel('Contrast (Log_1_0 ...
      Scale)','FontSize',14);title({'Contrast Curve',['Gain = ',num2str(gain)]},'FontSize',16);
legend('EFC DF contrast','vAPP DF contrast')
disp(['Number of loops to converge: ',num2str(LoopCounter)])
```

A.3.2 Field estimation

```
function [E,EfullREAL,EfullIMAG,probeCUBE_pos,probeCUBE_neg] = ...
      Field_Estimation_with_vAPP_FOR_BENCH(Field,vAPP_upper,vAPP_lower,locActs,IFmatACTIVE,CM_IFmatACTIVE,G,...
winPIXEL,CAMcrop,sys_params,sys_params_mats,stellar_plotting_params,PSFchoice,probe_specs,A,plot_choice)
%% Define Necessary Parameters
% Crop parameters
cropX = CAMcrop(1);
cropY = CAMcrop(2);
cropSIZE = CAMcrop(3);

% System parameters
PupilPlane = sys_params_mats{3};
x = linspace(-1,1,size(PupilPlane,1));
[X,Y] = meshgrid(x,x);
deg = sys_params_mats{5};
klam = sys_params(1);
BMC_choice = sys_params(3);

% Probe parameters
wx = probe_specs(1);
wy = probe_specs(2);
C = probe_specs(3);
b = probe_specs(4);

if BMC_choice == 1
    sf = 10;
    pixelshift = 4;
else
    sf = 9.8;
    pixelshift = 0;
end

% Stellar plotting parameters
cmin = stellar_plotting_params(1);
cmax = stellar_plotting_params(2);
maxStar = stellar_plotting_params(3);

%% Build DM Probes on Bench
DMprobe_pos = zeros(32,32);
DMprobe_neg = zeros(32,32);
probeCUBE_pos = zeros(32,32,length(A));
probeCUBE_neg = zeros(32,32,length(A));

```

```
%% Initialize Matrices
H = zeros(length(A),2*cropSIZE);
z = zeros(length(A),cropSIZE);
disp('------------------------------------------------------------------')
disp('Probing Field')
disp('------------------------------------------------------------------')

%% Define DM Probes
for i = 1: length(A)
% disp('------------------------------------------------------------------')
% disp('Building DM Probes')
% disp('------------------------------------------------------------------')
% Create rect probes in image plane by applying sincs in pupil plane:
% DMprobeSHAPE = C.*(sinc(wx.*X).*sinc(wy.*Y).*cos(a.*X).*cos(b.*Y));
    a = A(i).*sf;
    DMprobeSHAPE_pos = circshift(C.*sinc(wx.*X./cosd(deg)).*sinc(wy.*Y).*cos(a.*X./cosd(deg)).*cos(b.*Y),[0 ...
         pixelshift]);
    DMprobeSHAPE_neg = - DMprobeSHAPE_pos;
% Project sinc shapes onto DM to derive actuator amplitudes (u)
    u_pos = normIM(CM_IFmatACTIVE*reshape(DMprobeSHAPE_pos,[length(IFmatACTIVE),1])).*C;
    u_neg = normIM(CM_IFmatACTIVE*reshape(DMprobeSHAPE_neg,[length(IFmatACTIVE),1])).*C;
% Build +/- probe shapes on bench DM:
    DMprobe_pos(locActs) = u_pos;
    DMprobe_neg(locActs) = u_neg;
    probeCUBE_pos(:,:,i) = DMprobe_pos;
    probeCUBE_neg(:,:,i) = DMprobe_neg;
% Build +/- DM shapes:
% DM shape+ = IFmatACTIVE*u , DM shape- = -IFmatACTIVE*u
    BMC_pos = normIM(reshape(IFmatACTIVE*u_pos,[sqrt(length(IFmatACTIVE)) ...
         sqrt(length(IFmatACTIVE))])).*(10^-6).*C;
    BMC_neg = normIM(reshape(IFmatACTIVE*u_neg,[sqrt(length(IFmatACTIVE)) ...
         sqrt(length(IFmatACTIVE))])).*(10^-6).*C;

    if deg ≠ 0
        [BMC_pos] = angled_matrix_updated(BMC_pos,deg,-1);
        [BMC_neg] = angled_matrix_updated(BMC_neg,deg,-1);
    end

%% Build Observation Matrix (H) With Instrument Model
% disp('------------------------------------------------------------------')
% disp('Building Observation Matrix (H) in Model')
% disp('------------------------------------------------------------------')
% Propagate +/- probes to image plane using complex response matrix G:
% h+ = G*u_pos , h- = G*u_neg
    h_pos = G*u_pos;
    h_neg = G*u_neg;
% Loop through all i probes to build H(i,:) = (h+ - h-)'
%     H(i,:) = (normIM(h_pos) - normIM(h_neg))';
    H(i,:) = (h_pos - h_neg)';

%% Create Delta Intensity Images With Actual Instrument
% disp('------------------------------------------------------------------')
% disp('Applying Probes on Instrument and Measuring Delta I')
% disp('------------------------------------------------------------------')
% Propagate +/- probes to image plane by standard propagation:
% I+ = F{exp(1i*+DM shape) * Field} , I- = F{exp(1i*-DM shape) * Field}
%     h_POS_Intensity = ...
     rot90(fourierProp(fourierProp(fourierProp(exp(1i.*2.*klam.*BMC_pos).*Field,dx).*FPM,dxi).*LYOT,dx),2);
%     h_NEG_Intensity = ...
     rot90(fourierProp(fourierProp(fourierProp(exp(1i.*2.*klam.*BMC_neg).*Field,dx).*FPM,dxi).*LYOT,dx),2);
% Create PSFs from the fields
    [PSF_pos] = VAPP_PROPAGATOR(exp(1i.*2.*klam.*BMC_pos).*Field,vAPP_upper,vAPP_lower,PupilPlane);
    [PSF_neg] = VAPP_PROPAGATOR(exp(1i.*2.*klam.*BMC_neg).*Field,vAPP_upper,vAPP_lower,PupilPlane);
% Delta I = (I+ - I-)
    ΔI = normIM(PSF_pos) - normIM(PSF_neg);
%     ΔI = PSF_pos - PSF_neg;
    [ΔI_CROP] = vAPP_IMAGE_CENTERING_CHOICE(ΔI,CAMcrop,PSFchoice,0);
% Build z matrix by vectorizing Delta I into a row vector:
% z(i,:) = Delta I
    z(i,:) = reshape(ΔI_CROP,[1,cropSIZE]);

```

```
%% Plotting for Visual Verification of Probes
if plot_choice == 1
    hreal = h_pos(1:cropSIZE);himag = h_pos(cropSIZE+1:end);
    hField = reshape((hreal+(1i.*himag)),[cropX,cropY]);
    PSF_model = hField.*conj(hField);
    [PSFcrop] = vAPP_IMAGE_CENTERING_CHOICE(PSF_pos,CAMcrop,PSFchoice,0);
    figure(11);
    subplot(2,2,1);imagesc(BMC_pos - BMC_neg);axis off;axis square;colormap jet;colorbar;title({['Probe_+ - ...
         Probe_- ',num2str(i)],['Spatial frequency : ',num2str(A(i)),'\lambda/D']},'FontSize',12);drawnow
    subplot(2,2,2);imagesc(DMprobe_pos - DMprobe_neg);axis off;axis square;colormap ...
         jet;colorbar;title({['Bench DM Probe_+ - Probe_- ',num2str(i)],['Spatial frequency : ...
         ',num2str(A(i)),'\lambda/D']},'FontSize',12);drawnow
    subplot(2,2,3);imagesc(log10(PSFcrop./maxStar));axis off;axis square;colormap jet;colorbar;title('Actual ...
         Probe');caxis([cmin cmax]);drawnow
    subplot(2,2,4);imagesc(log10(PSF_model));axis off;axis square;caxis([cmin-3 cmax]);colormap ...
         jet;colorbar;title('Model Probe');drawnow;
end
end

%% Estimate Electric Field
% disp('-------------------------------------------------------------------')
% disp('Estimating Electric Field in Dark Hole')
% disp('-------------------------------------------------------------------')
% Filter H and z To Include Only Pixels In ROI
% Filter H to use only pixels in region of interest (ROI): H_ROI = H(ROI)
% Filter z to only include pixels in the ROI: z_ROI = z(ROI)
% Take the pseudo-inverse of H: pinv(H) = inv(transpose(H)*H)*transpose(H)
% Fit z vector to pinv(H) to estimate electric field in the ROI:
E_complex = zeros(2,length(winPIXEL));
for q = 1:length(winPIXEL)
    H_ROI_Real = H(:,winPIXEL(q));
    H_ROI_Imag = H(:,(winPIXEL(q)+cropSIZE));
    H_ROI = horzcat(H_ROI_Real,H_ROI_Imag);
    z_ROI = z(:,winPIXEL(q));
    E_complex(:,q) = (1/4).*(pinv(H_ROI)*z_ROI);
end

%% Sort and Reshape E
% Result is 2 row vectors where:
Ereal = E_complex(1,:);
Eimag = E_complex(2,:);

% Create single E column vector:
E = vertcat(Ereal',Eimag');

% Place all ROI pixels into correct position to rebuild ROI field
EfullREALvec = zeros(1,cropSIZE);
EfullIMAGvec = zeros(1,cropSIZE);

EfullREALvec(winPIXEL) = Ereal;
EfullIMAGvec(winPIXEL) = Eimag;

EfullREAL = reshape(EfullREALvec,[cropY,cropX]);
EfullIMAG = reshape(EfullIMAGvec,[cropY,cropX]);
```

A.4 Testbed code

A.4.1 LDFC

```
% TESTBED_LDFC_TEST.m
%-------------------------------------------------------------------------
% Author: Kelsey L. Miller                                   January 2018
% Contact: millerk2@email.arizona.edu
%-------------------------------------------------------------------------
```

```
addpath  /home/lab/Desktop/TESTBED_ACTIVATION_KM
addpath /home/lab/src/scripts

%% LOAD ACTIVE ACTUATORS
disp('-------------------------------------------------------------------')
disp('LOADING ACTIVE ACTUATOR POSITIONS')
disp('-------------------------------------------------------------------')
if (exist('locActs','var') == 0)
    load locActs_08_23_2018.mat % locActs_annular.mat %locActs.mat
%      locActs = locActs_annular;
end

%% DM SET UP
disp('-------------------------------------------------------------------')
disp('INITIALIZING DM')
disp('-------------------------------------------------------------------')
DM_command = cell(1,4);
DM_command{1} = 1;
DM_command{3} = locActs;

%% RUN ALIGNMENT CORRECTION
disp('-------------------------------------------------------------------')
disp('RUN ALIGNMENT CORRECTION?')
disp('NO      [0]')
disp('YES     [1]')
align_correct_choice = input(':');
disp('-------------------------------------------------------------------')
if align_correct_choice == 1
    [DM_ALIGNMENT_CORRECTION] = vAPP_ALIGNMENT_CORRECTION;
    DM_command{1} = 7;
    DM_command{4} = 1;
    DM_command{2} =  DM_ALIGNMENT_CORRECTION;
    [¬,¬] = BMC_DM_WRITE(DM_command);
end

%% CAMERA SETUP
disp('-------------------------------------------------------------------')
disp('INITIALIZING CAMERA SETTINGS')
disp('-------------------------------------------------------------------')
% CAMERA 1: REFLECTED IMAGE   (SCIENCE)
% CAMERA 2: TRANSMITTED IMAGE (WFS)

CAMchoice = 'Basler';

expT = 5*10^3;%5*10^4;
NumImages = 1;
CAMsettings = [expT NumImages];

% 15 lambda/D = 74 pixels, therefore 150 with the PSF centered should cover
% the dark hole and active bright field opposit the DH
% 11 lambda/D = 54 pixels for a total PSF crop of 108
cropX = 108;cropY = cropX; cropSIZE = cropX*cropY;

%% IMAGE CENTERING
disp('-------------------------------------------------------------------')
disp('CENTERING ON PSF')
disp('-------------------------------------------------------------------')
expT_centering = 5000;NumImages_centering = 1;
CAMsettings_centering = [expT_centering NumImages_centering];

cropCHOICE = 1; % Uses vAPP_IMAGE_CENTERING
xcen = 0; ycen = 0;
CAMcrop = [cropX cropY cropSIZE xcen xcen ycen ycen cropCHOICE];

[RefPSF_centering_SCI,RefPSF_centering_WFS,xcen1,ycen1,xcen2,ycen2,¬] = ...
     TAKE_IMAGE_2(CAMcrop,CAMsettings_centering,CAMchoice);
% [RefPSF_centering,xcen,ycen,¬] = TAKE_IMAGE(CAMcrop,CAMsettings_centering,CAMchoice);

%% TAKE CENTERED REFERENCE IMAGE
disp('-------------------------------------------------------------------')
disp('TAKING REFERENCE IMAGE')
```

```
disp('-------------------------------------------------------------------')
cropCHOICE = 0; % Uses vAPP_IMAGE_CENTERING
CAMcrop = [cropX cropY cropSIZE xcen1 xcen2 ycen1 ycen2 cropCHOICE];
[RefPSF0_SCI,RefPSF0_WFS] = TAKE_IMAGE_2(CAMcrop,CAMsettings,CAMchoice);
% [RefPSF0,¬,¬,¬] = TAKE_IMAGE(CAMcrop,CAMsettings,CAMchoice);

%% TAKE DARK IMAGE
% cropCHOICE = 0; % Uses xcen and ycen from reference image
% CAMcrop = [cropX cropY cropSIZE xcen ycen cropCHOICE];
% disp('-------------------------------------------------------------------')
% disp('TAKING DARK: BLOCK BEAM')
% disp('press enter when ready')
% disp('-------------------------------------------------------------------')
% pause
% disp('-------------------------------------------------------------------')
% disp('TAKING DARK IMAGE')
% disp('-------------------------------------------------------------------')
% [RefDARK] = TAKE_IMAGE(CAMcrop,CAMsettings,CAMchoice);
% disp('-------------------------------------------------------------------')
% disp('DARK TAKEN: REMOVE BEAM BLOCK')
% disp('press enter when ready')
% disp('-------------------------------------------------------------------')
% pause
RefDARK = zeros(size(RefPSF0_SCI));
RefPSF_SCI = (RefPSF0_SCI - RefDARK - min2(RefPSF0_SCI - RefDARK));
RefPSF_WFS = (RefPSF0_WFS - RefDARK - min2(RefPSF0_WFS - RefDARK));
starMax = max2(RefPSF_SCI);

figure;
subplot(1,2,1);imagesc(RefPSF_SCI);axis off;daspect([1 1 1]);colormap jet;colorbar;title('SCIENCE REFERENCE')
subplot(1,2,2);imagesc(RefPSF_WFS);axis off;daspect([1 1 1]);colormap jet;colorbar;title('WFS REFERENCE')

%% CREATE MASKS & REFERENCES
disp('-------------------------------------------------------------------')
disp('BUILDING WFS & DARK HOLE MASKS')
disp('-------------------------------------------------------------------')
% CAMERA 1: REFLECTED IMAGE   (SCIENCE)
% CAMERA 2: TRANSMITTED IMAGE (WFS)
sensorchoice = 2;

x = linspace(-1,1,size(RefPSF_WFS,2));
y = linspace(-1,1,size(RefPSF_WFS,1));
[X,Y] = meshgrid(x,y);
R = sqrt(X.^2 + Y.^2);
r_core = 0.5;%0.4;
r_outer = 1;

% DARK HOLE MASK & REFERENCE
DHmask_core = 1-abs(R<r_core);
DHmask_outer = abs(R<r_outer);
DHmask = DHmask_core.*DHmask_outer;
DHmask(:,1:round(size(DHmask,2)/2)) = 0;

RefDH = RefPSF_SCI.*DHmask;

% WFS MASK & REFERENCE
r_core_WFS = 0.35;
WFSmask_core = 1-abs(R<r_core_WFS);
WFSmask_outer = abs(R<r_outer);
WFSmask = WFSmask_core.*WFSmask_outer;
WFSmask(:,round(size(WFSmask,2)/2)+1:end) = 0;
WFSmaskFULL = WFSmask;

if sensorchoice == 1
    RefWFS = RefPSF_SCI.*WFSmask;
else
    RefWFS = RefPSF_WFS.*WFSmask;
end

% COUNTS THRESHOLD
BFthreshold = 4;%20;%2;
```

```
% WFS_pixels = find(RefWFS ≥ BFthreshold);
WFS_pixels = find(RefPSF_WFS ≥ BFthreshold);
WFSmask = zeros(size(RefPSF_WFS));
WFSmask(WFS_pixels) = 1;
figure;imagesc(WFSmask);axis off;daspect([1 1 1]);colormap gray;title('WFS Pixels')

%% WFS & DH REFERENCES
disp('--------------------------------------------------------------------')
disp('BUILDING BF & DH REFERENCES')
disp('--------------------------------------------------------------------')
% CAMERA 1: REFLECTED IMAGE   (SCIENCE)
% CAMERA 2: TRANSMITTED IMAGE (WFS)
cropCHOICE = 1; % Center on preset x and y
CAMcrop = [cropX cropY cropSIZE xcen1 xcen2 ycen1 ycen2 cropCHOICE];
[RefDH_contrast,DHref,DHcounts_scaled] = CALCULATE_DARK_HOLE_CONTRAST_QUICK_AND_DIRTY(DHmask,CAMcrop,1);
[RefBF_contrast,BFref,BFcounts_scaled] = CALCULATE_BRIGHT_FIELD_CONTRAST(WFSmaskFULL,CAMcrop,2);
[RefWFS_contrast,WFSref] = CALCULATE_BRIGHT_FIELD_CONTRAST(WFSmask,CAMcrop,2);

figure;
subplot(1,2,1);imagesc(BFref);axis off;axis square;colormap gray;colorbar;caxis([min2(DHref) 0]);title({'BF ...
      Reference',['Average log_1_0 Contrast of WFS Pixels: ',num2str(RefWFS_contrast)]})
subplot(1,2,2);imagesc(DHref);axis off;axis square;colormap gray;colorbar;caxis([min2(DHref) 0]);title({'DH ...
      Reference',['Average log_1_0 Contrast of DH: ',num2str(RefDH_contrast)]})

%% BUILD RESPONSE MATRIX
disp('--------------------------------------------------------------------')
disp('BUILDING FULL FIELD RESPONSE MATRIX')
disp('--------------------------------------------------------------------')
cropCHOICE = 0; % Centers on x and y presets
CAMcrop = [cropX cropY cropSIZE xcen1 xcen2 ycen1 ycen2 cropCHOICE];

% ZERNIKE MODAL SET
% DM_command{4} = 1;
% load Zernike_21_Modes.mat
% MODES = Zernike_21_Modes;

% MIRROR MODAL SET
DM_command{4} = 0;
load MIRROR_MODES_08_23_2018.mat % MIRROR_MODES_ANNULAR.mat %MIRROR_MODES_IDEAL.mat
numMODES_LOWF_CUTOFF = 1;%50;
numMODES_HOWF_CUTOFF = size(MIRROR_MODES,2);
MODES = MIRROR_MODES(:,numMODES_LOWF_CUTOFF:numMODES_HOWF_CUTOFF);
numMODES = size(MODES,2);

MODES_FULL = MODES;
numMODES_FULL = size(MODES_FULL,2);

% SET MODE AMPLITUDE FOR RESPONSE MATRIX
MODEamp = 0.1;

% USE CORRECT REFERENCE PSF FOR RESPONSE MATRIX
if sensorchoice == 1
    RefPSF_RM = RefPSF_SCI;
else
    RefPSF_RM = RefPSF_WFS;
end

% BUILD RESPONSE MATRIX FOR ALL MODES IN MODES_FULL
    RM = zeros(cropSIZE,numMODES);
    for i = 1:numMODES_FULL
        disp(['mode ',num2str(i),'/',num2str(numMODES)])
        DM_command{2} = MODEamp.*MODES(:,i);
        RM(:,i) = BUILD_RESPONSE_MATRIX(DM_command,RefPSF_RM,RefDARK,CAMcrop,CAMsettings,CAMchoice,sensorchoice);
    end
    dmzeroch_m(DM_command{1});

%% FILTER RM FOR LDFC RESPONSE MATRIX
disp('--------------------------------------------------------------------')
disp('SELECTING LDFC BRIGHT FIELD RESPONSE MATRIX')
disp('--------------------------------------------------------------------')

```

```
LOWEST_MODE = 1;
HIGHEST_MODE = 80;%60
MODES_TRUNC = MODES_FULL(:,LOWEST_MODE:HIGHEST_MODE);
numMODES = size(MODES_TRUNC,2);

    LDFC_RM = zeros(length(WFS_pixels),numMODES);
    counter = 0;
    for i = LOWEST_MODE:HIGHEST_MODE
        counter = counter+1;
        RMcol = RM(:,i);
        LDFC_RM(:,counter) = RMcol(WFS_pixels);
    end

    figure;
    RMimage = zeros(cropSIZE,1);
    counter = 0;
    for i = LOWEST_MODE:HIGHEST_MODE
        counter = counter + 1;
        RMimage(WFS_pixels) = LDFC_RM(:,counter);
        imagesc(reshape(RMimage,[cropX cropY]));axis off;axis square;colormap jet;colorbar;title(['mode: ...
              ',num2str(counter),'/',num2str(numMODES)]);drawnow;
        pause(0.01)
    end


%% BUILD COMMAND MATRIX
disp('-------------------------------------------------------------------')
disp('BUILDING COMMAND MATRIX')
disp('-------------------------------------------------------------------')
[CM,¬] = pinvN_choose_thresh(LDFC_RM);

%% MASK
% Sets DM mask over active actuators for RMS surface calculations
disp('-------------------------------------------------------------------')
disp('SETTING DM MASK')
disp('-------------------------------------------------------------------')
mask = zeros(32,32);
mask(locActs) = 1;

%% APPLY PHASE SCREEN TO DM
disp('-------------------------------------------------------------------')
disp('APPLYING PHASE SCREEN ABERRATION')
disp('-------------------------------------------------------------------')
DM_command{1} = 1;

% 1/F NOISE
%---------------------------------------------------------------------------
DM_command{4} = 0;
numScreens = 10;%100;
cd '/home/lab/Desktop/TESTBED_ACTIVATION_KM'
load oneoverf_squared_32x32.mat
PHASE = zeros(1024,numScreens);
for i = 1:numScreens
    PHASE(:,i) = (1/3).*(1/10).*reshape(cnoise(:,:,i),[1024 1]);
end
%---------------------------------------------------------------------------
%% LDFC CLOSED-LOOP CONTROL
disp('-------------------------------------------------------------------')
disp('RUNNING LDFC CLOSED-LOOP')
disp('-------------------------------------------------------------------')
% MAKE VIDEO
cd '/home/lab/Desktop/TESTBED_ACTIVATION_KM/LDFC_VIDEOS'
v = VideoWriter('LDFC_closed_loop_fsquared_lab_demo_50_screens.avi');
open(v);

aTOTAL = 0;
gain1 = 0.6;
gain2 = 0.1;

screen_counter = 0;

```

```
diff_LDFC = zeros(1,numScreens);
diff_noLDFC = zeros(1,numScreens);
surfaceRMS_AB = zeros(1,numScreens);
surfaceRMS_COR = zeros(1,numScreens);
DH_LDFC_images = zeros(size(RefPSF_SCI,1),size(RefPSF_SCI,2),numScreens);
DH_AB_images = zeros(size(RefPSF_SCI,1),size(RefPSF_SCI,2),numScreens);


figure(50);
for i = 1:numScreens
%---------------------------------------------------------------------------
% TURN OFF WHEN RUNNING CORRELATED 1/F^2 PHASE SCREENS
    aTOTAL = 0;
%---------------------------------------------------------------------------
    screen_counter = screen_counter + 1;
    DM_command{1} = 1;
    DM_command{2} = PHASE(:,i);
    [ABERRATION,¬] = BMC_DM_WRITE(DM_command);
    [RMS_AB,PV_AB] = RMS_PV_calculator(ABERRATION,mask);

    disp(['Phase shift ',num2str(i),'/',num2str(numScreens)])
    if screen_counter == 1
% TAKE IMAGE
        [AbPSF0_SCI,AbPSF0_WFS] = TAKE_IMAGE_2(CAMcrop,CAMsettings,CAMchoice);
        AbPSF_SCI = normIM(AbPSF0_SCI - RefDARK - min2(AbPSF0_SCI - RefDARK));
        AbPSF_WFS = normIM(AbPSF0_WFS - RefDARK - min2(AbPSF0_WFS - RefDARK));
% CALCULATE INITIAL DH CONTRAST
        [AbDH_contrast,DHab,DHab_counts] = CALCULATE_DARK_HOLE_CONTRAST_QUICK_AND_DIRTY(DHmask,CAMcrop,1);
        diff_noLDFC(i) = AbDH_contrast;
        DH_AB_images(:,:,i) = DHab;
% SUBTRACT REFERENCE & RESHAPE TO COLUMN
        if sensorchoice == 1
            IM = reshape(AbPSF_SCI - normIM(RefPSF_SCI),[cropSIZE,1]);
        else
            IM = reshape(AbPSF_WFS - normIM(RefPSF_WFS),[cropSIZE,1]);
        end
        IM_LDFC = IM(WFS_pixels);

    else
% SUBTRACT REFERENCE & RESHAPE TO COLUMN
        if sensorchoice == 1
            IM = reshape(CorrectedPSF_SCI - normIM(RefPSF_SCI),[cropSIZE,1]);
        else
            IM = reshape(CorrectedPSF_WFS - normIM(RefPSF_WFS),[cropSIZE,1]);
        end

        IM_LDFC = IM(WFS_pixels);

    end
% FIT TO CM
    if screen_counter == 1
        gain = gain1;
    else
        gain = gain2;
    end
    a = (CM*IM_LDFC).*MODEamp.*gain;
    aTOTAL = a + aTOTAL;
% APPLY CORRECTION TO DM
    DM_command{1} = 2;
    DM_command{2} = -(MODES_TRUNC)*aTOTAL;
    [DM_CORRECTION,DM_success] = BMC_DM_WRITE(DM_command);
% TAKE UPDATED IMAGE
    [CorrectedPSF0_SCI,CorrectedPSF0_WFS] = TAKE_IMAGE_2(CAMcrop,CAMsettings,CAMchoice);
    CorrectedPSF_SCI = normIM(CorrectedPSF0_SCI - RefDARK - min2(CorrectedPSF0_SCI - RefDARK));
    CorrectedPSF_WFS = normIM(CorrectedPSF0_WFS - RefDARK - min2(CorrectedPSF0_WFS - RefDARK));
% CALCULATE UPDATED DH CONTRAST
    [DH_contrast,DHcorrected,DHcorrected_counts] = ...
         CALCULATE_DARK_HOLE_CONTRAST_QUICK_AND_DIRTY(DHmask,CAMcrop,1);
    DH_LDFC_images(:,:,i) = DHcorrected;
    diff_LDFC(i) = DH_contrast;
% CALCULATED UPDATED SURFACE RMS
```

```
    UPDATED_SURFACE = (ABERRATION + DM_CORRECTION) - mean2(ABERRATION + DM_CORRECTION);
    [RMS_COR,PV_COR] = RMS_PV_calculator(UPDATED_SURFACE,mask);
% MAKE VIDEO
    cmax = max2(ABERRATION);cmin = min2(ABERRATION);
    subplot(1,3,1);imagesc(circshift(rot90(ABERRATION,1),[0 5]));axis off;axis square;colormap ...
         jet;colorbar;title({'Applied Aberration',['RMS = ',num2str(RMS_AB)]});caxis([cmin cmax]);drawnow
    subplot(1,3,2);imagesc(circshift(rot90(DM_CORRECTION,1),[0 5]));axis off;axis square;colormap ...
         jet;colorbar;title(['Applied Correction ',num2str(screen_counter)]);drawnow
    subplot(1,3,3);imagesc(circshift(rot90(UPDATED_SURFACE,1),[0 5]));axis off;axis square;colormap ...
         jet;colorbar;title({['Flattened Surface ',num2str(screen_counter)],['RMS = ...
         ',num2str(RMS_COR)]});caxis([cmin cmax]);drawnow
    set(gcf, 'Position',get(0, 'Screensize'));
    frame = getframe(gcf);
    writeVideo(v,frame);


% SAVE DATA
    surfaceRMS_COR(i) = RMS_COR;
    surfaceRMS_AB(i) = RMS_AB;
end
dmzeroch_m(1);dmzeroch_m(2);
close(v);

%% PLOT STABILIZATION
figure;
mean_stabilization = mean((10.^diff_noLDFC)./(10.^diff_LDFC));
plot(diff_noLDFC,'-or','LineWidth',3);hold on;plot(diff_LDFC,'-*g','LineWidth',3);hold ...
     on;plot(RefDH_contrast.*ones(size(diff_noLDFC)),'k','LineWidth',3);
grid minor;xlabel('time [screen #]','FontSize',24);ylabel('log_1_0 DH contrast','FontSize',24);title(['LDFC ...
     DH Stabilization: ',num2str(mean_stabilization),'x'],'FontSize',30)
legend('LDFC OFF','LDFC ON','DARK HOLE FLOOR')

ngood = find(diff_LDFC < diff_noLDFC);
DH_AB_images0 = DH_AB_images;
DH_LDFC_images0 = DH_LDFC_images;
DH_AB_images = DH_AB_images0(:,:,ngood);
DH_LDFC_images = DH_LDFC_images0(:,:,ngood);

figure;
plot(surfaceRMS_AB,'-or','LineWidth',3);hold on;plot(surfaceRMS_COR,'-og','LineWidth',3);axis square;grid minor;
xlabel('loop number','FontSize',18);ylabel('RMS WFE','FontSize',18);title('LDFC RMS WFE Tracking','FontSize',24)
legend('LDFC OFF','LDFC ON')

%% DARK HOLE CONTRAST
mrows = 1:cropY;
ncols = 85:130;% 85:130 is 2 - 11 lambda/D
DFcontrast = zeros(size(ncols));
ABcontrast = zeros(size(ncols));
LDFCcontrast = zeros(size(ncols));

DFcontrast_all_screens = zeros(size(ncols));
ABcontrast_all_screens = zeros(size(ncols));
LDFCcontrast_all_screens = zeros(size(ncols));

for j = 1:length(ngood)
    imAB = DH_AB_images(:,:,j);
    imLDFC = DH_LDFC_images(:,:,j);
    for i = 1:length(ncols)
        DHref_full = DHref(mrows,ncols(i));
        imAB_full = imAB(mrows,ncols(i));
        imLDFC_full = imLDFC(mrows,ncols(i));
        DFcontrast(i) = mean(DHref_full(DHref_full≠0));
        ABcontrast(i) = mean(imAB_full(imAB_full≠0));
        LDFCcontrast(i) = mean(imLDFC_full(imLDFC_full≠0));
    end

    DFcontrast_all_screens = DFcontrast_all_screens + DFcontrast;
    ABcontrast_all_screens = ABcontrast_all_screens + ABcontrast;
    LDFCcontrast_all_screens = LDFCcontrast_all_screens + LDFCcontrast;

end
```

```

DFcontrast_all_screens_mean = DFcontrast_all_screens./length(ngood);
ABcontrast_all_screens_mean = ABcontrast_all_screens./length(ngood);
LDFCcontrast_all_screens_mean = LDFCcontrast_all_screens./length(ngood);


n1 = isinf(DFcontrast_all_screens_mean);
n11 = find(n1 == 1);
DFcontrast_all_screens_mean(n11) = mean([DFcontrast_all_screens_mean(n11-1) DFcontrast_all_screens_mean(n11+1)]);
n2 = isinf(ABcontrast_all_screens_mean);
n22 = find(n2 == 1);
ABcontrast_all_screens_mean(n22) = mean([ABcontrast_all_screens_mean(n22-1) ABcontrast_all_screens_mean(n22+1)]);
n3 = isinf(LDFCcontrast_all_screens_mean);
n33 = find(n3 == 1);
LDFCcontrast_all_screens_mean(n33) = mean([LDFCcontrast_all_screens_mean(n33-1) ...
      LDFCcontrast_all_screens_mean(n33+1)]);


figure;
plot(ABcontrast_all_screens_mean,'r','LineWidth',3);hold on;
plot(LDFCcontrast_all_screens_mean,'g','LineWidth',3);
plot(mean(ABcontrast_all_screens_mean).*ones(size(ABcontrast_all_screens_mean)),'--k','LineWidth',2)
plot(mean(LDFCcontrast_all_screens_mean).*ones(size(ABcontrast_all_screens_mean)),'k','LineWidth',2)
axis square;grid minor;title('Mean DH Contrast','FontSize',24)
xlabel('\lambda/D','FontSize',18);ylabel('log_1_0 contrast','FontSize',18)
set(gca,'XTick',2:length(ncols)/10:length(ncols));set(gca,'XTickLabel',linspace(2,11,10));
legend('LDFC OFF','LDFC ON','Mean aberration','Mean LDFC correction')

%% PLOT CONTRAST TRACKING, APPLIED & SENSED MODES
last_val = length(diff_noLDFC);
contrast_tracking = contrast(:,1:last_val-1);
DH_LDFC_images = DH_LDFC_images(:,:,1:last_val-1);

figure;
plot(contrast_tracking,'-ok','LineWidth',3);axis square;grid minor;
xlabel('loop number','FontSize',18);ylabel('log_1_0 contrast','FontSize',18);title('LDFC Contrast ...
      Tracking','FontSize',24)

%% MODE TRACKING
figure;
plot(AbMODE_amplitudes,'-*r','LineWidth',2);hold on;
plot(aTOTAL,'-og','LineWidth',2);
xlabel('mode number','FontSize',18);ylabel('mode amplitude','FontSize',18);title('Applied vs Sensed ...
      Modes','FontSize',24);grid minor
legend('applied aberration','sensed mode')
```

A.4.2 Data analysis

```
%Testbed_data_analysis.m
%------------------------------------------------------------------------
addpath 'C:\Users\klmil\OneDrive\Documents\GitHub\Doctoral-Research\TESTBED-SIM-INTERFACE-CODE\...
TIME_EVOLVING_PHASE_SCREENS\TESTBED_DATA'
addpath 'C:\Users\klmil\OneDrive\Documents\GitHub\Doctoral-Research\UTILITIES'
%------------------------------------------------------------------------
%% LOAD DATA
%------------------------------------------------------------------------
disp('------------------------------------------------------------------')
disp('Choose data:')
disp('1/f^2 , defocused , 200 modes                 [0]')
disp('1/f , defocused , 200 modes                   [1]')
disp('1/f , focused , 100 modes                     [2]')
disp('1/f , focused , 200 modes, 300 screens        [3]')
disp('1/f , focused , 200 modes, 416 screens        [4]')
datachoice = input(':');
disp('------------------------------------------------------------------')
```

```
if datachoice == 0
    dataname = '_1_fsquared_defocused_200modes_';
    load PSF_SCI_CUBE_ABERRATED_09_08_2018.mat
    load PSF_SCI_CUBE_LDFC_09_08_2018.mat
    load PSF_SCI_REF_AB_09_08_2018.mat
    load PSF_SCI_REF_LDFC_09_08_2018.mat
    expT = 7*10^5;% exposure time of image set [microseconds]
    PSFmax = 0.0873*expT; % Determined on bench [counts]
    contrast_logscale_factor = 1/PSFmax;
    load RESIDUAL_PHASE_MAT_fsquared_09_07_2018_200modes_Defocused.mat
    load ABERRATED_PHASE_MAT_fsquared_09_07_2018_200modes_Defocused.mat
    LDFC_PHASE_MAT = zeros(size(ABERRATED_PHASE_MAT));
    for i = 1:size(ABERRATED_PHASE_MAT,2)
        LDFC_PHASE_MAT(:,i) = -(ABERRATED_PHASE_MAT(:,i) - RESIDUAL_PHASE_MAT(:,i));
    end

    cminCONTRAST = -3.5;
    cmaxCONTRAST = -2.5;
elseif datachoice == 1
    dataname = '_1_f_defocused_200modes_';
    load PSF_SCI_CUBE_ABERRATED_09_08_2018_oneoverf_higher_amp.mat
    load PSF_SCI_CUBE_LDFC_09_08_2018_oneoverf_higher_amp.mat
    load PSF_SCI_REF_AB_09_08_2018_oneoverf_higher_amp.mat
    load PSF_SCI_REF_LDFC_09_08_2018_oneoverf_higher_amp.mat
    expT = 5*10^5;% exposure time of image set [microseconds]
    PSFmax = 0.0873*expT; % Determined on bench [counts]
    contrast_logscale_factor = 1/PSFmax;
    load RESIDUAL_PHASE_MAT_oneoverf_09_08_2018_200modes_higher_amp.mat
    load ABERRATED_PHASE_MAT_oneoverf_09_08_2018_200modes_higher_amp.mat
    load LDFC_PHASE_MAT_oneoverf_09_08_2018_200modes_higher_amp.mat

    cminCONTRAST = -3.4;
    cmaxCONTRAST = -2.2;
elseif datachoice == 2
    dataname = '_1_f_focused_100modes_';
    load PSF_SCI_CUBE_ABERRATED_09_09_2018_oneoverf_higher_amp_100modes_atFocus.mat
    load PSF_SCI_CUBE_LDFC_09_09_2018_oneoverf_higher_amp_100modes_atFocus.mat
    load PSF_SCI_REF_AB_09_09_2018_oneoverf_higher_amp_100modes_atFocus.mat
    load PSF_SCI_REF_LDFC_09_09_2018_oneoverf_higher_amp_100modes_atFocus.mat
    expT = 4*10^5;% exposure time of image set [microseconds]
    PSFmax = 0.0873*expT; % Determined on bench [counts]
    contrast_logscale_factor = 1/PSFmax;
    load RESIDUAL_PHASE_MAT_oneoverf_09_09_2018_100modes_atFocus.mat
    load ABERRATED_PHASE_MAT_oneoverf_09_09_2018_100modes_atFocus.mat
    load LDFC_PHASE_MAT_oneoverf_09_09_2018_100modes_atFocus.mat

    cminCONTRAST = -3.4;
    cmaxCONTRAST = -2.2;
elseif datachoice == 3
    dataname = '_1_f_focused_200modes_';
    load PSF_SCI_CUBE_ABERRATED_09_10_2018_oneoverf_higher_amp_200modes_atFocus.mat
    load PSF_SCI_CUBE_LDFC_09_10_2018_oneoverf_higher_amp_200modes_atFocus.mat
    load PSF_SCI_REF_AB_09_10_2018_oneoverf_higher_amp_200modes_atFocus.mat
    load PSF_SCI_REF_LDFC_09_10_2018_oneoverf_higher_amp_200modes_atFocus.mat
    expT = 4*10^5;% exposure time of image set [microseconds]
    PSFmax = 0.0873*expT; % Determined on bench [counts]
    contrast_logscale_factor = 1/PSFmax;

    cminCONTRAST = -3.4;
    cmaxCONTRAST = -2.2;
elseif datachoice == 4
    dataname = '_1_f_focused_200modes_';
    load PSF_SCI_CUBE_ABERRATED_09_10_2018_416screens_oneoverf_higher_amp_200modes_atFocus_FAIL.mat
    load PSF_SCI_CUBE_LDFC_09_10_2018_416screens_oneoverf_higher_amp_200modes_atFocus_FAIL.mat
    load PSF_SCI_REF_AB_09_10_2018_416screens_oneoverf_higher_amp_200modes_atFocus_FAIL.mat
    load PSF_SCI_REF_LDFC_09_10_2018_416screens_oneoverf_higher_amp_200modes_atFocus_FAIL.mat
    expT = 4*10^5;% exposure time of image set [microseconds]
    PSFmax = 0.0873*expT; % Determined on bench [counts]
    contrast_logscale_factor = 1/PSFmax;
    load RESIDUAL_PHASE_MAT_oneoverf_09_10_2018_200modes_atFocus_416screensFAIL.mat
    load ABERRATED_PHASE_MAT_oneoverf_09_10_2018_200modes_atFocus_416screensFAIL.mat
```

```
    load LDFC_PHASE_MAT_oneoverf_09_10_2018_200modes_atFocus_416screensFAIL.mat

    cminCONTRAST = -3.4;
    cmaxCONTRAST = -2.2;
end
disp('-------------------------------------------------------------------')
numSCREENS = size(PSF_SCI_CUBE_ABERRATED,3);
disp(['Run full data cube of ',num2str(numSCREENS),' screens?'])
disp('NO           [0]')
disp('YES          [1]')
lengthchoice = input(':');
if lengthchoice == 0
    disp(['Use _____ of ',num2str(numSCREENS),' screens:'])
    numSCREENS = input(':');
end
disp('-------------------------------------------------------------------')
disp('-------------------------------------------------------------------')
disp('Choose dark hole extent: ')
disp('[Suggested: 4 - 11 lambda/D]')
IWA = input('IWA:  ');
OWA = input('OWA:  ');
disp('-------------------------------------------------------------------')
%---------------------------------------------------------------------------
%% CHOOSE ROI TO PLOT
%---------------------------------------------------------------------------
disp('-------------------------------------------------------------------')
disp('Choose ROI:')
disp('Full PSFs:                   [0]')
disp('Dark holes:                  [1]')
disp('Spatial frequency binning:   [2]')
ROIchoice = input(':');
disp('-------------------------------------------------------------------')

%---------------------------------------------------------------------------
%% DATA SAVING CHOICE
disp('-------------------------------------------------------------------')
disp('Choose how to save data:')
disp('Save movie:                                                         [0]')
disp('Save contrast stabilization plots:                                  [1]')
disp('Save DH convergence plots:                                          [2]')
disp('Save movie + contrast stabilization plots + DH convergence plots:   [3]')
disp('Do not save results:                                                [4]')
savechoice = input(':');
disp('-------------------------------------------------------------------')
todaysdate = date;
datatitle = char(horzcat('Testbed_LDFC_',dataname,'IWA_',num2str(IWA),'lamD_','OWA_',num2str(OWA),'lamD_'...
,num2str(numSCREENS),'screens'));

dircheck = exist(datatitle,'dir');

cd 'C:\Users\klmil\OneDrive\Documents\GitHub\Doctoral-Research\TESTBED-SIM-INTERFACE-CODE\...
TIME_EVOLVING_PHASE_SCREENS\TESTBED_DATA\TESTBED_DATA_ANALYSIS_RESULTS'
if dircheck == 7
    cd(datatitle)
else
    mkdir(datatitle)
end
%---------------------------------------------------------------------------
%% CROP DATA
%---------------------------------------------------------------------------
xcenUPPER = 242;
ycenUPPER = 109;

xcenLOWER = 245;
ycenLOWER = 287;

cropdim = 120;

LDFC_ref_UPPER = imcrop(PSF_SCI_REF_LDFC,[(xcenUPPER-cropdim/2) (ycenUPPER-cropdim/2) (cropdim-1) (cropdim-1)]);
LDFC_ref_LOWER = fliplr(imcrop(PSF_SCI_REF_LDFC,[(xcenLOWER-cropdim/2) (ycenLOWER-cropdim/2) (cropdim-1) ...
      (cropdim-1)]));
```

```
AB_ref_UPPER = imcrop(PSF_SCI_REF_AB,[(xcenUPPER-cropdim/2) (ycenUPPER-cropdim/2) (cropdim-1) (cropdim-1)]);
AB_ref_LOWER = fliplr(imcrop(PSF_SCI_REF_AB,[(xcenLOWER-cropdim/2) (ycenLOWER-cropdim/2) (cropdim-1) ...
      (cropdim-1)]));

ABERRATED_CUBE_UPPER = zeros(cropdim,cropdim,size(PSF_SCI_CUBE_ABERRATED,3));
ABERRATED_CUBE_LOWER = zeros(cropdim,cropdim,size(PSF_SCI_CUBE_ABERRATED,3));
LDFC_CUBE_UPPER = zeros(cropdim,cropdim,size(PSF_SCI_CUBE_ABERRATED,3));
LDFC_CUBE_LOWER = zeros(cropdim,cropdim,size(PSF_SCI_CUBE_ABERRATED,3));

for i = 1:numSCREENS
    ABERRATED_CUBE_UPPER(:,:,i) = imcrop(PSF_SCI_CUBE_ABERRATED(:,:,i),[(xcenUPPER-cropdim/2) ...
          (ycenUPPER-cropdim/2) (cropdim-1) (cropdim-1)]);
    ABERRATED_CUBE_LOWER(:,:,i) = fliplr(imcrop(PSF_SCI_CUBE_ABERRATED(:,:,i),[(xcenLOWER-cropdim/2) ...
          (ycenLOWER-cropdim/2) (cropdim-1) (cropdim-1)]));
    LDFC_CUBE_UPPER(:,:,i) = imcrop(PSF_SCI_CUBE_LDFC(:,:,i),[(xcenUPPER-cropdim/2) (ycenUPPER-cropdim/2) ...
          (cropdim-1) (cropdim-1)]);
    LDFC_CUBE_LOWER(:,:,i) = fliplr(imcrop(PSF_SCI_CUBE_LDFC(:,:,i),[(xcenLOWER-cropdim/2) ...
          (ycenLOWER-cropdim/2) (cropdim-1) (cropdim-1)]));
end
%-------------------------------------------------------------------------
%% CREATE MASK
%-------------------------------------------------------------------------
% pixel scale: 1 pixel = 0.25 lambda/D or 4 pixels = 1 lambda/D
pixelscale = 0.25;
x = linspace(-1,1,cropdim);
[X,Y] = meshgrid(x,x);
R = sqrt(X.^2 + Y.^2);
if ROIchoice == 0
    DHLimit = -floor(cropdim/2);
    numBINS = 1;
elseif ROIchoice == 1
    DHLimit = 0;
    numBINS = 1;
elseif ROIchoice == 2
    DHLimit = 0;
    numBINS = OWA - IWA; % Returns 1 lambda/D bins
end
    IWA_pixels = IWA/pixelscale;
    OWA_pixels = OWA/pixelscale;
    lamDbins = linspace(IWA,OWA,numBINS+1);
    lamDbins_pixels = linspace(IWA_pixels,OWA_pixels,numBINS + 1);
    r = 2.*lamDbins_pixels./cropdim;
    mask = zeros(cropdim,cropdim,numBINS);
    for i = 1:numBINS
        mask(:,:,i) = (abs(R<r(i+1))-abs(R<r(i))).*(X>DHLimit);
    end
%-------------------------------------------------------------------------
%% DARK HOLE COUNTS
%-------------------------------------------------------------------------

DH_REF_U = zeros(1,numBINS);
DH_REF_L = zeros(1,numBINS);
DH_ABERRATED_UPPER_COUNTS = zeros(numBINS,numSCREENS);
DH_LDFC_UPPER_COUNTS = zeros(numBINS,numSCREENS);
DH_ABERRATED_LOWER_COUNTS = zeros(numBINS,numSCREENS);
DH_LDFC_LOWER_COUNTS = zeros(numBINS,numSCREENS);

for j = 1:numBINS

    DH_REF_U(j) = mean2(AB_ref_UPPER(mask(:,:,j) == 1)).*contrast_logscale_factor;
    DH_REF_L(j) = mean2(AB_ref_LOWER(mask(:,:,j) == 1)).*contrast_logscale_factor;
    for i = 1:numSCREENS

        im_AB_U = abs(ABERRATED_CUBE_UPPER(:,:,i));
        im_LDFC_U = abs(LDFC_CUBE_UPPER(:,:,i));
        im_AB_L = abs(ABERRATED_CUBE_LOWER(:,:,i));
        im_LDFC_L = abs(LDFC_CUBE_LOWER(:,:,i));


        DH_ABERRATED_UPPER_COUNTS(j,i) = mean2(im_AB_U(mask(:,:,j) == 1)).*contrast_logscale_factor;
        DH_LDFC_UPPER_COUNTS(j,i) = mean2(im_LDFC_U(mask(:,:,j) == 1)).*contrast_logscale_factor;
```

```
        DH_ABERRATED_LOWER_COUNTS(j,i) = mean2(im_AB_L(mask(:,:,j) == 1)).*contrast_logscale_factor;
        DH_LDFC_LOWER_COUNTS(j,i) = mean2(im_LDFC_L(mask(:,:,j) == 1)).*contrast_logscale_factor;
    end
end

if ROIchoice ≠ 2
    figure;
    plot(log10(DH_ABERRATED_UPPER_COUNTS),'r','LineWidth',3);hold on
    plot(log10(mean(DH_ABERRATED_UPPER_COUNTS).*ones(1,numSCREENS)),'--r','LineWidth',3);hold on
    plot(log10(DH_LDFC_UPPER_COUNTS),'g','LineWidth',3);hold on
    plot(log10(mean(DH_LDFC_UPPER_COUNTS).*ones(1,numSCREENS)),'--g','LineWidth',3);hold on
    plot(log10(DH_REF_U.*ones(1,numSCREENS)),'b','LineWidth',3)
    grid minor;
    xlabel('screen #','FontSize',18);ylabel('dark hole log scale contrast','FontSize',18)
    title('Upper Dark Hole Contrast','FontSize',18)
    legend('Aberrated DH contrast','average contrast','LDFC corrected DH contrast','average contrast','ideal ...
         DH contrast')
    xlim([1 numSCREENS]);
%     ylim([cminCONTRAST cmaxCONTRAST])

    figure;
    plot(log10(DH_ABERRATED_LOWER_COUNTS),'r','LineWidth',3);hold on
    plot(log10(mean(DH_ABERRATED_LOWER_COUNTS)).*ones(1,numSCREENS),'--r','LineWidth',3);hold on
    plot(log10(DH_LDFC_LOWER_COUNTS),'g','LineWidth',3);hold on
    plot(log10(mean(DH_LDFC_LOWER_COUNTS)).*ones(1,numSCREENS),'--g','LineWidth',3);hold on
    plot(log10(DH_REF_L.*ones(1,numSCREENS)),'b','LineWidth',3)
    grid minor;
    xlabel('screen #','FontSize',18);ylabel('dark hole contrast [counts]','FontSize',18)
    title('Lower Dark Hole Contrast','FontSize',18)
    legend('Aberrated DH contrast','average contrast','LDFC corrected DH contrast','average contrast','ideal ...
         DH contrast')
    xlim([1 numSCREENS]);
%     ylim([cminCONTRAST cmaxCONTRAST])
else
    for j = 1:numBINS
        figure;
        subplot(1,2,1)
        plot(real(log10(DH_ABERRATED_UPPER_COUNTS(j,:))),'r','LineWidth',3);hold on
        plot(real(log10(mean(DH_ABERRATED_UPPER_COUNTS(j,:))).*ones(1,numSCREENS)),'--r','LineWidth',3);hold on
        plot(real(log10(DH_LDFC_UPPER_COUNTS(j,:))),'g','LineWidth',3);hold on
        plot(real(log10(mean(DH_LDFC_UPPER_COUNTS(j,:))).*ones(1,numSCREENS)),'--g','LineWidth',3);hold on
        plot(real(log10(DH_REF_U(j).*ones(1,numSCREENS))),'b','LineWidth',3)
        grid minor;
        xlabel('screen #','FontSize',18);ylabel('log_1_0 scale contrast','FontSize',18)
        title(['Upper Dark Hole Speckle Contrast: ',num2str(lamDbins(j)),' - ...
             ',num2str(lamDbins(j+1)),'\lambda/D'],'FontSize',18)
        legend('Aberrated DH contrast','average contrast','LDFC corrected DH contrast','average ...
             contrast','ideal DH contrast','Location','best')
        xlim([1 numSCREENS]);
        ylim([cminCONTRAST cmaxCONTRAST])

        subplot(1,2,2)
        plot(real(log10(DH_ABERRATED_LOWER_COUNTS(j,:))),'r','LineWidth',3);hold on
        plot(real(log10(mean(DH_ABERRATED_LOWER_COUNTS(j,:)))).*ones(1,numSCREENS),'--r','LineWidth',3);hold on
        plot(real(log10(DH_LDFC_LOWER_COUNTS(j,:))),'g','LineWidth',3);hold on
        plot(real(log10(mean(DH_LDFC_LOWER_COUNTS(j,:)))).*ones(1,numSCREENS),'--g','LineWidth',3);hold on
        plot(real(log10(DH_REF_L(j).*ones(1,numSCREENS))),'b','LineWidth',3)
        grid minor;
        xlabel('screen #','FontSize',18);ylabel('log_1_0 scale contrast','FontSize',18)
        title(['Lower Dark Hole Speckle Contrast: ',num2str(lamDbins(j)),' - ...
             ',num2str(lamDbins(j+1)),'\lambda/D'],'FontSize',18)
        legend('Aberrated DH contrast','average contrast','LDFC corrected DH contrast','average ...
             contrast','ideal DH contrast','Location','best')
        xlim([1 numSCREENS]);
        ylim([cminCONTRAST cmaxCONTRAST])
        if ((savechoice == 1) || (savechoice == 3))
            set(gcf, 'Position', get(0, 'Screensize'));
            datatitle_jpg = horzcat(dataname,'_',num2str(lamDbins(j)),'_',num2str(lamDbins(j+1)),'lamD',...
char('_contrast_stabilization.jpg'));
            datatitle_fig = horzcat(dataname,'_',num2str(lamDbins(j)),'_',num2str(lamDbins(j+1)),'lamD',...
char('_contrast_stabilization.fig'));
```

```
            set(gcf, 'Position', get(0, 'Screensize'));
            cd 'C:\Users\klmil\OneDrive\Documents\GitHub\Doctoral-Research\TESTBED-SIM-INTERFACE-CODE\...
TIME_EVOLVING_PHASE_SCREENS\TESTBED_DATA\TESTBED_DATA_ANALYSIS_RESULTS'
            cd(datatitle)
            saveas(gcf,datatitle_jpg,'jpg')
            saveas(gcf,datatitle_fig,'fig')
        end
        contrastmin = find(DH_LDFC_LOWER_COUNTS(1,1:100) == min(DH_LDFC_LOWER_COUNTS(1,1:100)),1,'first');

    end
end

%-----------------------------------------------------------------------------
%% PLOT SPECKLE AND ASSOCIATED PHASE IMAGES
%-----------------------------------------------------------------------------
if ((savechoice == 0) || (savechoice == 3))
    cd 'C:\Users\klmil\OneDrive\Documents\GitHub\Doctoral-Research\TESTBED-SIM-INTERFACE-CODE\...
TIME_EVOLVING_PHASE_SCREENS\TESTBED_DATA\TESTBED_DATA_ANALYSIS_RESULTS'
    cd(datatitle)
    filename_video = horzcat(datatitle,char('.avi'));
    v = VideoWriter(filename_video);
    open(v);
end

cmaxPUPIL = max2(CONVERT_MIRROR_UNITS_TO_NM(ABERRATED_PHASE_MAT));
cminPUPIL = min2(CONVERT_MIRROR_UNITS_TO_NM(ABERRATED_PHASE_MAT));

cmax = max2(sum(mask,3).*contrast_logscale_factor.*((ABERRATED_CUBE_UPPER(:,:,1)) - (AB_ref_UPPER)));
cmin = -cmax;

 numticks = 7;

 figure;
for i = 1:numSCREENS
    subplot(2,4,1);imagesc(sum(mask,3).*contrast_logscale_factor.*((ABERRATED_CUBE_UPPER(:,:,i)) - ...
         (AB_ref_UPPER)));daspect([1 1 1]);caxis([cmin ...
         cmax]);title({[num2str(i),'/',num2str(numSCREENS)],'Upper Dark Hole','Aberrated'},'FontSize',14);
    xticks(linspace(1, cropdim, numticks));xticklabels(linspace(-15 , 15 , ...
         numticks));xlabel('\lambda/D','FontSize',14)
    yticks(linspace(1, cropdim, numticks));yticklabels(linspace(-15 , 15 , ...
         numticks));ylabel('\lambda/D','FontSize',14)
    drawcircle_color(11./pixelscale,'r',cropdim,cropdim,0,0,3);
    subplot(2,4,2);imagesc(sum(mask,3).*contrast_logscale_factor.*((LDFC_CUBE_UPPER(:,:,i)) - ...
         (AB_ref_UPPER)));daspect([1 1 1]);caxis([cmin cmax]);title({'Upper Dark Hole','LDFC - ...
         Corrected'},'FontSize',14);
    xticks(linspace(1, cropdim, numticks));xticklabels(linspace(-15 , 15 , ...
         numticks));xlabel('\lambda/D','FontSize',14)
    yticks(linspace(1, cropdim, numticks));yticklabels(linspace(-15 , 15 , ...
         numticks));ylabel('\lambda/D','FontSize',14)
    drawcircle_color(11./pixelscale,'r',cropdim,cropdim,0,0,3);
    subplot(2,4,3);imagesc(sum(mask,3).*contrast_logscale_factor.*((ABERRATED_CUBE_LOWER(:,:,i)) - ...
         (LDFC_ref_LOWER)));daspect([1 1 1]);caxis([cmin cmax]);title({'Lower Dark ...
         Hole','Aberrated'},'FontSize',14);
    xticks(linspace(1, cropdim, numticks));xticklabels(linspace(-15 , 15 , ...
         numticks));xlabel('\lambda/D','FontSize',14)
    yticks(linspace(1, cropdim, numticks));yticklabels(linspace(-15 , 15 , ...
         numticks));ylabel('\lambda/D','FontSize',14)
    drawcircle_color(11./pixelscale,'r',cropdim,cropdim,0,0,3);
    subplot(2,4,4);imagesc(sum(mask,3).*contrast_logscale_factor.*((LDFC_CUBE_LOWER(:,:,i)) - ...
         (LDFC_ref_LOWER)));daspect([1 1 1]);caxis([cmin cmax]);title({'Lower Dark Hole','LDFC - ...
         Corrected'},'FontSize',14);
    xticks(linspace(1, cropdim, numticks));xticklabels(linspace(-15 , 15 , ...
         numticks));xlabel('\lambda/D','FontSize',14)
    yticks(linspace(1, cropdim, numticks));yticklabels(linspace(-15 , 15 , ...
         numticks));ylabel('\lambda/D','FontSize',14)
    drawcircle_color(11./pixelscale,'r',cropdim,cropdim,0,0,3);
    g = colorbar('southoutside','Position',[0.13 0.5 0.78 0.03],'FontSize',14);
    set(get(g,'title'),'string','Speckle Contrast','FontSize',14);

    pupilAB = CONVERT_MIRROR_UNITS_TO_NM(reshape(ABERRATED_PHASE_MAT(:,i),[32 32]));
    pupilDM = CONVERT_MIRROR_UNITS_TO_NM(reshape(LDFC_PHASE_MAT(:,i),[32 32]));
```

```
    pupilLDFC = CONVERT_MIRROR_UNITS_TO_NM(reshape(RESIDUAL_PHASE_MAT(:,i),[32 32]));
    subplot(2,4,5);imagesc(circshift(pupilAB,[0 -3]));axis off;axis square;colormap jet;caxis([cminPUPIL ...
        cmaxPUPIL]);title('Aberrated Pupil Phase','FontSize',14)
    subplot(2,4,6);imagesc(circshift(pupilDM,[0 -3]));axis off;axis square;colormap jet;title('LDFC DM ...
        Correction','FontSize',14)
    h = colorbar('southoutside','Position',[0.13 0.05 0.57 0.03],'FontSize',14);caxis([cminPUPIL cmaxPUPIL]);
    set(get(h,'title'),'string','Wavefront Error P-V [nm]','FontSize',14);
    subplot(2,4,7);imagesc(circshift(pupilLDFC,[0 -3]));axis off;axis square;colormap jet;caxis([cminPUPIL ...
        cmaxPUPIL]);title('Residual Pupil Phase','FontSize',14)
    colormap jet
    drawnow;
    if ((savechoice == 0) || (savechoice == 3))
        set(gcf, 'Position', get(0, 'Screensize'));
        frame = getframe(gcf);
        writeVideo(v,frame);
    end
    clf
end
if ((savechoice == 0) || (savechoice == 3))
    close(v);
end

%--------------------------------------------------------------------------
%--------------------------------------------------------------------------
%% PLOT DARK HOLE CONVERGENCE
%--------------------------------------------------------------------------
cmax = max2(sum(mask,3).*contrast_logscale_factor.*((ABERRATED_CUBE_UPPER(:,:,1)) - (AB_ref_UPPER)));
cmin = -cmax;

numticks = 7;
n_conv_screens = 8;
screennumber = round(linspace(1,contrastmin,8));

%--------------------------UPPER LDFC CUBE-------------------------------
for i = 1:n_conv_screens
    figure(28);
     if i == 1
        subplot(2,n_conv_screens/2,1);imagesc(sum(mask,3).*contrast_logscale_factor.*...
((ABERRATED_CUBE_UPPER(:,:,1)) - (AB_ref_UPPER)));daspect([1 1 1]);caxis([cmin cmax]);title('Initial ...
     Aberration','FontSize',14);
    else
        subplot(2,n_conv_screens/2,i);imagesc(sum(mask,3).*contrast_logscale_factor.*...
((LDFC_CUBE_UPPER(:,:,screennumber(i-1))) - (AB_ref_UPPER)));daspect([1 1 1]);caxis([cmin ...
     cmax]);title(['Iteration ',num2str(screennumber(i-1))],'FontSize',14)
    end

    xticks(linspace(1, cropdim, numticks));xticklabels(linspace(-15 , 15 , ...
        numticks));xlabel('\lambda/D','FontSize',10)
    yticks(linspace(1, cropdim, numticks));yticklabels(linspace(-15 , 15 , ...
        numticks));ylabel('\lambda/D','FontSize',10)
    drawcircle_color(11./pixelscale,'r',cropdim,cropdim,0,0,3);
end
    h = colorbar('southoutside','Position',[0.13 0.47 0.78 0.03],'FontSize',10);
    set(get(h,'title'),'string','Speckle Contrast','FontSize',14);
    colormap jet;
if ((savechoice == 2) || (savechoice == 3))
        set(gcf, 'Position', get(0, 'Screensize'));
        datatitle_jpg = horzcat(datatitle,char('_DH_CONVERGENCE_LDFC_upper.jpg'));
        datatitle_fig = horzcat(datatitle,char('_DH_CONVERGENCE_LDFC_upper.fig'));
        set(gcf, 'Position', get(0, 'Screensize'));
        cd 'C:\Users\klmil\OneDrive\Documents\GitHub\Doctoral-Research\TESTBED-SIM-INTERFACE-CODE\...
TIME_EVOLVING_PHASE_SCREENS\TESTBED_DATA\TESTBED_DATA_ANALYSIS_RESULTS'
        cd(datatitle)
        saveas(gcf,datatitle_jpg,'jpg')
        saveas(gcf,datatitle_fig,'fig')
end

%--------------------------LOWER LDFC CUBE-------------------------------
for i = 1:n_conv_screens
    figure(30);
     if i == 1
```

```
        subplot(2,n_conv_screens/2,1);imagesc(sum(mask,3).*contrast_logscale_factor.*...
((ABERRATED_CUBE_LOWER(:,:,1)) - (AB_ref_LOWER)));daspect([1 1 1]);caxis([cmin cmax]);title('Initial ...
    Aberration','FontSize',14);
    else
        subplot(2,n_conv_screens/2,i);imagesc(sum(mask,3).*contrast_logscale_factor.*...
((LDFC_CUBE_LOWER(:,:,screennumber(i-1))) - (AB_ref_LOWER)));daspect([1 1 1]);caxis([cmin ...
    cmax]);title(['Iteration ',num2str(screennumber(i-1))],'FontSize',14);
    end
    xticks(linspace(1, cropdim, numticks));xticklabels(linspace(-15 , 15 , ...
        numticks));xlabel('\lambda/D','FontSize',10)
    yticks(linspace(1, cropdim, numticks));yticklabels(linspace(-15 , 15 , ...
        numticks));ylabel('\lambda/D','FontSize',10)
    drawcircle_color(11./pixelscale,'r',cropdim,cropdim,0,0,3);
end
    k = colorbar('southoutside','Position',[0.13 0.47 0.78 0.03],'FontSize',10);
    set(get(k,'title'),'string','Speckle Contrast','FontSize',14);
    colormap jet;
if ((savechoice == 2) || (savechoice == 3))
        set(gcf, 'Position', get(0, 'Screensize'));
        datatitle_jpg = horzcat(datatitle,char('_DH_CONVERGENCE_LDFC_lower.jpg'));
        datatitle_fig = horzcat(datatitle,char('_DH_CONVERGENCE_LDFC_lower.fig'));
        set(gcf, 'Position', get(0, 'Screensize'));
        cd 'C:\Users\klmil\OneDrive\Documents\GitHub\Doctoral-Research\TESTBED-SIM-INTERFACE-CODE\...
TIME_EVOLVING_PHASE_SCREENS\TESTBED_DATA\TESTBED_DATA_ANALYSIS_RESULTS'
        cd(datatitle)
        saveas(gcf,datatitle_jpg,'jpg')
        saveas(gcf,datatitle_fig,'fig')
end

%% WRITE DATA TO FILE
cd 'C:\Users\klmil\OneDrive\Documents\GitHub\Doctoral-Research\TESTBED-SIM-INTERFACE-CODE\...
TIME_EVOLVING_PHASE_SCREENS\TESTBED_DATA\TESTBED_DATA_ANALYSIS_RESULTS'
cd(datatitle)

fileID = fopen('DATA_PARAMETERS.txt','w');
fprintf(fileID,todaysdate,' \r\n');
fprintf(fileID,' \r\n');
fprintf(fileID,' \r\n');
fprintf(fileID,'Spatial frequency content / WFS / number of control modes: ');
fprintf(fileID,dataname,'\r\n');
fprintf(fileID,' \r\n');
fprintf(fileID,' \r\n');
fprintf(fileID,'IWA [lambda/D]: ');
fprintf(fileID,'%d\r\n',IWA);
fprintf(fileID,' \r\n');
fprintf(fileID,'OWA [lambda/D]: ');
fprintf(fileID,'%d\r\n',OWA);
fprintf(fileID,' \r\n');
fprintf(fileID,'Max log scale speckle contrast: ');
fprintf(fileID,'%e\r\n',cmax);
fprintf(fileID,' \r\n');
fprintf(fileID,'Max pupil phase amplitude [nm]: ');
fprintf(fileID,'%g\r\n',cmaxPUPIL);
fprintf(fileID,' \r\n');
fprintf(fileID,'Minimum pupil phase amplitude [nm]: ');
fprintf(fileID,'%g\r\n',cminPUPIL);
fprintf(fileID,' \r\n');
fprintf(fileID,'Exposure time [microseconds]: ');
fprintf(fileID,'%e\r\n',expT);
fprintf(fileID,' \r\n');
fprintf(fileID,'PSF max counts: ');
fprintf(fileID,'%g\r\n',PSFmax);
fprintf(fileID,' \r\n');
fprintf(fileID,'Contrast scale factor [1/PSF max]: ');
fprintf(fileID,'%e\r\n',contrast_logscale_factor);
fprintf(fileID,' \r\n');
fprintf(fileID,'Number of screens: ');
fprintf(fileID,'%d\r\n',numSCREENS);
fclose(fileID);
```

REFERENCES

ALPAO (2017). Deformable mirrors. Technical report.

Bos, S. P., D. S. Doelman, J. de Boer, E. H. Por, B. Norris, M. J. Escuti, and F. Snik (2018). Fully broadband vAPP coronagraphs enabling polarimetric high contrast imaging. doi:10.1117/12.2312798.

Bottom, M., B. Femenia, E. Huby, D. Mawet, R. Dekany, J. Milburn, and E. Serabyn (2016). Speckle nulling wavefront control for Palomar and Keck. *SPIE*, **9909**, pp. 990955–990955–16. doi:10.1117/12.2233025.

Cady, E., C. Baranec, C. Beichman, D. Brenner, R. Burruss, J. Crepp, R. Dekany, D. Hale, L. Hillenbrand, S. Hinkley, E. R. Ligon, T. Lockhart, B. Oppenheimer, I. Parry, L. Pueyo, E. Rice, L. C. Roberts, J. Roberts, M. Shao, A. Sivaramakrishnan, R. Soummer, H. Tang, T. Truong, G. Vasisht, F. Vescelus, J. K. Wallace, C. Zhai, and N. Zimmerman (2013). Electric field conjugation with the Project 1640 coronagraph. *SPIE*, **8864**, pp. 88640K–88640K–9. doi:10.1117/12.2024635.

Close, L. et al. (2018). Optical and mechanical design status of the extreme AO coronagraphic instrument MagAO-X. In *Adaptive Optics System VI*, Proc. SPIE.

Delorme, J. R., Galicher, R., Baudoz, P., Rousset, G., Mazoyer, J., and Dupuis, O. (2016). Focal plane wavefront sensor achromatization: The multireference self-coherent camera. *Astronomy and Astrophysics*, **588**, p. A136. doi:10.1051/0004-6361/201527657.

Doelman, D. et al. (2018). Multiplexed holographic aperture masking with liquid-crystal geometric phase masks. In *Techniques I*, Proc. SPIE.

Fried, D. L. (1966). Optical Resolution Through a Randomly Inhomogeneous Medium for Very Long and Very Short Exposures. *J. Opt. Soc. Am.*, **56**(10), pp. 1372–1379. doi:10.1364/JOSA.56.001372.

Give'on, A., B. Kern, S. Shaklan, D. C. Moody, and L. Pueyo (2007). Broadband wavefront correction algorithm for high-contrast imaging systems. *SPIE*, **6691**, pp. 66910A–66910A–11. doi:10.1117/12.733122.

Goodman, J. (1996). *Introduction to Fourier Optics*. MaGraw-Hill, 2 edition.

Groff, T. D., A. J. Eldorado Riggs, B. Kern, and N. Jeremy Kasdin (2015). Methods and limitations of focal plane sensing, estimation, and control in high-contrast imaging. *Journal of Astronomical Telescopes, Instruments, and Systems*, **2**(1), p. 011009. doi:10.1117/1.JATIS.2.1.011009.

Guyon, O. (2005). Limits of Adaptive Optics for High-Contrast Imaging. *The Astrophysical Journal*, **629**(1), p. 592.

Guyon, O., J. Codona, K. Miller, J. Knight, and A. Rodack (February 2015). Wavefront Sensing, Control, and PSF Calibration. NASA-JPL LOWFSC Conference.

Guyon, O., B. Kern, A. Kuhnert, and A. Niessner (May 2014). Phase-Induced Amplitude Apodization (PIAA) Technology Development, Milestone 3: 10% Bandpass Contrast Demonstration. Technology Development for Exoplanet Missions Technology Milestone Report.

Guyon, O., T. Matsuo, and R. Angel (2009). Coronagraphic Low-Order Wave-Front Sensor: Principle and Application to a Phase-Induced Amplitude Coronagraph. *The Astrophysical Journal*, **693**(1), p. 75.

Guyon, O., K. Miller, J. Males, B. Kern, and R. Belikov (2018). Spectral LDFC: Stabilizing deep contrast for exoplanet imaging using out-of-band light. *Publications of the Astronomical Society of the Pacific*. In-progress.

Guyon, O., E. A. Pluzhnik, S. T. Ridgway, R. A. Woodruff, C. Blain, F. Martinache, and R. Galicher (2006). The Phase-Induced Amplitude Coronagraph (PIAA). *Proceedings of the International Astronomical Union*, **1**(C200), p. 385–392. doi: 10.1017/S174392130600963X.

Hecht, E. (2002). *Optics*. Pearson education. Addison-Wesley. ISBN 9780321188786.

Huby, E., M. Bottom, B. Femenia, H. Ngo, D. Mawet, E. Serabyn, and O. Absil (2017). On-sky performance of the QACITS pointing control technique with the Keck/NIRC2 vortex coronagraph. *AAP*, **600**, A46. doi:10.1051/0004-6361/201630232.

Jovanovic, N., F. Martinache, O. Guyon, C. Clergeon, G. Singh, T. Kudo, V. Garrel, K. Newman, D. Doughty, J. Lozi, J. Males, Y. Minowa, Y. Hayano, N. Takato, J. Morino, J. Kuhn, E. Serabyn, B. Norris, P. Tuthill, G. Schworer, P. Stewart, L. Close, E. Huby, G. Perrin, S. Lacour, L. Gauchet, S. Vievard, N. Murakami, F. Oshiyama, N. Baba, T. Matsuo, J. Nishikawa, M. Tamura, O. Lai, F. Marchis, G. Duchene, T. Kotani, and J. Woillez (2015). The Subaru Coronagraphic Extreme Adaptive Optics System: Enabling High-Contrast Imaging on Solar-System Scales. *PASP*, **127**, p. 890. doi:10.1086/682989.

Krist, J., B. Nemati, and B. Mennesson (2016). Numerical modeling of the proposed WFIRST-AFTA coronagraphs and their predicted performances. *Journal of Astronomical Telescopes, Instruments, and Systems*, **2**(1), 011003. doi: 10.1117/1.JATIS.2.1.011003.

Lumbres, J. et al. (2018). Modeling coronagraphic extreme wavefront control systems for high contrast imaging in ground and space telescope missions. In *Adaptive Optics System VI*, Proc. SPIE.

Males, J. R. and O. Guyon (2018). Ground-based adaptive optics coronagraphic performance under closed-loop predictive control. *Journal of Astronomical Telescopes, Instruments, and Systems*, **4**(1), 019001. doi:10.1117/1.JATIS.4.1.019001.

Males, J. R. and MagAO-X team (2017). MagAO-X Prelimnary Design Review. *Technical Document*.

Matthews, C., J. Crepp, G. Vasisht, and E. Cady (2017). Electric field conjugation for ground-based high-contrast imaging: robustness study and tests with the Project 1640 coronagraph. *Journal of Astronomical Telescopes, Instruments, and Systems*, **3**, pp. 3 – 3 – 12. doi:10.1117/1.JATIS.3.4.045001.

Mawet, D., J. Milli, Z. Wahhaj, D. Pelat, O. Absil, C. Delacroix, A. Boccaletti, M. Kasper, M. Kenworthy, C. Marois, B. Mennesson, and L. Pueyo (2014). Fundamental Limitations of High Contrast Imaging Set by Small Sample Statistics. *The Astrophysical Journal*, **792**(2), p. 97.

Mawet, D., L. Pueyo, and P. Lawson (2012). Review of small-angle coronagraphic techniques in the wake of ground-based second-generation adaptive optics systems. volume 8442 of *SPIE*, pp. 8442 – 8442 – 21. doi:10.1117/12.927245.

Miller, K. and O. Guyon (2016). Linear dark field control: simulation for implementation and testing on the UA wavefront control testbed. *SPIE*, **9909**, pp. 99094G–99094G–9. doi:10.1117/12.2232120.

Miller, K., O. Guyon, and J. Males (2017). Spatial linear dark field control: stabilizing deep contrast for exoplanet imaging using bright speckles. *Journal of Astronomical Telescopes, Instruments, and Systems*, **3**, pp. 3 – 3 – 11. doi:10.1117/1.JATIS.3.4.049002.

Newman, K. (2013). An introduction to off-axis parabolic mirrors. Technical report.

Optics, E. (2017). Off-axis parabolic first surface metal mirrors. Technical report.

Otten, G. P. P. L., F. Snik, M. A. Kenworthy, C. U. Keller, J. R. Males, K. M. Morzinski, L. M. Close, J. L. Codona, P. M. Hinz, K. J. Hornburg, L. L. Brickson, and M. J. Escuti (2017). On-sky Performance Analysis of the Vector Apodizing Phase Plate Coronagraph on MagAO/Clio2. *ApJ*, **834**, 175. doi:10.3847/1538-4357/834/2/175.

Poyneer, L. A. and J.-P. Véran (2005). Optimal modal Fourier-transform wavefront control. *J. Opt. Soc. Am. A*, **22**(8), pp. 1515–1526. doi:10.1364/JOSAA.22.001515.

Ragazzoni, R. (1996). Pupil plane wavefront sensing with an oscillating prism. *Journal of Modern Optics*, **43**(2), pp. 289–293. doi:10.1080/09500349608232742.

Roddier, F. (1999). *Adaptive Optics in Astronomy*. Cambridge University Press, 1 edition.

Ruffio, J.-B. (2014). *Non Common Path Aberrations Correction*. Master's thesis, ESO Adaptive Optics Department.

SHI, F. (2016). Low Order Wavefront Sensing and Control for WFIRST-AFTA Coronagraph. In *American Astronomical Society Meeting Abstracts*, volume 227 of *American Astronomical Society Meeting Abstracts*, p. 430.04.

Singh, G., J. Lozi, O. Guyon, P. Baudoz, N. Jovanovic, F. Martinache, T. Kudo, E. Serabyn, and J. Kuhn (2015). On-Sky Demonstration of Low-Order Wavefront Sensing and Control with Focal Plane Phase Mask Coronagraphs. *Publications of the Astronomical Society of the Pacific*, **127**(955), p. 857.

Snellen, I. A. G. (2017). Detecting Proxima b's Atmosphere with JWST Targeting CO 2 at 15 microns Using a High-pass Spectral Filtering Technique. *The Astronomical Journal*, **154**(2), p. 77.

Snik, F., G. Otten, M. Kenworthy, M. Miskiewicz, M. Escuti, C. Packham, and J. Codona (2012). The vector-APP: a broadband apodizing phase plate that yields complementary PSFs. In *Modern Technologies in Space- and Ground-based Telescopes and Instrumentation II*, volume 8450 of *SPIE*, p. 84500M. doi:10.1117/12.926222.

Traub, W. and B. Oppenheimer (2010). Direct Imaging of Exoplanets. Exoplanets (Tucson: Univ. Arizona Press).

Tyson, R. K. (2015). *Principles of adaptive optics*. CRC press.

Van Gorkom, K., K. L. Miller, J. R. Males, O. Guyon, A. T. Rodack, J. Lumbres, and J. M. Knight (2018). Characterization of deformable mirrors for the MagAO-X project. In *Society of Photo-Optical Instrumentation Engineers (SPIE) Conference Series*, volume 10703 of *Society of Photo-Optical Instrumentation Engineers (SPIE) Conference Series*, p. 107035A. doi:10.1117/12.2323450.

Vogt, F., F. Martinache, O. Guyon, T. Yoshikawa, K. Yokochi, V. Garrel, and T. Matsuo (2011). Coronagraphic low-order wavefront sensor: Postprocessing sensitivity enhancer for high-performance coronagraphs. *Publications of the Astronomical Society of the Pacific*, **123**(910), pp. 1434–1441. ISSN 0004-6280. doi:10.1086/663723.

Wilby, M. J., C. U. Keller, F. Snik, V. Korkiakoski, and A. G. M. Pietrow (2017). The coronagraphic Modal Wavefront Sensor: a hybrid focal-plane sensor for the high-contrast imaging of circumstellar environments. *AAP*, **597**, A112. doi:10.1051/0004-6361/201628628.

Zygo (2017). Verifire. Technical report.